Universitat de València

FACULTAT DE QUÍMICA

INSTITUTO DE CIENCIA MOLECULAR

Nuevos materiales moleculares de hierro(II) multipropiedad basados en el fenómeno de transición de espín

Programa de Doctorado:
3045 "Nanociencia y Nanotecnología"

Doctorando:
Lucía Piñeiro López

Director de la tesis:
Dr. José Antonio Real Cabezos

Abril, 2017

José Antonio Real Cabezos, Catedrático del Departamento de Química Inorgánica de la Universitat de València,

CERTIFICA:

Que la presente Tesis Doctoral, titulada:
Nuevos materiales moleculares de hierro(II) multipropiedad basados en el fenómeno de transición de espín, se ha realizado bajo su dirección en el Instituto de Ciencia Molecular (ICMol) en la Universitat de València por la Licenciada en Química Lucía Piñeiro López, y autoriza su presentación para ser calificada como Tesis Doctoral.

Abril, 2017

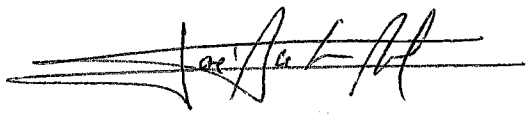

Dr. José Antonio Real Cabezos

AGRADECIMIENTOS

La realización de la presente Tesis Doctoral ha sido posible gracias a muchas personas cuya ayuda y apoyo me ha impulsado e inspirado durante estos últimos cinco años.

En primer lugar, agradezco a mi Director José Antonio Real y a Mª Carmen Muñoz, la posibilidad de realizar mi Tesis Doctoral en su grupo de investigación. Gracias por vuestra dedicación y el conocimiento que me habéis inculcado. Ha sido una experiencia muy enriquecedora. Muchas gracias por vuestra infinita paciencia, os pido disculpas por mis momentos de estrés máximo.

En segundo lugar, agradezco a los miembros del tribunal por acceder a formar parte del mismo y a los evaluadores por aceptar evaluar esta Tesis Doctoral.

En tercer lugar, agradezco a mis compañeros Zulema Arcís, Tania Romero, Maksym Seredyuk y Javier Valverde, su gran ayuda y apoyo en estos años. Gracias Zulema, por acogerme en el laboratorio e introducirme en el mundo SCO. Eres una persona maravillosa y una gran compañera. Gracias Tania, porque hemos tenido mil conversaciones y siempre me has aportado un punto de vista nuevo, una nueva perspectiva. Gracias Maksym, por tu paciencia y por tu ayuda tanto en el laboratorio como en la redacción de los artículos del bpb. Gracias Javi, porque me has ayudado y apoyado durante estos años, bien en el SQUID o en el laboratorio, o contándome alguna singularidad de SCO para que nuestro campo resulte más inspirador. Gracias por las anécdotas y mil chorradas que hemos compartido en el día a día y que hacen que esté a gusto las horas que echamos aquí que no son pocas.

En cuarto lugar, gracias Thais Grancha, por tu apoyo, por darle coherencia a mis embrollos mentales, por impulsarme siempre, por tus más que buenos consejos, por compartir tu experiencia y tu sentir conmigo. Sabes que has sido un gran apoyo para mí y que me tienes para lo que necesites.

En quinto lugar, gracias Néstor Calvo, porque, a pesar de que cuando nos conocimos, yo no te caí bien ni tu a mí tampoco, tardaste unas semanas en convertirte en mi gran amigo. A ti te agradezco mucho más que estos últimos cinco años, te

agradezco los otros cinco anteriores y los que vendrán, porque no te librarás de mí. Gracias por tu paciencia, tu buen humor, tu carácter más bien despreocupado que siempre me saca del vaso de agua que intenta ahogarme. Porque has sabido devolverme la cordura y el buen humor en muchos momentos en los que la toalla se hubiera quedado en el suelo y hasta la hubiera pisado.

En sexto lugar, gracias a los técnicos del ICMol Gloria Agustí y José María Martínez por su profesionalidad y su ayuda en lo que respecta a las medidas de magnetismo, DSC y TGA que han hecho posible la presente Tesis Doctoral. Gracias por ser siempre encantadores a pesar de la faena que os dan tanto los equipos como los que trabajamos en el ICMol.

En séptimo lugar, agradezco a Gábor Molnár y a Azzedine Bousseksou la oportunidad de realizar mi estancia en su grupo de investigación dónde aprendí a utilizar equipos muy diferentes y conocí otro enfoque del fenómeno SCO. Agradezco la ayuda y el apoyo prestado por todos los miembros del grupo Switchable Molecular Materials en Toulouse.

En octavo lugar, agradezco a Carlos Barreto, amigo y profesor, el infundirme conocimiento, herramientas y valor a la hora de comunicarme, ya sea conmigo misma o con otros en diversas situaciones. Gracias Carlos, porque me has dado muchísimas respuestas y me has regalado momentos de todo tipo, de risas, de lágrimas, de reflexión de anhelos, de esperanza.

En noveno lugar, agradezco a mi cuñado, Nicolás Dubarry, una de las personas más dispuestas y accesibles que he conocido. Porque emanas esa tranquilidad que si bien aún no he aprendido, al menos disfruto cuando estoy a tu lado o te cuento algo absurdo.

En décimo lugar, gracias a las personas más importantes de mi vida: mis padres, mi hermana y mis abuelas. Aquí lo suyo es llorar, pero esto no deja de ser un documento de acceso público, así que seré breve. Infinitas gracias, ¿por qué? Por todo. Por el apoyo de la más diversa naturaleza. Gracias, Ceci, por todas tus sesiones de coaching y de terapia que me han sacado de la caja en la que a veces me hubiera quedado a esperar, no sé muy bien qué. Por tus infinitas muestras de afecto, por tu dulzura, por tu paciencia, por tu ejemplo, eres una luchadora nata. Por brindarme tu

calor y tu color, que sola, muchas veces me impregno de distintos tonos de grises. Gracias a mis abuelas, mis soles, que tienen fe en mí para lo que sea. Si digo que voy a la Luna, me preparáis el tupper para el viaje. Gracias por vuestra fuerza de voluntad y dedicación, por vuestro amor incondicional para con todos en la familia. Padres, infinitas gracias por vuestro amor, por cuidarme, por mimarme, por soltarme alguna que otra perla que me ha venido bien oír. En muchas situaciones he podido apreciar vuestra entereza, fuerza de voluntad, valor, sabiduría, paciencia, entrega a Ceci, a mí, a vuestros padres, a vuestros amigos. Gracias, porque cada uno a su manera y cada uno en su terreno, os olvidáis de vosotros para cuidar de Ceci y de mí. Os amo y os admiro.

A mis padres

A mi Ceci

Indice

Capítulo 1.- Introducción

1.1.- Introducción general al fenómeno de la transición de espín 5
1.1.1.- Teoría del campo de ligandos y transiciones de espín 6
1.1.2.- Fotoconversión de estados de espín 12
1.1.3.- Comportamiento colectivo del conjunto de los centros activos: cooperatividad 15
1.1.4.- Detección de la transición de espín 19
1.2.- Objetivos 20
1.3.- Metodología 21
1.4.- Blibliografía 22

Capítulo 2.- Electronic structure modulation in an exceptionally stable non-heme nitrosyl iron(II) spin-crossover complex

2.1.- Abstract 27
2.2.- Introduction 27
2.3.- Results and discussion 30
2.3.1.- Synthesis 30
2.3.2.- Magnetic properties 30
2.3.3.- Spectroscopic characterization of compound 1 32
2.3.3.1.- EPR spectra 32
2.3.3.2.- Mössbauer spectra 34
2.3.3.3.- Electronic spectra 34
2.3.3.4.- Vibrational spectra 36
2.3.3.5.- Structure of compound 1 37
2.3.3.6.- Electronic structure modeling 43
2.4.- Conclusion 47
2.5.- Experimental Section 49
2.5.1.- General 49
2.5.1.1.- Single-crystal X-ray measurements 50
2.5.1.2.- Materials 50
2.5.2.- Computational details 51
2.6.- References 51
2.7.- Supporting Information 56

Capítulo 3.- Clathration of five-membered aromatic rings in the bimetallic spin crossover metal-organic framework $[Fe(TPT)_{2/3}\{M^{I}(CN)_2\}_2]\cdot G$ (M^{I} = Ag, Au)

3.1.- Abstract 67
3.2.- Introduction 67
3.3.- Results 69
3.3.1.- Synthesis 69
3.3.2.- Structure 70
3.3.3.- Spin-crossover properties 78
3.4.- Discussion 80
3.5.- Conclusion 83
3.6.- Experimental Section 83
3.6.1.- Materials 83
3.6.2.- Crystal growth 83
3.6.3.- Physical characterization 84
3.6.4.- Single-crystal X-ray diffraction 84
3.7.- References 85
3.8.- Supporting Information 88

Capítulo 4.- Two- and one-step cooperative spin transitions in Hofmann-like clathrates with enhanced loading capacity

4.1.- Abstract 95
4.2.- Introduction 95
4.3.- Results and discussion 96
4.3.1.- Synthesis 96
4.3.2.- Structure 97
4.3.3.- Magnetic and calorimetric properties 98
4.3.4.- Mössbauer spectra 100
4.4.- Conclusion 101
4.5.- Notes and references 102
4.6.- Supporting Information 104

Capítulo 5.- Guest induced strong cooperative one and two-step spin crossover in a highly porous iron(II) Hofmann-type metal-organic framework

5.1.- Abstract 117
5.2.- Introduction 117
5.3.- Results 119
5.3.1.- Synthesis and stability 119
5.3.2.- Magnetic Properties 120
5.3.3.- Mössbauer studies 123
5.3.4.- Calorimetric studies 125
5.3.5.- Single crystal X-ray studies 126
5.4.- Concluding remarks 134
5.5.- Experimental Section 136
5.5.1.- Physical measurements 136
5.5.2.- Single crystal X-ray diffraction 136
5.5.3.- Synthesis 137
5.6.- References 138
5.7.- Supporting Information 140

Capítulo 6.- Spin-crossover behaviour in a new family of porous coordination polymers formulated $\{Fe(3,8\text{-phen})_2[Au(CN)_2]_2 \cdot G\}$

6.1.- Abstract 153
6.2.- Introduction 153
6.3.- Results 156
6.3.1.- Synthesis 156
6.3.2.- Magnetic Properties 156
6.3.3.- Calorimetric and thermogravimetric studies 161
6.3.4.- Structure 165
6.4.- Discussion 171
6.5.- Conclusion 176
6.6.- Experimental Section 177
6.6.1.- Materials 177
6.6.2.- Crystal growth 177
6.6.3.- Physical characterization 178

6.6.4.- X-ray diffraction 178
6.6.4.1.- Single-crystal X-ray diffraction 178
6.6.4.2.- Powder X-ray diffraction 179
6.7.- References 179
6.8.- Supporting Information 183

Capítulo 7.- Conclusiones finales

Conclusiones 193
Conclusions 205

Apéndice
Lista de Publicaciones 217
Artículos 219

Nuevos materiales moleculares de hierro(II) multipropiedad basados en el fenómeno de transición de espín

RESUMEN

En esta Tesis Doctoral se presenta la síntesis y caracterización de una serie de materiales multifuncionales de Fe^{II} que tienen como denominador común el fenómeno de transición de espín (TS). El objetivo general es investigar sinergias entre la TS y otra propiedad fisicoquímica mediante el estudio de su estructura molecular y sus propiedades magnéticas y calorimétricas, entre otras.

En el Capítulo Uno se exponen los conceptos más relevantes del fenómeno TS en el cual los centros TS experimentan una conversión de espín HS↔LS (HS: estado de espín alto, LS: estado de espín bajo) en respuesta a un estímulo externo tal como temperatura, presión, luz o la presencia de analitos. En particular, una TS térmicamente inducida es un proceso controlado por la entropía cuya mayor contribución proviene de cambios en las vibraciones intramoleculares y, en menor medida, en las vibraciones intermoleculares. En concreto para centros de Fe^{II}, alrededor del 25% de la entropía asociada a la TS es de origen electrónico y se debe al notable cambio en la multiplicidad de espín que experimentan los centros de Fe^{II} durante el proceso HS↔LS (HS, S = 2↔LS, S = 0). De forma análoga, la foto-irradiación de un sistema TS de Fe^{II} en estado sólido a temperatura baja puede inducir una conversión parcial o completa de los centros de Fe^{II} en el estado LS al estado metaestable HS* (efecto LIESST: Light Induced Excited Spin State Trapping). La subsiguiente irradiación con luz roja (λ = 820 nm) puede inducir la transformación de los centros de Fe^{II} en el estado HS* al estado LS termodinámicamente estable (efecto LIESST inverso). Ambos efectos evidencian que los sistemas TS de Fe^{II} son potencialmente útiles en el desarrollo de interruptores y dispositivos de almacenamiento o memoria ópticos. Asimismo, la aplicación de una presión externa generalmente estabiliza el estado LS, hecho que se refleja en el consiguiente aumento de las temperaturas de transición. Además, un mismo sistema TS bajo presión suele experimentar cambios en la anchura de la histéresis y transiciones más incompletas. Por otro lado, compuestos que permanecen en el estado HS con independencia de la temperatura, pueden experimentar el fenómeno TS bajo una

presión externa. Por el contrario, se ha comprobado que en algunos sistemas TS la presión aplicada estabiliza el estado HS, hecho que generalmente se atribuye a un cambio de fase fruto de dicha presión.

El modelo teórico presentado por Slichter y Drickamer (modelo SD) permite la interpretación, el análisis e incluso la simulación de los comportamientos TS más relevantes tales como transformaciones graduales, de primer orden, con histéresis e incompletas, así como sus correspondientes temperaturas críticas. El modelo SD describe las interacciones intermoleculares entre los centros TS mediante un término que refleja la magnetización promedio del cristal (a través de la fracción molar HS, γ_{HS}) y un parámetro de interacción fenomenológico Γ. La ecuación de estado SD relaciona la energía libre por mol, G, expresada en función de ΔH, ΔS, ΔV y Γ, con γ_{HS}. Los parámetros ΔH y ΔS corresponden a la variación promedio de la entalpía (ΔH) y entropía (ΔS) por mol asociadas al fenómeno TS y pueden deducirse a partir de los datos correspondientes a las medidas de calorimetría diferencial de barrido. ΔV alude a la variación de volumen molar resultado de la TS y puede extraerse de los estudios de difracción de rayos X a temperatura baja. Finalmente, γ_{HS} puede calcularse a partir de los datos proporcionados por las medidas magnéticas, difracción de rayos X o espectroscopias Mössbauer, electrónica y vibracional. Desafortunadamente, los resultados aportados por el modelo SD son aproximados ya que no contempla multitud de factores como, por ejemplo, la presencia de puentes de hidrogeno, interacciones π-π, analitos o polimorfismo, los cuales inducen cambios electrónicos y estructurales que repercuten en el campo de ligando percibido por los centros TS de Fe^{II} y en la cooperatividad de la TS.

En este capítulo se describen de forma general los objetivos que han motivado el desarrollo de la presente Tesis Doctoral así como la metodología utilizada en la síntesis y caracterización físico-química de los compuestos fruto de este trabajo.

El Capítulo Dos presenta la síntesis y caracterización del complejo nitrosilo mononuclear no hemo de Fe^{II} $[Fe(bztpen)(NO)](PF_6)_2]$ (**1**) (bztpen = N-benzil-N,N',N'-tris(2-piridilmetil)etilenediamina). **1** experimenta una TS gradual entre los estados de espín S = 1/2↔S = 3/2 que se extiende más allá de 400 K. La asignación de estados de oxidación y de espín a las especies Fe y NO se ve gravemente impedida debido al elevado grado de covalencia presente en la unidad {FeNO}. En consecuencia, se han

realizado estudios de espectroscopia EPR, Mössbauer, IR, Raman y UV-Vis en función de la temperatura acompañados de cálculos teóricos en un intento de establecer los estados electrónicos implícitos en el equilibrio de espín S = 3/2↔S = 1/2. En la estructura cristalina de **1**, estudiada en el intervalo de temperatura 120-420 K, la dependencia térmica del enlace Fe-NO y el ángulo Fe-N-O evidencian la naturaleza covalente del enlace Fe-NO. Finalmente, los cálculos DFT (Density Functional Theory) reproducen razonablemente la estructura de **1** en los dos estados de espín y sugieren que la conversión S = 1/2↔S = 3/2 resulta del equilibrio entre los estados S = 2↔S = 0 de Fe^{II} y el radical NO (S = 1/2) acoplados antiferromagnéticamente.

En el Capítulo Tres se presenta la síntesis y caracterización de seis clatratos de la red metal-orgánica tridimensional (3D) formulada $[Fe(TPT)_{2/3}\{M^{I}(CN)_2\}_2]\cdot G$ [TPT = 2,4,6-tris(4-piridil)-1,3,5-triazina, M^{I} = Ag (**1**·nG), Au (**2**·nG), G representa las moléculas huésped furano, pirrol y tiofeno]. Estos compuestos fueron caracterizados mediante medidas de difracción de rayos X sobre monocristal a 120 y 300 K, análisis termogravimétricos (TGA) y medidas de susceptibilidad magnética en función de la temperatura. Su estructura cristalina consiste en una red porosa 3D doblemente interpenetrada tipo NbO. En general, el tamaño del poro aumenta al incrementarse el volumen de la molécula huésped. **1**·1.5pirrol y **1**·1tiofeno muestran una TS completa en tres etapas mientras que **1**·0.5furano presenta una TS prácticamente completa en una sola etapa. Por el contrario, **2**·2pirrol y **2**·0.5tiofeno experimentan una TS incompleta. Dada la mayor electronegatividad de Au frente a Ag, los valores de la temperatura de transición ($T_{1/2}$) de **2**·nG son inferiores a las $T_{1/2}$ de sus homólogos **1**·nG. En general, las propiedades magnéticas de estos clatratos sugieren una estabilización gradual del estado HS conforme aumenta el volumen de las moléculas huésped.

En el Capítulo Cuatro se presenta la síntesis y caracterización de dos clatratos tipo Hofmann basados en una nueva red 3D formulados $\{Fe(bpb)[Pt(CN)_4]\cdot G\}$ (bpb = bis(4-piridil)butadiino, G = naftaleno (**1**) y nitrobenceno (**2**)). Estos compuestos han sido caracterizados mediante difracción de rayos X sobre monocristal (a 120 y 300 K), TGA, medidas de susceptibilidad magnética en función de la temperatura, calorimetría diferencial de barrido (DSC) y espectroscopia Mössbauer. Ambos clatratos son isoestructurales (red 3D tipo α-Po distorsionada) y están formados por capas $\{Fe[Pt(CN)_4]\}_\infty$ onduladas y conectadas entre sí a través de los ligandos bpb que se coordinan a las posiciones axiales de los centros de Fe^{II}. **1** muestra una TS completa en

dos etapas en el intervalo de temperatura 180-230 K mientras que **2** transita en una única etapa (190-250 K). Ambos casos exhiben una marcada histéresis (≈ 15 K para **1** y ≈ 30 K para **2**). Las medidas DSC de **1** y **2** muestran valores promedio de ΔH y ΔS comparables a otros clatratos tipo Hofmann basados en Fe^{II} que exhiben TS cooperativas. Finalmente, los espectros Mössbauer de **1** (medidos a 80, 199 y 300 K) y **2** (80 y 300 K) son consistentes con las propiedades magnéticas y estructurales obtenidas para cada compuesto.

En el Capítulo Cinco se presenta la síntesis y caracterización del sistema $\{Fe(bpb)[Ag^{I}(CN)_2]_2\}$ (**1Ag**), $\{Fe(bpb)[M^{II}(CN)_4]\}\cdot 2Guest$ (**2M-Guest** (M^{II} = Ni, Pd, Guest = naftaleno (**naph**), nitrobenceno (**phNO$_2$**)) y de los compuestos microcristalinos $\{Fe(bpb)_{1.1}[M^{II}(CN)_4]\}\cdot nCH_3OH$ (**2M**; M^{II} = Ni, Pd, Pt; n: 0-1). En **1Ag**, los ligandos bpb conectan capas $\{[FeAg(CN)_2]_4\}_n$ onduladas dando lugar a una red 3D tipo α-Po distorsionada. La estructura cristalina de **1Ag** resulta de la interpenetración de cuatro redes idénticas dispuestas en dos pares ortogonales entre sí. Notables contactos C···C se establecen entre los anillos de piridina de los ligandos bpb así como entre los grupos C≡N de redes vecinas. De igual manera que en **2Pt-Guest**, los ligandos bpb conectan capas $\{Fe[M^{II}(CN)_4]\}_n$ onduladas generando una red tipo α-Po distorsionada provista de canales que se extienden a lo largo de la dirección [100] en donde se introducen las moléculas huésped. En particular, **2Ni-phNO$_2$** cristaliza en el sistema *P2/m* (monoclínico), hecho que contrasta con los restantes **2M-Guest**, los cuales cristalizan en el grupo espacial *P-1* (triclínico). Por su lado, **2M** son isostructurales y presentan el mismo patrón de difracción de rayos X en polvo que el simulado para **2M-Guest** en ausencia de moléculas huésped. En lo referente a las propiedades magnéticas, el 50% de los centros de Fe^{II} en **1Ag** experimenta una TS centrada a 130 K mientras que **2M** se caracterizan por TS muy incompletas (8-13%) por debajo de 150 K. Estos compuestos, sometidos a una presión hidrostática de 8 kbar, muestran TS más completas a mayor temperatura. Por el contrario, **2M-Guest** presentan TS a presión ambiente. **2M-naph** y **2Pd-naph** muestran TS completas en dos etapas mientras que la TS asociada a **2Ni-phNO$_2$** tiene lugar en dos etapas separadas por una pequeña meseta centrada a 224 K. Su homologo **2Pd-phNO$_2$,** transita en una única etapa en el intervalo de temperatura 215-250 K. El modo de calentamiento manifiesta la existencia de bucles de histéresis en las diferentes etapas para **2Ni-Guest** y **2Pd-Guest**. Además, **2Ni-naph** presenta el efecto LIESST caracterizado por una T_{LIESST} = 54 K. El comportamiento magnético de

1Ag y **2Ni-naph** se estudia mediante espectroscopia Mössbauer. Los resultados son consistentes con los datos obtenidos a través de medidas magnéticas y estudios cristalográficos. Finalmente, los valores de los parámetros termodinámicos ΔH y ΔS asociados a la TS son consistente con ΔH y ΔS característicos de los polímeros de coordinación tipo Hofmann basados en Fe^{II} con TS fuertemente cooperativas.

En el Capítulo Seis se presenta la síntesis y caracterización de nueve clatratos basados en una nueva red metal-orgánica tipo Hofmann formulada {Fe(3,8-phen)$[Au(CN)_2]_2$·G} (**1**·G) (3,8-phen = 3,8-fenantrolina, G = tiofeno, 2,5-dimetiltiofeno, benzonitrilo, benzaldehído, nitrobenceno, fluorobenceno, clorobenceno, bromobenceno y 1,3-dibromobenceno). Se presentan y discuten sus propiedades magnéticas (**1**·G), fotomagnéticas (**1**·$bzNO_2$, **1**·thiophene), estructurales (**1**·$bzNO_2$) calorimétricas (**1**·G) y su estabilidad térmica (**1**·G). En general, los compuestos **1**·G son el resultado de la interpenetración de dos redes 3D A y B con topología tipo α-Po. A su vez, A y B están formada por capas 2D $\{Fe[Au(CN)_2]_2\}_n$ que se unen en la dirección [001] mediante el ligando orgánico 3,8-phen axialmente coordinado a los centros de Fe^{II}. Además, las capas de ambas redes se alternan y establecen fuertes interacciones aurofílicas entre sí que cambian con la temperatura. Por su lado, las moléculas huésped ocupan el canal 1D que se extiende a lo largo del eje *b* (787.5 $Å^3$, 35% de la celda unidad a 120 K) y establecen interacciones π-π con el ligando puente 3,8-phen. Los clatratos **1**·G exhiben TS abruptas y completas que tienen lugar en varias etapas en el intervalo de temperatura 80-280 K. La inclusión de moléculas huésped en los poros de la presente red metal-orgánica, así como las correspondientes interacciones intermoleculares anfitrión-huésped, determinan la naturaleza de la TS (número de etapas, temperaturas críticas y la existencia y anchura de bucles de histéresis).

En el Capítulo Siete se presentan las conclusiones finales.

Finalmente, se ha incluido un apéndice que recoge los artículos que han dado lugar a la presente Tesis Doctoral.

Nuevos materiales moleculares de hierro(II) multipropiedad basados en el fenómeno de transición de espín

Summary

The herein presented dissertation shows the synthesis and characterization of new multi-functional materials based on Fe^{II} centers which display the well-known Spin-crossover (SCO) phenomena. The main motivation for the present Doctoral Thesis has been the search for molecular-based materials which feature the SCO behaviour together with other interesting physico-chemical property. In particular, a synergetic relationship between them has been pursued and studied by crystallographic, magnetic and calorimetric measurements, among others.

In Chapter One we present the most relevant concepts related to the SCO phenomena where SCO centers undergo HS↔LS spin conversion (HS: high spin state, LS: low spin state) in response to an external stimuli i.e. temperature, pressure, light irradiation or analytes. In particular, thermally-induced SCO is an entropy-driven process with its major entropic contribution arising from changes in the intramolecular and, from a lesser extent, intermolecular vibrations. In the case of Fe^{II} SCO centers, a remarkable ≈ 25% of the total entropy gain during spin conversion comes from the change in spin multiplicity (HS, S = 2↔LS, S = 0). Similarly, the photo-excitation of an Fe^{II} SCO system in the solid state at low temperature can induce a partial or complete conversion from the LS state to the metastable HS* state, known as the LIESST effect (Light Induced Excited Spin State Trapping). Subsequent irradiation of the Fe^{II} SCO system with red light (λ = 820 nm) causes the relaxation of the Fe^{II} SCO centers back to the thermodynamically stable LS state (reverse LIESST effect). Altogether, these light-induced effects opened up the potential use of the Fe^{II} SCO systems for the development of optical switching, storage and memory devices. Additionally, it is known that an external pressure generally stabilizes the LS state i.e. higher transition temperatures since the LS state displays a smaller volume than the HS state. Moreover, pressure might also change the width of the hysteresis loop, increase the LS and HS residual fractions or even induce SCO in a HS system for which a thermal transition does not occur. Reversely, an applied

pressure can stabilize the HS state in some cases, a fact generally ascribed to a pressure-induced phase change.

The simple theoretical model presented by Slichter and Drickamer (SD model) can interpret, analyse and even simulate representative SCO behaviours i.e. gradual, first order, hysteretic or incomplete SCO behaviours with their critical temperatures. The SD model describes the intermolecular interactions between the SCO centers by a term that contains the average magnetization of the crystal (given by the HS molar fraction, γ_{HS}) and a phenomenological interaction parameter Γ. The SD equation state relates the free energy per mol G, a function of ΔH, ΔS, ΔV and Γ, with γ_{HS}. The ΔH and ΔS parameters are the average enthalpy and entropy variations per mol, respectively, associated with the SCO phenomenon and can be deduced from differential scanning calorimetric data (DSC) whereas the ΔV is the molar volume change due to the occurrence of SCO, extracted from X-ray diffraction studies at low temperature. Finally, γ_{HS} can be calculated from the magnetic measurements, X-ray diffraction data or Mössbauer, electronic and vibrational spectroscopy. Unfortunately, the accuracy of the SD model is limited since it does not consider structural and electronic changes induce by e.g. the presence of hydrogen bonds, π-π interactions, analytes or polymorphism, which ultimately affect the ligand field felt by the SCO centers and the SCO cooperativity.

In addition, the main motivations leading to the present Doctoral Thesis together with a general experimental procedure regarding the synthesis and physico-chemical characterization of the herein presented compounds are also briefly summarized in this chapter.

Chapter Two describes the synthesis and characterization of the nitrosyl Fe^{II} mononuclear complex $[Fe(bztpen)(NO)](PF_6)_2]$ (**1**) (bztpen = N-benzyl-N,N',N'-tris(2-pyridylmethyl)ethylenediamine). A new non-heme $\{FeNO\}^7$ species displaying an S = 1/2↔S = 3/2 gradual SCO behaviour that extends beyond 400 K. The substantial degree of covalence involved in the {FeNO} unit precludes easy assignation of specific oxidation and ground spin states. Hence, multi-temperature EPR, Mössbauer, IR, Raman, and UV-Vis spectroscopy as well as theoretical calculations have been carried out to clarify the nature of the observed S = 3/2↔S = 1/2 equilibrium. In the crystal structure of **1,** investigated in the temperature range 120-420 K, the N-O bond length and the Fe-N-O

tilt angle change greatly due to the occurrence of SCO and clearly reflects the strong covalence of the Fe-NO bond. The thermal variation of the λ = 555 nm band in the UV-Vis spectrum and the thermochromism displayed by **1** are reminiscent of the LS↔HS spin state change in Fe^{II} SCO complexes. Finally, Density Functional Theory calculations (DFT) reproduce reasonably well the structure of **1** in both spin states supporting that the S = 2↔S = 0 spin equilibrium in the Fe^{II} strongly coupled with the radical NO explains the observed S = 3/2↔S = 1/2 spin equilibrium.

In Chapter Three we present the synthesis of six clathrate compounds of the 3D SCO metal-organic framework formulated $[Fe(TPT)_{2/3}\{M^{I}(CN)_2\}_2]\cdot G$ [TPT = 2,4,6-tris(4-pyridyl)-1,3,5-triazine, M^{I} = Ag (**1**·nG), Au (**2**·nG), G represent the guest molecules furan, pyrrole and thiophene]. These compounds were characterized by single-crystal X-ray diffraction at 120 and 300 K, thermogravimetric analyses (TGA) and thermal dependence of the magnetic susceptibility. Their crystal structures consist of two identical, independent and mutually interpenetrated coordination frameworks with the topology of the NbO and large voids where the guest molecules are located. In general, the size of the pores increases with the volume of the guest molecule. **1**·1.5pyrrole and **1**·1thiophene derivatives display complete three-step SCO behaviours whereas an almost complete one-step spin transition occurs for **1**·0.5furan. In contrast, **2**·2pyrrole and **2**·0.5thiophene undergo incomplete SCO behaviours. Due to the much higher electronegativity of Au with respect to Ag, the critical temperatures ($T_{1/2}$) displayed by **2**·nG are lower than those featured by **1**·nG**.** In general, the magnetic properties of these clathrates suggest a gradual stabilization of the HS state as the volume of the guest molecule increases.

In Chapter Four we present the synthesis and characterization of the novel Fe^{II} Hofmann-like porous metal-organic framework $\{Fe(bpb)[Pt(CN)_4]\cdot 2G\}$ (bpb = bis(4-pyridyl)butadiyne, G = naphthalene (**1**) or nitrobenzene (**2**)). These compounds were characterized by single-crystal X-ray diffraction studies (at 120 and 300 K), TGA, thermal dependence of the magnetic susceptibility, DSC and Mössbauer spectroscopy. Both clathrates are isostructural and consist of infinite corrugated 2D $\{Fe[Pt(CN)_4]\}_\infty$ layers pillared by bent bpb ligands axially coordinated to the Fe^{II} centers. The magnetic studies show that **1** undergoes a complete two-step SCO in the temperature interval 180-230 K whereas **2** displays a complete one-step SCO between 190 and 250 K. The heating mode evidences the occurrence of wide hysteresis loops in both clathrates (≈ 15 K and ≈

30 K wide for **1** and **2**, respectively). DSC measurements performed on **1** and **2** resulted in ΔH and ΔS average variations within the expected range of values generally displayed by cooperative Fe^{II} SCO Hofmann-like clathrates. Finally, the Mössbauer spectrum of **1** (collected at 80, 199 and 300 K) and **2** (80 and 300 K) are consistent with the magnetic and structural properties displayed by each clathrate.

In Chapter Five we present the synthesis and characterization of $\{Fe(bpb)[Ag^{I}(CN)_2]_2\}$ (**1Ag**), $\{Fe(bpb)[M^{II}(CN)_4]\}\cdot 2Guest$ (**2M-Guest** (M^{II} = Ni, Pd, Guest = naphthalene (**naph**), nitrobenzene (**phNO$_2$**)) and the microcrystalline compounds $\{Fe(bpb)_{1.1}[M^{II}(CN)_4]\}\cdot nCH_3OH$ (**2M**; M^{II} = Ni, Pd, Pt; n: 0-1). In **1Ag**, slightly undulating $\{[FeAg(CN)_2]_4\}_n$ 2D grids are pillared by bpb ligands generating a distorted α-Po type framework. In addition, three other identical frameworks are formed and pass through the windows of the previous grid. These four networks are organized in two sets which are orthogonally oriented. Short C···C contacts between pyridine rings of neighbour concatenated networks and between the C≡N groups of neighbour networks are observed. As in **2Pt-Guest**, **2Ni-Guest** and **2Pd-Guest** feature slightly corrugated 2D $\{Fe[M^{II}(CN)_4]\}_n$ layers pillared by bpb ligands, generating a 3D Hofmann SCO-MOF with large channels running along [100] where the guest molecules are located. Numerous short C···C contacts are defined between the guest molecules and the bpb ligands. Interestingly, **2Ni-phNO$_2$** crystallizes in the space group *P2/m* (monoclinic) instead of the expected *P-1* (triclinic) space group. **2M** are isostructural and display the same PXRD pattern that the simulated one for **2M-Guest** where the guest molecules were artificially removed. Regarding their magnetic properties, **1Ag** undergoes half SCO centered at 130 K while **2M** show 8-13% HS-to-LS conversions below 150 K. External hydrostatic pressure on them resulted in higher equilibrium transition temperatures and enhanced completeness of HS$\leftrightarrow$LS transitions. In contrast, **2M-naph** and **2Pd-naph** display complete and cooperative two-step SCO behaviours. **2Ni-phNO$_2$** features two sharp steps separated by a narrow plateau (ca. 224 K) while **2Pd-phNO$_2$** presents a complete one step SCO in the temperature interval 215-250 K. The heating mode evidences the occurrence of hysteresis loops in each step for **2Ni-Guest** and **2Pd-Guest**. In addition, **2Ni-naph** exhibits the well-known LIESST effect (T_{LIESST} = 54 K). **1Ag** and **2Ni-naph** SCO behaviours were also confirmed by Mössbauer spectroscopy. Finally, the thermodynamic parameters ΔH and ΔS associated with the SCO are consistent with

those typically displayed by Hofmann-like SCO-MOFs based on Fe^{II} centers featuring strong cooperative SCO behaviours.

In Chapter Six we present the synthesis and characterization of a new 3D porous Hofmann-like SCO-MOFs generally formulated $\{Fe(3,8\text{-phen})[Au(CN)_2]_2 \cdot G\}$ (3,8-phen = 3,8-phenantroline, G = thiophene, 2,5-dimethylthiophene, benzonitrile, benzaldehyde, nitrobenzene, fluorobenzene, chlorobenzene, bromobenzene and 1,3-dibromobenzene), (**1**·G). Magnetic (**1**·G), photomagnetic (**1**·$bzNO_2$, **1**·thiopnene), structural (**1**·$bzNO_2$) calorimetric (**1**·G) and thermostability (**1**·G) studies are also presented. In general, **1**·G are made of two interpenetrating 3D networks A and B with the topology of the archetypal α-Po structure. Each network consists of parallel 2D $\{Fe[Au(CN)_2]_2\}_n$ layers pillared by the organic ligand 3,8-phen along the [001] direction. A and B 2D layers alternate and are held together by strong aurophilic interactions that change with temperature. A 1D channel runs along the *b* axis (787.5 $Å^3$, 35% of the unit cell at 120 K) and hosts the aromatic guest molecules which interact with the pillar ligand through π-π intermolecular interactions. **1**·G display abrupt, multi-step SCO behaviours in the temperature interval 80-280 K. The presence of guest molecules within the pores dramatically influences the nature of the SCO behaviours i.e. the number of SCO steps, its characteristic temperatures, the occurrence of hysteresis loop and its width.

Chapter Seven includes the most relevant conclusions regarding the synthesis and characterization of the herein presented molecular-based multi-property materials.

Finally, an appendix containing the scientific publications which have led to this Doctoral Thesis has been added.

CAPÍTULO 1

INTRODUCCIÓN

CAPÍTULO 1
INTRODUCCIÓN

1.1.- Introducción general al fenómeno de la transición de espín

El fenómeno de la transición de espín (TS) se enmarca en el campo de la magnetoquímica, y ha estado enlazado históricamente y de manera fundamental al desarrollo de la química de coordinación.[1] Los centros TS muestran configuraciones electrónicas lábiles intercambiables entre los estados de espín alto (HS) y espín bajo (LS), dando lugar a cambios característicos en el magnetismo, el color y la estructura de la materia, que pueden ser inducidos por variaciones de temperatura, presión, y por irradiación con luz. Cuando los cambios estructurales asociados a la transición de espín se transmiten de forma cooperativa a través del cristal se producen transiciones de espín cooperativas acompañadas de histéresis (efecto "memoria"), confiriendo carácter biestable al material.

La idea de que una molécula o conjunto de moléculas puede comportarse como un dispositivo electrónico ha estimulado la imaginación de los científicos desde hace mucho tiempo.[2-11] Una de las estrategias más simples se basa en el concepto de biestabilidad molecular que se fundamenta en el cambio entre dos estados moleculares tal y como sucede en un interruptor binario.[12]

La biestabilidad molecular ha sido definida como "la propiedad de un sistema molecular para cambiar entre dos estados estables de una manera reversible y detectable en respuesta a una perturbación apropiada".[13] En este contexto, el fenómeno de la transición de espín representa un ejemplo destacado de biestabilidad molecular. Este fenómeno tiene lugar tanto en disolución, en cristales líquidos y en estado sólido. En el primer caso, el proceso es esencialmente molecular debido al aislamiento de las moléculas. En estado sólido y en cristales líquidos la situación es muy diferente y, en general, el fenómeno viene acompañado por efectos cooperativos. La cooperatividad es una de las facetas más interesantes de las transiciones de espín, pues implica discontinuidad en las propiedades ópticas y magnéticas y, en ocasiones,

viene acompañada de histéresis térmica. Esto le confiere a dichos sistemas capacidad potencial para almacenar información a nivel molecular.

La dificultad en el estudio de la cooperatividad reside en su naturaleza intermolecular. El control de las interacciones no covalentes entre unidades individuales que constituyen un sólido es uno de los campos más activos de lo que hoy en día se conoce como química supramolecular[14-15] y, en particular, de la ingeniería cristalina. Sin embargo, a pesar de lo mucho que se ha avanzado en la última década, no es posible todavía predecir si una disposición molecular en una red puede ser más o menos efectiva que otra desde el punto de vista de la cooperatividad, o incluso si va a favorecer o impedir la conversión de espín. A este respecto, podemos decir que actualmente el químico carece de una guía conceptual que le permita la síntesis dirigida de sólidos con unas propiedades magnéticas determinadas.

A pesar de todos estos inconvenientes, el estudio de las transiciones de espín presenta una riqueza conceptual poco imaginable a primera vista. En este apartado se presentan los conceptos más importantes de las transiciones de espín.

1.1.1.- Teoría del campo de ligandos y transiciones de espín

En simetría octaédrica los complejos de metales de transición con configuraciones electrónicas $[Ar]3d^4$-$3d^7$ pueden presentar dos estados electrónicos fundamentales distintos, según el desdoblamiento de los orbitales d en los subconjuntos e_g y t_{2g}. Cuando la separación energética entre estos subconjuntos (fuerza del campo de ligandos), Δ, es mayor que la energía de repulsión interelectrónica, P, los electrones tienden a ocupar los orbitales de más baja energía, t_{2g}, y el complejo metálico adopta el estado de espín bajo (LS). Si Δ es menor que P los electrones d cumplen la regla de máxima multiplicidad de Hund y el complejo adopta el estado de espín alto (HS). La mayoría de los complejos de Cr^{II}, Mn^{II}, Mn^{III}, Fe^{II}, Fe^{III}, Co^{II} y Co^{III} pueden presentar estas dos posibilidades electrónicas, si bien la familia de compuestos de Fe^{II} presentando transición de espín es la más importante y la más numerosa.

En los alrededores del punto de cruce, Δ_c, donde Δ y P tienen valores similares, la diferencia de energía entre los estados HS y LS es del orden de magnitud de la energía térmica (k_BT). En esta región singular nace una nueva familia de compuestos

denominados de transición de espín. Éstos pueden adoptar ambos estados de espín e interconvertirse de manera controlada, detectable y reversible bajo el efecto de la temperatura, presión o irradiación de luz.

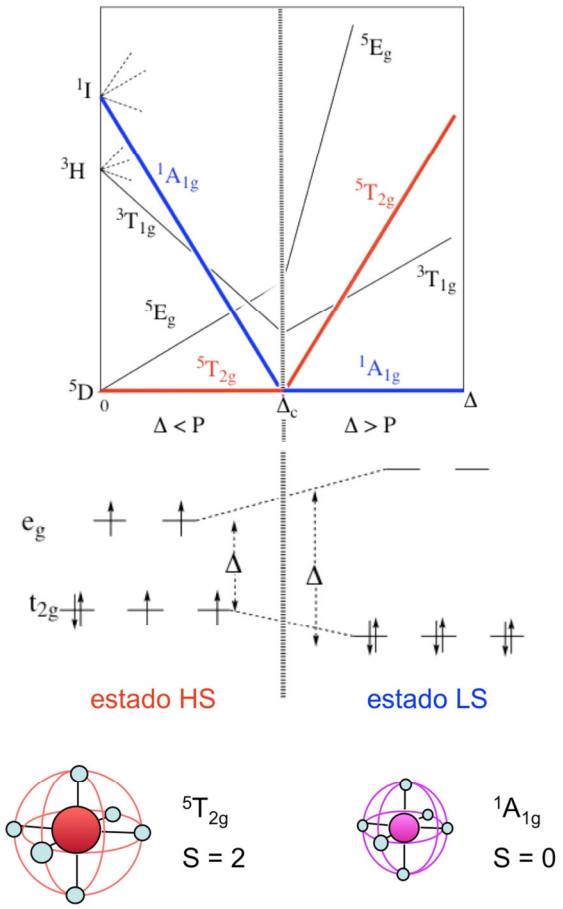

Figura 1.- Diagrama Tanabe-Sugano simplificado ilustrando la dependencia relativa de los estados HS y LS y las configuraciones electrónicas correspondientes.

En el caso de compuestos de Fe^{II} los ligandos de campo débil, como el H_2O, favorecen la estabilización del estado HS (cuyo estado fundamental es el $^5T_{2g}$), mientras que al aumentar la fuerza del campo de ligandos el estado LS (cuyo estado fundamental es el $^1A_{1g}$), se estabiliza automáticamente, disminuyendo su energía.

El fenómeno de las transiciones de espín puede considerarse como una transferencia electrónica intra-iónica, donde los electrones se mueven entre los orbitales e_g y t_{2g}. Dado que el subconjunto e_g tiene carácter antienlazante, su población/despoblación tiene lugar junto a un aumento/disminución de las distancias de enlace metal-ligando. Un cambio opuesto se da en la población del subconjunto t_{2g} que afecta a la retro-donación entre el ion metálico y los orbitales π^* vacantes de los ligandos. Ambos factores σ y π contribuyen al cambio de las distancias de enlace metal-ligando. El cambio en las distancias de enlace metal-ligando, ΔR, es de aproximadamente 0.2, 0.15 y 0.10 Å para el Fe^{II}, Fe^{III} y Co^{II}, respectivamente. Así pues, un cambio considerable de tamaño tiene lugar durante la transición de espín, no sólo en las distancias de enlace sino también en los ángulos. Consecuentemente, las moléculas experimentan un cambio drástico de Δ con la TS, que se estima de $\Delta_{LS}/\Delta_{LS} \approx (\Delta R_{HS}/\Delta R_{LS})^n$ con n = 5-6. Por ejemplo $\Delta_{LS} \approx 1.75\Delta_{HS}$ para el Fe^{II}. Esta estimación abandona la dependencia angular de Δ y considera que ΔR es el parámetro de cambio estructural más importante.[16]

La fuerza del campo de ligandos depende no sólo del ligando coordinado al centro metálico sino también de la distancia de enlace metal-ligando. Al pasar al estado de LS las distancias Fe-N disminuyen, lo que implica un cambio en el orden de enlace y por lo tanto un aumento de la energía de vibración (fácilmente observado por las espectroscopias IR y Raman), como consecuencia del aumento de la constante de fuerza del enlace, f.

Así pues, cada estado de espín puede asociarse en primera aproximación a una parábola caracterizada por una energía potencial:

$$Ep_i = 1/2(f_i R^2_i) \qquad i = HS, LS \qquad (1)$$

R_i = distancia media Fe-N

Esta energía potencial representa esencialmente la energía electrónica de los estados HS y LS. Ambas parábolas están separadas en sus mínimos por las distancias R características para iones Fe^{II}, $R_{LS} \approx 2.0$ Å y $R_{HS} \approx 2.2$ Å (siendo $\Delta R_{HL} \approx 0.2$ Å). Estas curvas contienen información acerca de la energía vibracional. Así pues, dichas parábolas representan también el modo de vibración totalmente simétrico de octaedro (A_{1g}). Una representación de las energías Ep_i de las parábolas asociadas a los estados HS y LS frente a R se presenta en la Figura 1.2. El desplazamiento horizontal de ambas parábolas corresponde a $\Delta R_{HL} \approx 0.2$ Å, mientras que el desplazamiento vertical indica que para una molécula aislada el estado LS está estabilizado con respecto al HS por una energía ΔE_{HL}.

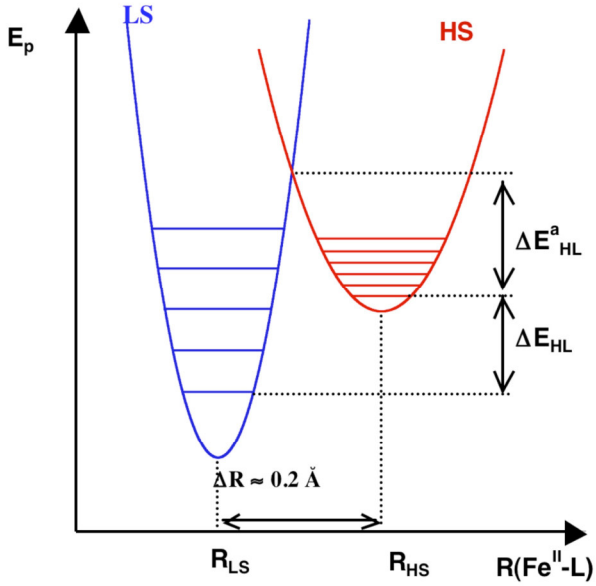

Figura 2.- Curvas de energía potencial de los estados HS y LS mostrando la diferencia entálpica ΔE_{HL}, la energía de activación E^a_{HL} y los estados vibracionales correspondientes.

La energía vibracional de los diferentes niveles será:

$$E^{vibr}_i (n) = (n + 1/2)\, h\nu_i \qquad \nu_i = 1/2\pi\, (f_i/m)^{1/2} \text{ (m es la masa reducida)} \qquad (2)$$

Los niveles vibracionales se representan como líneas horizontales igualmente espaciadas dentro de las correspondientes parábolas (Figura 1.2). Dado que $f_{LS} > f_{HS}$ el

número de niveles vibracionales por unidad de energía es mayor para el estado HS que para el LS, es decir, la separación entre los diferentes niveles vibracionales es menor en el estado HS. Igualmente, la multipilicidad de espín del estado HS es mayor que la del estado LS.

A muy bajas temperaturas, la molécula se encuentra en el nivel vibracional fundamental (n = 0) del estado LS. A medida que aumenta la temperatura, la molécula va transformando la energía térmica aportada en energía vibracional ocupando niveles vibracionales excitados hasta alcanzar el punto de cruce de ambas parábolas donde se produce el cambio de estado de espín, en el que la geometría del estado precursor, el LS, y el sucesor, el HS, es la misma. De acuerdo con el principio de Franck-Condon es en este punto donde tiene lugar la transformación HS $\leftrightarrow$ LS. Este punto de cruce, Δ_c, representa una región inestable donde las especies transitorias pueden cambiar su estado de espín.

El coste energético para salvar la diferencia entálpica, ΔE_{HL}, entre ambos estados es compensado por la diferencia de entropía de los mismos, que favorece la población del estado HS a altas temperaturas. Visto de otra forma, la molécula absorbe energía para compensar la diferencia entálpica ΔE_{HL} que desfavorece el estado HS. Dicha energía absorbida es de origen entrópico y tiene dos componentes diferentes. Por un lado, hay una componente electrónica relacionada con el cambio de multiplicidad de espín (2S + 1) [HS (S = 2) y LS (S = 0) para el ion Fe^{II}]:

$$\Delta S_{el.} = R \ln [(2S + 1)_{HS}/[(2S + 1)_{LS}] = R \ln (5/1) = 13.45 \text{ J K}^{-1} \text{ mol}^{-1} \quad (3)$$

Por otro lado, hay una componente vibracional que deriva del mayor número de niveles vibracionales por unidad de energía (g_i) asociado al estado HS, dada la menor magnitud de la constante de fuerza de enlace f_{HS}:

$$\Delta S_{vibr.intr.} = R \ln (g_{HS}/g_{LS}) \quad (4)$$

El acceso experimental a la relación g_{HS}/g_{LS} conlleva serias dificultades pero es posible estimarla a partir de la entropía total obtenida de las medidas de calorimetría y del análisis de los espectros IR y/o Raman correspondientes a los estados HS y LS.[17] Por consiguiente una TS térmicamente inducida es un proceso controlado por la entropía.

La influencia de la presión en la transición de espín también puede entenderse a partir de los pozos de potencial. Sin tener en cuenta la fuente de la presión (química o mecánica) el efecto principal de la presión es la desestabilización del estado HS, ya que el volumen de éste es mayor que el del LS. Así pues, la presión disminuye ΔR_{HL} y aumenta ΔE_{HL}, por lo que la parábola se desplaza verticalmente.[18] Como consecuencia, la presión produce la disminución de la energía de activación, E^a_{HL}, correspondiente a la diferencia en energía entre el nivel vibracional n = 0 del estado HS y el punto de cruce definido por los dos pozos de potencial.

Generalmente, a temperaturas mayores de 100 K la energía térmica, k_BT, es mayor que la energía de activación, E^a_{HL}, hecho que determina la cinética de la conversión HS $\leftrightarrow$ LS, incluso a presión atmosférica. Por ello la cinética del proceso se caracteriza por una constante de velocidad, $k_{HL} \approx 10^6$-10^8 s^{-1}, que garantiza el equilibrio termodinámico de las magnitudes físicas observadas.

Cuando la energía térmica es del orden o menor que la energía de activación, $k_BT \leq E^a_{HL}$, esta afirmación ya no es válida y la constante k_{HL} disminuye hasta valores del orden de 10^{-1}-10^{-7} s^{-1}, con lo que es posible "congelar" el estado HS a temperaturas donde no es estable, ya que la molécula no dispone de la energía suficiente para superar la barrera de paso E^a_{HL} desde el estado HS al LS.

A temperaturas del orden de 50-90 K es fácil estudiar las cinéticas de relajación, que en principio son de primer orden, pudiéndose correlacionar la variación térmica de k_{HL} en términos de la representación de Arrhenius.

Para temperaturas muy bajas, en los compuestos típicos de Fe^{II} con transición de espín, se observa que el proceso de relajación ya no sigue una ley de Arrhenius pura, sino que se desvía, más cuanto menor es la temperatura, hasta observar una independencia térmica de $\ln(k_{HL})$, hecho que suele tener lugar por debajo de 40 K. De hecho por debajo de 30 K, k_{HL} es muy pequeña, $[k_{HL}(T \rightarrow 0)] \approx 10^{-7}$ s^{-1}, e independiente de T, y el proceso de relajación tiene lugar esencialmente vía efecto túnel. La velocidad de relajación en la región túnel puede relacionarse con los desplazamientos "vertical" y "horizontal" de las curvas de energía potencial de los estados HS y LS a través del marco conceptual de los procesos de relajación no adiabáticos multifonónicos.[19]

Sin embargo este no es el caso para compuestos de Fe^{III} y Co^{II}, que normalmente presentan relajaciones muy rápidas incluso a temperaturas por debajo de 10 K. Para estos sistemas el cambio de energía configuracional es menor que para los compuestos de Fe^{II}, ya que el cambio en las distancias de enlace es mucho menor también. La relajación HS $\leftrightarrow$ LS en compuestos con transición de espín es un proceso modelo que participa del comportamiento clásico y el mecano-cuántico, y ha sido estudiado en profundidad por Hauser y colaboradores entre otros.[20]

1.1.2.- Fotoconversión de estados de espín

La luz es un camino muy eficaz para "comunicarse" con un sistema molecular sobre todo cuando se trata de encontrar posibles aplicaciones tecnológicas. La foto-inducción de la TS fue observada por primera vez por primera vez por McGarvey y Lawthers en disolución a temperaturas relativamente altas,[21] sin embargo, el tiempo de vida media de los estados inducidos era muy corto. Más adelante, en 1994, Decurtins y colaboradores observaron por primera vez el proceso de foto-inducción de la TS en estado sólido a bajas temperaturas para el complejo $[Fe(1\text{-propiltetrazol})_6](BF_4)_2$.[22] Al irradiar la muestra en el estado LS con luz verde (λ = 514.5 nm) a temperaturas por debajo de 50 K el color de la muestra pasa del púrpura del estado LS al blanco, propio del HS. El fenómeno fue denominado "light induced spin state trapping" (LIESST).

A temperaturas suficientemente bajas el estado LS está totalmente poblado y el espectro visible del sistema d^6 en simetría octaédrica se caracteriza por dos bandas relativamente intensas correspondientes a las transiciones $\nu_1(^1A_{1g}\rightarrow{}^1T_{1g})$ (≈ 12000-20000 cm^{-1}) y $\nu_2(^1A_{1g}\rightarrow{}^1T_{2g})$ (≈ 20000-25000 cm^{-1}) que a menudo están enmascaradas por las bandas de transferencia de carga metal ligando TCML ($d_M\rightarrow\pi^*_L$).

La irradiación con luz verde estimula la transición $^1A_{1g}\rightarrow{}^1T_{1g}$. El tiempo de vida media del estado excitado $^1T_{1g}$ es de tan sólo nanosegundos, por lo que el sistema se relaja rápidamente. Dicha relajación debería tener lugar normalmente al estado inicial $^1A_{1g}$. No obstante, existe una pequeña probabilidad de relajación a través de los estados de espín intermedio $^3T_{1g}$ y $^3T_{2g}$ por mecanismos de cruce entre sistemas ("intersystem crossing", ISC) permitidos por acoplamiento espín-órbita de segundo orden. La relajación desde los estados de espín intermedio puede ocurrir de nuevo por medio de

dos procesos ISC, uno implica la relajación al estado fundamental $^1A_{1g}$ y otro al metastable $^5T_{2g}$ donde las moléculas permanecerán atrapadas, siempre que k_BT sea suficientemente menor que E^a_{HL}. A bajas temperaturas el estado metaestable $^5T_{2g}$ tiene un tiempo de vida media muy largo, dado que la relajación $^5T_{2g} \rightarrow {}^1A_{1g}$ está prohibida.

La foto-excitación durante un período de tiempo suficiente, implica la población total del estado metaestable HS, $^5T_{2g}$, a costa del despoblamiento del LS, con lo que se invierte la población de los estados. El estado metaestable HS puede volver al estado LS de partida irradiando con luz roja (λ = 820 nm), el llamado efecto LIESST inverso ($^5T_{2g} \rightarrow {}^3T_{1g} \rightarrow {}^1A_{1g}$), o simplemente aumentado la temperatura.

El descubrimiento del efecto LIESST representó un avance importante el estudio de la dinámica de la TS en estado sólido, dado que el rango de temperaturas en las cuales el equilibrio termodinámico podía ser foto-perturbado se extendió considerablemente. Desde entonces, el número de compuestos en los que se ha observado el efecto LIESST ha aumentado considerablemente.

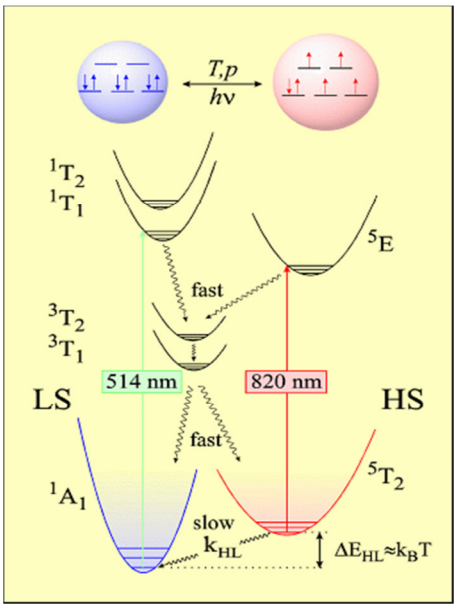

Figura 3.- Esquema representativo del fenómeno de foto-inducción de una transición de espín, efecto LIESST.

El foto-control del estado de espín alimentó la idea de que los compuestos con TS podrían usarse como conmutadores ópticos en dispositivos de memoria. Sin embargo, el estado HS foto-inducido de la mayoría de los compuestos con TS se relaja al estado LS a temperaturas por debajo del nitrógeno líquido. Zarembowitch y colaboradores desarrollaron una estrategia alternativa para conseguir la foto-conversión de estados de espín llamada "ligand-driven light-induced spin changes" (LD-LISC).[23] Esta aproximación requiere la síntesis de complejos en los que una modificacion foto-inducida en uno o más de sus ligandos resulta en un cambio en el campo de ligandos y produce la conversión del estado de espín del ion metálico. Esto permitiría la foto-inducción entre estados con tiempos de vida media más largos y a temperaturas mayores. Los autores arriba mencionados demostraron la viabilidad de esta aproximación empleando ligandos basados en moléculas foto-isomerizables cis-trans de tipo estilbeno, como el 1-fenil-2-(4-piridil)etano (stpy), del cual se sintetizó el complejo $[Fe(stpy)_4(NCS)_2]$ en sus formas cis y trans (Figura 1.4).

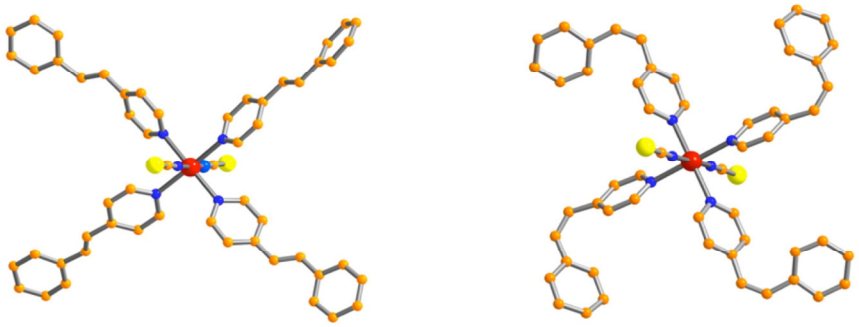

Figura 4.- Estructuras moleculares de los isómeros del complejo $[Fe(stpy)_4(NCS)_2]$ mostrando las conformaciones trans (izquierda) y cis (derecha) del ligando 1-fenil-2-(4-piridil)etano (stpy). Código de colores: C naranja, N azul, S amarillo y Fe rojo.

El complejo $[Fe(trans\text{-}stpy)_4(NCS)_2]$ presenta una transición de espín térmicamente inducida centrada alrededor de 108 K, mientras que el $[Fe(cis\text{-}stpy)_4(NCS)_2]$ es HS en todo el rango de temperaturas. En principio, irradiando las muestras con luz de longitud de onda apropiada, a temperaturas justo por debajo de T_c,

es posible inducir un cambio de espín en el sistema como resultado de la foto-conversión del ligando. En la práctica, el fenómeno no ha podido ser observado en el estado cristalino debido a las fuerzas mecánicas envueltas en el proceso de conversión cis-trans. Sin embargo, Boillot y colaboradores han observado el efecto LD-LISC a 140 K en películas de acetato de celulosa y a temperatura ambiente en una disolución de acetonitrilo.[24]

1.1.3.- Comportamiento colectivo del conjunto de centros activos: cooperatividad

Aunque el origen del fenómeno de transición de espín es puramente molecular la manifestación macroscópica del sólido es el resultado de la interacción cooperativa entre las moléculas que constituyen el material. La naturaleza cooperativa de la conversión de espín ha estimulado mucho interés dado que las transiciones de fase de primer orden que se producen acompañadas de histéresis térmica confieren a estos materiales un cierto grado de memoria, que podría ser potencialmente aprovechada en futuras aplicaciones. La cooperatividad radica esencialmente en la diferencia de tamaño que presenta la molécula en cada uno de los estados de espín. Así pues, tiene un origen elástico que da lugar a interacciones de largo alcance. Estas interacciones podrían ilustrarse como una presión interna, que crece con el aumento de las especies LS e interactúa con todas las moléculas del cristal con la misma intensidad, independientemente de las distancias.[25]

Es posible explicar el carácter continuo, discontinuo, histéresis o incluso la temperatura crítica $T_{1/2}$ (temperatura para la cual la fracción molar de especies HS y LS es 0.5) en términos de la termodinámica de transiciones de fase debida a Slichter y Drickamer.[26]

Si se considera un número N de moléculas que pueden dar lugar a TS, cada molécula podrá existir en el estado HS o en el estado LS, de manera que podemos definir la fracción molar de las moléculas HS como γ_{HS}, siendo la fracción molar de moléculas LS (1 - γ_{HS}). En ausencia de interacciones intermoleculares podemos introducir en la expresión de la energía libre de Gibbs, G, un término para la entropía de mezcla, S_{mix}, Este término representa las diferentes posibilidades de distribución de las

poblaciones HS (γ_{HS}) y LS (1 - γ_{HS}), para el total de moléculas N. La entropía de mezcla S_{mix} se expresa como:

$$S_{mix} = k [N \ln N - \gamma_{HS} N \ln \gamma_{HS} N - (1 - \gamma_{HS}) N \ln (1 - \gamma_{HS}) N] \quad (5)$$

que puede reescribirse como:

$$S_{mix} = -R[\gamma_{HS} \ln \gamma_{HS} - (1 - \gamma_{HS})\ln(1 - \gamma_{HS})] \quad (6)$$

donde R es la constante de gases. S_{mix} es máxima para γ_{HS} = 0.5 y desaparece para γ_{HS} = 0 o 1. Al tener en cuenta el término S_{mix}, la expresión de la energía libre de Gibbs queda:

$$G = \gamma_{HS} G_{HS} + (1- \gamma_{HS})G_{LS} – T S_{mix} \quad (7)$$

donde G_{HS} y G_{LS} corresponden a las energías libres de Gibbs para los estados electrónicos HS y LS, respectivamente. La derivada parcial de G con respecto a γ_{HS} es

$$\left(\frac{\partial G}{\partial \gamma_{HS}}\right) = \Delta G + RT \ln\left(\frac{\gamma_{HS}}{1-\gamma_{HS}}\right) \quad (8)$$

La condición de equilibrio termodinámico para la TS a cualquier temperatura y presión es:

$$\left(\frac{\partial G}{\partial \gamma_{HS}}\right)_{T,P} = 0 \quad (9)$$

por lo que

$$\ln\left(\frac{1-\gamma_{HS}}{\gamma_{HS}}\right) = \frac{\Delta G}{RT} = \frac{\Delta H}{RT} - \frac{\Delta S}{R} \quad (10)$$

Teniendo en cuenta que ΔG = 0 cuando γ_{HS} = γ_{LS} = 0.5 y que por tanto $T_{1/2}$ = $\Delta H/\Delta S$, se obtiene

$$\gamma_{HS} = \frac{1}{1 + \exp\left[\frac{\Delta H}{R}\left(\frac{1}{T} - \frac{1}{T_{1/2}}\right)\right]} \quad (11)$$

Las interacciones moleculares vienen reflejadas en el modelo de Slichter y Drickamer por un parámetro de interacción, G_{int}.

$$G_{int} = \Gamma\, \gamma_{HS} (1 - \gamma_{HS}) \qquad (12)$$

donde Γ es el parámetro de la cooperatividad.

Tomando G_{LS} como el origen de energías, podemos escribir,

$$G = \gamma_{HS}\Delta H + \Gamma\, \gamma_{HS} (1 - \gamma_{HS}) + T[R\gamma_{HS}\ln\gamma_{HS} + R(1 - \gamma_{HS})\ln(1 - \gamma_{HS}) - \gamma_{HS}\Delta S] \qquad (13)$$

Esta ecuación permite representar curvas de energía libre, G, frente a fracción molar de HS, γ_{HS}, para diferentes valores de ΔH, ΔS, Γ y T. Teniendo en cuenta de nuevo, la condición de equilibrio se llega a

$$\ln\left(\frac{1-\gamma_{HS}}{\gamma_{HS}}\right) = \frac{\Delta H + \Gamma(1-2\gamma_{HS})}{RT} - \frac{\Delta S}{R} \qquad (14)$$

Si $\Delta G < 0$ el estado electrónico de las moléculas es HS y cuando $\Delta G > 0$ el estado de las moléculas es el LS. En condiciones de equilibrio termodinámico, $\Delta G = 0$ y $\gamma_{HS} = \gamma_{LS}$. Si además, se tiene en cuenta la influencia de la presión en la TS, se introduce un nuevo término en la ecuación, quedando:

$$\ln\left(\frac{1-\gamma_{HS}}{\gamma_{HS}}\right) = \frac{\Delta H + P\Delta V + \Gamma(1-2\gamma_{HS})}{RT} - \frac{\Delta S}{R} \qquad (15)$$

Resumiendo, la ecuación de estado puede escribirse de la forma siguiente:

$$\ln[(1-\gamma_{HS})/\gamma_{HS}] = [\Delta H + P\Delta V + \Gamma\,(1 - 2\,\gamma_{HS}) - T\,\Delta S] / RT$$

siendo γ_{HS} la fracción molar de HS. ΔH y ΔS son las variaciones de entalpía y entropía por mol involucradas en la TS y se pueden obtener directamente a partir de las medidas de calorimetría (Cp vs. T), y ΔV es el cambio de volumen molar asociado a la TS que se suele obtener directamente de las medidas de difracción de Rayos X a bajas temperaturas (este término es despreciable a presión atmosférica). Es importante resaltar que la relación $\Delta H/\Delta S$ corresponde a la temperatura característica de la transición, T_c o $T_{1/2}$, a la cual $\gamma_{HS} = \gamma_{LS} = 0.5$, y se obtiene directamente de la curva de

conversión de espín. Por otro lado, se considera que el término $P\Delta V$ es puramente entálpico y aumenta principalmente la diferencia de energía libre entre las fases HS y LS.

El parámetro de la cooperatividad, Γ, representa la tendencia que tiene una molécula o centro activo, en un estado de espín determinado, a rodearse de moléculas o centros activos con el mismo espín. Por tanto, Γ es un reflejo de la eficacia con que se transmiten a lo largo del cristal los cambios estructurales asociados a la transición de espín vía interacciones intermoleculares y es responsable de la manifestación cooperativa de las propiedades físicas del sistema.

La ecuación de estado hace posible simular los comportamientos más representativos de las curvas TS, que van desde la transición gradual o equilibrio de espín ($\Gamma = 0$) a una transición de primer orden y con histéresis ($\Gamma > 2RT_c$) (Figura 1.5 izquierda y centro, respectivamente). Si se modifica esta ecuación de la manera conveniente pueden simularse también transiciones incompletas con fracciones residuales de HS y/o LS a temperaturas bajas y altas respectivamente, o incluso transiciones en dos etapas (Figura 1.5 derecha).

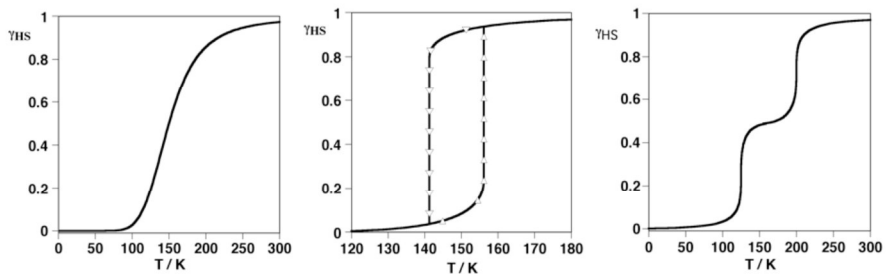

Figura 5.- Tipos principales de curvas de transición de espín representadas en la forma de γ_{HS} frente a T: gradual (izquierda), abrupta y con histéresis (centro) y en dos etapas (derecha).

El parámetro γ_{HS} se obtiene normalmente a partir de medidas magnéticas, espectroscopía Mössbauer (en el caso de compuestos con hierro), espectroscopia electrónica (en el visible) y vibracional o incluso a partir de medidas de difracción de Rayos X.

Este modelo, al igual que otros equivalentes explica los aspectos principales de la transición de fase. Por lo tanto, es insensible con respecto a pequeñas modificaciones estructurales y electrónicas, que afectan drásticamente a la cooperatividad y al campo de ligandos del centro metálico. Estas modificaciones vienen inducidas normalmente por grupos voluminosos, o ligandos capaces de dar lugar a apilamiento π o a interacción por puentes de H, pero también por la presencia de moléculas de disolvente y aniones en la red cristalina.

Otro punto importante es la aparición de polimorfismo, que puede surgir a raíz de pequeñas diferencias en el proceso de cristalización, tales como temperaturas distintas, métodos distintos, mezclas de disolventes, etc. Por desgracia, la racionalización de estos factores es relativamente difícil, dado que no son siempre coherentes de un sistema a otro y por lo general son impredecibles.

1.1.4.- Detección de la transición de espín

Las técnicas experimentales que se emplean en la caracterización de los materiales con transición de espín pueden agruparse según el tipo de información que proporcionen.

Por un lado se emplean técnicas para investigar las configuraciones electrónicas de los centros TS, entre las que se encuentran la espectroscopia UV-Visible, la espectroscopia IR, la espectroscopia Mössbauer y las medidas de susceptibilidad magnética. Por otro lado, encontramos técnicas que permiten obtener los parámetros termodinámicos asociados a la TS, entre las que se encuentran las medidas de calorimetría (DSC). Por último, los métodos de resolución estructural permiten estudiar los cambios estructurales que tienen lugar en la esfera de coordinación de los centros TS, así como cambios en la red cristalina. Entre los distintos métodos encontramos la difracción de Rayos X (para polvo y monocristal), estudios de radiación sincrotrón (XAS o “X-ray Absorption Spectroscopy”, EXAFS o “Extended X-ray Absorption Fine Structure”, XANES o “X-ray absorption near edge structure”, NFS o “Nuclear Forward Scattering”).[27]

Además de las técnicas arriba mencionadas, el desarrollo y el avance en el estudio de las transiciones de espín ha comenzado a hacer uso de técnicas no tan

convencionales que permiten obtener información y realizar un seguimiento de la conversión, como por ejemplo la resonancia magnética nuclear (RMN), la resonancia paramagnética electrónica (EPR, sólo para compuestos de Fe^{III} y Co^{II}), la elipsometría, la espectroscopía de aniquilación de positrones (PAS) o la rotación del espín muónico (MuSR).[27]

1.2.- Objetivos

En general y, valiéndonos de la amplia experiencia de nuestro grupo de investigación en lo que respecta a materiales multifuncionales conmutables que exhiben el fenómeno TS, la presente Tesis Doctoral ha participado en el desarrollo de nuevos y versátiles complejos de coordinación nD que exhiben propiedades TS en interacción con otras propiedades físico-químicas de interés.

Durante este trabajo, se sintetizaron polímeros de coordinación porosos (PCP: Porous Cordination Polymers), también denominados redes metal-orgánicas porosas (PMOF: Porous Metal-Organic Frameworks), que exhiben propiedades TS cooperativas. Estos compuestos fueron caracterizados mediante técnicas físico-químicas tales como medidas magnéticas, medidas DSC, medidas de difracción de rayos X sobre monocristal y/o polvo, TGA y espectroscopia Mössbauer, electrónica y vibracional. Además, se investigó la capacidad de inclusión de moléculas huésped en el interior de los poros de estos PCP (selectividad) así como su influencia sobre las propiedades TS inherentes a cada red. En particular, se sintetizaron y caracterizaron nuevas redes tipo Hofmann formuladas $\{Fe(bpb)[M^{II}(CN)_4]\cdot G\}$ (M^{II} = Ni, Pd, Pt; G = naftaleno, benzonitrilo) basados en el ligando puente no comercial bpb y las redes 3D $\{Fe(3,8phen)[Au(CN)_2]_2\cdot G\}$ (G = tiofeno, 2,5-dimetiltiofeno, benzonitrilo, benzaldehído, nitrobenceno, fluorobenceno, clorobenceno, bromobenceno y 1,3-dibromobenceno) basadas en el ligando orgánico no comercial 3,8-phen. Ambas familias presentan TS fuertemente cooperativas y han supuesto un notable aumento de la porosidad de los clatratos tipo Hofmann conocidos hasta la fecha.

La presente tésis doctoral incluye la síntesis y caracterización de una nueva serie de clatratos formulados $\{[Fe(TPT)_{2/3}[M^{I}(CN)_2]\cdot nG\}$ (M^{I} = Ag (**1**·nG), Au (**2**·nG) G= furano,

pirrol, tiofeno) que ha supuesto el primer ejemplo de PCP con propiedades TS del tipo $[Fe(L)[M^{I}(CN)_2]_2]$ el cual incluye moléculas aromáticas como moléculas huésped.

De manera excepcional, y motivados por la posibilidad de estudiar la interacción entre el fenómeno TS y el acoplamiento magnético, se abordó la síntesis y caracterización del complejo $[Fe(bztpen)(NO)](PF_6)_2$, uno de los pocos ejemplos de especies no hemo $\{FeNO\}^7$ que exhiben el fenómeno TS.

1.3.- Metodología

Diseño y síntesis. Los ligandos orgánicos no comerciales bpb, 3,8-phen y bztpen se sintetizaron según procedimientos experimentales estandarizados y previamente publicados. Posteriormente, fueron caracterizados mediante estudios de Resonancia Magnética Nuclear (RMN). La síntesis de los precursores orgánicos y de los correspondientes compuestos TS obtenidos mediante reacciones de precipitación, se llevaron a cabo utilizando métodos generales en disolución bajo atmósfera inerte. Además, se implementaron técnicas de cristalización basadas en difusión lenta (gas-líquido, líquido-líquido) y de evaporación bajo atmósfera inerte, con objeto de obtener los correspondientes cristales cuya estructura cristalina se estudió mediante difracción de rayos X sobre monocristal.

Caracterización físico-química. En una primera etapa, los compuestos TS sintetizados se caracterizaron a través de análisis elemental, analisis EDAX, TGA y espectroscopia infra-roja. Posteriormente, las propiedades magnéticas de cada producto se midieron mediante un magnetómetro SQUID en el rango de temperaturas 2-400 K. A continuación, se realizaron medidas DSC en el intervalo de temperatura 150-400 K lo cual permitió conocer los parámetros termodinámicos ΔH y ΔS asociados al fenómeno TS. Por su lado, las espectroscopias Raman, UV-Visible y Mössbauer, realizadas a diferentes temperaturas, se utilizaron en casos puntuales. En particular, la espectroscopia Mössbauer permitió la detección de las poblaciones correspondiente a los estados HS y LS. Finalmente, la estructura cristalina de los compuestos TS se determinó a diferentes temperaturas mediante técnicas de difracción de rayos X sobre monocristal y/o polvo microcristalino.

1.4.- Bibliografía

[1] O. Kahn, *Molecular Magnetism*; VCH, New York, **1993**.

[2] R. Feynman, *Miniturization*, *Ed. A . Gilbert* (Reinhold, New York), **1961**, 282.

[3] W. A. Little, *Phys. Rev*., **1964**, *A 134*, 1416.

[4] W. A. Little, *J. Polym. Sci*., *Polym. Lett. Ed*., **1970**, 29.

[5] K. E. Drexler, *Proc. Natl. Acad. Sci. USA*, **1981**, *78*, 5275.

[6] F. L. Cater, *Ed., Molecular Electronic Devices* (M. Dekker, New York), **1982**.

[7] F. L. Cater, *Ed., Molecular Electronic Devices II* (M. Dekker, New York), **1987**.

[8] J. S. Miller, *Adv. Mater*., **1990**, *2*, 378.

[9] J. S. Miller, *Adv. Mater*., **1990**, *2*, 495.

[10] J. S. Miller, *Adv. Mater*., **1990**, *2*, 601.

[11] D. Goldhaber-Gordon, M. S. Montemerlo, J. C. Love, G. J. Opiteck, J. C. Ellenbogen, *Proceeding of the IEEE*, **1997**, *85*, 521.

[12] R. C. Haddon, A. A. Lamola, *Proc. Natl. Acad. Sci. USA*, **1985**, *82*, 1874.

[13] O. Kahn, J. P. Launay, *Chemtronics 3*, **1988**, 151.

[14] J. M. Lehn, *Supramolecular Chemistry. Concepts and persepctives*, VCH, Weinheim, **1995**.

[15] J. P. Sauvage, *Acc. Chem. Res*., **1990**, *23*, 151.

[16] A. Hauser, *J. Chem. Phys*., **1991**, *94*, 2741.

[17] a) A. Bousseksou, J. J. McGarvey, F. Varret, J. A. Real, J. P. Tuchagues, A. C. Dennis, M. L. Boillot, *Chem. Phys. Lett.*, **2000**, *318*, 419; b) N. Moliner, L. Salmon, L. Capes, M. C. Muñoz, J. F. Létard, A. Bousseksou, J. P. Tuchagues, J. J. McGarvey, A. C. Dennis, M. Castro, R. Burriel, J. A. Real, *J. Phys. Chem. B.,* **2002**, *106*, 4276; c) G. Molnár, V. Niel, A. B. Gaspar, J. A. Real, A. Zwick, A.

Bousseksou, J. J. McGarvey, *J. Phys. Chem. B.*, **2002**, *106*, 9701; d) M. Sorai, S. Seki, *J. Phys. Chem. Solids,* **1974**, *35*, 555.

[18] a) T. Granier, B. Gallois, J. Gaultier, J. A. Real, J. Zarembowitch, *Inorg. Chem.*, **1993**, *32,* 5305; b) P. Gütlich, V. Ksenofontov, A. B. Gaspar, *Coord. Chem. Rev.*, **2005**, *249*, 1811-1829.

[19] a) E. Buhks, M. Bixon, J. Jortner, *J. Am. Chem. Soc.*, **1980**, *102*, 2918; b) C. L. Xie, D. N. Hendrickson, *J. Am. Chem. Soc*., **1987**, *109*, 6981.

[20] A. Hauser, *Comments Inorg. Chem.*, **1995**, *17*, 17.

[21] J. J. McGarvey y I. Lawthers, *J. Chem. Soc., Chem. Commun.,* **1982**, 906.

[22] a) S. Decurtins, P. Gütlich, C. P. Köhler, H. Spiering, A. Hauser, *Chem. Phys. Lett.*, **1984**, *139*, 1; b) S. Decurtins, P. Gütlich, K. M. Hasselbach, H. Spiering, A. Hauser, *Inorg. Chem.,* **1985**, *24*, 2174.

[23] C. Roux, J. Zarembowitch, B. Gallois, T. Granier, R. Claude, *Inorg. Chem.*, **1994**, *33*, 2273.

[24] M. L. Boillot, A. Sour, P. Delhaès, C. Mingotaud, H. Soyer, *Coord. Chem. Rev.*, **1999**, *190-192*, 47.

[25] H. Spiering, T. Kohlhaas, H. Romstedt, A. Hauser, C. Bruns-Yilmaz, J. Kusz, P. Gütlich, *Coord. Chem. Rev*., **1999**, *190-192*, 471.

[26] a) C. P. Slichter, H G. Drickamer, *J. Chem. Phys*., **1972**, *56*, 2142; b) J. M. Honig, *J. Chem. Ed*., **1999**, *76*, 848.

[27] a) Eds. Gütlich, Goodwin, *Top. Curr. Chem*., **2004**, vol. *233-235*; b) Ed. M. A. Halcrow, John Wiley & Sons, Ltd., **2013**.

CAPÍTULO 2

Electronic structure modulation in an exceptionally stable non-heme nitrosyl iron(II) spin-crossover complex

REVISTA: Chemistry A European Journal

ÍNDICE DE IMPACTO: 5.771

CAPÍTULO 2

Electronic structure modulation in an exceptionally stable non-heme nitrosyl iron(II) spin-crossover complex

2.1.- Abstract

The highly stable nitrosyl iron (II) mononuclear complex $[Fe(bztpen)(NO)](PF_6)_2$ (bztpen = N-benzyl-N,N',N'-tris(2-pyridylmethyl)ethylenediamine) displays an S = 1/2↔S = 3/2 SCO behaviour $T_{1/2}$ = 370 K, ΔH = 12.48 kJ mol^{-1}, ΔS = 33 J K^{-1} mol^{-1}) steming from strong magnetic coupling between the NO radical (S = 1/2) and thermally interconverted (S = 0↔S = 2) ferrous spin states. The crystal structure of this robust complex has been investigated in the temperature range 120-420 K affording a detailed picture of how the electronic distribution of the t_{2g}-e_g orbitals modulates the structure of the $\{FeNO\}^7$ bond providing valuable magneto-structural and spectroscopic correlation and DFT analysis.

2.2.- Introduction

Heme and non-heme iron nitrosyl complexes have been intensively investigated during the last three decades as chemical models of active Fe-NO biologically relevant sites.[1] Ferric heme-nitrosyl complexes derive from the LS state of Fe^{III} (S = 1/2) and afford singlet ground spin state (S = 0) species.[2] In contrast, non-heme iron-nitrosyl complexes can exist either in the S = 3/2 or the S = 1/2 spin states depending on the ancillary ligands.[3] Interestingly, a small number of non-heme iron-nitrosyl complexes show S = 3/2↔S = 1/2 SCO behaviour. Six of them are pentacoordinate complexes formulated [FeL(NO)] (with L = salen,[4] salphen,[5] (L^1),[6] (L^{1a}),[6] (L^2)[7]) and $[Fe(TMC)(NO)](BF_4)_2$ (TMC = 1,4,8,11-tetramethyl-1,4,8,11-tetraazacyclotetradecane),[8] whereas the remaining are the hexacoordinate complexes $[FeL^3(NO)(CH_3OH)]$,[7] $[FeL_4(NO)(CH_3OH)]$,[7] and $[FeL^{pr}(NO)]$[9] (see Scheme 1).

In the Enemark and Feltham systematization of the M-NO bonding, non-heme iron-nitrosyl complexes are considered $\{FeNO\}^7$ species, where seven is the total

number of electrons in the Fe d and NO π^* orbitals.[10] The radical character of the non-innocent NO ligand and the close energetic proximity to the Fe d orbitals determine the essence of the bonding in the $\{FeNO\}^7$ moiety. Depending on the d-π^* energy difference, different electronic structures have been envisaged. However, the substantial degree of covalence involved in the {FeNO} unit makes an unambiguous assignation of specific oxidation and ground spin states difficult.[11] For example, from an analysis of the Fe K-edge X-ray absorption spectra of a series of S = 3/2 non-heme iron-nitrosyl complexes, which included [Fe(salen)-(NO)], Solomon et al. concluded that the S = 3/2 $\{FeNO\}^7$ species are more precisely specified as a HS (S = 5/2) ferric center antiferromagnetically coupled with the NO^- (S = 1) ion.[12] The same conclusion was achieved by Lehnert et al. from vibrational correlations along with DFT calculations for the complexes [Fe(BMPA-Pr)(NO)(X)] (BMPA-Pr = N-propanoate-N,N-bis(2-pyridylmethyl)amine; X = Cl^-, ClO_4^-, I^- or $CF_3SO_3^-$) and $[Fe(TPA)(NO)(CH_3CN)](ClO_4)_2$ (TPA = tris(2-pyridylmethyl)-amine).[13] This study also indicates that the NO^- ion acts mostly as a π-donor ligand in these complexes. Based on a combination of electron spin resonance (EPR) and Mössbauer spectroscopy and DFT methods, Wieghardt et al. reached the same conclusion for the SCO complex $[FeL^{pr}(NO)]$ in the S = 3/2 state.[9] Furthermore, these authors proposed for the S = 1/2 spin state a LS (S = 0) ferrous center coupled with $NO^{\cdot}$ (S = 1/2). The latter conclusion has recently been supported by Salomon et al. from sulfur-K-edge X-ray absorption spectroscopy and DFT studies on two model complexes that contain sulfur ligands.[14] In this respect, non-heme $\{FeNO\}^7$ complexes with S = 1/2 ground states have very similar electronic structures as the corresponding heme complexes.[2, 15] Thus, for $\{FeNO\}^7$ SCO species the observed S = 3/2↔S = 1/2 equilibrium could be more precisely described as a valence tautomerism process.[9] In contrast, based on DFT calculations of the Mössbauer parameters of the [Fe(salen)(NO)] SCO complex and other studies on the isopenicillin N synthase, Oldfield et al. have concluded that the investigated S = 3/2 $\{FeNO\}^7$ species can be described as a HS (S = 2) ferrous Fe^{II} antiferromagnetically coupled with NO (S = 1/2).[16] The same conclusion was drawn from a recent spectroscopic and computational study of a non-heme iron-nitrosyl center in a biosynthetic model of nitric oxide reductase.[17]

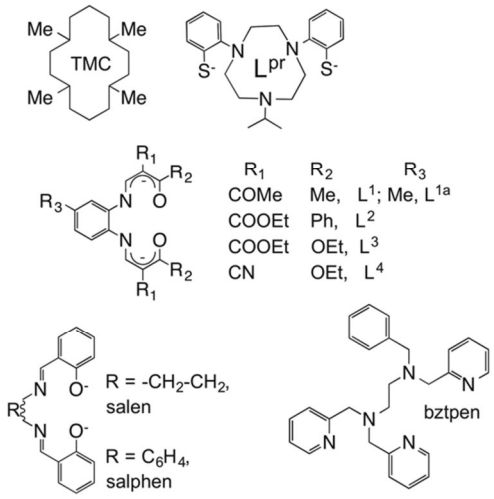

Scheme 1.- Ligands concerned with the synthesis of iron-nitrosyl complexes exhibiting SCO properties.

In previous studies, we investigated the suitability of the pentadentate N-benzyl-N,N',N''-tris(2-pyridylmethyl)ethylenedi-amine (bztpen) ligand in the synthesis of new $\{[Fe^{II,III}(bztpen)]_xL\}(PF_6)_y$ SCO complexes with the sixth coordination site occupied by suitable ancillary monodentate L^- ligands such as dicyanamide (Fe^{II}, x = 2, y = 3)[18] or alkoxydes (Fe^{III}, x = 1, y = 2).[19] In addition, Schindler et al. have compared the stability of the $[Fe(bztpen)(NO)]^{2+}$ ion in solution with respect to that of the homologous Fe^{III} peroxo and hydroperoxo complexes, and the crystal structure of the triflate derivative $[Fe(bztpen)(NO)](CF_3SO_3)_2$ was succinctly described in this study.[20]

Following our research line and in principle motivated by the study of the interplay between the SCO phenomenon and strong magnetic coupling, here we report the synthesis and characterization of the complex $[Fe(bztpen)(NO)](PF_6)_2$ (**1**) in the solid state. Complex **1** is a new non-heme $\{FeNO\}^7$ species displaying a SCO equilibrium that extends beyond 400 K. Facilitated by the extraordinary robustness of the single crystals, a detailed single-crystal analysis carried out in the temperature range 120-420 K shows the adaptability of the NO molecule to the change of spin states in the Fe center. Furthermore, multi-temperature EPR, Mössbauer, IR, Raman, and UV-Vis spectroscopy as well as theoretical calculations have been carried out to clarify the nature of the observed S = 3/2↔S = 1/2 equilibrium.

2.3.- Results and discussion

2.3.1.- Synthesis

When NO(g) is bubbled under anaerobic conditions into a saturated pale yellow methanolic solution of $[Fe^{II}(bztpen)(MeOH)]^{2+}$ (≈ 3 x 10^{-3} M) a deep purple solution is instantaneously formed followed by rapid and quantitative precipitation of the microcrystalline brown-purple solid **1**. Starting from diluted solutions (≥ 9 x 10^{-4} M) of $[Fe^{II}(bztpen)(MeOH)]^{2+}$ and following the same procedure single crystals of compound **1** were obtained in a few days.

2.3.2.- Magnetic properties

The thermal dependence of the product $\chi_M T$ in the temperature interval 2-400 K for compound **1** is shown in Figure 1 (χ_M is the magnetic susceptibility and T is the temperature). At 400 K the product $\chi_M T$ is 1.35 cm^3 K mol^{-1} and continuously decreases with cooling until 0.38 cm^3 K mol^{-1} at approximately 150 K. Below this temperature the value of $\chi_M T$ remains practically constant down to 15 K. In the temperature range 15-2 K a quite small decrease denotes the onset of very weak intermolecular antiferromagnetic interactions. The value $\chi_M T$ = 0.38 cm^3 K mol^{-1} is consistent with an S = 1/2 ground state with g = 2.01.

The increase of the product $\chi_M T$ above 150 K is consistent with a gradual SCO. Assuming that the SCO takes place between the LS (S = 0) and HS (S = 2) states of a Fe^{II} strongly antiferromagnetically coupled to the S = 1/2 state of NO, the SCO can be considered to occur in an effective way between the resulting S = 1/2 and 3/2 states. In this framework approximately 54.3% of the molecules are in the S = 3/2 state at 400 K. According to previous work,[9, 14] an equivalent scenario could involve the occurrence of valence tautomerism in the Fe-NO moiety. This would afford the strong antiferromagnetically coupled S = 5/2 (Fe^{III}) and S = 1 (NO^-) spin states and the uncoupled S = 0 (Fe^{II}) and S = 1/2 (NO) spin states.

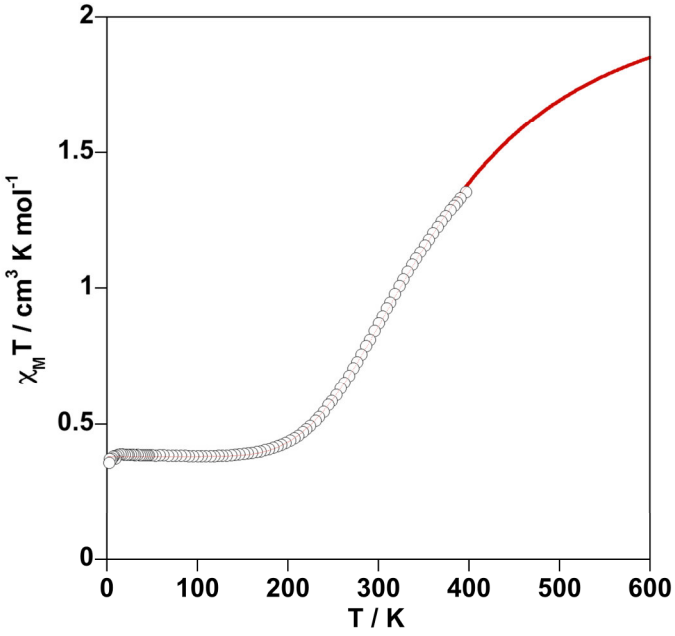

Figure 1.- Magnetic behaviour of complex **1** in the temperature range 2-400 K. The black line corresponds to the best fit of the experimental data (see text).

In order to evaluate the thermodynamic parameters associated with the spin change we have considered that the term $\chi_M T$ can be expressed as given in Equation (1):

$$x_M T^{obs} = (x_M T)_{NO}(1 - f) + (x_M T)_{Fe-NO} f \quad (1)$$

$$f = \frac{1}{\left\{1+exp\left[\left(\frac{\Delta H}{R}\right)\left(\frac{1}{T}-\frac{1}{T_{1/2}}\right)\right]\right\}} \quad (2)$$

where $(\chi_M T)_{NO}$ is the $\chi_M T$ value at low temperatures due to the presence of the radical NO (S = 1/2) and Fe^{II} (S = 0), $(\chi_M T)_{Fe\text{-}NO}$ is the expression of a dinuclear species derived from the Hamiltonian $H = -JS_aS_b$ with S_a = 1/2 or 1 and S_b = 2 or 5/2 species, respectively,[21a] f is the molar fraction of the HS species expressed by the theory of regular solutions in the form given by Slichter and Drickamer.[21b] In equation (2), ΔH is the enthalpy variation, R is the universal constant of gases, and $T_{1/2}$ is the temperature at which HS and LS species are present at 50% (ΔG = 0). Given the expected large magnitude of the antiferromagnetic coupling constat (J), it is safe to consider that only the S = 3/2 state plays and effective role in $(\chi_M T)_{Fe\text{-}NO}$. A least-squares fit procedure,

which minimizes the function $R_{min} = \sum(x_M T^{obs} - x_M T^{calcd})^2 / \sum(x_M T^{obs})^2$, leads as adjustable parameters $g_{3/2}$ = 2.15, ΔH = 12.48 kJ mol^{-1}, $T_{1/2}$ = 377.6 K, and R_{min} = 7·10^{-5}. The total entropy variation is given by $\Delta S = \Delta H/T_{1/2}$ = 33 J K^{-1} mol^{-1}.

The excellent agreement between the calculated and experimental data supports the assumption of synchronous reversible spin-state conversion and strong antiferromagnetic coupling between Fe^{II} and NO. This strong antiferromagnetic coupling is in line with the magnitude of the *J* parameter estimated from our DFT calculations for complex **1** (see below) and those reported by Wieghardt and co-workers for the complex [Tp*Co(NO)] (Tp* = hydro-tris(3,5-Me$_2$-pyrazolyl)borate).[22] The ΔS value is found clearly smaller than typically observed for Fe^{II} SCO complexes[24] but consistent with a S = 1/2↔S = 3/2 transformation.[25]

It is worth mentioning the similarities between the magnetic behaviour of complex **1** and that reported by Krügger and co-workers for [Fe(L-N$_4$Me$_2$)(bian$^-$)](ClO$_4$), where L-N$_4$Me$_2$ and bian$^-$ are N,N'-dimethyl-2,11-diaza[3.3]-(2,6)pyridinophane and the radical anion of N,N'-diphenylacenaphtene-1,2-diimine, respectively.[26] In the temperature interval 22-240 K, this compound displays a χ_MT value of 0.37 cm^3 K mol^{-1}, which is consistent with an S = 1/2 ground state. Then upon heating the value of χ_MT smoothly increases reaching a value of 0.75 cm^3 K mol^{-1} at 380 K indicating partial population of the S = 3/2 state. Based on the magnetic properties as well as EPR and Mössbauer spectra Krügger et al. concluded that the observed behaviour corresponds to a combined effect of strong antiferromagnetic coupling between the radical ligand bian$^-$ and the Fe^{II} ion switching between the S = 0 and S = 2 states. Much weaker magnetic coupling was reported for a series of five-coordinate halido and pseudohalido-bis(o-iminobenzo-semiquinonato)iron(III) complexes that undergo SCO between the effective spin states S = 3/2 and S = 1/2.[27]

2.3.3.- Spectroscopic characterization of compound 1

2.3.3.1.- EPR spectra

The X-band EPR solid-state spectra of compound **1** collected at 4 and 300 K are shown in Figure 2a. At 4 K the spectrum is characterized by a sharp signal centered at g = 2.02, which becomes wider without moving significantly (g = 2.05) at 300 K where, according to the magnetic properties, approximately 30% of the molecules are in the S =

3/2 state. This EPR spectrum is reminiscent of that reported for the classical SCO nitrosyl compound [Fe(salen)(NO)], for which no signal at g ≈ 4, which is characteristic of the S = 3/2 state, is observed, which was considered consistent with an electron essentially residing in the NO molecule.[28] Similarly, no observation of the S = 3/2 signal was reported for the SCO complex [FeL^{pr}(NO)].[9] In contrast, the EPR spectrum of the non-heme HS iron(II)-nitrosyl model complex [Fe(bmpa-Pr)(NO)(Cl)][13] is characterized by a dominant signal at g ≈ 4 attributable to the S = 3/2 state.

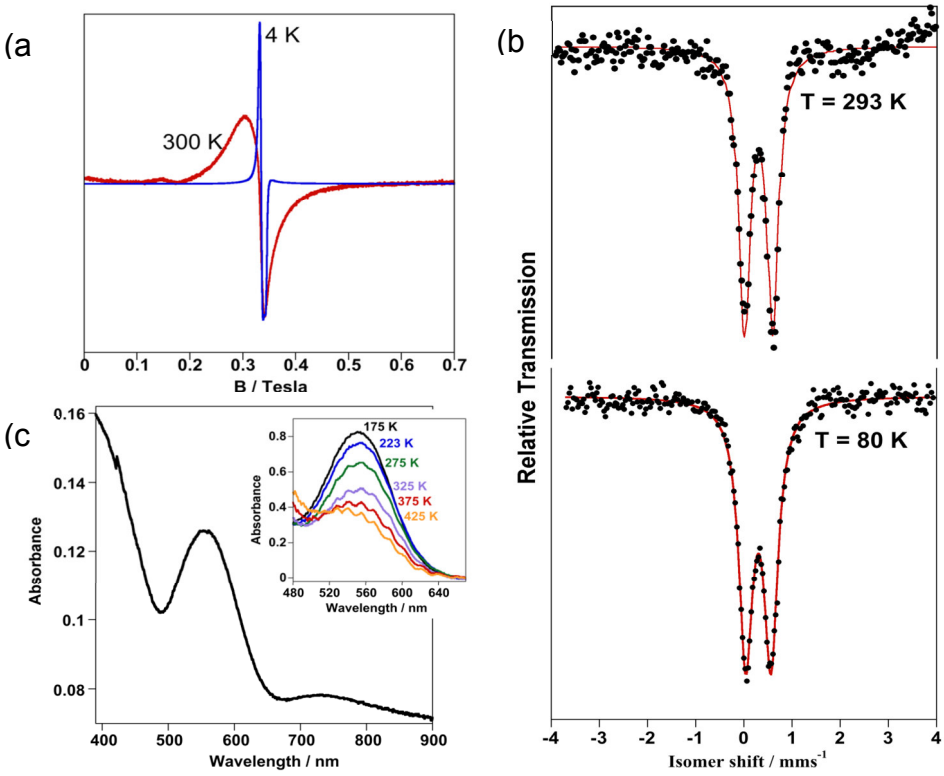

Figure 2.- Spectroscopic measurements for compound **1**. a) EPR spectra at 4 (black line) and 300 K (gray line). b) Mössbauer spectra at 293 and 80 K (lines are fitted spectra). c) Diffuse reflectance spectrum at 300 K (the inset shows the thermal variation of the λ = 555 nm peak in the temperature interval 175-425 K).

2.3.3.2.- Mössbauer spectra

Zero-field ^{57}Fe Mössbauer spectra at 80 and 293 K for compound **1** are shown in Figure 2b. The poor signal-to-noise ratio of the 293 K spectrum discouraged us from recording Mössbauer spectra at higher temperatures. The fitted spectral parameters (assuming Lorentzian line shapes) are given in Table S1 in the Supporting Information. The 80 K spectrum can be assigned to a LS ferrous or ferric species (not distinguishable by Mössbauer spectroscopy) with an isomer shift δ = 0.306(5) mm s^{-1} and a quadrupole splitting ΔE_Q = 0.523(9) mm s^{-1}. Detection of only one doublet at 293 K, δ = 0.295(4) mm s^{-1} and ΔE_Q = 0.590(8) mm s^{-1}, is consistent with a fast spin-state interconversion rate compared to the time scale of Mössbauer spectroscopy leading to an averaged spectrum. This is also supported by the unusual and almost insignificant thermal variation of the spectrum parameters ΔE_Q and δ. A similar situation was reported for the nitrosyl SCO complexes [Fe(tmc)NO](BF$_4$)$_2$],[8] [FeL^1(NO)],[29] and [FeL^{1a}(NO)][29] (see Scheme 1) and for the aforementioned SCO complex [Fe(L-N$_4$Me$_2$)(bian$^-$)](ClO$_4$).[26] In contrast, the characteristic signals of both spin states were observed for [Fe(salen)(NO)],[28] [Fe(sal-phen)(NO)],[5] and [Fe(L^{pr})(NO)].[9] All these Fe^{II} SCO nitrosyl complexes, including complex **1**, display δ values of the same order of magnitude, found in the interval 0.3-0.5 mm s^{-1}.

2.3.3.3.- Electronic spectra

Figure 2c displays the diffuse reflectance spectrum of compound **1** at 293 K, where the relative population of the S = 1/2 and S = 3/2 states is estimated to be LS/HS 73:23. This spectrum is characterized by three absorption bands centered at approximately λ = 400, 555, and 730 nm. The two first maxima are reminiscent of Fe^{II} complexes in the LS state and could be tentatively ascribed to the ^{1}A$\rightarrow$^{1}T$_2$ and ^{1}A$\rightarrow$^{1}T$_1$ transitions, respectively.[30] However, a number of metal-ligand (pyridine and NO) charge-transfer (CT) bands may occur in the same energy window making difficult a precise identification of the d-d bands. In this respect, a similar spectrum has been reported for the S = 1/2 {FeNO}^{7} complex *trans*-[(cyclam)Fe^{II}(NO)Cl](ClO$_4$) in acetonitrile with bands at λ = 398 (ε = 300) and 560 nm (ε = 145 M^{-1} cm^{-1}). These bands were reasonably ascribed to the Fe^{II} in the LS state, because they disappear after one-electron oxidation suggesting a metal-centered process.[31] Interestingly, compound **1** displays thermochromism in the temperature interval 175-425 K. Upon heating, the

brown-violet color of the crystal becomes pale (see Figure S1 in the Supporting Information). This color change is primarily related to the bleaching of the λ = 555 nm absorption, which starts above approximately 200 K to be completed to around 80% at 425 K (see the inset of Figure 2c). The remarkably good correlation between the temperature dependence of its intensity and the magnetic behaviour of complex **1**, which is shown in Figure 3, supports the idea that the $^1A \rightarrow {}^1T_1$ transition is a relevant component of the λ = 555 nm absorption band. In this respect, it is worth mentioning that this thermochromism is reminiscent of the thermochromism associated with the LS↔HS state change in Fe^{II} SCO complexes observed in the λ = 500-600 nm window in solution and the solid state.

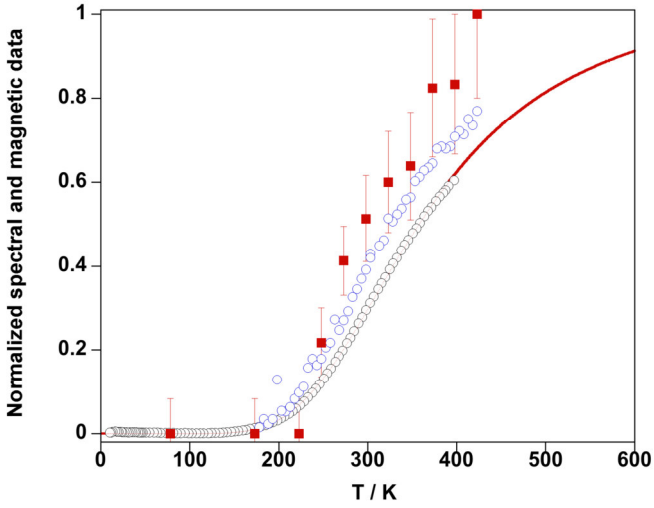

Figure 3.- Correlation of the magnetic (experimental = open circles and calculated = lines) and spectroscopic (UV/VIS and Raman) data. Full squares indicate the Raman peak intensity ratio $\lambda_{1789}/(\lambda_{1789}+\lambda_{1684})$ of the ν_{NO} stretching mode. Open crosses show the (normalized and inversed) absorbance variation at λ = 555 nm.

A number of relevant studies, by Brunold et al.[32] and Solomon and co-workers,[12, 33] which combine UV/VIS absorption spectroscopy, magnetic circular dichroism measurements, and DFT studies have been devoted to analyze the electronic spectra of $\{FeNO\}^7$ species in the S = 3/2 state. They display characteristic broad CT bands centered at approximately λ = 660 and 430 nm. These bands have been formally attributed to $NO^- \rightarrow Fe^{3+}$ CT processes, in complexes with much weaker ligand-field donor

groups than complex **1**. Then, the λ = 730 nm maximum in compound **1** should be tentatively assigned to such CT transitions because, at 293 K the LS state co-exists with 27% of the Fe centers in the HS state.

2.3.3.4.- Vibrational spectra

Variable-temperature, single-crystal Raman spectra were acquired by using both λ = 532 and 633 nm laser excitations. Representative spectra are shown in Figure 4a. The NO stretching mode ν_{NO} undergoes a remarkable shift from ν =1789 to 1684 cm^{-1} (for both excitation wavelengths) when going from 400 to 100 K. These characteristic vibrational modes can be clearly associated with the S = 3/2 and S = 1/2 states, respectively, because they co-exist (in different proportions) in the temperature interval where the conversion between these two magnetic states takes place. Indeed, as shown in Figure 3, the relative intensity of these modes follows reasonably well the magnetic changes (a better correlation would be rather fortuitous as the intensity of the Raman modes is not directly proportional to the population of the two electronic states).

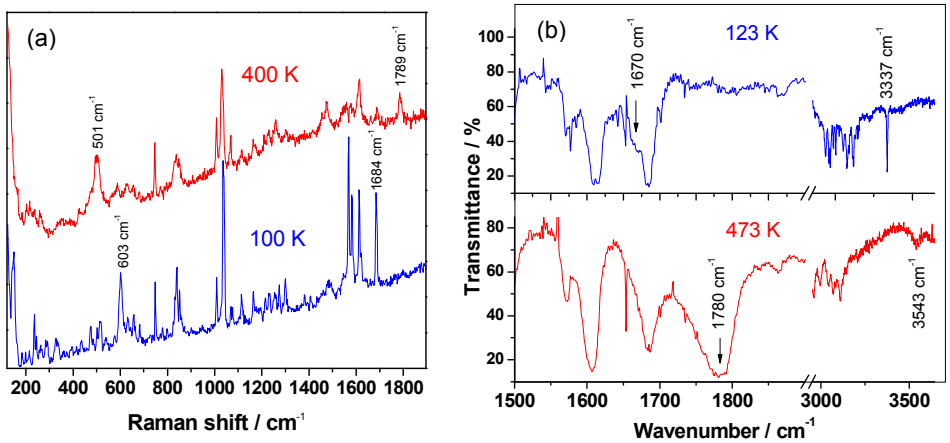

Figure 4.- Representative variable-temperature a) Raman scattering (λ = 532 nm excitation, *-z(yy)z* configuration) and b) non-polarized infrared absorption spectra of a single crystal of compound **1**.

The temperature-dependent, single-crystal IR absorption spectra (Figure 4b) confirm well the Raman data. At 473 K, a broad absorption band is observed at around ν = 1780 cm^{-1} as well as its overtone around ν = 3543 cm^{-1}, which can be attributed to the ν_{NO} mode of the complex in the S = 3/2 state. At 123 K, these bands disappear and

an ill-resolved shoulder, assigned to the ν_{NO} mode in the S = 1/2 state, appears at around ν = 1670 cm^{-1}. This assignment is further substantiated by the observation of the overtone of this mode at ν = 3337 cm^{-1}. Similar to the Raman spectra, the NO stretching peaks (fundamental as well as overtone) associated with the S = 3/2 state are much broader than their S = 1/2 state counter-parts, which may indicate a disorder in the former. These results agree reasonably well with the corresponding ν_{NO} IR modes reported for [Fe(salen)(NO)], that is, ν = 1712 (S = 3/2) and 1630 cm^{-1} (S = 1/2).[4] Nevertheless, the shift of the ν_{NO} mode is approximately 20% larger for complex **1** most likely reflecting the distinct chemical nature of the ligands salen and bztpen and the coordination number of both complexes.[2, 13] In the case of the IR absorption spectra, the temperature dependence of the peak intensities is considerably altered by heating due to the IR probe beam. For this reason, the quantitative correlation of IR absorbance changes with the magnetic data was not possible. It is important to note, however, that the spin conversion at low temperatures is fully complete because the characteristic ν_{NO} IR absorption bands (and also Raman peaks) of the high-temperature form disappear completely below approximately 200 K. Due to the weak spectral intensities above 400 K, it is more difficult to conclude about the completeness of the transition at high temperatures, but we can note that no residual fraction is observed in the IR spectra at 473 K, indicating a nearly complete transition (Figure 4b).

Besides the ν_{NO} stretching mode, several other spectral changes are observed in the Raman spectra. At high temperature, where the S = 3/2 state is significantly populated, a medium band dominates over ν = 503 cm^{-1} the Raman spectrum of compound **1**. Interestingly, the intensity of this peak decreases upon cooling down to 100 K at expense of a new peak centered at ν = 603 cm^{-1}. According to the important previous work, which include ^{15}NO isotope labeling, it is reasonable to tentatively assign the ν = 603 and 501 cm^{-1} frequencies to coupled Fe-NO stretching and Fe-NO bending modes (see below) in the S = 1/2 and S = 3/2 states, respectively.[3,34-37]

*2.3.3.5.- Structure of compound **1***

The crystal structure of the title compound was investigated at 120, 200, 250, 275, 300, 340, 380, 400, and 420 K on the same single crystal. The crystal belongs to the orthorhombic *Pbca* space group in the temperature range investigated. Selected crystallographic data are gathered in Table 1. The molecular structure is displayed in

Figure 5 together with the atom-numbering scheme and representative bond lengths and angles are collected in Table 2. The iron atom is in a distorted octahedral [FeN_6] environment defined by five nitrogen atoms belonging to the pentadentate bztpen ligand and the nitrogen atom of the nitroxyl group. Two PF_6^- ions balance the charge of the $[Fe(bztpen)(NO)]^{2+}$ ion. The bztpen ligand coordinates the Fe, defining a distorted square pyramid, in which the N_2 atom lies on the axial apex. The opposite apex is occupied by the N_6 atom of the NO molecule. The N atom is in the center of a tripod whose arms are defined by two picolylamine-type moieties [N_2-C_7-C_8-N_3 and N_2-C_6-C_5-N_1] and an ethylenedia-mine-type moiety [N_2-C_{13}-C_{14}-N_4]. These arms are anchored to the Fe through the atoms N_3, N_1 and N_4, respectively. An additional picolylamine-type arm, [N_4-C_{15}-C_{16}-N_5], originates at the N(4) atom and coordinates the remaining equatorial position of the Fe center through the N_5 atom.

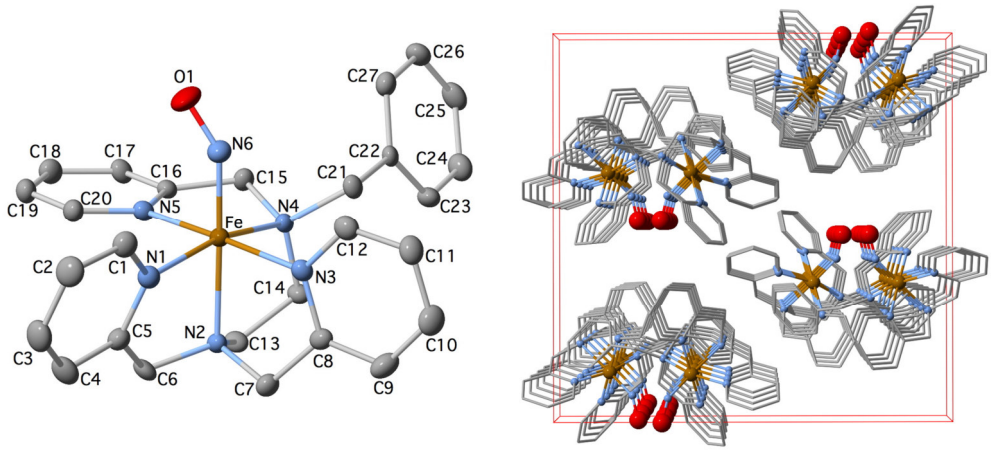

Figure 5.- Molecular structure (left) and perspective view of the crystal packing in the [100] direction (PF_6^- ions are not shown) (right) of compound **1**.

Table 1.- Crystal data of compound **1**.

Empirical formula	$C_{27}H_{29}N_6OP_2F_{12}Fe$			
Mr	799.35			
Crystal system	orthorhombic			
Space group	*Pbca*			
Z	8			
Crystal size (mm)	0.06 x 0.10 x 0.10			
F(000)	3240			
T / K	**120 K**	**200 K**	**250 K**	**275 K**
a (Å)	17.1485(3)	17.2552(2)	17.3540(5)	17.3638(2)
b (Å)	18.8049(4)	18.8664(2)	18.9388(5)	18.9585(2)
c (Å)	19.2745(4)	19.3440(2)	19.4544(5)	19.4477(2)
V (Å^3)	6215.6(2)	6297.31(12)	6393.9(3)	6402.05(12)
D_c (g cm^{-3})	1.708	1.686	1.661	1.659
μ (Mo-K$_\alpha$)(mm^{-1})	0.696	0.687	0.676	0.676
No. of total reflections	8462	8475	9262	9293
No. of reflections [$I>2\sigma(I)$]	4874	6568	6468	6309
R_1 [$I>2\sigma(I)$]	0.0584	0.0453	0.0606	0.0651
R_1 [all data]	0.1255	0.0638	0.0902	0.0968
S	0.862	0.812	0.904	0.831

$R_1 = \Sigma \, ||Fo| - |Fc|| \, / \, \Sigma \, |Fo|$; $wR = [\, \Sigma \, [w(Fo^2 - Fc^2)^2] \, / \, \Sigma \, [w(Fo^2)^2]]^{1/2}$; $w = 1/ \, [\sigma^2(Fo^2) + (m \, P)^2 + n \, P]$ where $P = (Fo^2 + 2Fc^2)/3$;
m = 0.1058 (**120 K**), 0.1088 (**200 K**), 0.1355 (**250 K**), 0.1635 (**275 K**);
n = 16.5463 (**120 K**), 12.8834 (**200 K**), 9.4233 (**250 K**), 13.1359 (**275 K**).

Table 1 cont.- Crystal data of compound **1**.

Empirical formula	$C_{27}H_{29}N_6OP_2F_{12}Fe$				
Mr	799.35				
Crystal system	orthorhombic				
Space group	*Pbca*				
Z	8				
Crystal size (mm)	0.06 x 0.10 x 0.10				
F(000)	3240				
T / K	**300 K**	**340 K**	**380 K**	**400 K**	**420 K**
a (Å)	17.4065(4)	17.4527(2)	17.4819(5)	17.5159(3)	17.5396(4)
b (Å)	18.9710(5)	19.0622(3)	19.1080(4)	19.1566(4)	19.2019(5)
c (Å)	19.5023(5)	19.5749(2)	19.6398(5)	19.6896(3)	19.7292(4)
V (Å^3)	6440.0(3)	6512.33(14)	6560.6(3)	6606.8(2)	6644.7(3)
D_c (g cm^{-3})	1.649	1.631	1.619	1.607	1.598
μ (Mo-K$_\alpha$)(mm^{-1})	0.672	0.664	0.659	0.655	0.651
No. of total reflections	8579	8941	8940	9057	9017
No. of reflections [$I>2\sigma(I)$]	5865	5669	5424	4881	4276
R_1 [$I>2\sigma(I)$]	0.0677	0.0740	0.0749	0.0930	0.1031
R_1 [all data]	0.0983	0.1140	0.1182	0.1495	0.1363
S	0.860	1.036	1.028	1.133	1.223

$R_1 = \Sigma \, ||Fo| - |Fc|| \, / \, \Sigma \, |Fo|$; $wR = [\, \Sigma \, [w(Fo^2 - Fc^2)^2] \, / \, \Sigma \, [w(Fo^2)^2]]^{1/2}$; $w = 1/ \, [\sigma^2(Fo^2) + (m \, P)^2 + n \, P]$ where $P = (Fo^2 + 2Fc^2)/3$;
m = 0.1809 (**300 K**), 0.1282 (**340 K**), 0.1316 (**380 K**), 0.2000 (**400 K**), 0.2000 (**420 K**);
n = 11.1178 (**300 K**), 7.2081 (**340 K**), 4.877 (**380 K**), 0.0000 (**400 K**), 0.0000 (**420 K**).

Table 2.- Selected experimental and computed bond lengths [Å] and angles [º] for **1**.

	Experimental					
	120 K S = 1/2	**200 K**	**250 K**	**275 K**	**300 K**	**340 K**
Fe-N1	1.994(3)	1.999(2)	2.012(3)	2.023(3)	2.034(3)	2.056(3)
Fe-N2	2.100(3)	2.105(2)	2.115(2)	2.123(2)	2.138(3)	2.154(3)
Fe-N3	1.987(3)	1.999(2)	2.014(3)	2.025(3)	2.033(3)	2.063(3)
Fe-N4	2.084(3)	2.084(2)	2.102(2)	2.113(2)	2.128(3)	2.163(3)
Fe-N5	1.992(3)	1.992(2)	2.007(2)	2.021(3)	2.032(3)	2.065(3)
Fe-N6	1.733(3)	1.738(2)	1.745(3)	1.740(3)	1.745(3)	1.751(4)
N6-O	1.170(4)	1.157(3)	1.143(4)	1.133(4)	1.126(5)	1.111(5)
Fe-N_{bztpen}	2.031	2.036	2.050	2.061	2.073	2.100
Fe-N^{av}	1.982	1.986	1.999	2.008	2.018	2.042
Fe-N-O	144.0(3)	144.5(2)	145.8(3)	147.4(3)	148.8(4)	151.0(4)
Σ	60.88	60.87	62.20	65.16	67.34	71.31
Φ	4.4	4.4	4.4	4.6	4.8	5.1

Table 2 cont.- Selected experimental and computed bond lengths [Å] and angles [º] for **1**.

	Experimental				**Computed**	
	380 K	**400 K**	**420 K**	**Extrapolated S = 3/2***	**{FeNO}^{7} (S= 1/2)**	**{FeNO}^{7} (S= 3/2)**
Fe-N1	2.072(3)	2.085(4)	2.098(7)	2.085	2.004	2.175
Fe-N2	2.166(3)	2.171(4)	2.190(5)	2.231	2.082	2.255
Fe-N3	2.078(3)	2.080(4)	2.085(7)	2.158	2.005	2.161
Fe-N4	2.179(3)	2.193(3)	2.203(5)	2.285	2.071	2.260
Fe-N5	2.087(3)	2.094(4)	2.099(6)	2.180	2.006	2.193
Fe-N6	1.753(3)	1.745(5)	1.751(7)	1.755	1.759	1.782
N6-O	1.102(5)	1.106(7)	1.099(10)	1.052	1.170	1.156
Fe-N_{bztpen}	2.116	2.125	2.135	2.204	2.034	2.209
Fe-N^{av}	2.056	2.061	2.071	2.127	1.988	2.138
Fe-N-O	154.7(9)	156.5(6)	157.9(10)	167	143.4	165.6
Σ	74.55	77.24	76.80	90.95	59.23	92.48
Φ	5.3	5.5	5.5	6.42	3.63	5.60

The average Fe-N bond length of the Fe-bztpen moiety, <Fe-N_{bztpen}>N_{av}, gradually increases with increasing temperature from 2.031 Å (120 K) until 2.135 Å (420 K) involving a total variation of practically 0.1 Å. Consistently, the sum of deviations from the ideal octahedron of the twelve "*cis*" N-Fe-N angles ($\Sigma = \sum_{i=1}^{12} |\theta_i - 90|$) shows that the coordination center is strongly distorted at 120 K with Σ = 60.98° and this distortion increases as the temperature increases until reaching a value of 76.88° at 420 K. In contrast, the trigonal distortion parameter defined as $\Phi = \sum_{i=1}^{24} (|\phi|)/24$ (there are twenty-four Φ_i angles generated by superposition of four pairs opposite triangular faces of an octahedron; Φ = 60° for a regular octahedron), is small at 120 K (Φ = 4,4°) and increases up to 5.58° at 420 K. The Fe-NO bond length (Fe-N6) displays a

very small increase from 1.733(3) to 1.751(7) Å making slightly less pronounced the overall change of the average [FeN_6] bond length, ΔR (<Fe-N6>) = 0.089 Å (Table 2). The thermal dependence of <Fe-N6> shows an excellent correlation with the thermal dependence of the product $\chi_M T$ (Figure 6a). As mentioned above approximately 54.4% of the cations populate the S = 3/2 state at 400 K. Extrapolation of this population to 100% gives a total variation $\Delta R(Fe\text{-}N_{av})$ ≈ 0.145 Å, which is about 27% shorter than usually observed for an Fe^{II} center undergoing complete SCO behaviour (0.2 Å). In part, this is mitigated by the small variation observed for the Fe-N6O bond length, which contrasts with the approximate 100 cm^{-1} shift of the $\nu_{Fe\text{-}NO}$ mode upon spin-state change. A fact that suggests a complete change in the Fe-NO bonding between the S = 1/2 and S = 3/2 spin states. The strong covalence of the Fe-NO bond is reflected specially on the thermal dependence of the N6-O bond length and the Fe-N-O tilt angle (Table 2). Upon heating from 120 to 420 K, the N-O bond length gradually decreases from 1.170(4) to 1.099(10) Å. This latter value is slightly shorter than usually observed for non-heme S = 3/2 $\{FeNO\}^7$ species (≈ 1.114 Å). Short values of the N-O bond length have been observed associated with the occurrence of reversible thermally driven rotational disorder and phase transition in the [Co(tetraphenylporphinato)(NO)] complex.[38] However, we have not detected this type of disorder in the title compound. The significant decrease of 0.071 Å, resulting from the gradual population of the S = 3/2 state, can be rationalized from the molecular orbital (MO) diagrams calculated for both spin states (see below). In the S = 1/2 state, the small Fe-N-O bond angle favors significant contribution of the nitrosyl N atom thus imparting an antibonding character to the five occupied MOs, namely, three α orbitals (i.e., d_{xz}, d_{yz}, and π(NO)) and two β orbitals (i.e., d_{xz}, d_{yz}). In contrast, in the S = 3/2 state, only two occupied β-MO with nitrosyl contribution have N-O antibonding character (i.e., d_{xz} and π(NO)). The Fe-N-O1 angle increases from 144.0(3)° to 157.9(10)° when moving from 120 to 420 K.

This thermal dependence clearly follows the thermal dependence of the $Fe\text{-}N^{av}$ bond length and the product $\chi_M T$ (Figure 6b). Hence, the Fe-N-O1 angle also changes with the population of the S = 3/2 and S = 1/2 molecular states, each one characterized by a different Fe-N-O bond angle. Extrapolation of this variation to 100% of the S = 3/2 state population predicts an increase of the Fe-N-O angle up to 167°. Interestingly, this extrapolated angle is similar to that found by Speelman and Lehnert for the

pentacoordinate S = 3/2 complex [Fe(tmg_3tren)(NO)]$(OTf)_2$ (tmg_3tren = 1,1,1-tris{2-[N2-(1,1,3,3-tetramethylguanidinio)]ethyl}amine).[39]

The only known crystal structure of a $\{FeNO\}^7$ SCO system in the pure S = 1/2 and S = 3/2 states were reported for [Fe(salen)(NO)].[40] For this compound, the average Fe-N-O angle changes from 127° in the S = 1/2 state to 147° in the S = 3/2 state. Although the magnitude of these angles is markedly smaller than the one found for compound **1**, the change of 20° is very close to the 23° variation estimated upon complete SCO in complex **1**. Furthermore, the average variation of the bond lengths in the FeN_2O_2 core, that is, 0.040 Å, is approximately 50% smaller than observed for compound **1** at 420 K or about 73% smaller than expected for a complete conversion in compound **1**. As mentioned above, this large difference could be accounted for the distinct chemical nature of the ligands and coordination number and geometry of both complexes.

A perspective of the crystal packing in the [100] direction is displayed in Figure 5 (right). This perspective shows an apparent organization of the cationic species by pairs that indeed correspond to the two first members of infinite supramolecular zigzag "chains" running along the [100] direction with shortest Fe···Fe distances ranging in the interval 9.4237(8)-9.5697(10) Å in the temperature range 120-400 K. There are C···C intermolecular contacts between the infinite supramolecular chains, namely C23···C11 = 3.652(6), C26···C2 = 3.600(6), C24···C10 = 3.645(6), C25···C1 = 3.641(6), and C24···C11 = 3.588(6) Å at 120 K (see Figure S2 in the Supporting Information). Furthermore, in the low-temperature (LT) crystal packing the cationic molecules interact directly with each other through weak C···C intermolecular contacts defining a three-dimensional network. Most of these contacts are in the interval 3.6-3.7 Å. These interactions are reinforced by a number of C···F cation-anion contacts. Table S2 in the Supporting Information gathers the intermolecular distances smaller than the sum of the van der Waals radii C···C and C···F.

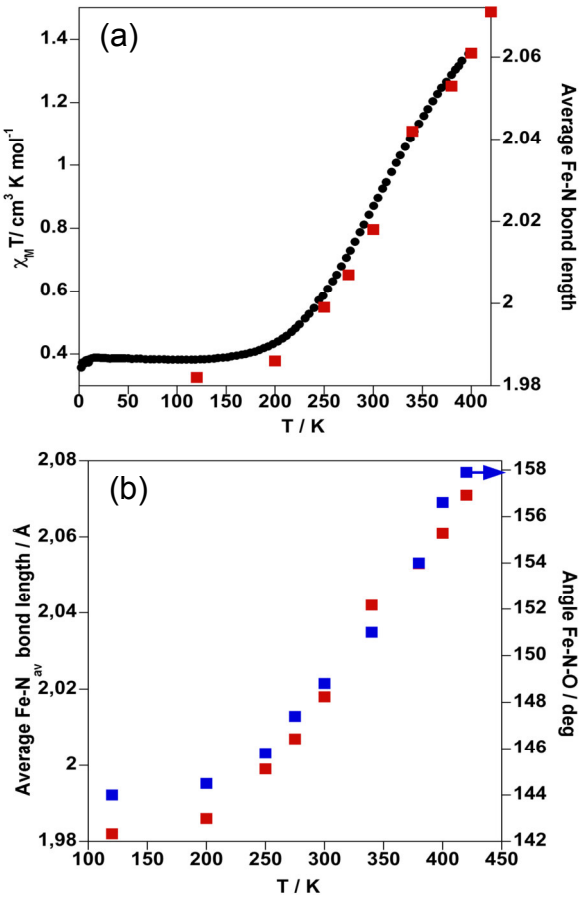

Figure 6.- Magneto-structural correlation. a) Thermal variation of the product χ_MT (open circles) and the average Fe-N bond length (full squares). b) Thermal variation of the average Fe-N bond length (full squares) and the Fe-NO bond angle (white squares).

2.3.3.6.- Electronic structure modeling

The $[Fe(bztpen)(NO)]^{2+}$ molecule has been fully optimized (see the section Computational Details) in the different possible spin topologies, this is, Fe^{II}-NO and Fe^{III}-NO^- in both ferromagnetic and antiferromagnetic schemes between the paramagnetic centers, and also allowing the iron centers to be in the HS or LS state. A complete list of atomic Cartesian coordinates for the optimized structures, as well as its energies can be found in Table S3 in the Supporting Information. When optimizing the systems in the Fe^{III}-NO^- motif, an electron transfer from the NO^- ligand to the Fe^{III} center is always

observed, thus, reducing the metal to Fe^{II} and generating an NO radical. This is in line with the conclusion raised by Solomon and coworkers[14] and Lehnert et al.,[2] which states that six coordinate strong ligand field $\{FeNO\}^7$ complexes and especially those with a strong axial donor atom in trans position to the NO molecule, as is the case of compound **1**, destabilizes the Fe^{III}-NO^- configuration in favor of the Fe^{II}-NO configuration. The optimized bond lengths and angles for the $[Fe(bztpen)(NO)]^{2+}$ molecule in the S = 1/2 and S = 3/2 states are, in general, in good agreement with the corresponding experimental data at 120 K (LS state) and extrapolated to 100% populated S = 3/2 state (see Table 2). The most relevant discrepancy corresponds to the extrapolated N6-O bond length, that is, 1.053 Å, whereas the calculated one is 1.156 Å. This latter value is even larger than the one obtained experimentally at 420 K, that is, 1.099(10) Å, where approximately 60% of the HS state are populated. Despite discrepancies in the magnitude of the variation of this bond length, its tendency to shorten with the increase of the population of the HS state is clearly reproduced.

The corresponding vibrational analysis was also done to ensure the minimum nature of the optimized structures. It is worth mentioning at this point that the calculated $\nu = {}_{NO}$(S = 1/2) = 1774.2 cm^{-1} and $\nu = {}_{NO}$(S = 3/2) = 1837.4 cm^{-1} frequencies are respectively approximately 100 and 56 cm^{-1} larger than the corresponding experimental values but are within the normal limits found for DFT calculations (about 5%). In contrast, the calculated $\nu = {}_{Fe\text{-}NO}$(S = 3/2) = 501 cm^{-1} frequency is about 5% smaller than the experimental one. The most important difference corresponds to the calculated $\nu = {}_{Fe\text{-}NO}$(S = 1/2) = 494.2 cm^{-1}, which is approximately 18% smaller than the experimental value. This finding suggests again that the experimentally observed mode has probably an important $\delta_{Fe\text{-}NO}$ character.

A theoretical modeling of the SCO curve and the transition temperature based on the thermochemical contributions has been performed, which is in fair agreement with the experimental data (see the Supporting Information).

Significant differences in the Fe-NO bonding interactions can be observed as a function of the metal spin state when analysing the electronic structure of the molecule in terms of the relevant molecular orbitals. In the LS state (S = 1/2), the α and β double-occupied orbitals include the Fe-NO bonding d_{xz} and d_{yz} pair of orbitals strongly mixed with the π(NO) orbitals, and the non-bonding d_{xy} orbital. The main contributions to the

antibonding SOMO comes from a mixture of the d_{xz} and d_{z^2} metal orbitals (with larger d_{z^2} participation) and one π(NO) orbital. The $d_{x^2-y^2}$ and d_{z^2} orbitals (both α and β) are strongly antibonding with the pentadentate ligand and the NO group, but remain unoccupied. Thus, despite the non-innocent nature of the ligand, the electronic structure in that spin state can be represented as a LS (S = 0) Fe^{II} state coordinated to an NO radical. With the transition to the HS state (S = 3/2), the α-$d_{x^2-y^2}$ and d_{z^2} metal-centered orbitals remain strongly antibonding, but are now single-occupied. Simultaneously, the Fe-NO bonding interactions are strongly reduced, and the α-occupied orbitals with important d_{xz} and d_{yz} contributions turn into formally non-bonding orbitals with the NO ligand. This situation leads to an enlargement of the Fe-NO bond length upon SCO of around 0.02 Å. The two β-SOMOs can now be described as a large mixture between the d_{xz} and d_{yz} orbitals with the two π(NO)-centered orbitals (Figure 7). In this case, the non-innocent behaviour of the NO ligand makes a single assignment of the electronic structure difficult. These two orbitals contain around 40% contribution from the metal and 60% contribution from the NO ligand. Thus, we can distinguish between two limit situations: whether the two β-SOMOs are ascribed to the metal [Fe^{I}(S = 3/2)-NO^{+}(S = 0)] or to the NO ligand [Fe^{III}(S = 5/2)- NO^{-}(S = 1)]. Taking into account the mentioned orbital percentage, and considering the presence of two equivalent β-SOMOs, the β occupation of the metal is slightly smaller than one. Hence, we can describe the electronic structure as an intermediate situation between [Fe^{II}(S = 0)-NO(S = 1/2)] and [Fe^{III}(S = 5/2)- NO^{-}(S = 1)]. A similar proposal was done by McQuilken et al. for a non-heme Fe-NO complex.[41]

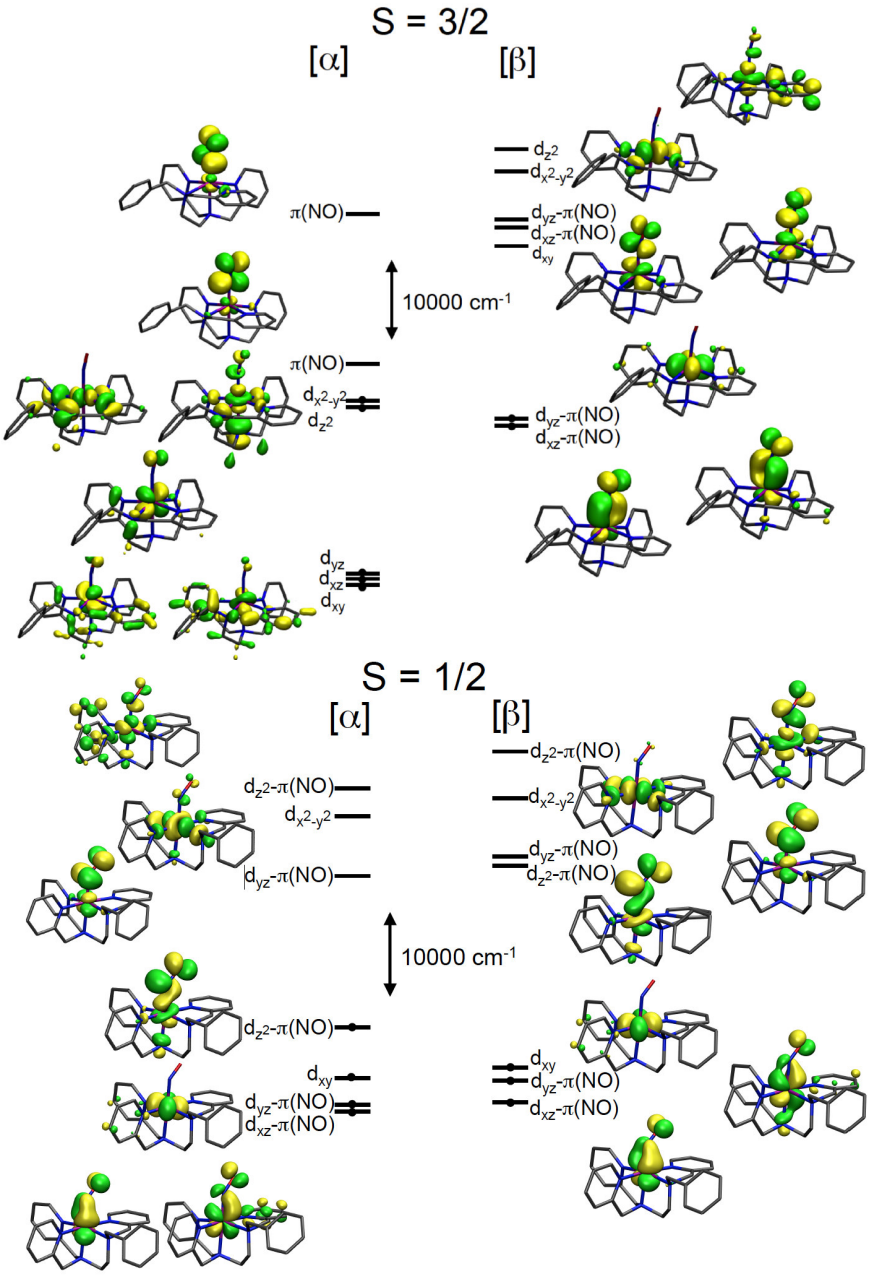

Figure 7.- MO diagrams of complex **1** in the LS (S = 1/2) (bottom) and HS (S = 3/2) states.

The electronic structures for each spin state correspond with a LS Fe^{II} (d^6, S = 0) and a HS Fe^{II} (d^6, S = 2) antiferromagnetically coupled with an NO radical (S = 1/2),

thus leading to the observed spin states, that is, S = 1/2 and S = 3/2, respectively. The corresponding plot of the spin density shows (see Figure 8) that, indeed, for the S = 1/2 spin state the electron is mainly located on the NO ligand. In the metal, there is a blue region due to delocalization of the spin density of the radical in the orbital oriented towards the NO group whereas the red region corresponds to some spin polarization mechanism in the orbitals without overlap with the NO orbitals bearing the unpaired electron. The S = 3/2 spin state has spin density in both, the metal center and the NO ligand with opposite signs and the N atoms of the bztpen ligand have the same sign as the metal due to the large spin delocalization (strong mixing of the orbitals with unpaired electrons of the iron center). To calculate the magnetic exchange constant, the HS Fe^{II} (d^6, S = 2) ferromagnetically coupled to the NO radical (S = 1/2) solution was also calculated.

This system has a total spin state of S = 5/2, and by using the expression in Equation (3) together with the electronic energy of the S = 3/2 spin state, a value of J_{calcd} = -2843 cm^{-1} is obtained, which is in the right range and comparable with the calculated value for the complex [Tp*Co(NO)].[22]

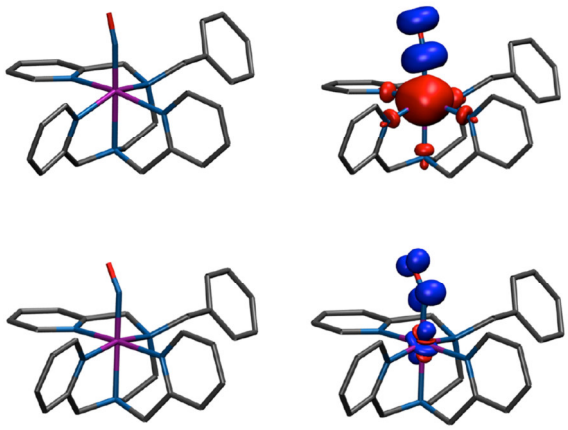

Figure 8.- Optimized structures (left) and spin density (right) isocontours (0.02 $Å^{-3}$) for the $[Fe(bztpen)(NO)]^{2+}$ molecule in the S = 3/2 (top) and S = 1/2 (bottom) states.

2.4.- Conclusion

Nitrosyl iron complexes exhibiting SCO properties are scarce $\{FeNO\}^7$ species that in virtue of strong magnetic coupling invariably display S = 3/2↔S = 1/2 spin-state

conversion. The large thermal stability of compound **1** has allowed, for the first time, to describe in a precise way how the changes in the electronic distribution of the t_{2g}-e_g orbitals due to SCO modulates the structure of the $\{FeNO\}^7$ species providing valuable magneto-structural and spectroscopic correlations.

The magnetic properties of compound **1** show the occurrence of a very gradual SCO, which extends far beyond 400 K where the population of the HS species is estimated to be 54.4%. The narrow EPR signal at g ≈ 2 suggests that the unpaired electron essentially resides in the π^* orbitals of the NO ligand in the S = 1/2 state. This signal widens at room temperature but remains approximately at the same g value. No feature at g ≈ 4 associated with the S = 3/2 state is observed despite it is approximately 30% populated at 300 K. The Mössbauer spectra of compound **1** at 80 and 293 K is consistent with the occurrence of fast spin-state interconversion rate with a nearly temperature-independent isomer shift parameter in the temperature interval 80-293 K, a fact that strongly limits the characterization of the electronic structure of the $\{FeNO\}^7$ moiety from this technique. The room temperature visible absorption spectrum of compound **1** is consistent with the presence of bands characteristic of the Fe^{II} ions in the LS state. Furthermore, the thermal variation of the λ = 555 nm band tentatively attributed to the $^1A_1 \rightarrow {}^1T_1$ absorption and the concomitant change of color of the complex are reminiscent of Fe^{II} complexes, which exhibit a S = 0↔S = 2 spin-state change. The thermal dependence of the Raman and IR spectra have enabled to characterize the ν_{NO} and $\nu_{Fe\text{-}NO}$ stretching modes in the S = 3/2 and S = 1/2 states. All these changes in magnetism, electronic, and vibrational spectra correlate well with the structural changes observed in the coordination $[FeN_6]$ core of compound **1**, namely, average Fe-N bonds and angles including the tilt Fe-N-O angle and the N-O bond length. Furthermore, the DFT calculations reproduce reasonably well the structure of compound **1** in the LS and HS states and support the idea that the pentadentate strong ligand field ligand bztpen stabilizes the Fe^{II} and the NO. Consequently, the S = 3/2↔S = 1/2 spin equilibrium accommodates well with the concurrence of an S = 2↔S = 0 spin equilibrium in the Fe^{II} and strong magnetic coupling with the radical NO.

2.5.- Experimental Section

2.5.1.- General

Variable-temperature magnetic susceptibility data were recorded for single crystals and microcrystalline samples of compound **1** at a scanning rate of 1 K min^{-1} with a Quantum Design MPMS2 SQUID susceptometer equipped with a 7 T magnet, operating at 1 T and at temperatures between 2-400 K. Experimental susceptibilities were corrected from diamagnetism of the constituent atoms by the use of Pascal's constants. UV/Vis diffuse reflectance spectra of the microcrystalline powder of compound **1** were acquired at room temperature in the spectral range of λ = 328-1000 nm by using a Lambda35 spectrophotometer (Perkin-Elmer) equipped with an integrating sphere. Variable-temperature absorbance data were obtained in the range λ = 480-680 nm on a flat single crystal of approximately 90 mm thickness in the transmission mode by using an Olympus BX51 microscope, which was fiber-coupled to a CCD spectrometer (BWTek). Temperature-dependent, polarized Raman spectra of oriented single crystals were recorded between ν = 100-2000 cm^{-1} by using a LabramHR (Horiba) Raman microspectrometer (resolution ≈ 3 cm^{-1}) by using λ = 633 and 532 nm laser excitations. Laser light was focused on the sample and the scattered light was collected by using the same x50 objective (0.5 numerical aperture). Laser-induced heating effects were carefully checked by monitoring at room temperature the intensity ratio of the ν(NO) modes as a function of the laser intensity and found practically negligible below approximately 0.1 mW, which was then used in the experiments. The polarization behaviour of the scattered photons versus the polarization state of the incident laser and the crystal orientation was also studied. As expected, the ν(NO) modes are strongly polarized and the highest intensity spectra were obtained in the configuration *-z(yy)z* (Porto's notation). Non-polarized infrared absorption spectra as a function of the temperature were collected between ν = 600-4000 cm^{-1} in the transmission mode on a flat single crystal of approximately 30 mm thickness by using a Spectrum Frontier FTIR instrument (Perkin-Elmer) coupled to a Spotlight-400 microscope. To acquire variable temperature vibrational and electronic spectra the same liquid nitrogen microscopy cryostage (THMS-600, Linkam Scientific) was used with either glass or CdSe windows. ^{57}Fe Mössbauer spectra were recorded by using a conventional constant-acceleration-type spectrometer equipped with a 50 mCi ^{57}Co

source and a flow-type, liquid-nitrogen cryostat. Spectra of the powder samples were recorded at 80 and 293 K. Least-squares fittings of the Mössbauer spectra have been carried out with the assumption of Lorentzian line shapes by using the Recoil software package. Isomer shift values were given relative to metallic iron at room temperature. Elemental analysis (C, H, N) was performed by the Centro de Microanlisis Elemental de la Universidad Complutense de Madrid (Spain) by using a LECO CHNS-932 analyzer.

Variable-temperature EPR spectra were recorded on microcrystalline samples by using a Bruker ELEXYS E580 spectrometer equipped with Bruker standard resonators for the X and Q bands. Data were collected in the 20-9980.0 G field range at 4 K (frequency = 9.472 GHz, power = 0.0063 mW, power attenuation = 45.0 dB, modulation frequency = 100.00 kHz, modulation amplitude = 1.000 G, gain = 60 dB) and at 300 K (frequency = 9.472 GHz, power = 62.84 mW, power attenuation = 5.0 dB, modulation frequency = 100.00 kHz, modulation amplitude = 1.000 G, gain = 60 dB).

2.5.1.2.- Single-crystal X-ray measurements

Single-crystal X-ray data of compound **1** were collected on an Oxford Diffraction Supernova single-crystal diffractometer by using MoKα radiation (λ = 0.71073 Å). Data scaling and empirical absorption correction were performed. The structures were solved by direct methods by using SHELXS-97 and refined by full-matrix least squares on F^2 by using SHELXL-97.[42] Non-hydrogen atoms were refined anisotropically. Hydrogen atoms were geometrically placed (riding model) and assigned fixed isotropic displacement parameters. CCDC 1440671 (**1**, 120 K), 1440672 (**1**, 200 K), 1440673 (**1**, 250 K), 1440674 (**1**, 275 K), 1440675 (**1**, 300 K), 1440676 (**1**, 340 K), 1440677 (**1**, 380 K), 1440678 (**1**, 400 K), and 1440679 (**1**, 420 K) contain the supplementary crystallographic data for this paper. These data can be obtained free of charge from The Cambridge Crystallographic Data Centre via www.ccdc.cam.ac.uk/data_request/cif.

2.5.1.3.- Materials

Synthesis of compound **1**: Samples of compound **1** essentially constituted of single crystals were obtained in a very good yield (≈ 90%) by bubbling nitric oxide for 10 min through diluted solutions of $[Fe(bztpen)CH_3CN](PF_6)_2$[43] (≈ 30 mg 0.037 mmol in 40 mL of MeOH). The final violet solution was kept under argon in repose and closed for three days to lead the precipitation of single crystals of appropriate size for single-crystal

X-ray diffraction. The crystals melt with decomposition at approximately 480 K. Elemental analysis calcd (%) for $C_{27}H_{29}F_{12}FeN_6OP_2$: C 40.57, H 3.66, N 10.51; found: C 39.81, H 3.73, N 10.39.

2.5.2.- Computational details

All density functional theory calculations were carried out by using the Gaussian 09[44] electronic structure package with a tight convergence criterion (10^{-8} a.u. in the energy) for the density matrix elements, by using the hybrid-meta GGA functional TPSSh.[45, 46] This functional has been previously used with success in the modelling of accurate thermochemical quantities for several mononuclear and dinuclear Fe^{II} SCO systems.[47-50] The fully optimized contracted triple-z all-electron Gaussian basis set with polarization functions developed by Ahlrichs and co-workers was employed for all the elements in the molecule.[51] The different spin topologies were modeled by using the fragments option, which allows the definition of specific charges and electronic structures for the metal and for the different ligands. To calculate the exchange interaction,[52, 53] a phenomenological Heisenberg-Dirac-van Vleck Hamiltonian (HDVV) was used, excluding the terms relating to magnetic anisotropy, to describe the exchange coupling [Eq. (3)]:

$$\hat{H} = -J_{ab}\widehat{S_a}\widehat{S_b}$$

where $\widehat{S_a}$ and $\widehat{S_b}$ are the spin operators of the different paramagnetic centers. The J_{ab} parameter is the pairwise coupling constant between the paramagnetic centers of the molecule.

2.6.- References

[1] a) J. C. Toledo, Jr. O. Augusto, *Chem. Res. Toxicol.*, **2012**, *25*, 975; b) F. Roncaroli, M. Videla, L. D. Slep, J. A. Olabe, *Coord. Chem. Rev.*, **2007**, *251*, 1903; c) J. A. McCleverty, *Chem. Rev.*, **2004**, *104*, 403.

[2] N. Lehnert, W. R. Scheidt, M. W. Wolf, *Struct. Bonding* (Berlin), **2013**, *154*, 155.

[3] T. C. Berto, A. L. Speelman, S. Zheng, N. Lehnert, *Coord. Chem. Rev.*, **2013**, *257*, 244.

[4] A. Earnshaw, E. A. King, L. F. Larkworthy, *J. Chem. Soc. A*, **1969**, 2459.

[5] B. W. Fitzsimmons, L. F. Larkworthy, K. A. Rogers, *Inorg. Chim. Acta*, **1980**, *44*, L53.

[6] Y. Numata, K. Kubokura, Y. Nonaka, H. Okawa, S. Kida, *Inorg. Chim. Acta*, **1980**, *43*, 193.

[7] B. Weber, H. Görls, M. Rudolph, E. G. Jäger, *Inorg. Chim. Acta*, **2002**, *337*, 247.

[8] K. D. Hodges, R. G. Wollmann, S. L. Kessel, D. N. Hendrickson, D. G. Van Derveer, E. K. Barefield, *J. Am. Chem. Soc.*, **1979**, *101*, 906.

[9] M. Li, D. Bonnet, E. Bill, F. Neese, T. Weyhermìller, N. Blum, D. Sellmann, K. Wieghardt, *Inorg. Chem.*, **2002**, *41*, 3444.

[10] J. H. Enemark, R. D. Feltham, *Coord. Chem. Rev.*, **1974**, *13*, 339.

[11] D. M. P. Mingos, *Struct. Bonding* (Berlin), **2014**, *153*, 1.

[12] C. A. Brown, M. A. Pavlosky, T. E. Westre, Y. Zhang, B. Hedman, K. O. Hodgson, E. I. Solomon, *J. Am. Chem. Soc.*, **1995**, *117*, 715.

[13] T. C. Berto, M. B. Hoffman, Y. Murata, K. B. Landenberger, E. E. Alp, J. Zhao, N. Lehnert, *J. Am. Chem. Soc.*, **2011**, *133*, 16714.

[14] N. Sun, L. V. Liu, A. Dey, G. Villar-Acevedo, J. A. Kovacs, M. Y. Darensbourg, K. O. Hodgson, B. Hedman, E. I. Solomon, *Inorg. Chem.*, **2011**, *50*, 427.

[15] L. E. Goodrich, F. Paulat, V. K. K. Praneeth, N. Lehnert, *Inorg. Chem.*, **2010**, *49*, 6293.

[16] a) Y. Zhang, E. Oldfield, *J. Phys. Chem. A*, **2003**, *107*, 4141; b) Y. Zhang, E. Oldfield, *J. Am. Chem. Soc.*, **2004**, *126*, 9494.

[17] S. Chakraborty, J. Reed, M. Ross, M. J. Nilges, I. D. Petrik, S. Ghosh, S. Hammes-Schiffer, J. T. Sage, Y. Zhang, C. E. Schulz, Y. Lu, *Angew. Chem. Int. Ed.*, **2014**, *53*, 2417.

[18] N. Ortega-Villar, A. L. Thompson, M. C. Muñoz, V. M. Ugalde-Saldívar, A. E. Goeta, R. Moreno-Esparza, J. A. Real, *Chem. Eur. J.*, **2005**, *11*, 5721.

[19] N. Ortega-Villar, A. Y. Guerrero-Estrada, L. Piñeiro-López, M. C. Muñoz, M. Flores-Álamo, R. Moreno-Esparza, J. A. Real, V. M. Ugalde-Saldívar, *Inorg. Chem.*, **2015**, *54*, 3413.

[20] T. Nebe, A. Beitat, C. Wìrtele, C. Dìcker-Benfer, R. van Eldik, C. J. McKenzie, S. Schindler, *Dalton Trans.*, **2010**, *39*, 7768.

[21] a) O. Kahn, Molecular Magnetism, VCH, Weinheim, **1993**; b) C. P. Slichter, H. G. Drickamer, *J. Chem. Phys.*, **1972**, *56*, 2142.

[22] N. C. Tomson, M. R. Crimmin, T. Petrenko, L. E. Rosebrugh, S. Sproules, W. C. Boyd, R. G. Bergman, S. DeBeer, F. D. Toste, K. Wieghardt, *J. Am. Chem. Soc.*, **2011**, *133*, 18785.

[23] M. Sorai, *Top. Curr. Chem.*, **2004**, *235*, 153.

[24] P. J. van Koningsbruggen, Y. Maeda, H. Oshio, *Top. Curr. Chem.*, **2004**, *233*, 259.

[25] H. A. Goodwin, *Top. Curr. Chem.*, **2004**, *234*, 23.

[26] M. Schmitz, M. Seibel, H. Kelm, S. Demeshko, F. Meyer, H. J. Krìger, *Angew. Chem. Int. Ed.*, **2014**, *53*, 1; *Angew. Chem.*, **2014**, *126*, 1.

[27] H. Chun, E. Bill, T. Weyhermìller, K. Wieghardt, *Inorg. Chem.*, **2003**, *42*, 5612.

[28] F. V. Wells, S. W. McCann, H. H. Wickman, S. L. Kessel, D. N. Hendrickson, R. D. Feltham, *Inorg. Chem.*, **1982**, *21*, 2306.

[29] E. König, J. G. Ritter, J. Dengler, L. F. Larkworthy, *Inorg. Chem.*, **1992**, *31*, 1196.

[30] A. Hauser, *J. Chem. Phys.*, **1991**, *94*, 2741.

[31] C. Hauser, T. Glaser, E. Bill, T. Weyhermìller, K. Wieghardt, *J. Am. Chem. Soc.*, **2000**, *122*, 4352.

[32] T. A. Jackson, E. Yikilmaz, A. F. Miller, T. C. Brunold, *J. Am. Chem. Soc.*, **2003**, *125*, 8348.

[33] A. R. Diebold, C. D. Brown-Marshall, M. L. Neidig, J. M. Brownlee, G. R. Moran, E. I. Solomon, *J. Am. Chem. Soc.*, **2011**, *133*, 18148.

[34] V. K. K. Praneeth, F. Paulat, T. C. Berto, S. D. George, C. Näther, C. D. Sulok, N. Lehnert, *J. Am. Chem. Soc.*, **2008**, *130*, 15288.

[35] J. A. Olabe, *Dalton Trans.*, **2008**, 3633.

[36] D. P. Linder, K. R. Rodgers, J. Banister, G. R. A. Wyllie, M. K. Ellison, W. R. Scheidt, *J. Am. Chem. Soc.*, **2004**, *126*, 14136.

[37] P. Gans, A. Sabatini, L. Sacconi, *Inorg. Chem.*, **1966**, *5*, 1877.

[38] L. M. Grande, B. C. Noll, A. G. Oliver, W. R. Scheidt, *J. Am. Chem. Soc*., **2009**, *131*, 2131.

[39] A. L. Speelman, N. Lehnert, *Angew. Chem. Int. Ed.*, **2013**, *52*, 12283.

[40] K. J. Haller, P. L. Johnson, R. D. Feltham, J. H. Enemark, J. R. Ferraro, L. J. Basile, *Inorg. Chem. Acta*, **1979**, *33*, 119.

[41] A. C. McQuilken, Y. Ha, K. D. Sutherlin, M. A. Siegler, K. O. Hodgson, B. Hedman, E. I. Solomon, G. N. L. Jameson, D. P. Goldberg, *J. Am. Chem. Soc.*, **2013**, *135*, 14024.

[42] G. M. Sheldrick, *Acta Crystallogr. Sect. A*, **2008**, *64*, 112.

[43] N. Ortega-Villar, V. M. Ugalde-Saldívar, M. C. Muñoz, L. A. Ortiz-Frade, J. G. Alvarado-Rodríguez, J. A. Real, R. Moreno-Esparza, *Inorg. Chem.*, **2007**, *46*, 7285.

[44] M. J. Frisch, G. W. Trucks, H. B. Schlegel, G. E. Scuseria, M. A. Robb, J. R. Cheeseman, G. Scalmani, V. Barone, B. Mennucci, G. A. Petersson, H. Nakatsuji, M. Caricato, X. Li, H. P. Hratchian, A. F. Izmaylov, J. Bloino, G. Zheng, J. L. Sonnenberg, M. Hada, M. Ehara, K. Toyota, R. Fukuda, J. Hasegawa, M. Ishida, T. Nakajima, Y. Honda, O. Kitao, H. Nakai, T. Vreven, J. A. Montgomery Jr. , J. E. Peralta, F. Ogliaro, M. J. Bearpark, J. Heyd, E. N. Brothers, K. N. Kudin, V. N. Staroverov, R. Kobayashi, J. Normand, K. Raghavachari, A. P. Rendell, J. C. Burant, S. S. Iyengar, J. Tomasi, M. Cossi, N. Rega, N. J. Millam, M. Klene, J. E. Knox, J. B. Cross, V. Bakken, C. Adamo, J. Jaramillo, R. Gomperts, R. E. Stratmann, O. Yazyev, A. J. Austin, R. Cammi, C. Pomelli, J. W. Ochterski, R. L. Martin, K. Morokuma, V. G. Zakrzewski, G. A. Voth, P. Salvador, J. J.

Dannenberg, S. Dapprich, A. D. Daniels, Ö. Farkas, J. B. Foresman, J. V. Ortiz, J. Cioslowski, D. J. Fox, *Gaussian 09, Revision D.01,* Wallingford, CT, USA **2009**.

[45] V. N. Staroverov, G. E. Scuseria, J. M. Tao, J. P. Perdew, *J. Chem. Phys.*, **2003**, *119*, 12129.

[46] J. M. Tao, J. P. Perdew, V. N. Staroverov, G. E. Scuseria, *Phys. Rev. Lett.*, **2003**, *91*,1.

[47] J. Cirera, F. Paesani, *Inorg. Chem*., **2012**, *51*, 8194.

[48] K. P. Jensen, J. Cirera, *J. Phys. Chem. A*, **2009**, *113*, 10033.

[49] J. Cirera, E. Ruiz, *J. Mater. Chem. C*, **2015**, *3*, 7954.

[50] E. Ruiz, *Phys. Chem. Chem. Phys*, **2014**, *16*, 14.

[51] A. Schäfer, C. Huber, R. Ahlrichs, *J. Chem. Phys.*, **1994**, *100*, 5829.

[52] E. Ruiz, P. Alemany, S. Alvarez, J. Cano, *J. Am. Chem. Soc.*, **1997**, *119*, 1297.

[53] E. Ruiz, J. Cano, S. Alvarez, P. Alemany, *J. Comput. Chem.*, **1999**, *20*, 1391.

2.7.- Supporting Information

Table S1.- ^{57}Fe Mössbauer data for **1.** δ (isomer shift vs. metallic α-Fe), ΔE_Q (quadrupolar splitting), $\Gamma/2$ (half-height at half width).

T (K)	δ (mm/s)	ΔE_Q (mm/s)	$\Gamma/2$ (mm/s)
80	0.306(5)	0.523(9)	0.175 (7)
293	0.295(5)	0.591(8)	0.146(6)

Figure S1.- Photographs of a crystalline sample of **1** at 296 K (left) and at 425 K (right) showing the change of colour upon SCO.

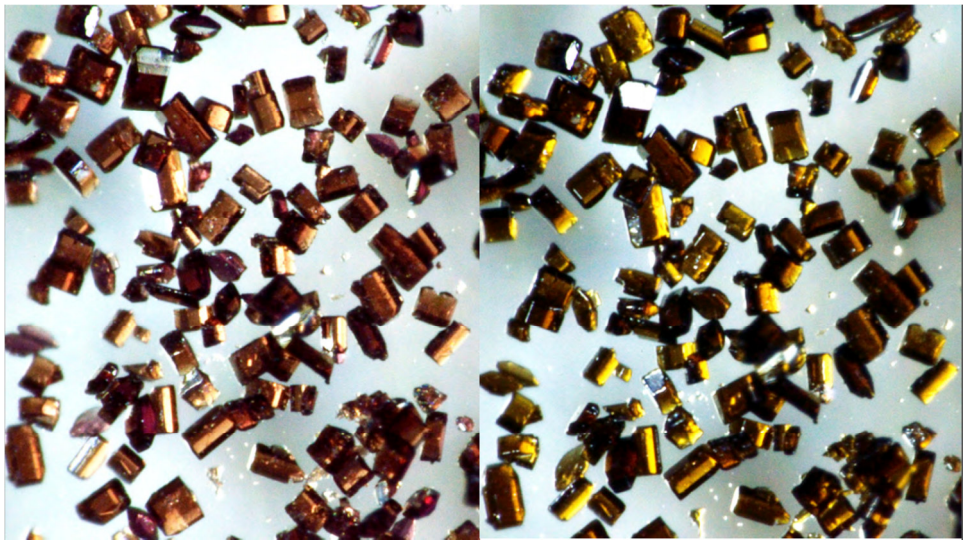

Figure S2.- Intermolecular interactions between complex cations.

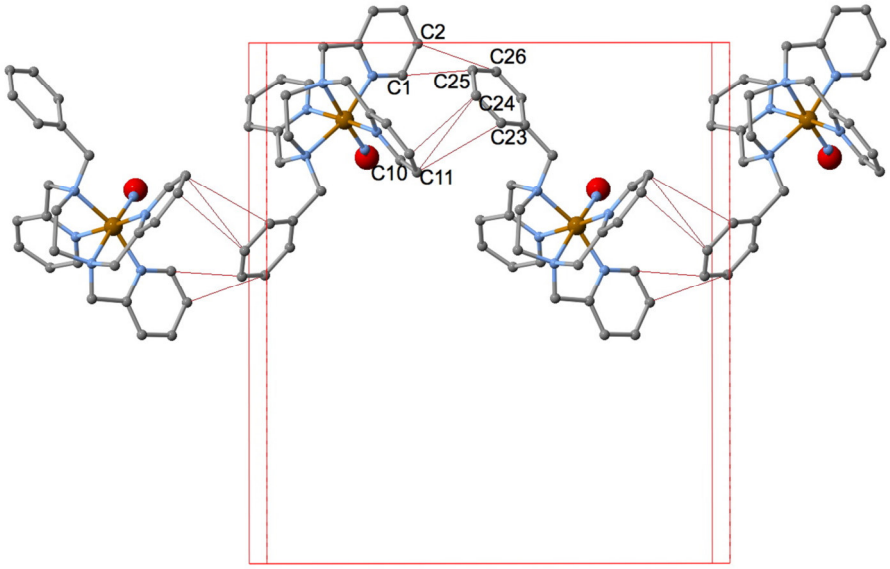

Table S2.- Intermolecular C···C and C···F contacts.

T / K	120	200	250	275
C(1)···C(25)^{i}	3.641(6)	3.674(4)	3.714(5)	3.712(6)
C(2)···C(26)^{i}	3.600(6)	3.624(4)	3.652(6)	3.661(6)
C(10)···C(24)^{i}	3.645(6)	3.657(4)	3.698(6)	3.705(6)
C(11)···C(23)^{i}	3.652(6)	3.685(4)	3.719(5)	3.733(6)
C(11)···C(24)^{i}	3.588(6)	3.593(4)	3.612(5)	3.618(6)
C(13)···C(25)^{ii}	3.616(6)	3.638(4)	3.664(5)	3.680(5)
C(19)···C(19)^{iii}	3.572(6)	3.574(4)	3.580(5)	3.574(5)
C(2)···F(1)^{iv}	3.112(5)	3.145(4)	3.184(5)	3.187(6)
C(7)···F(11)	3.146(5)	3.184(4)	3.214(6)	3.222(6)
C(13)···F(2)	3.163(5)	3.171(3)	3.191(4)	3.198(4)
C(14)···F(2)	3.078(5)	3.109(3)	3.154(4)	3.158(4)
C(15)···F(4)	3.133(4)	3.143(3)	3.172(4)	3.181(4)
C(15)···F(5)	3.163(5)	3.180(3)	3.201(4)	3.207(5)
C(17)···F(4)	3.142(4)	3.159(3)	3.185(4)	3.183(4)
C(17)···F(6)	3.144(5)	3.173(3)	3.205(4)	3.216(5)
C(17)···F(12)^{iii}	3.000(5)	3.035(3)	3.074(5)	3.081(5)
C(18)···F(12)^{iii}	3.068(5)	3.083(4)	3.095(5)	3.095(6)
C(19)···F(12)	3.097(5)	3.121(3)	3.157(5)	3.171(5)
C(20)···F(12)	3.122(5)	3.157(3)	3.195(4)	3.199(5)

Table S2 cont.- Intermolecular C···C and C···F contacts.

T / K	300	340	380	400
C(1)···C(25)^{i}	3.729(6)	3.761(7)	3.781(7)	3.84(2)
C(2)···C(26)^{i}	3.675(7)	3.719(8)	3.749(8)	3.77(2)
C(10)···C(24)^{i}	3.714(7)	3.753(8)	3.778(8)	3.84(2)
C(11)···C(23)^{i}	3.748(6)	3.759(7)	3.772(7)	3.834(14)
C(11)···C(24)^{i}	3.628(6)	3.658(7)	3.667(7)	3.679(14)
C(13)···C(25)^{ii}	3.699(5)	3.740(6)	3.788(6)	3.813(13)
C(19)···C(19)^{iii}	3.584(6)	3.599(7)	3.614(7)	3.601(14)
C(2)···F(1)^{iv}	3.201(6)	3.229(7)	3.233(7)	3.270(14)
C(7)···F(11)	3.233(7)	3.278(9)	3.316(10)	3.399(13)
C(13)···F(2)	3.209(5)	3.232(5)	3.247(5)	3.277(10)
C(14)···F(2)	3.178(5)	3.217(5)	3.232(5)	3.257(10)
C(15)···F(4)	3.194(4)	3.217(5)	3.235(5)	3.252(10)
C(15)···F(5)	3.220(5)	3.233(5)	3.252(5)	3.283(10)
C(17)···F(4)	3.194(4)	3.209(5)	3.223(5)	3.247(10)
C(17)···F(6)	3.221(5)	3.265(6)	3.299(6)	3.352(13)
C(17)···F(12)^{iii}	3.094(6)	3.118(7)	3.143(7)	3.155(12)
C(18)···F(12)^{iii}	3.095(6)	3.121(7)	3.135(7)	3.171(13)
C(19)···F(12)	3.185(6)	3.219(7)	3.233(7)	3.314(12)
C(20)···F(12)	3.214(5)	3.243(6)	3.271(6)	3.332(12)

Table S3.- Cartesian atomic coordinates for the optimized geometries.

S3.1.- *[Fe(bztpen)(NO)]$^{2+}$ S = 1/2, E= -2713.94483906 au, ν_1 = 21.0953 cm^{-1}*

Fe	-0.041534	0.659053	-0.357101
N	0.227161	2.644857	-0.387026
N	0.328329	0.992216	1.664010
N	1.949305	0.432061	-0.433460
N	-0.366013	-1.310941	0.191479
N	-2.028060	0.809281	-0.126519
N	-0.296384	0.415456	-2.080215
O	-1.112593	0.181564	-2.884902
C	0.530777	3.388330	-1.468630
C	0.746520	4.756073	-1.390931
C	0.658331	5.383582	-0.152793
C	0.359176	4.616783	0.970362
C	0.144590	3.253510	0.822503
C	-0.228174	2.339162	1.959981
C	1.803528	0.975182	1.932611
C	2.615834	0.578649	0.727992
C	3.996083	0.418824	0.808628
C	4.713557	0.115949	-0.341255
C	4.025925	-0.013670	-1.545536
C	2.651660	0.146855	-1.550931
C	-0.373959	-0.111793	2.375171
C	-0.038621	-1.403516	1.656119
C	-1.812849	-1.593175	-0.053334
C	-2.662147	-0.366663	0.079165
C	-4.035643	-0.436705	0.285241

S3.1 cont.- *[Fe(bztpen)(NO)]$^{2+}$ S = 1/2, E = -2713.94483906 au, ν_1 = 21.0953 cm^{-1}*

C	-4.789626	0.729358	0.243910
C	-4.143220	1.935243	-0.013201
C	-2.769897	1.935986	-0.188257
C	0.460709	-2.351067	-0.567709
C	0.155226	-3.791960	-0.239565
C	0.806198	-4.443869	0.815159
C	0.532750	-5.777887	1.101001
C	-0.387136	-6.482180	0.327229
C	-1.021031	-5.853462	-0.741842
C	-0.748056	-4.518605	-1.024742
H	0.597021	2.859645	-2.410872
H	0.982250	5.311729	-2.289702
H	0.826903	6.449893	-0.060163
H	0.292350	5.070243	1.952261
H	-1.315009	2.246617	2.022217
H	0.128085	2.724447	2.920063
H	2.111345	1.976454	2.244978
H	2.015287	0.309753	2.774422
H	4.498715	0.537916	1.761590
H	5.788865	-0.010735	-0.300748
H	4.542294	-0.241506	-2.469354
H	2.073787	0.047728	-2.460593
H	-0.068085	-0.168391	3.425521
H	-1.443259	0.096996	2.348120
H	-0.550310	-2.256387	2.108373
H	1.033845	-1.593751	1.727215
H	-1.902433	-1.942270	-1.085768
H	-2.163743	-2.406901	0.585484
H	-4.504403	-1.397840	0.459467
H	-5.862015	0.696950	0.395361
H	-4.690962	2.866791	-0.077404
H	-2.235092	2.853193	-0.390916
H	0.279218	-2.158646	-1.625918
H	1.501992	-2.118947	-0.349778
H	1.554619	-3.919655	1.401975
H	1.050188	-6.273244	1.914218
H	-0.592432	-7.524010	0.543212
H	-1.713659	-6.406782	-1.365099
H	-1.220560	-4.050974	-1.883924

S3.2.- *[Fe(bztpen)(NO)]$^{2+}$ S = 3/2, E = -2713.93366629 au, ν_1 = 21.2625 cm^{-1}*

Fe	-0.007656	-0.725660	-0.616869
N	-0.174232	-2.883405	-0.398227
N	-0.365026	-1.047485	1.585934
N	-2.138194	-0.396000	-0.460740
N	0.391727	1.371342	0.126116
N	2.151065	-0.774196	-0.236188
N	0.236852	-0.546433	-2.372544
O	0.675121	-0.454953	-3.438645
C	-0.435756	-3.743215	-1.401993
C	-0.593502	-5.105003	-1.195655
C	-0.480858	-5.600935	0.099644
C	-0.219180	-4.715720	1.142055
C	-0.067904	-3.363558	0.861111
C	0.264598	-2.345291	1.925985
C	-1.828426	-1.109246	1.855681
C	-2.691712	-0.533845	0.758039
C	-4.034337	-0.245267	0.989257
C	-4.830490	0.174307	-0.069193
C	-4.262569	0.294466	-1.336113
C	-2.917356	0.008890	-1.486749
C	0.285414	0.097815	2.274722
C	-0.043710	1.394590	1.554165
C	1.850176	1.633065	-0.004261
C	2.713343	0.402795	0.098965
C	4.065470	0.502228	0.418341
C	4.863888	-0.632960	0.358737
C	4.287746	-1.842304	-0.023590
C	2.932429	-1.871636	-0.304801
C	-0.371286	2.428904	-0.661437
C	-0.094746	3.862648	-0.276137
C	0.851395	4.612940	-0.984137
C	1.106019	5.938427	-0.644837
C	0.411224	6.533634	0.405174
C	-0.549838	5.805276	1.102936
C	-0.804781	4.480891	0.760292
H	-0.519402	-3.315634	-2.393914
H	-0.802220	-5.757291	-2.034120
H	-0.602257	-6.659527	0.297409
H	-0.134299	-5.069483	2.162887
H	1.346487	-2.194721	1.956814
H	-0.044973	-2.703710	2.913570
H	-2.058274	-0.626849	2.811444
H	-2.105781	-2.162175	1.963620
H	-4.449289	-0.357565	1.984327
H	-5.878649	0.399597	0.089138
H	-4.847653	0.611094	-2.190117
H	-2.430151	0.102369	-2.449755
H	-0.039501	0.165348	3.319777
H	1.360877	-0.082341	2.277079
H	0.407863	2.241862	2.079096
H	-1.123932	1.553088	1.557101
H	2.172715	2.395702	0.710447
H	2.013956	2.055450	-0.999836
H	4.483947	1.462335	0.696708
H	5.919452	-0.574720	0.596906

***S3.2* cont.-** *[Fe(bztpen)(NO)]$^{2+}$ S = 3/2, E = -2713.93366629 au, ν_1 = 21.2625 cm^{-1}*

H	4.874961	-2.748618	-0.099688
H	2.441470	-2.790569	-0.599135
H	-0.112179	2.268357	-1.709949
H	-1.427656	2.194229	-0.530897
H	1.373995	4.171429	-1.828178
H	1.833023	6.510460	-1.209340
H	0.602530	7.567997	0.665384
H	-1.112499	6.274663	1.901461
H	-1.582609	3.937472	1.288403

S3.3.- *[Fe(bztpen)(NO)]$^{2+}$ S = 5/2, E = -2713.90128732 au, ν_1 = 22.5178 cm^{-1}*

Fe	-0.013756	-0.706622	-0.512071
N	-0.186104	-2.877874	-0.360130
N	-0.390174	-1.054085	1.629288
N	-2.135359	-0.408097	-0.464364
N	0.397560	1.390008	0.190608
N	2.147727	-0.728426	-0.286446
N	0.267905	-0.644390	-2.536271
O	0.857722	-0.700034	-3.535802
C	-0.443508	-3.729035	-1.371470
C	-0.590820	-5.093968	-1.177022
C	-0.476495	-5.600058	0.114302
C	-0.223579	-4.722556	1.165540
C	-0.080130	-3.367450	0.895650
C	0.240699	-2.353025	1.968923
C	-1.860827	-1.113138	1.867530
C	-2.706346	-0.544928	0.748197
C	-4.053172	-0.260509	0.957691
C	-4.834642	0.153499	-0.114296
C	-4.248852	0.272449	-1.372962
C	-2.900445	-0.009736	-1.502583
C	0.253338	0.094150	2.325080
C	-0.071180	1.396705	1.608807
C	1.857541	1.663080	0.094827
C	2.718463	0.426180	0.109597
C	4.075328	0.504418	0.415555
C	4.869079	-0.627321	0.283067
C	4.283776	-1.813081	-0.156956
C	2.925985	-1.823354	-0.423238
C	-0.361864	2.432217	-0.619326
C	-0.085263	3.872750	-0.261053
C	0.838489	4.617162	-1.003625
C	1.097708	5.947624	-0.687539
C	0.429714	6.553248	0.373679
C	-0.509621	5.830378	1.105994
C	-0.769414	4.501066	0.786753
H	-0.531527	-3.290527	-2.358462
H	-0.794603	-5.740837	-2.020871
H	-0.591219	-6.661111	0.302643
H	-0.139747	-5.085006	2.183383
H	1.322043	-2.196942	2.006977
H	-0.074672	-2.716043	2.952853
H	-2.109593	-0.623031	2.814378

S3.3 cont.- *[Fe(bztpen)(NO)]$^{2+}$ S = 5/2, E = -2713.90128732 au, ν_1 = 22.5178 cm^{-1}*

H	-2.138505	-2.165575	1.978441
H	-4.483654	-0.370518	1.946408
H	-5.885759	0.375709	0.027988
H	-4.822566	0.584917	-2.236134
H	-2.398360	0.081795	-2.458602
H	-0.077836	0.154952	3.368349
H	1.329575	-0.085093	2.331373
H	0.362492	2.240390	2.154212
H	-1.152544	1.546605	1.589342
H	2.174090	2.366680	0.870026
H	2.032630	2.164134	-0.860943
H	4.500537	1.446655	0.740989
H	5.927883	-0.584953	0.509912
H	4.867156	-2.715393	-0.289262
H	2.428352	-2.723603	-0.760946
H	-0.097214	2.250389	-1.663609
H	-1.419077	2.199529	-0.490030
H	1.339163	4.166597	-1.856326
H	1.807368	6.514829	-1.278354
H	0.624503	7.591228	0.616281
H	-1.052040	6.307796	1.913730
H	-1.531501	3.962535	1.341997

S4.- Modeling SCO in the [Fe(bztpen)(NO)]$^{2+}$ molecule.

To model the spin transition between the S = 1/2 and S = 3/2 states one must first calculate the corresponding temperature dependence change in the free energy associated with this process. That can be achieved by correcting the corresponding electronic energies for each spin state with the vibrational contribution using the harmonic approximation.[1-3] Thus, at each temperature we can compute the corresponding ΔG(T), and from this thermochemical quantity extract relative populations for each spin state. The Gibbs free energy change (ΔG) associated with this process corresponds to:

$$\Delta G = G^{HS} - G^{LS} = \Delta H - T\Delta S \quad [1]$$

Where

$$G^i = H^i - TS^i = E_{el}^i + E_{vib}^i - TS^i \quad [2]$$

is the Gibbs free energy associated with spin state *i*. The enthalpy term (H^i) includes both electronic (E_{el}^i) and vibrational (E_{vib}^i) contributions. For molecular complexes, E_{vib}^i can be properly estimated using the harmonic approximation, while the term E_{el}^i, describing the electronic energy of spin state *i*, can be obtained directly from *ab initio* calculations, in this case, at DFT level. The entropy contribution to the free energy (S^i) can also be estimated using the harmonic approximation.

Using the equilibrium constant, we can write down the corresponding molar fractions of each spin state as follows,

$$\Delta G(T) = -RTlnK_{eq} = -RTln\frac{\gamma_{HS}}{\gamma_{LS}} = -RTln\frac{\gamma_{HS}}{1-\gamma_{HS}} \quad [3]$$

that can be rewritten as,

$$\gamma_{HS}(T) = [1 + e^{\Delta G(T)/RT}]^{-1} \quad [4]$$

where R is the gas constant and T the temperature. This last expression provides with the molar fraction of the HS state at each temperature, which can be used to compute magnetic susceptibility as follows. From the molar fraction, one can estimate the magnetic moment using the spin only formula, and if the Curie law holds, from that quantity we can extract the magnetic susceptibility.

$$\mu_{eff}(T) = \gamma_{HS}(T)\mu_{eff}(S = 3/2) + \gamma_{LS}(T)\mu_{eff}(S = 1/2) \quad [5]$$

$$\mu_{eff}(T) = C\sqrt{\chi_M T} \approx 2.82787\sqrt{\chi_M T} \quad [6]$$

Equation 6 can be recast as,

$$\chi_M T = \left(\frac{\mu_{eff}(T)}{2.82787}\right)^2 \quad [7]$$

which already provides with the temperature dependence of the magnetic susceptibility.

In Figure S3 we report the magnetic behaviour of **1** in the temperature range 0-600 K compared with the experimental data. As can be seen, the calculations reasonably agree with the experimental data, although the computed equilibrium transition temperature ($T_{1/2}^{calc}$ = 546.8 K), at which $\Delta G(T) = 0$, is significantly shifted towards higher values with respect to the experimental value ($T_{1/2}^{exp}$ = 378 K). This circumstance has been previously reported for other Fe^{II} SCO mononuclear complexes, and corresponds to an error of 0.33 kcal mol^{-1}, similar to previously reported calculations, and can be explained on the basis of the amount of exact exchange Hartree-Fock mixed into the TPSSh functional.[1,2]

Figure S3.- Computed (red line) and experimental (open circles) magnetic behaviour of **1** in the temperature range 0-1000 K. The computed equilibrium temperature $T_{1/2}^{calc}$ at which $\Delta G = 0$ is 546 K.

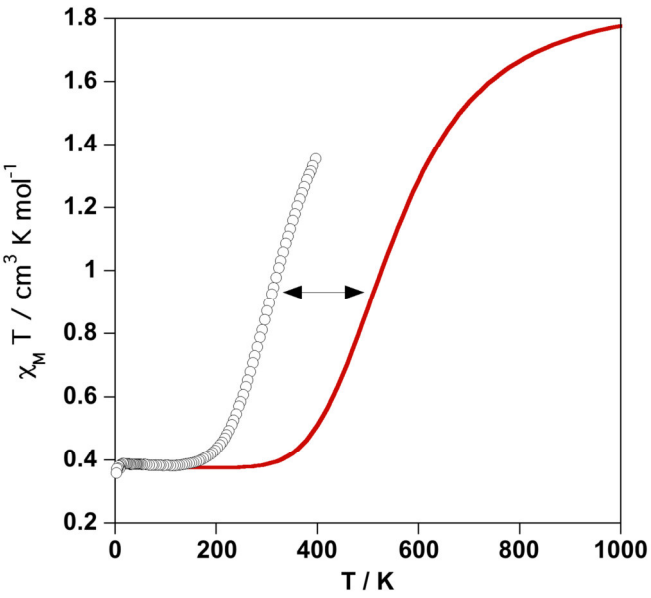

S5.- References

[1] J. Cirera, F. Paesani, *Inorg. Chem.*, **2012**, *51*, 8194.

[2] K. P. Jensen, J. Cirera, *J. Phys. Chem. A*, **2009**, *113*, 10033.

[3] J. Cirera, E. Ruiz, *J. Mat. Chem. C*, **2015**, *3*, 7954.

CAPÍTULO 3

Clathration of five-membered aromatic rings in the bimetallic spin-crossover metal-organic framework $[Fe(TPT)_{2/3}\{M^{I}(CN)_2\}_2]\cdot G$ (M^{I} = Ag, Au)

REVISTA: Crystal Growth & Design

ÍNDICE DE IMPACTO: 4.425

CAPÍTULO 3

Clathration of five-membered aromatic rings in the bimetallic spin-crossover metal-organic framework $[Fe(TPT)_{2/3}\{M^{I}(CN)_2\}_2]\cdot G$ (M^{I} = Ag, Au)

3.1.- Abstract

Six clathrate compounds of the 3D SCO metal-organic framework formulated $[Fe(TPT)_{2/3}\{M^{I}(CN)_2\}_2]\cdot nG$, where TPT is 2,4,6-tris(4-pyridyl)-1,3,5-triazine, M^{I} = Ag or Au and G represent the guest molecules furan, pyrrole and thiophene, were synthesized using slow diffusion techniques. The clathrate compounds were characterized by single-crystal X-ray diffraction at 120 and 300 K, thermogravimetric analysis and thermal dependence of the magnetic susceptibility. All compounds crystallize in the *R-3m* trigonal space group. The Fe^{II} defines a unique $[FeN_6]$ crystallographic site with the equatorial positions occupied by four dicyanometallate ligands while the axial positions are occupied by the TPT ligands. Each TPT ligand links three Fe^{II} sites, while the dicyanometallate ligands bridge two Fe^{II} sites thereby generating two interlocked 3D frameworks with the NbO topology. The choice of the TPT ligand favors the generation of pores where the guest molecules are located. The thermal dependence of the magnetic susceptibility of samples constituted of single crystals was investigated for the six compounds to assess the influence of the guest molecules on the SCO behaviour. In general, the magnetic properties of the six clathrates suggest a gradual stabilization of the HS state as the molecular volume of the guest increases.

3.2.- Introduction

SCO in first-row transition metal complexes with electronic configurations $3d^4$-$3d^7$ afford one of the most spectacular examples of molecule-based switchable materials. They can switch in a controllable, detectable and reversible manner between the HS state and the LS state by means of external stimuli (usually temperature, pressure and light). This change of electronic spin state, strongly coupled with a structural reorganization, occurs with concomitant changes in magnetic, dielectric and optical properties of the material. The structural reorganization, taking place primarily in

the metal coordination sites (M-L bond distances and angles), are transmitted cooperatively in the solid by means of elastic interactions. In favorable conditions this cooperativity manifest hysteretic behaviour and produces bistability in the physical properties, a necessary condition to deliver advanced materials with sensory and memory functions.[1-18]

By far, six-coordinate Fe^{II} SCO complexes ($3d^6$) have been the most investigated.[9,18] They switch between the paramagnetic HS state ($t_{2g}^4e_g^2$) and the diamagnetic LS state ($t_{2g}^6e_g^0$). The search for cooperativity in Fe^{II} SCO complexes led to the development of the so-called polymeric approach.[19,20] It was believed that partial or total replacement of intermolecular contacts (typically hydrogen bonds and/or π-π interactions) between discrete SCO molecules by more reliable coordination bonds (provided by rigid bridging ligands) could enhance the transmission of elastic interactions between active SCO centers and hence the cooperative nature of the SCO event. This strategy has stimulated the synthesis of a considerable number of (1-3)D SCO-CPs also known as metal-organic frameworks (SCO-MOFs). Some of them are relevant examples of multifunctional molecular materials since they combine SCO and porosity functions. In particular the complex $[Fe(tvp)_2(NCS)_2]\cdot MeOH$ (tvp = trans-1,2-bis(4-pyridyl)ethylene), made up of orthogonal interpenetration of identical $[Fe(tvp)_2(NCS)_2]_n$ layers, represents the first porous SCO-CP.[21] Nevertheless, direct correlation between the spin state of the Fe^{II} ion and host-guest interactions in the pores was evidenced for the first time for the related complex $[Fe(azpy)_2(NCS)_2]\cdot$Guest (azpy = 4,4′-azopyridine).[22] Another important class of metal-organic frameworks combining SCO and porosity functions are the so-called Hofmann-type clathrates formulated $\{Fe(L)M^{II}(CN)_4]\}\cdot$Guest, where L is a pyridine-like rod-shaped bridging ligand and M^{II} = Ni, Pd, Pt. In this framework an infinite stack of 2D $\{Fe[M^{II}(CN)_4]\}_n$ layers are pillared by the organic ligand L thereby defining a 3D framework with well-defined channels. These SCO-CPs are able to express physi-and chemi-sorptive host-guest interactions in terms of changes in the spin state of the Fe^{II} ion.[23-32]

The use of dicyanometallate complexes $[M^{I}(CN)_2]^-$ (M^{I} = Cu, Ag, Au) as building blocks in combination with ligands, typically derived from pyridine- or bis-monodentate pyridine-like linear bridging ligands, has afforded a rich variety of one- two- and three-dimensional SCO-CPs without permanent porosity.[23] Aiming at exploring the possibility of obtaining dicyanometallate based porous SCO-CPs, we decided to employ pyridine-

type bridging ligands with denticity higher than two. Thus, we recently reported the synthesis, crystal structures, magnetic, Mössbauer and calorimetric studies of a new series of SCO-CPs formulated $\{Fe(TPT)_{2/3}[M^{I}(CN)_2]_2 \cdot nSolv\}$ [M^{I} = Ag (**1**·nSolv), Au (**2**·nSolv)], where TPT is 2,4,6,-tris(4-pyridyl)-1,3,5-triazine, a tritopic C_3 symmetric pyridine-type bridging ligand, and Solv are the solvent molecules CH_2Cl_2 or CH_3OH.[33]

As a new step in this research, here we describe the synthesis, crystal structures and magnetic properties of a new series of furan, pyrrole and thiophene clathrates of $[Fe(TPT)_{2/3}\{M^{I}(CN)_2\}_2]\cdot G$ [M^{I} = Ag (**1**·nG), Au (**2**·nG)].

3.3.- Results

3.3.1.- Synthesis

Self-assembly of the constituent building blocks (Fe^{II}, $[M^{I}(CN)_2]^{-}$ and TPT) in the presence of the guest molecules (G = furan, pyrrole, or thiophene) in CH_2Cl_2/CH_3OH solutions was unsuccessful due to the high insolubility and hence rapid precipitation of **1**·nSolv and **2**·nSolv (Solv = CH_2Cl_2 or CH_3OH). Furthermore, we did not find evidence of sorption after soaking the empty host SCO-CPs **1** and **2** with the guest molecules for 2 weeks. Slow diffusion (see Experimental Section) produced the best conditions for self-assembling and clathration of the selected guest molecules in the open frameworks **1** and **2**. Combination of single crystal diffraction studies (*vide infra*) together with thermogravimetric (Figure S1, Supporting Information) and elemental analyses have showed the presence of the targeted guest molecules without noticeable amounts of the solvents CH_2Cl_2 or CH_3OH. In principle, these solvents must compete with the five-membered rings for the voids in which both could co-exist. However, the presence of solvent-accessible void and hence partial occupation of the void by the guest molecules in some of the structures here described (*vide infra*), is consistent with the fact that these solvent molecules are loosely attached to the frameworks **1** and **2** giving immediately the unsolvated species when the solid is not impregnated with the mother liquor at room temperature.[33]

3.3.2.- Structure

Single crystals of **1**·nG and **2**·nG were picked out from the mother liquor, soaked in Paratone oil and mounted on a goniometer at 120 K. Then, they were measured successively at 120 K and at 300 K. At both temperatures the crystal parameters correspond to the trigonal *R-3m* space group. These data are shown in Tables 1 and 2 together with other relevant crystallographic parameters for **1**·nG and **2**·nG, respectively. A selection of significant bond distances and angles is gathered in Table 3.

Table 1.- Crystal data for **1**·nG.

	1·0.5furan		**1**·1.5pyrrole		**1**·1thiophene	
	120 K	**300 K**	**120 K**	**300 K**	**120 K**	**300 K**
Empirical formula	$C_{18}H_{10}N_8O_{0.5}Ag_2Fe$		$C_{22}H_{15.5}N_{9.5}Ag_2Fe$		$C_{20}H_{12}N_8SAg_2Fe$	
Mr	617.93		684.53		668.03	
Crystal system	Trigonal		Trigonal		Trigonal	
Space group	*R-3m*		*R-3m*		*R-3m*	
a (Å)	26.2174(12)	26.8761(8)	26.2525(9)	26.8913(12)	26.2003(8)	26.8824(10)
c (Å)	9.5734(5)	10.0456(4)	9.6515(4)	10.0069(7)	9.8014(3)	10.2072(5)
V (Å^3)	5698.7(5)	6284.1(4)	5760.6(3)	6266.9(6)	5826.8(3)	6388.1(5)
Z	9		9		9	
D_c (mg cm^{-3})	1.621	1.470	1.776	1.632	1.713	1.563
F(000)	2682	2682	3006	3006	2916	2916
μ (Mo-K$_\alpha$) (mm^{-1})	2.116	1.919	2.103	1.933	2.153	1.963
Crystal size (mm)	0.08x0.15x0.15		0.08x0.10x0.10		0.08x0.08x0.10	
No. of total reflections	2273	2085	2309	2101	1837	2138
No. of reflections [$I > 2\sigma(I)$]	1840	1501	2029	1414	1448	1443
R_1 [$I > 2\sigma(I)$][a]	0.0600	0.0560	0.0475	0.0654	0.0813	0.0785
ωR [$I > 2\sigma(I)$][a]	0.1713	0.1655	0.1357	0.2118	0.2283	0.2108
S	1.081	1.011	1.087	1.096	1.040	1.154

$R_1 = \Sigma\ ||Fo| - |Fc|| / \Sigma\ |Fo|$; $\omega R = [\Sigma\ [\omega(Fo^2 - Fc^2)^2] / \Sigma\ [\omega(Fo^2)^2]]^{1/2}$.
$\omega = 1/\ [\sigma^2(Fo^2) + (m\ P)^2 + n\ P]$ where $P = (Fo^2 + 2Fc^2) / 3$;
m = 0.1148 (**1** (**120 K**)), 0.1214 (**1** (**300 K**)) 0.0702 (**2** (**120 K**)), 0.1265 (**2** (**300 K**)), 0.1574 (**3** (**120 K**)) and 0.1678 (**3** (**300 K**));
n = 56.2195 (**1** (**120 K**)), 10.5162 (**1** (**300 K**)) 66.7343 (**2** (**120 K**)), 25.3970 (**2** (**300 K**)), 107.5530 (**3** (**120 K**)) and 18.9693 (**3** (**300 K**)

Table 2.- Crystal data for **2**·nG.

	2·1furan		**2**·2pyrrole		**2**·0.5thiophene	
	120 K	**300 K**	**120 K**	**300 K**	**120 K**	**300 K**
Empirical formula	$C_{20}H_{12}N_8OAu_2Fe$		$C_{24}H_{18}N_{10}Au_2Fe$		$C_{18}H_{10}N_8S_{0.5}Au_2Fe$	
Mr	830.16		896.27		804.15	
Crystal system	Trigonal		Trigonal		Trigonal	
Space group	*R-3m*		*R-3m*		*R-3m*	
a (Å)	26.1934(10)	26.852(2)	26.4590(10)	26.9010(14)	26.4013(9)	26.8078(12)
c (Å)	9.3978(8)	9.6735(13)	9.5783(5)	9.7742(8)	9.6662(7)	9.9406(6)
V (Å^3)	5583.9(6)	6040.4(11)	5807.2(4)	6125.6(7)	5834.9(5)	6186.8(5)
Z	9		9		9	
D_c (mg cm^{-3})	2.222	2.054	2.307	2.187	2.060	1.943
F(000)	3420	3420	3744	3744	3294	3294
μ (Mo-K_α) (mm^{-1})	12.397	11.460	11.929	11.309	11.896	11.220
Crystal size (mm)	0.06x0.10x0.10		0.05x0.10x0.10		0.05x0.06x0.10	
No. of total reflections	2250	1997	2269	2027	2364	1923
No. of reflections [$I > 2\sigma(I)$]	1905	1067	1823	1575	1425	1245
R_1 [$I > 2\sigma(I)$][a]	0.0455	0.0926	0.0518	0.0405	0.0864	0.0705
ωR [$I > 2\sigma(I)$][a]	0.1289	0.2004	0.1195	0.1067	0.2089	0.1850
S	1.005	1.049	1.062	0.968	1.028	1.097

$R_1 = \Sigma ||Fo| - |Fc|| / \Sigma |Fo|$; $\omega R = [\Sigma [\omega(Fo^2 - Fc^2)^2] / \Sigma [w(Fo^2)^2]]^{1/2}$.
$\omega = 1/ [\sigma^2(Fo^2) + (m\ P)^2 + n\ P]$ where $P = (Fo^2 + 2Fc^2) / 3$;
m = 0.0824 (**1** (**120 K**)), 0.1510 (**1** (**300 K**)) 0.0461 (**2** (**120 K**)), 0.0641 (**2** (**300 K**)), 0.0970 (**3** (**120 K**)) and 0.0921 (**3** (**300 K**));
n = 149.9454 (**1** (**120 K**)), 90.3794 (**1** (**300 K**)) 190.5547 (**2** (**120 K**)), 71.2422 (**2** (**300 K**)), 411.9829 (**3** (**120 K**)) and 157.4274 (**3** (**300 K**))

The crystal structures are similar to those of the parent compounds, **1**·nSolv and **2**·nSolv (Solv = CH_2Cl_2, MeOH), previously reported.[33] The TPT molecule acts as a tritopic ligand associated with a trigonal axis perpendicular to the plane containing the TPT molecule and passing through the center of the triazine ring. The TPT ligand coordinates three crystallographically equivalent Fe^{II} ions. The pyridine moieties occupy the axial positions of the Fe^{II} sites while the equatorial positions are occupied by the cyanide groups of four crystallographically identical $[M^I(CN)_2]^-$ anions, thereby defining an axially elongated $[FeN_6]$ octahedron with the Fe^{II} ions lying in an inversion center (Figure 1).

Table 3.- Selected bond lengths [Å] and angles [°] for **1**·nG and **2**·nG.

	furan		**pyrrole**		**thiophene**	
	120 K	**300 K**	**120 K**	**300 K**	**120 K**	**300 K**
Fe-N(1)	1.993(5) [1.987(8)]	2.208(5) [2.20(2)]	1.998(4) [2.071(9)]	2.202(6) [2.197(7)]	1.986(8) [2.04(2)]	2.207(7) [2.17(2)]
Fe-N(2)	1.950(4) [1.950(6)]	2.154(4) [2.14(2)]	1.947(3) [2.033(7)]	2.149(5) [2.163(5)]	1.962(6) [2.049(14)]	2.159(6) [2.180(11)]
<Fe-N>[a]	1.964(5) [1.962(8)]	2.172(5) [2.160(2)]	1.964(4) [2.046(9)]	2.167(6) [2.174(7)]	1.970(8) [2.045(19)]	2.175(7) [2.177(15)]
Δ[<Fe-N>][b]	0.208 [0.198]		0.203 [0.128]		0.205 [0.132]	
N(1)-Fe-N(2)	90.0(2) [89.2(3)]	89.69(14) [89.7(6)]	89.57(12) [89.8(3)]	89.3(2) [89.6(2)]	89.7(2) [89.9(5)]	89.3(2)] [89.1(4)]
Fe-N(2)-C(5)	171.9(4) [169.9(7)]	169.7(5) [164.9(18)]	172.2(3) [167.4(6)]	167.8(6) [164.2(6)]	173.1(6) [169.4(15)]	170.8(7)] [165.9(14)]
Σ[c]	8.4 [14.4]	17.3 [16.4]	15.2 [12.8]	20.5 [16.4]	13.6 [9.6]	25.2 [16.0]
Φ[d]	0.82 [0.77]	1.44 [1.37]	1.13 [1.08]	1.45 [1.22]	1.09 [0.87]	1.87 [0.93]
M^{I}-C(5)	2.063(5) [1.992(7)]	2.052(5) [1.965(18)]	2.064(4) [1.990(8)]	2.047(6) [1.979(6)]	2.068(7) [1.990(10)]	2.051(7) [2.001(12)]
C(5)-M^{I}-C(5)	165.6(3) [169.7(4)]	167.6(3) [171.5(12)]	167.1(2) [172.1(9)]	168.3(4) [172.0(4)]	166.6(4) [172.1(9)]	166.9(5) [173.4(9)]
$M^{I}\cdots M^{I}$	3.5466(3)[i] [3.6104(4)[iv]]	3.7252(4)[ii] [3.7169(9)[ii]]	3.6218(3)[iii] [3.6890(4)[v]]	3.7234(6)[ii] [3.7519(4)[ii]]	3.6541(6)[ii] [3.7291(5)[iv]]	3.7760(6)[i] [3.8355(5)[iv]]

[a]<Fe-N> average Fe-N bond length; [b]Δ[<Fe-N>] difference between average bond lengths of the 300 K and 120 K structures; [c]$\Sigma = \sum_{i=1}^{12}(|\theta_i - 90|)$ represents the sum of the deviation from 90º of the 12 angles defined by the bonds of the pseudoctahedral $[FeN_6]$ core; [d]$\Phi = \sum_{i=1}^{24}(|\phi_i - 60|)/24$ is the angle of trigonal distortion. i = x-y+1, -y+2, -z+1; ii = x-y, -y, -z+1; iii = x-y, -y, -z+2; iv = x-y+1/3, -y+2/3, -z-1/3; v = y, x, -z+2.

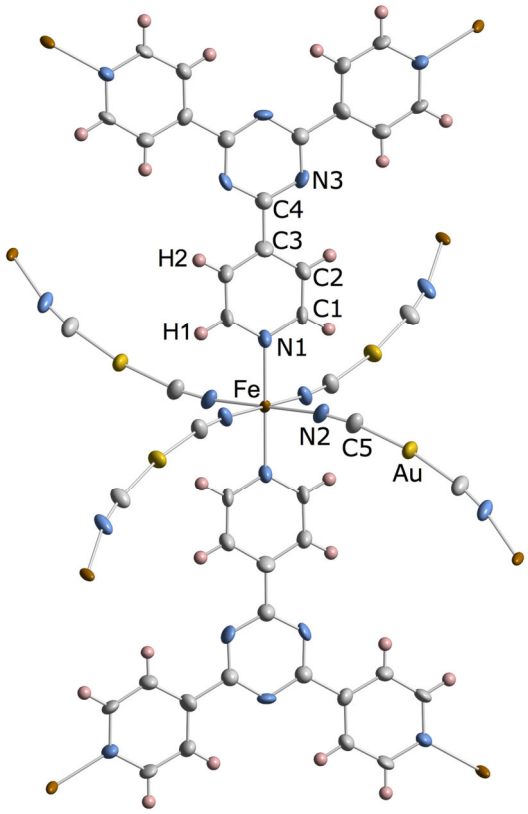

Figure 1.- ORTEP representation of a significant fragment of the compound $[Fe(TPT)_{2/3}\{Au(CN)_2\}_2]\cdot 2$pyrrole (**2**·2pyrrole) at 120 K displaying the atom numbering of the asymmetric unit. Same atom numbering is applied to all silver and gold clathrates **1**·nG and **2**·nG. Thermal ellipsoids are shown at 50% probability.

The average <Fe-N> bond length is in the range 1.960(5)-1.970(8) Å at 120 K and increases until 2.164-2.175 Å at 300 K, for the Ag derivatives. These values are characteristic for the Fe^{II} ion in the LS and HS spin state, respectively. The difference between the average bond lengths associated with the HS and LS spin states, Δ[<Fe-N>], found in the range 0.203-0.208 Å is consistent with the occurrence of a complete SCO in the three silver clathrates. The spin state change is also accompanied by changes of the bond angles of the coordination core [FeN_6] (see Table 3). For example, the sum of the deviations from the ideal octahedron of the 12 cis N-Fe-N angles ($\sum_{i=1}^{12}|\theta_i - 90|$) falls in the range 8-15° in the LS state and increases until 17-25° in the HS state. The average value of the trigonal distortion parameter, $\Phi = \sum_{i=1}^{24}(|\Phi_i - 60|)/$

24, has been estimated to be in the interval 0.82-1.13° and 1.44-1.87° for the LS and HS states, respectively (Φ_i represents each of the six angles defined by the superposition of two opposed triangles angles, being 60° for a regular octahedron). The Fe-cyanide linkage [Fe-N(2)-C(5)] is not linear being about 170° in the LS state. This linearity even decreases by 2-5° when the compounds change to the HS state. Similarly, the $[Ag(CN)_2]^-$ anion departs ca. 13° from linearity in the LS state and increases by 2°, 1.2° and 0.3° in the HS state for **1**·0.5furan, **1**·1.5pyrrole and **1**·1thiophene, respectively. Concomitantly with this change of angle the Ag-C(5) bond length decrease by 0.01 Å when moving from the LS state to the HS state (Table 3).

Concerning the Au derivatives, only the furan clathrate shows practically complete SCO with Δ[<Fe-N>] = 0.198 Å. The Δ[<Fe-N>] value for pyrrole and thiophene derivatives (about 0.13 Å) suggests that, considering Δ[<Fe-N>] = 0.20 Å for a complete SCO, a fraction of about 35% of Fe^{II} centers remain in the HS state at 120 K. The angular parameters of the coordination centers (Fe and Au) are comparable to those of the Ag derivatives (see Table 3). However, it is not possible to establish a similar trend for the Au-C(5) bond lengths because of the incomplete SCO and larger standard deviations.

The Fe^{II}-TPT assembly defines infinite hexagonal layers (Figure 2a). A view of two consecutive layers (hereafter named A and B) projected in *c*-direction shows that they stack in such a way that the triazine groups of one layer superpose alternately either the center of the hexagonal windows or the triazine group of the other layer (Figure 2b). The $[M^{I}(CN)_2]^-$ anions connect layers of the same type (A or B) generating two identical, independent and mutually interpenetrated coordination frameworks (Figure 2c,d) with the topology of the NbO (Figure S2, Supporting Information). The shortest distance between two consecutive A-B layers, d, is determined by the characteristic π-π interaction observed between the triazine groups of the TPT ligands. A large volume available for clathration is formed between two consecutive A-A and B-B layers defined by the TPT ligands located over the centers of the hexagonal windows and separated by a distance hereafter called D (Table 4, Figure 3, and Figure S3, Supporting Information). For both series of clathrates there is, in general, a reasonably good correlation between the size of the guest molecule and the increase of D at both 120 and 300 K. Furthermore, the D and d values experience an increase of about 4% and 3%, respectively, when moving from the LS state to the HS state for the Ag derivatives and

2·1furan. For **2**·2pyrrole and **2**·0.5thiophene, these variations are limited by the completeness of the SCO (*vide infra*).

The structural modifications associated with the SCO phenomenon are also accompanied by changes in host-guest and guest-guest intermolecular interactions. Tables 5 and 6 show a selection of relevant C···C and C···Ag or C···Au contacts. The most important interactions occur for the LS state between the guest molecules and both, the pyridine group of the TPT ligand and the $[M^{I}(CN)_2]^-$ groups (Figure 3). Short guest···guest contacts (Tables 5 and 6) are only observed for the furan derivative in both series (we consider relevant contacts those smaller than the sum of the van der Waals radii, ie. smaller than 3.70 Å for C···C). There are also short $M^{I}\cdots M^{I}$ contacts between the two interpenetrated networks.

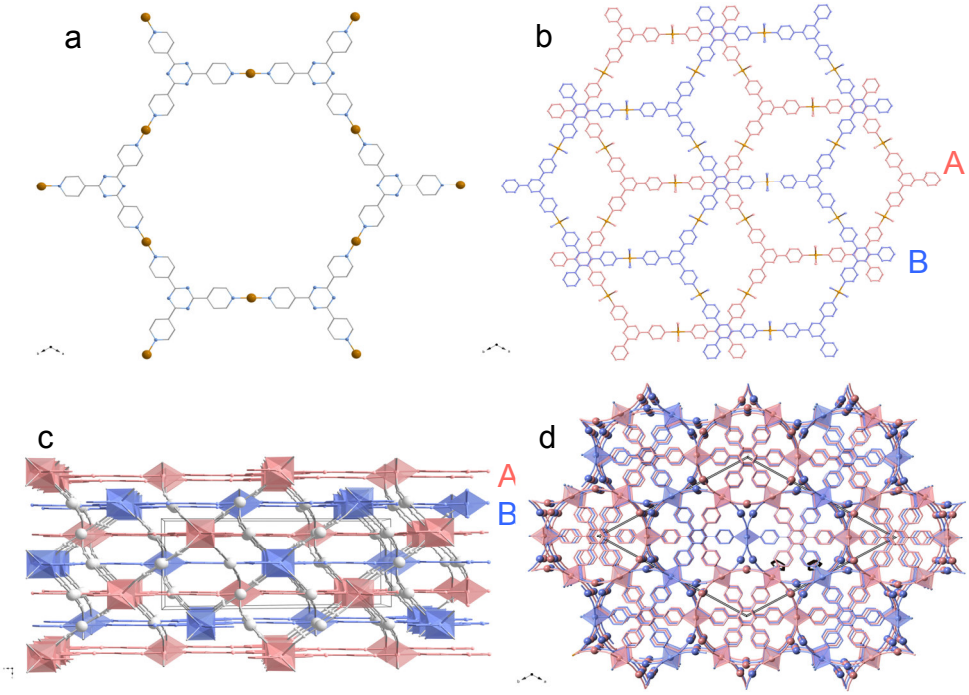

Figure 2.- (a) Hexagonal motive defined by a $[Fe(TPT)]_6$ unit; (b) projection of two consecutive A and B hexagonal layers along the [001] direction; (c) view along the [010] direction of the stacking of a series of layers (blue and red colors represent the two independent interpenetrated networks); (d) Projection along the [001] direction displaying the hexagonal motives defined by interpenetration of two identical framework with NbO topology.

These contacts related by a helical axis running along the *c*-direction define characteristic pseudotrigonal motives when the structure is projected on the *a*-*b* plane (see Figure 2d). Two consecutive pseudotrigonal motives display opposite chirality. Although these contacts clearly change with the spin state of the Fe^{II}, no relevant intermetallic interactions are observed in these series.

All the changes associated with the SCO can be expressed in terms of the unit cell volume variation per Fe^{II} atom: ΔV_{HL} = 65.04, 56.29, and 62.37 $Å^3$ for **1**·0.5furan, **1**·1.5pyrrole, and **1**·1thiophene and ΔV_{HL} = 50.72, 54.43, and 60.15 $Å^3$ for **2**·1furan, **2**·2pyrrole, and **2**·0.5thiophene (the two latter volumes have been extrapolated to 100% of SCO conversion), respectively.

Table 4.- Average distances D_{av} and d_{av} (Å) between hexagonal Fe-TPT layers

	D		d	
	120 K	**300 K**	**120 K**	**300 K**
1·0.5furan	6.396	6.773	3.179	3.274
1·1.5pyrrole	6.452	6.715	3.201	3.293
1·1thiophene	6.636	6.942	3.167	3.266
2·1furan	6.262	6.382	3.136	3.294
2·2pyrrole	6.405	6.535	3.174	3.240
2·0.5thiophene	6.538	6.734	3.129	3.209

Table 5.- Intermolecular contacts between the guest molecule and different fragments of **1**·nGuest[a].

Compound	**1**·0.5furan		**1**·1.5pyrrole		**1**·1thiophene	
	Guest···Pyridine					
Guest···Host	**120 K**	**300 K**	**120 K**	**300 K**	**120 K**	**300 K**
C(6)···C(1)	3.60(2)^{i}	3.74(3)^{iii}	3.723(11)^{vii}	3.83(2)^{x}	3.573(11)^{xiii}	3.707(13)^{xiv}
C(6)···C(2)	3.37(2)^{i}	3.54(3)^{iv}	3.514(11)^{vii}	3.65(2)^{x}	3.487(11)^{xiii}	3.620(13)^{xiv}
C(7)···C(2)	3.67(4)^{i}	3.94(3)^{iv}	3.761(12)^{vii}	3.83(2)^{x}	3.81(3)^{xiii}	3.99(2)^{xiv}
	Guest···Cyanide					
C(6)···C(5)	3.60(3)^{ii}	3.89(2)^{v}	3.718(10)^{viii}	3.91(2)^{iv}	3.531(14)^{ii}	3.68(2)^{xv}
C(7)···C(5)	3.62(5)^{ii}	----	3.530(10)^{viii}	3.75(2)^{iv}	3.49(4)^{ii}	3.63(3)^{xv}
	Guest···Ag					
C(6)···Ag	3.49(2)	3.65(3)	3.562(10)^{viii}	3.74(2)^{xi}	3.23(12)^{ii}	3.70(2)^{xv}
C(7)···Ag	------	-------	3.799(10)^{viii}	3.94(2)^{xi}	3.71(4)^{ii}	3.85(3)^{xv}
	Guest···Guest					
C(7)···C(7)^{i}	3.49(5)^{ii}	4.10(4)^{vi}	4.15(2)^{ix}	4.38(3)^{xii}	4.14(3)^{ii}	4.11(2)^{vi}

i = -x+1, -y+2, -z+2; ii = -x+2/3, -x+y+1/3, -z+4/3; iii = -x,+y+4/3, -x+2/3, z+2/3; iv = -y+2/3, x-y-2/3, z-2/3; v = x-y, -y, -z+1; vi = -x+4/3, -x+y+2/3, -z+2/3; vii = -y+2/3, x-y-2/3, z+1/3; viii = x-y, -y, -z+2; ix = y+2/3, x-2/3, -z+7/3; x = x, x-y-1, z; xi = -x+1, -x+y, -z; xii = x-y-1/3, -y-2/3, -z-2/3; xiii = -x+2/3, -x+y+1/3, -z+1/3; xiv = x+1/3, x-y+2/3, z-1/3; xv = -x+1, -y+1, -z+1.

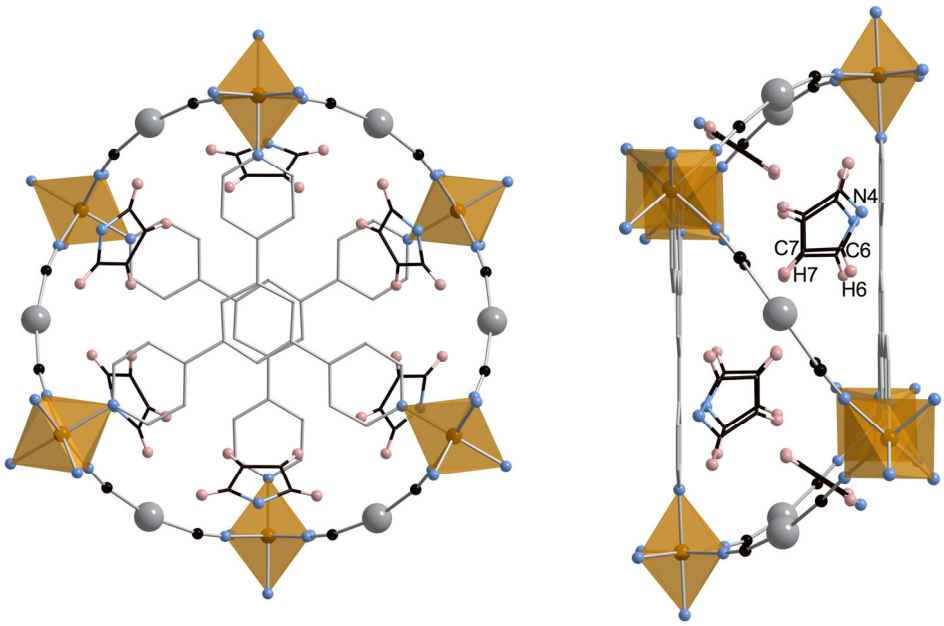

Figure 3.- Views in [001] (left) and [100] (right) directions of the same fragment of **1**·1.5pyrrole at 120 K showing the pyrrole guest together with the atom numbering.

Table 6.- Intermolecular contacts between the guest molecule and different fragments of **2**·nG[a] [Å].

Compound	**2**·1furan		**2**·2pyrrole		**2**·0.5thiophene	
	Guest···Pyridine					
Guest···Host	**120 K**	**300 K**	**120 K**	**300 K**	**120 K**	**300 K**
C(6)···C(1)	3.58(3)[i]	3.80(8)[v]	3.73(2)	3.7480(2)	3.60(4)[x]	3.73(9)
C(6)···C(2)	3.29(3)[i]	3.62(9)[v]	3.563(14)	3.5597(2)	3.48(4)[x]	3.55(8)
C(7)···C(2)	3.68(4)[i]	3.55(9)[v]	3.71(2)	3.7897(2)	3.59(8)[x]	3.90(6)
C(7)···C(1)	3.68(3)[ii]	3.84(8)[vi]				
	Guest···Cyanide					
C(6)···C(5)	3.63(2)[iii]	3.49(6)[vii]	3.65(2)[vii]	3.7960(2)[ix]	3.53(3)	3.69(10)[xi]
C(7)···C(5)	3.53(3)[iii]	3.88(6)[vii]	3.55(2)[vii]	3.6656(2)[ix]	3.64(5)	3.63(8)[xi]
	Guest···Ag					
C(6)···Au	3.52(2)[iii]	3.47(5)[vii]	3.51(2)[vii]	3.6367(4)[ix]	3.25(3)	3.48(12)[xi]
C(7)···Au	3.77(2)[iii]	4.02(4)[vii]	3.75(2)[vii]	3.8696(5)[ix]	3.75(4)	3.80(9)[xi]
	Guest···Guest					
C(7)···C(7)[i]	3.43(5)[iv]	3.47(12)[iv]	4.19(2)[viii]	4.1244(2)[ix]	4.21(10)[iv]	3.79(9)[ix]

i = x-y+1/3, -y+2/3, -z+2/3; ii = -y+2/3, x-y+1/3, z-2/3; iii = y, -x+y, -z; iv = y, x, -z; v = x-1/3, y+1/3, z+1/3; vi = y+1/3, x-1/3, -z-1/3; vii = -x+y+2/3; y+1/3, z-2/3; viii = x-y+2/3, -y+4/3, -z+1/3; ix = -x+4/3, -x+y+2/3, z+2/3; x = -y+1/3, -x+2/3, z+2/3; xi = x-1/3, x-y-2/3, z-2/3

3.3.3.- Spin-crossover properties

The thermal dependence of the $\chi_M T$ product, where χ_M is the molar magnetic susceptibility and T is the temperature, was measured in the temperature region 4-300 K for **1**·nG and **2**·nG series. In order to minimize any loss of guest molecules, the magnetic properties of samples constituted exclusively of single crystals soaked in the corresponding guest were measured in sealed tubes. This was particularly important for the furan and thiophene derivatives since their boiling points are relatively low (304.4 and 357 K, respectively). The corresponding $\chi_M T$ versus T curves are shown in Figure 4. Table 7 summarizes the extreme values of $\chi_M T$ versus T curves obtained from the low- $[(\chi_M T)_{LT}$, T = 50 K] and high-temperature limits $[(\chi_M T)_{HT}$, T = 300 K] together with the characteristic temperature $T_{1/2}$ at which the HS and LS molar fractions are equal to 0.5, where the free Gibbs energy is equal to zero for the whole series.

The clathrates **1**·nG display relatively poor cooperative thermal induced SCO without hysteretic behaviour. For **1**·0.5furan the SCO is rather complete and characterized by two steps. One step centered at ca. 233 K involves 2/3 of the total spin state conversion, whereas the remaining HS↔LS conversion takes place at ca. 173 K. In contrast, **1**·1.5pyrrole and **1**·1thiophene undergo three-step SCO with characteristic temperatures 211.5 K, 167.3 K, and ≈ 103.2 and 193.5 K, 148.3 K, and ≈ 82 K, respectively. Each step involves approximately the same degree of HS↔LS conversion. However, due to the low temperatures involved in the low-temperature transition, the SCO is clearly incomplete for both derivatives. This thermal quenching is common below 100 K since the rate of the HS↔LS transformation becomes so small that no thermodynamic equilibrium can be achieved and consequently a fraction the Fe^{II} ions remain blocked in the HS state.[35]

The **2**·nG clathrates display even less cooperative one-step SCO with characteristic temperatures smaller than those of the silver homologous (Table 7). The conversion is essentially complete for **2**·1furan, however, 30-45% of Fe^{II} centers remain HS at low temperatures for **2**·2pyrrole and **2**·0.5thiophene in agreement with the crystallographic analysis of the three derivatives.

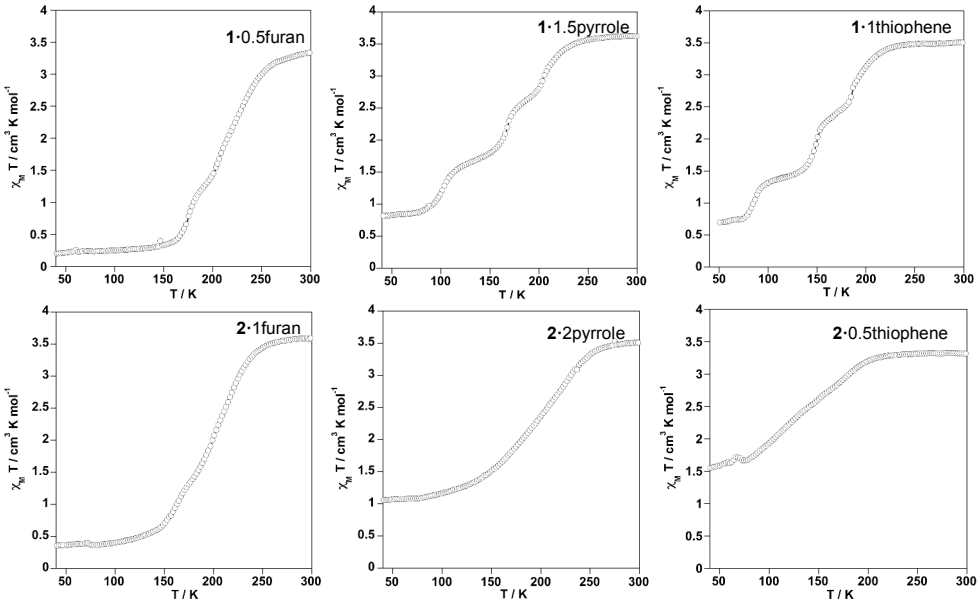

Figure 4.- Magnetic behaviour of **1**·nG and **2**·nG.

Table 7.- Significant extreme values of $\chi_M T$ evaluated for the low (LT) and high (HT) temperature limits of the $\chi_M T$ versus T plots and $T_{1/2}$ (see text).

	$(\chi_M T)_{LT}$	$(\chi_M T)_{HT}$	$T_{1/2}$[a]
1·0.5furan	0.21	3.33	208.9
1·1.5pyrrole	0.83	3.62	167.3
1·1thiophene	0.69	3.50	152.0
2·1furan	0.36	3.59	198.9
2·2pyrrole	1.07	3.51	197.1
2·0.5thiophene	1.58	3.32	136.6
1·2CH_2Cl_2	0.51	3.77	244.4[b]
2·2CH_2Cl_2	0.30	3.17	222.4[b]

3.4.- Discussion

This work was undertaken to investigate clathration capabilities of the open metal-organic frameworks **1** and **2**. We also were interested in how selected five-membered aromatic guest molecules influence the SCO properties of the parent CPs **1**·nSolv and **2**·nSolv previously investigated in our group. Concerning the first point, the title compounds represent the first examples made by design involving clathration of aromatic molecules in a SCO-CP of the type $\{Fe(L)[M^I(CN)_2]_2\}$. In this family of compounds, L is usually a monodentate or bismonodentate pyridine-type ligand, and $[M^I(CN)_2]^-$ are long building blocks that facilitate generation of open frameworks with marked tendency to fill void spaces through interpenetration of identical networks. This is the reason why most investigated SCO-CPs of the type $\{Fe(L)_x[M^I(CN)_2]_2\}$ show poor clathration capacity. For example, when L is 4,4′- bipyridine (4,4′-bipy) or *trans*-1,2-bis(4-pyridyl)ethylene (tvp) the resulting $\{Fe(L)_2[M^I(CN)_2]_2\}$ SCO-CPs display double interpenetrated 3D frameworks with no space even for solvent molecules.[36] Similarly, the 3D SCO-CPs $\{Fe(3\text{-cyanopyridine})_2[M^I(CN)_2]_2\}\cdot 2/3H_2O$[37,38] and $\{Fe(pyrimidine)(H_2O)[M^I(CN)_2]_2\}\cdot H_2O$[39] consist of triple interpenetration of identical open frameworks with the topology of NbO and $CdSO_4$, respectively. Both series of compounds retain one loosely attached molecule of water in the small available space. Accidental clathration of aromatic ligands has been observed in the 2D layered SCO-CPs $\{Fe(3\text{-Xpy})_2[Ag\text{-}(CN)_2][Ag(3\text{-Xpy})(CN)_2]\}\cdot 3\text{-Xpy}$ (3-Xpy = 3-Xpyridine and X = Br, I)[40] and $\{Fe(3\text{-Ipy})_2[Au(CN)_2]_2\}\cdot 1/2(3\text{-Ipy})$[41] when a large excess of 3-Xpy is present during the formation of the crystals.

It deserves to be noted that the systems $\{Fe(3\text{-cyanopyridine})_2[M^I(CN)_2]_2\}$ (M^I = Ag, Au)[36] and **1**·nG and **2**·nG display the same NbO topology. The organic ligand occupies the axial positions of the Fe^{II} sites in both examples. However, the tritopic C_3 nature of the TPT ligand determines the generation of robust hexagonal 2D $[Fe(TPT)_{2/3}]_\infty$ layers, thereby determining the orientation of the $[FeN_6]$ coordination octahedrons and hence the geometry of the Fe-NC-M-CN-Fe linkages. Thus, these linkages strongly deviate from linearity; indeed the average angle defined by the three metallic atoms is about 153°. The lack of such structural constraints in the $\{Fe(3\text{-cyanopyridine})_2[M^I(CN)_2]_2\}$ system, due to the monodentate nature of the 3-cyanopyridine, apparently confers more orientational freedom to the $[FeN_6]$ sites during the formation of the framework, and consequently the average Fe-NC-M-CN-Fe angle is

19° larger (see Figure S4, Supporting Information). This makes the NbO framework more open, thus allowing triple interpenetration of identical frameworks.

Although double interpenetration takes place in **1**·nG and **2**·nG, the C_3 symmetry of the TPT ligand generates large voids defined by the relative disposition of the hexagonal $[Fe\text{-}TPT]_n$ layers (see Figure 2b). Indeed, 50% of the TPT ligands are involved in the formation of strong π-π interactions determining a perfect offset disposition between consecutive A-B-A-B layers. The remaining 50% TPT ligands define the walls of the voids formed by alternate A-A or B-B layers. Despite different guest occupation, the size of the pores expressed in terms of the distance D between A-A or B-B layers (Table 4) increases as the volume of the guest molecule increases [furan, 77.9 $Å^3$; pyrrole, 80.8 $Å^3$; thiophene, 86.5 $Å^3$]. This fact denotes a certain degree of flexibility of the 3D networks, which is more prominent for **1**·nG. This flexibility is also reflected in the change of the linkage angles Fe-N-C and C-M-C upon SCO. Interestingly, the characteristic temperature $T_{1/2}$, and hence the stabilization of the LS species, decreases as the size of the guest molecule increases. A similar trend has recently been observed for the 3D porous SCO-CPs $\{Fe(pyrazine)[Pt(CN)_4]\}\cdot G$ with average $T_{1/2}$ = 201, 167, and 114 K for G = furan, pyrrole and thiophene, respectively. In this case, it was inferred from the calculated host-guest energies that bulky guest molecules are stabilized by the bigger HS host framework, while small guest molecules present similar interaction energies for both spin states of the framework.[42] Hence, $T_{1/2}$ values are expected to decrease as the size of the guest increases. This correlation is in general observed for the title compounds.

1·1thiophene displays, in a first cycle, a three-step SCO with average $T_{1/2}$ = 149 K, which is smaller than that shown by the stable three-step SCO shown by **1**·1.5pyrrole, $T_{1/2}$ = 167.2 K. However, after a second cooling-heating cycle the SCO of **1**·1thiophene becomes two-step with average $T_{1/2}$ = 194.7 K. Modification of the intermolecular host-guest interactions and/or subtle changes in the more flexible host network **1** could be the cause of the observed high-temperature shift of $T_{1/2}$.

1·1.5pyrrole and **1**·1thiophene display three-step SCO behaviour. Three-step transitions are rare events in SCO phenomena. A first example was reported for $\{Fe(3\text{-cyanopyridine})_2[Au(CN)_2]_2\}\cdot 2/3H_2O$.[37,38,43] In this compound, only 1/3 of the Fe^{II} ions undergo LS↔HS, while the other 2/3 remain HS at all temperatures at ambient pressure

(10^5 Pa). However, in the interval of pressures 0.24-0.30 GPa, it shows a two-step thermal induced spin transition, but interestingly, at 0.47 GPa undergoes an almost complete three-step thermal induced spin transition.[43] A three-step SCO behaviour at 10^5 Pa has been reported for the 2D SCO-CP $\{Fe(4\text{-methylpyridine})_2[Au(CN)_2]_2\}$.[44] More recently, an ambient pressure structural, magnetic, and photomagnetic study of the three-step SCO 3D-Hofmann-like MOF $\{Fe(dpsme)[Pt(CN)_4]\}\cdot 2/3 dpsme\cdot xEtOH\cdot yH_2O$ (dpsme = 4,4′-di(pyridylthio)methane) has demonstrated the occurrence of different long-range orderings of the LS and HS sites with subtle structural modulation yielding inequivalent Fe^{II} sites in the four corresponding plateaus.[45] Similarly, only one Fe^{II} site was observed for the LS and HS structures of **1**· 1.5pyrrole and **1**·1thiophene; however, development of elastic constrains during the HS↔LS transformation and hence generation of different Fe^{II} sites seem to be the most reasonable explanation for the occurrence of three steps.

Comparison of $T_{1/2}$ values of both **1**·nG silver and **2**·nG series evidence a general down-shift tendency when moving from silver to gold. This tendency has been previously noted for the two different series of isostructural compounds $\{Fe(3\text{-cyanopyridine})_2[M^{I}(CN)_2]_2\}\cdot 2/3H_2O$[37,38] and $\{Fe\text{-(pyrimidine)}(H_2O)[M^{I}(CN)_2]_2\}\cdot H_2O$[39] where a decrease of the average critical temperature by ca. 52 and 62 K was observed, respectively. This effect can be understood in terms of the well-known relativistic effects observed for heavy atoms, which explain the much higher electronegativity of gold with respect to silver.[46] In this respect, stronger electron withdrawing (polarizing) effect over the CN groups of the $[M(CN)_2]^-$ anions, and hence a poorer donor capacity of the nitrogen atoms for the gold derivative should be expected. This should be reflected on the occurrence of shorter Au-C and longer CN-Fe bonds with respect to the Ag counterpart. In fact, this was the case for the pyrimidine and 3-cyanopyridine derivatives mentioned above. However, in the present case, like for the previously investigated compounds $\{Fe(3\text{-Xpyridine})_2[M(CN)_2]_2\}$ (X = F, Cl; M = Ag, Au),[40,41] this tendency has been only clearly observed for Au-C bonds, which are shorter than the corresponding Ag-C bonds (Table 3).

3.5.- Conclusion

Here we have demonstrated for the first time that the 3D SCO PCP formulated $[Fe(TPT)_{2/3}\{M^{I}(CN)_2\}_2]$ (M^{I} = Ag, Au) are able to form clathrate compounds with five-membered cyclic aromatic molecules such as furan, pyrrole, and thiophene. The presence of these guest molecules in the pores does not influence the cooperative nature of the SCO, but modifies its characteristic temperature, $T_{1/2}$. The general trend is a larger stabilization of the HS state as the molecular volume of the guest increases. Interestingly, **1**·1.5pyrrole and **1**·1thiophene derivatives display three-step SCO behaviour. Similar two-step transition occurs for **1**·0.5furan and **2**·1furan. In contrast, the remaining gold derivatives undergo incomplete SCO behaviours.

3.6.- Experimental Section

3.6.1.- Materials

TPT, $K[Ag(CN)_2]$, $K[Au(CN)_2]$, and $Fe(BF_4)_2{\cdot}7H_2O$ were purchased from commercial sources and used as received.

3.6.2.- Crystal growth

As previously described for the parent compounds **1**·nSolv and **2**·nSolv,[33] single crystals of **1**·nG and **2**·nG were grown by slow liquid-liquid diffusion technique using a modified H-vessel with a third tube added. This peculiar conformation was dictated by the poor solubility of the ligand TPT in common hydroxylic solvents (ethanol, methanol, etc.) where the $Fe(BF_4)_2{\cdot}7H_2O$ and $K[M(CN)_2]$ salts are usually dissolved. The peripheral tubes (total volume ca. 10 mL) contained methanolic solutions of $Fe(BF_4)_2{\cdot}7H_2O$ (0.08 mmol, 27 mg, 0.5 mL) and $K[M(CN)_2]$ (0.16 mmol, 32 mg [M = Ag] / 46 mg [M = Au], 0.5 mL) salts, respectively. The central tube (total volume ca. 10 mL) contained a dichloromethane solution of TPT (0.053 mmol, 16 mg, 0.5 mL) mixed with an excess of the guest molecule (furan, pyrrole or thiophene). Each individual tube was filled with the corresponding solvents while the top was filled with methanol and sealed with rubber stoppers. Dark violet (**1**·nG) or red (**2**·nG) prisms suitable for single crystal X-ray analysis were formed in the central tube after 1 week with relative high yield (ca. 50%). The presence and quantification of the guest molecules were confirmed by means of

single crystal X-ray diffraction, thermogravimetric and elemental analyses of samples constituted exclusively of single crystals. EDX microanalysis was used to confirm the Fe:Ag and Fe:Au stoichiometric relation 1:2. The content of furan was exclusively inferred from thermogravimetric analysis due to the lability of this molecule in the pores. Anal. Calcd for $C_{16}H_8N_8FeAg_2$ (**1**): C 32.91, H 1.38, N 19.19. Found: C 33.36, H 1.30, N 18.83. Anal. Calcd for $C_{16}H_8N_8FeAu_2$ (**2**): C 25.22, H 1.06, N 14.70. Found: C 25.55, H 1.09, N 14.05. Anal. Calcd for $C_{22}H_{15.5}N_{9.5}FeAg_2$ (**1**·1.5pyrrole): C, 38.60; H, 2.28; N, 19.44. Found: C, 37.85; H, 2.32; N,18.79. Calcd for $C_{20}H_{12}N_8SFeAg_2$ (**1**·1thiophene): C, 35.96; H, 1.81; N, 16.77. Found: C, 35.44; H, 1.87; N, 16.38. Calcd for $C_{24}H_{18}N_{10}FeAu_2$ (**2**·2pyrrole): C, 32.16; H, 2.02; N, 15.63. Found: C, 31.73; H, 1.99; N, 15.39. Calcd for $C_{18}H_{10}N_8S_{0.5}FeAu_2$ (**2**·0.5thiophene): C, 26.89; H, 1.25; N, 13.93. Found: C, 26.51; H, 1.23; N, 13.72.

3.6.3.- Physical characterization

Variable-temperature magnetic susceptibility measurements of samples (15-20 mg) were recorded at the rate of 2 K min^{-1} with a Quantum Design MPMS2 SQUID susceptometer equipped with a 5.5 T magnet, operating at 1 T and at temperatures from 1.8-400 K. Experimental susceptibilities were corrected for diamagnetism of the constituent atoms by the use of Pascal's constants. TGA measurements were performed on a Mettler Toledo TGA/SDTA 851e instrument in the 300-700 K temperature range in nitrogen atmosphere with a rate of 10 K min^{-1}. Microanalysis was done by using a PV 9760 EDX system, in conjunction with a PHILIPS XL 30 ESEM scanning electron microscope.

3.6.4.- Single-crystal X-ray diffraction

For each compound, single crystal X-ray data were collected successively at 120 and at 300 K on a Nonius Kappa-CCD single crystal diffractometer using graphite monochromated MoKα radiation (λ = 0.71073 Å). A multiscan absorption correction was performed. The structures were solved by direct methods using SHELXS-97 and refined by full-matrix least-squares on F^2 using SHELXL-97.[34] Non-hydrogen atoms were refined anisotropically and hydrogen atoms were placed in calculated positions refined using idealized geometries (riding model) and assigned fixed isotropic displacement parameters. The check-CIFs of the pyrrole and thiophene derivatives detect a void of about 2% of the total volume of the unit cell situated between the triazine rings of two

consecutive TPT ligand belonging to equivalent A-A or B-B layers (see below). Despite the presence of the mentioned voids no residual electronic density was found neither at 300 nor 120 K.

3.7.- References

[1] H. A. Goodwin, *Coord. Chem. Rev*., **1976**, *18*, 293.

[2] P. Gütlich, *Struct. Bonding* (Berlin), **1981**, *44*, 83.

[3] E. König, G. Ritter, S. K. Kulshreshtha, *Chem. Rev*., **1985**, *85*, 219.

[4] A. Hauser, *Comments Inorg. Chem*., **1995**, *17*, 17.

[5] E. König, *Struct. Bonding* (Berlin), **1991**, *76*, 51.

[6] P. Gütlich, A. Hauser, H. Spiering, *Angew. Chem., Int. Ed.*, **1994**, *33*, 2024.

[7] O. Sato, *Acc. Chem. Res*., **2003**, *36*, 692.

[8] J. A. Real, A. B. Gaspar, V. Niel, M. C. Muñoz, *Coord. Chem. Rev*., **2003**, *236*, 121.

[9] P. Gütlich, H. A. Goodwin, Eds., *Top. Curr. Chem.*, **2004**, Vols. *233*.

[10] J. A. Real, A. B. Gaspar, M. C. Muñoz, *Dalton Trans*., **2005**, 2062.

[11] M. A. Halcrow, *Polyhedron*, **2007**, *26*, 3523.

[12] M. Nihei, T. Shiga, Y. Maeda, H. Oshio, *Coord. Chem. Rev*., **2007**, *251*, 2606.

[13] P. Gamez, J. Sánchez-Costa, M. Quesada, G. Aromí, *Dalton Trans.*, **2009**, 7845.

[14] M. A. Halcrow, *Coord. Chem. Rev*., **2009,** *253*, 2493.

[15] I. Salitros, N. T. Madhu, R. Boca, J. Pavlik, M. Ruben, *Monatsh. Chem*., **2009**, *140*, 65.

[16] J. Olguin, S. Brooker, *Coord. Chem. Rev*., **2011**, *255*, 203.

[17] A. Bousseksou, G. Molnár, L. Salmon, W. Nicolazzi, *Chem. Soc. Rev*., **2011**, *40*, 3313.

[18] M.A. Halcrow, Ed.; John Wiley & Sons: Chichester, **2013**.

[19] O. Kahn, J. Kröber, C. Jay, *Adv. Mater*., **1992**, *4*, 718.

[20] O. Kahn, C. Jay, *Science*, **1998**, *279*, 44.

[21] J. A. Real, E. Andrés, M. C. Muñoz, M. Julve, T. Granier, A. Bousseksou, F. Varret, *Science*, **1995**, *268*, 265.

[22] G. J. Halder, C. J. Kepert, B. Moubaraki, K. S. Murray, J. D. Cashion, *Science*, **2002**, *298*, 1762.

[23] M. C. Muñoz, J. A. Real, *Coord. Chem. Rev*., **2011**, *255*, 2068.

[24] M. Ohba, K. Yoneda, G. Agustí, M. C. Muñoz, A. B. Gaspar, J. A. Real, M. Yamasaki, H. Ando, Y. Nakao, S. Sakaki, S. Kitagawa, *Angew. Chem., Int. Ed*., **2009**, *48*, 4767.

[25] G. Agustí, R. Ohtani, K. Yoneda, A. B. Gaspar, M. Ohba, J. F. Sánchez-Royo, M. C. Muñoz, S. Kitagawa, J. A. Real, *Angew. Chem. Int.*, *Ed*., **2009**, *48*, 8944.

[26] P. D. Southon, L. Liu, E. A. Fellows, D. J. Price, G. J. Halder, K. W. Chapman, B. Moubaraki, K. S. Murray, J.-F. Létard, C. J. Kepert, *J. Am. Chem. Soc*., **2009**, *131*, 10998.

[27] R. Ohtani, K. Yoneda, S. Furukawa, N. Horike, S. Kitagawa, A. B. Gaspar, M. C. Muñoz, J. A. Real, M. Ohba, *J. Am. Chem. Soc.,* **2011**, *133*, 8600.

[28] J. A. Rodríguez-Velamazán, M. A. González, J. A. Real, M. Castro, M. C. Muñoz, A. B. Gaspar, R. Ohtani, M. Ohba, K. Yoneda, Y. Hijikata, N. Yanai, M. Mizuno, H. Ando, S. *J.* Kitagawa, *Am. Chem. Soc*., **2012**, *134*, 5083.

[29] N. F. Sciortino, K. R. Scherl-Gruenwald, G. Chastanet, G. J. Halder, K. W. Chapman, J.-F. Létard, C. J. Kepert, *Angew. Chem., Int. Ed*., **2012**, *51*, 10154.

[30] F. J. Muñoz-Lara, A. B. Gaspar, D. Aravena, E. Ruiz, M. C. Muñoz, M. Ohba, R. Ohtani, S. Kitagawa, J. A. Real, *Chem. Commun*., **2012**, *48*, 4686.

[31] Z. Arcís-Castillo, F. J. Muñoz-Lara, M. C. Muñoz, D. Aravena, A. B. Gaspar, J. F. Sánchez-Royo, E. Ruiz, M. Ohba, R. Matsuda, S. Kitagawa, J. A. Real, *Inorg. Chem*., **2013**, *52*, 12777.

[32] L. Piñeiro-López, M. Seredyuk, M. C. Muñoz, J. A. Real, *Chem. Commun*., **2014**, *50*, 1833.

[33] Z. Arcís-Castillo, M. C. Muñoz, G. Molnár, A. Bousseksou, J. A. Real, *Chem. Eur.*, *J*. **2013**, *19*, 6851.

[34] G. M. Sheldrick, *Acta Crystallogr. A*, **2008**, *64*, 112.

[35] A. Hauser, *Comm. Inorg. Chem*., **1995**, *17*, 17.

[36] V. Niel, M. C. Muñoz, A. B. Gaspar, A. Galet, G. Levchenko, J. A. Real, *Chem. Eur. J*., **2002**, *8*, 2446.

[37] A. Galet, V. Niel, M. C. Muñoz, J. A. Real, *J. Am. Chem. Soc*., **2003**, *125*, 14224.

[38] A. Galet, M. C. Muñoz, V. Martínez, J. A. Real, *Chem. Commun*., **2004**, 2268.

[39] V. Niel, A. L. Thompson, M. C. Muñoz, A. Galet, A. E. Goeta, J. A. Real, *Angew. Chem., Int. Ed*., **2003**, *42*, 3760.

[40] M. C. Muñoz, A. B. Gaspar, A. Galet, J. A. Real, *Inorg. Chem*., **2007**, *46*, 8182.

[41] G. Agustí, M. C. Muñoz, A. B. Gaspar, J. A. Real, *Inorg. Chem*., **2008**, *47*, 2552.

[42] D. Aravena, Z. Arcís-Castillo, M. C. Muñoz, A. B. Gaspar, K. Yoneda, R. Ohtani, A. Mishima, S. Kitagawa, M. Ohba, J. A. Real, E. Ruiz, *Chem. Eur. J*., **2014**, *20*, 12864.

[43] A. Galet, A. B. Gaspar, G. Agustí, M. C. Muñoz, J. A. Real, *Chem. Phys. Lett*., **2007**, *434*, 68.

[44] T. Kosone, I. Tomori, C. Kanadani, T. Saito, T. Mochida, T. Kitazawa, *Dalton Trans.*, **2010**, *39*, 1719.

[45] N. F. Sciortino, K. R. Scherl-Gruenwald, G. Chastanet, G. J. Halder, W. Chapman, J.-F. Létard

[46] , C. J. Kepert, *Angew. Chem. Int. Ed*., **2012**, *51*, 10154.

[47] M. Jansen, *Angew. Chem., Int. Ed. Engl*., **1987**, *26*, 1098.

3.8.- Supporting Information

Figure S1.- Thermogravimetric analysis of the clathrates **1**·nG and **2**·nG (G = furan, pyrrole and thiophene)

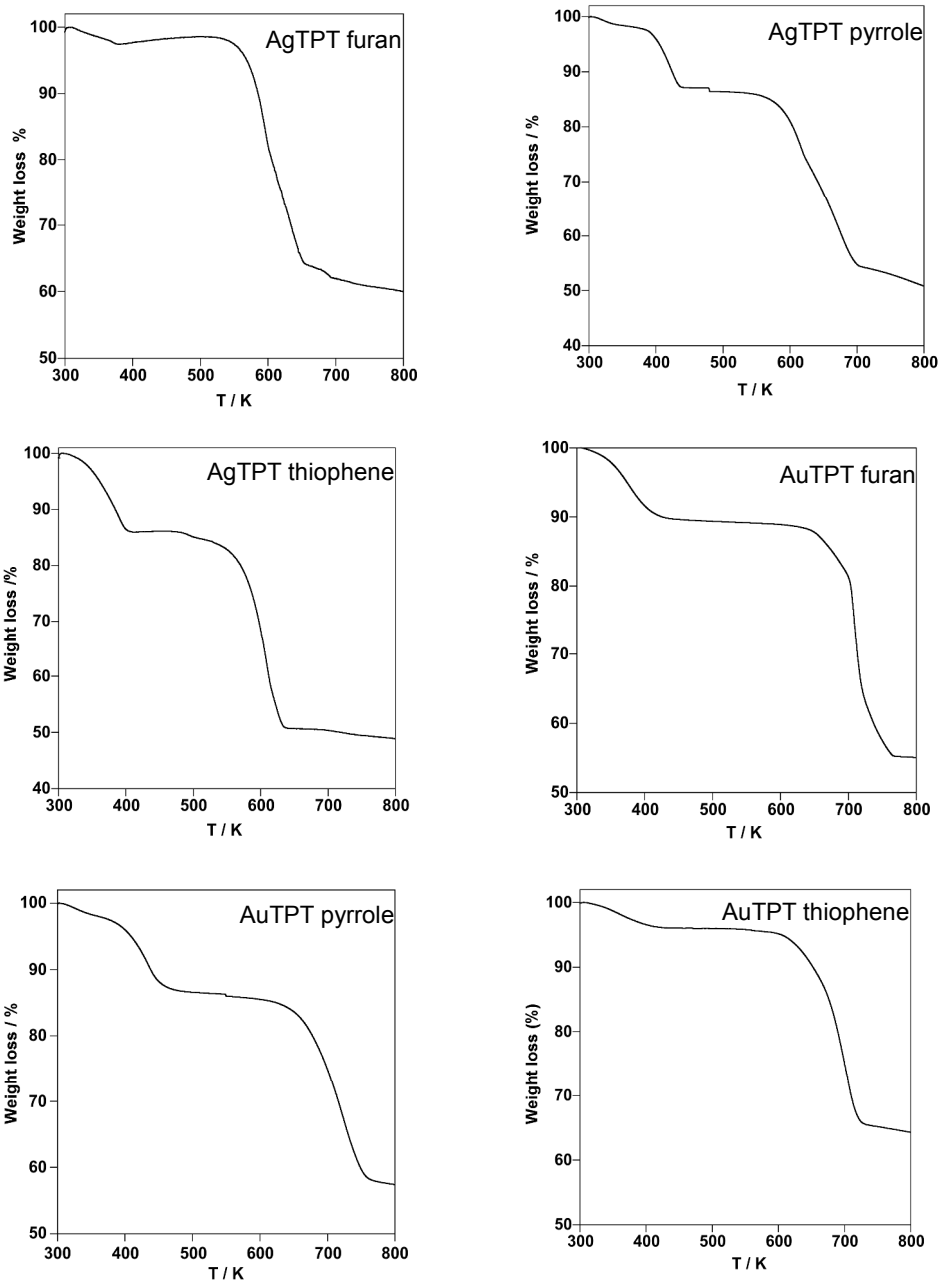

Figure S2.- ORTEP representation of the NbO structure defined by the Fe^{II}-$[M^{I}(CN)_2]^-$ moieties (120 K). Thermal ellipsoids are shown at 70% probability. Colour code: Fe, orange; Ag or Au, yellow; C, grey; N, blue.

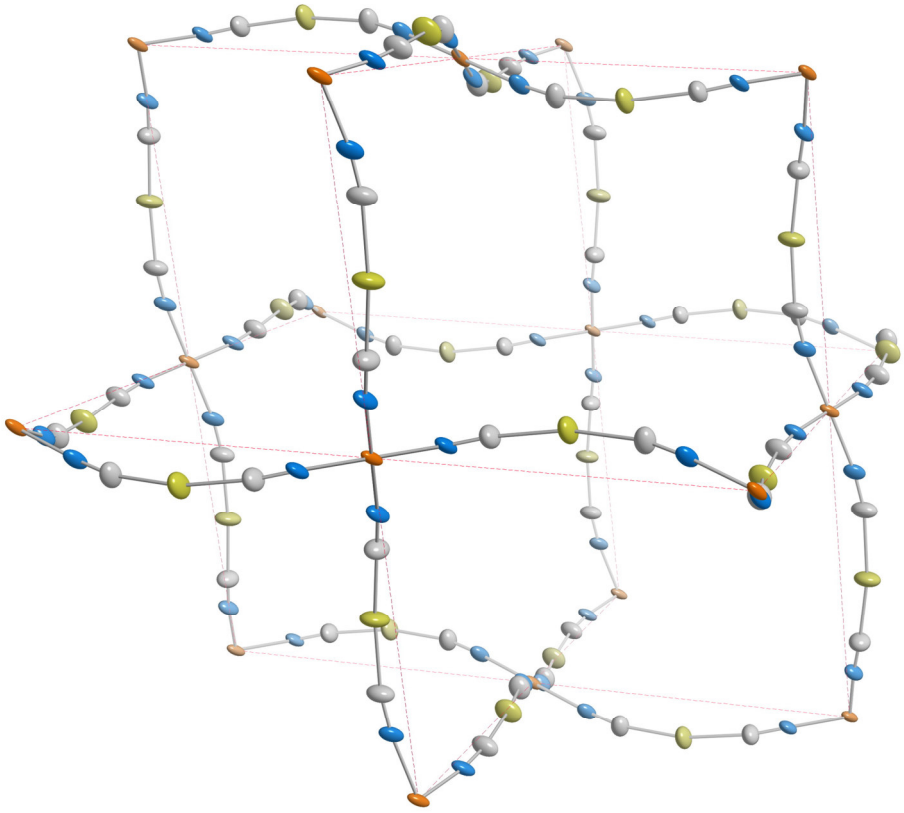

Figure S3.- Views in [001] (left) and [100] (right) directions of the pore where the guest molecules, furan or thiophene, are located: (a) **1**·0.5furan (120 K), and (b) **1**·1thiophene (120 K) (the atom numbering is the same as for **1**·1.5pyrrole in Figure 3). Colour code: Fe, orange; Ag, grey; C, black; N, blue; O, red; S, yellow.

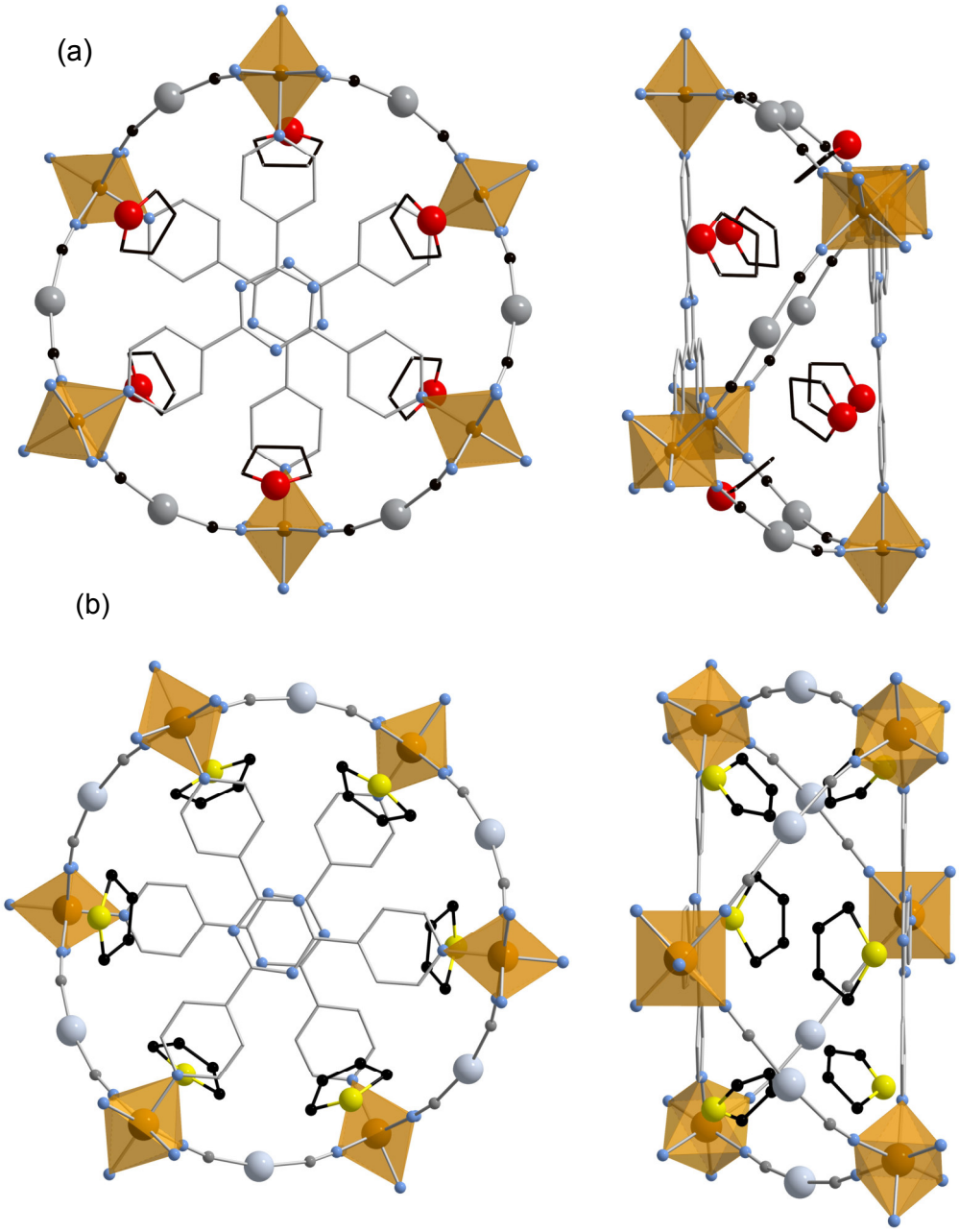

Figure S4.- Perspective views along [001] (left) and [100] (right) directions of the structures of {Fe(3-cyanopyridine)$_2$[M^{I}(CN)$_2$]$_2$} (a) and **1**·nG and **2**·nG (b) (only one of the three or two frameworks is shown, respectively). Note the different orientation of the [FeN$_6$] octahedrons (left) and the difference in the angles Fe-M-Fe (M = Ag, Au) defined by the two structures (right). Colour code: Fe, orange; M, grey; C, black; N, blue.

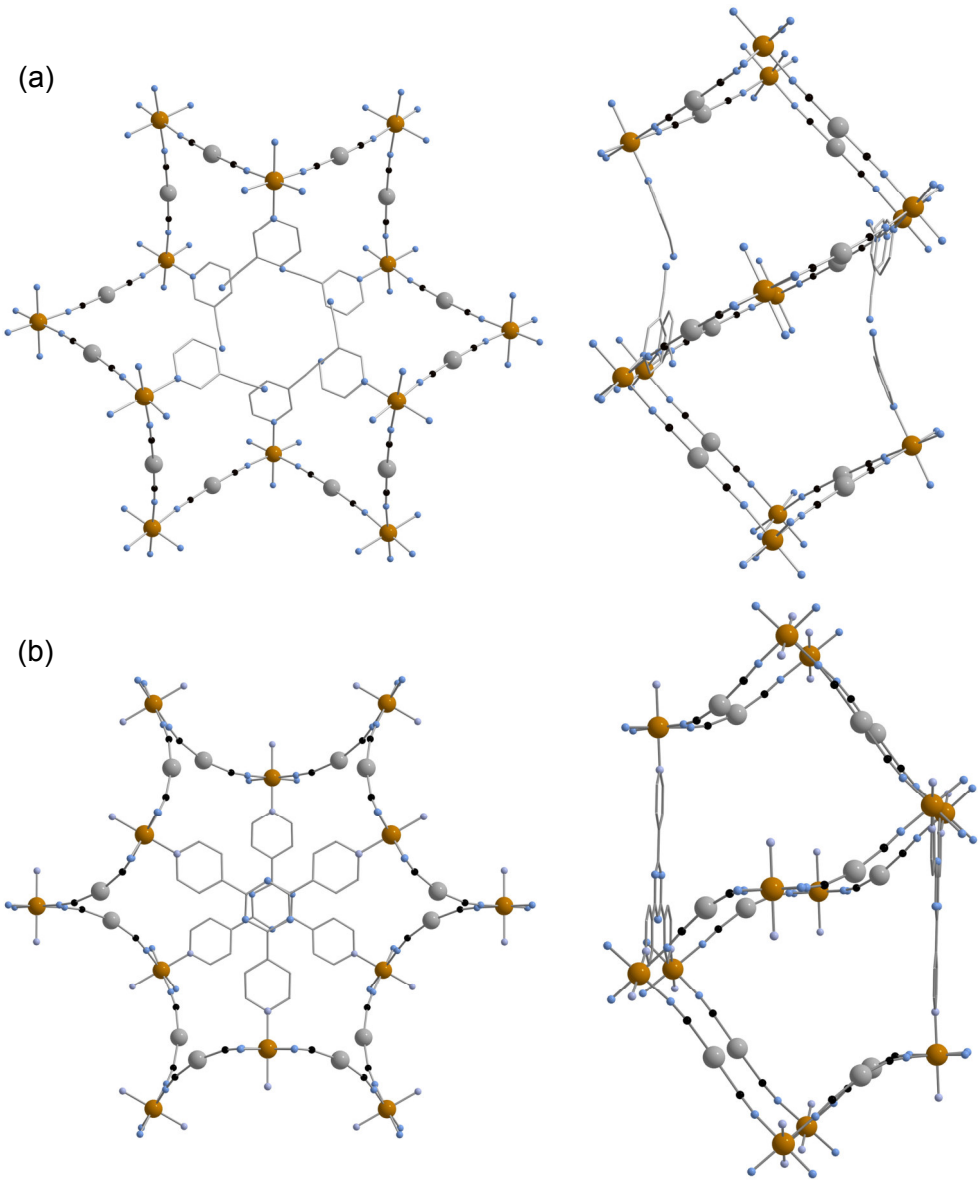

CAPÍTULO 4

Two- and one-step cooperative spin transitions in Hofmann-like clathrates with enhanced loading capacity

REVISTA: Chemical Communications

ÍNDICE DE IMPACTO: 6.567

CAPÍTULO 4

Two- and one-step cooperative spin transitions in Hofmann-like clathrates with enhanced loading capacity

4.1.- Abstract

Structural, magnetic, calorimetric and Mössbauer studies of the cooperative SCO naphthalene and nitrobenzene clathrates of the novel Fe^{II} Hofmann-like porous metal-organic framework {Fe(bpb)[Pt(CN)$_4$]}·2Guest are described (bpb = bis(4-pyridyl)butadiyne).

4.2.- Introduction

Porous 3D metal-organic frameworks (PMOFs) exhibit useful physical properties such as electrical and hydrogen conductivity,[1] storage,[2] luminescence,[3] catalysis[4] and separation.[5] PMOFs provide synthetic accessibility, chemical robustness and easy modification to meet particular practical demands. Furthermore, they can offer tunable physical properties if prepared from bistable building blocks. Indeed, in the case of PMOFs based on $3d^6$ Fe^{II} ions, the SCO phenomenon can be observed with reversible switch between the diamagnetic LS (LS, S = 0) and the paramagnetic HS (HS, S = 2) states involving magnetic, optical, and structural changes in response to the change of temperature, pressure, or light irradiation.[6] It is well known that SCO characteristics (critical temperature, abruptness, completeness) are related to the chemical nature of the ligands coordinated to the Fe^{II} ion, however, they are also greatly influenced by crystal packing effects, particularly, exerted by non-coordinated inclusions (anions, solvents and guest molecules).[7] Particularly, the sensitivity of SCO in Fe^{II} PMOFs toward the guest molecules confers sensory function to the materials and makes them attractive from the viewpoint of the possible practical application as sensors.

Cyanide-bridged Fe^{II}-M^{II} (M = Ni, Pd, Pt) bimetallic 3D networks, also known as Hofmann-like PMOFs, represent an example of materials with exceptionally abrupt hysteretic SCO and capability to sense guest molecules. Generically formulated {Fe(L)[M^{II}(CN)$_4$]}·G have been reported for L = pz,[8-10] azpy,[11] dpe,[12] bpe,[13] bpac,[14,15]

dpmse[16] or bpeben[17] (Scheme 1). These SCO-PMOFs possess both accessible voids responsible for the uptake of guest molecules by the framework and coordinatively unsaturated M^{II} centres that enable oxidative addition of halogens.[10] Further development of SCO-PMOFs is guided toward increasing the pore size and pore functionality. Here we report the synthesis and characterization of two Fe^{II} Hofmann-like 3D clathrates of the unprecedented SCO-PMOF $\{Fe(bpb)[Pt(CN)_4]\}\cdot 2G$ [G is naphthalene (**1**) or nitrobenzene (**2**)] based on the elongated ditopic ligand bis(4-pyridyl)butadiyne (bpb, Scheme 1). These clathrates exhibit cooperative SCO and, to the best of our knowledge, this new MOF system shows the highest load capacity reported up to now.

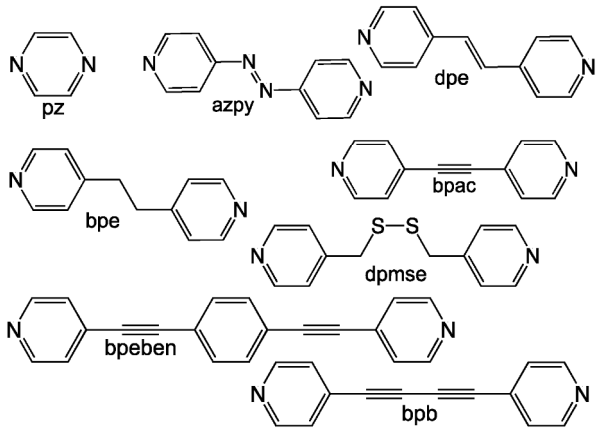

Scheme 1.- Pillar ligands for $\{Fe(L)[M^{II}(CN)_4]\}\cdot G$ Hofmann-like PMOFs.

4.3.- Results and discussion

4.3.1.- Synthesis

Both clathrates were synthesized by slow diffusion in multiarm-shaped vessels (see synthesis and Figure S1 and S2 in the Supporting Information).

4.3.2.- Structure

Both clathrates are isostructural and adopt the general topology of 3D {FeL[$M^{II}(CN)_4$]} PMOFs consisting of infinite 2D {Fe[$Pt(CN)_4$]}$_\infty$ layers bridged by pillaring ligands through axially coordinated Fe^{II} ions (Figure 1). However, in contrast to the rest of the members of the {FeL[$M^{II}(CN)_4$]} series, **1** and **2** crystallize in the triclinic *P-1* space group.

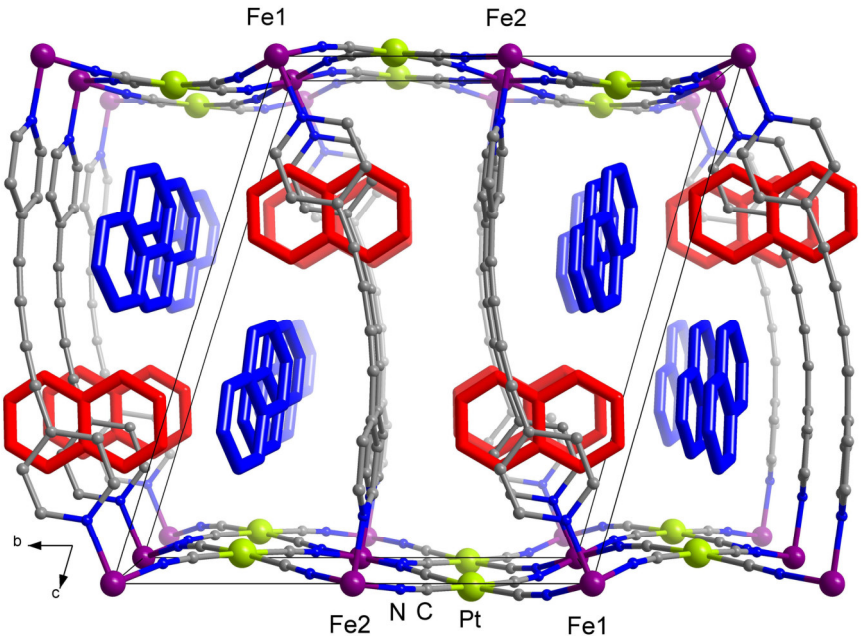

Figure 1.- Projection of the structure of **1** along *a*. Two types of guest naphthalene molecules are coloured in red and blue.

The crystallographic parameters for both compounds are collected in Table S1 (Supporting Information), and selected angles and distances in Tables S2 and S3 (Supporting Information). The ligand bpb adopts a markedly bent conformation in contrast to other unsaturated bridging ligands mentioned above and, additionally, the pyridine moieties locate practically perpendicular to each other. Similar geometries were observed in the triply interlocked catenane SCO [$Fe(bpb)_2(NCS)_2$]·1/2MeOH complex.[18] Due to the curvature shown by the bpb ligand, the axially elongated [FeN_6] octahedrons are alternatively tilted, within the *bc* plane, in opposite directions, thereby conferring to the {Fe[$Pt(CN)_4$]}$_\infty$ layers a corrugated geometry.

Two guest molecules per unit cell are found in **1** and **2**. One is located half-way between the pyridine rings of the bpb ligand, which coordinate to Fe(1), while the second lies closer to the pyridine ring coordinated to Fe(2) (see Figure 1 and Figure S3 in the Supporting Information). There are numerous C···C contacts between the guest molecules and the pyridine rings changing with temperature according to expansion/contraction of the lattice due to the SCO of the Fe^{II} ions (Table S4 in the Supporting Information). These contacts influence the coordination spheres of the two Fe^{II} ions in a different way. Indeed, the averaged bond length <Fe-N> (*vide infra*) is slightly different for Fe(1) and Fe(2). In the case of **1**, <Fe(1)-N> changes from 2.13(2) Å at 250 K to 1.957(2) Å at 195 K and further remains constant upon cooling to 120 K (1.959(5) Å) where the complete transition to the LS state takes place. At 250 K, the value for <Fe(2)-N> is 2.14(2) Å and does not vary much upon cooling to 195 K (2.160(2) Å), but decreases to 1.966(5) Å at 120 K. Evidently, Fe(1) undergoes transition above 195 K, while Fe(2) undergoes transition below this temperature. In the case of **2**, <Fe(1)-N> changes from 2.175(12) Å at 250 K to 1.955(5) Å at 120 K and <Fe(2)-N> from 2.175(11) Å at 250 K to 1.956(5) Å at 120 K. The transition of both Fe^{II} ions takes place simultaneously.

There are two different types of pores running, respectively, along *a* and *b* axes hosting the guest molecules. The pores running along *a* are much wider than those running along *b* due to the bent shape of bpb. The cross-section of the expanded pores, defined by Fe···Fe distances through the bent bpb ligand and the corrugated $[Pt(CN)_4]^{2-}$ anions, shows ca. 15.87(1) Å x 6.98(1) Å at 120 K. The accessible volume[19] of the frameworks **1** (**2**) (without considering guest molecules) is 849.6 (801.8) $Å^3$ and corresponds to 53.8% (52.6%) of the unit cell volume at 120 K (1579.2 $Å^3$ (**1**) and 1523.3 $Å^3$ (**2**)). The porosity of the frameworks in **1** and **2** is larger in comparison with that found for SCO clathrates {FeL[$Pt(CN)_4$]}, which is 22% for pz, ca. 40% for azpy,[11] dpe[12] and bpac[15] and 48% for bpeben.[17]

4.3.3.- Magnetic and calorimetric properties

Figure 2 displays the magnetic and calorimetric properties of **1** and **2**. At 300 K, the $\chi_M T$ product (χ_M is the molar magnetic susceptibility and T is the temperature) is ca. 3.5-3.6 cm^3 K mol^{-1} and remains constant until approaching the SCO transition. In the case of **1**, the Fe^{II} ions undergo spin transition in two equal steps. The critical

temperatures are $T_{c1}^{\downarrow} = 205$ K and $T_{c2}^{\downarrow} = 188$ K in the cooling mode. In the heating mode the steps appear at higher temperatures, $T_{c2}^{\uparrow} = 203$ K and $T_{c1}^{\uparrow} = 216$ K, thereby defining two hysteresis loops 11 K (ΔT_{c1}) and 15 K (ΔT_{c2}) wide. In **2**, the transition takes place in one step at $T_c^{\downarrow} = 210$ K and $T_c^{\uparrow} = 237$ K with the hysteresis loop of 27 K. In the low temperature region the $\chi_M T$ values are near to zero.

The calorimetric measurements performed on samples of **1** and **2** and the anomalous heat capacity ΔCp vs. T are shown in Figure 2. The ΔH and ΔS average variations associated with the spin transitions are: ΔH = 9.45 kJ mol^{-1} and ΔS = 44.9 J K^{-1} mol^{-1} for the high temperature hysteresis loop and ΔH = 8.62 kJ mol^{-1} and ΔS = 44.1 J K^{-1} mol^{-1} for the low temperature hysteresis loop of **1**; ΔH = 19.29 kJ mol^{-1} and ΔS = 86.3 J K^{-1} mol^{-1} for **2**. These values are typical for cooperative SCO in Hofmann-like clathrates of Fe^{II}.[6c]

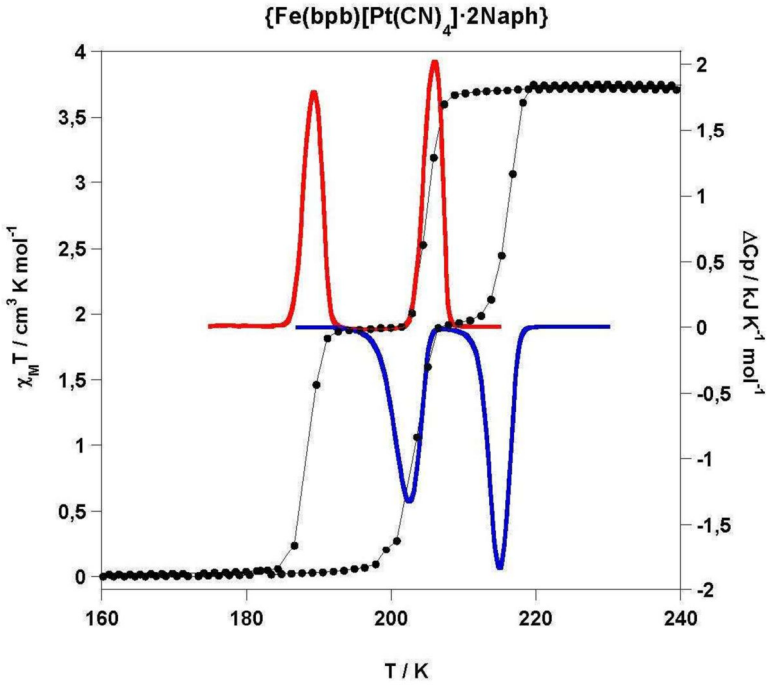

Figure 2.- Magnetic (filled circles) and calorimetric (blue and red lines refer to cooling and heating modes, respectively) measurements for **1**.

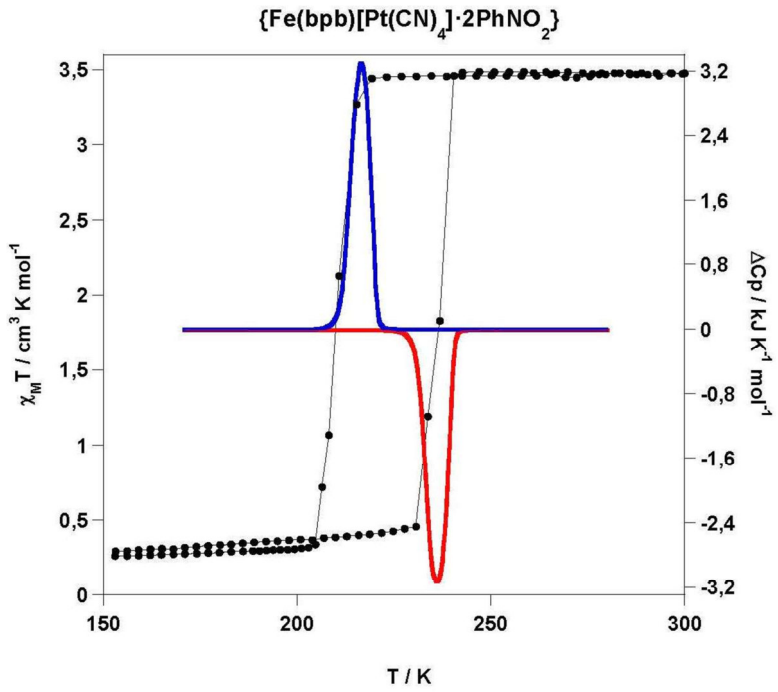

Figure 2 cont.- Magnetic (filled circles) and calorimetric (blue and red lines refer to cooling and heating modes, respectively) measurements for **2**.

4.3.4.- Mössbauer spectra

The Mössbauer spectrum of **1** at 80 K consists of two LS doublets with almost identical isomer shift values (δ^{LS1} = 0.47(2) mm s^{-1} and δ^{LS2} = 0.49(2) mm s^{-1}) and different quadrupole splitting parameters ΔE_Q^{LS1} = 0.32(1) mm s^{-1} and ΔE_Q^{LS2} = 0.16(2) mm s^{-1}) (Figura 3, left). The relative areas *A* of the two doublets have a ratio close to 1:1. Evidently, the doublets correspond to two different Fe^{II} sites observed in the crystal lattice of the compound. Upon increasing the temperature to 199 K and according to the transition of one of the Fe^{II}-sites to the HS state, the spectrum shows disappearance of a LS doublet and instead a HS doublet is detected (δ^{HS} = 1.11(2) mm s^{-1} and ΔE_Q^{HS} = 1.53(4) mm s^{-1}). The parameters of the second LS doublet remain almost unchanged at this temperature (δ^{LS} = 0.47(1) mm s^{-1} and ΔE_Q^{LS} = 0.14(3) mm s^{-1}). Upon heating to 300 K, the spectrum of **1** shows two overlapping equally populated HS doublets with similar isomer shift values (δ^{LS1} = 1.05(1) mm s^{-1} and δ^{HS2} = 1.06(1) mm s^{-1}) and strongly different quadrupole splitting parameters (ΔE_Q^{HS1} = 0.51(2) mm s^{-1} and ΔE_Q^{HS2} = 1.21(2)

mm s^{-1}). The ΔE_Q values reflect different geometric distortion of the corresponding coordination polyhedrons. The spectra of **2** recorded at 80 and 300 K in the LS and HS states, respectively, are very similar to those of **1** at the same temperatures (Figure 3, right; Table S6 in the Supporting Information).

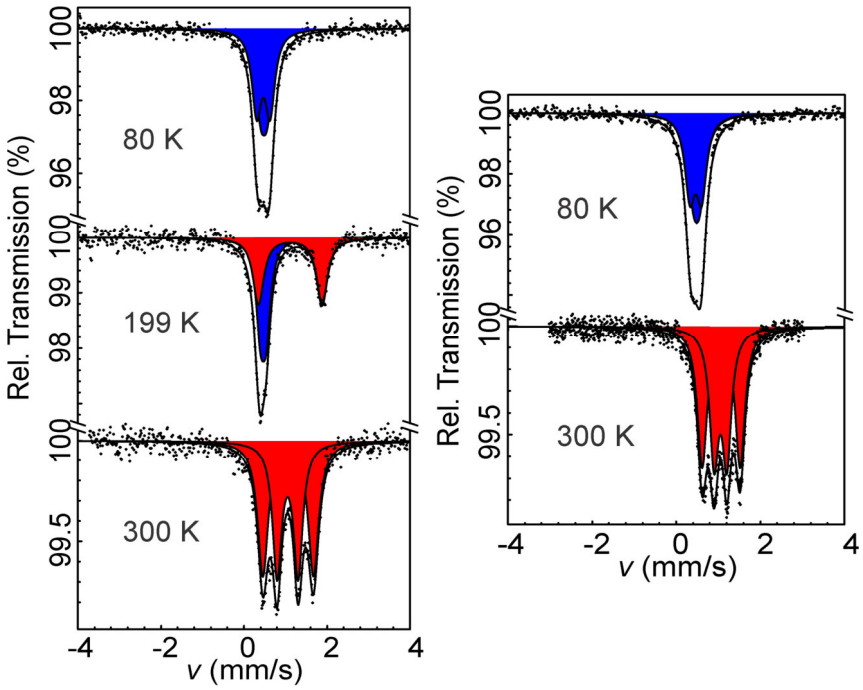

Figure 3.- Mössbauer spectra of **1** (left) and **2** (right). Red and blue colours represent the HS and LS components of the spectra.

4.4.- Conclusion

In conclusion we have reported the synthesis, structure, spectroscopic, magnetic and calorimetric characterization of a new type of Hofmann-like SCO-MOFs exhibiting large thermal hysteresis and the largest effective porosity among Hofmann-like SCO-PMOF reported up to now. The host framework {Fe(bpb)[$Pt(CN)_4$]} displays distinct magnetic behaviour depending on the nature of the guest molecule enclathrated in the pores (naphthalene or nitrobenzene), a fact which in principle confers to the host system

a sensory function. Extended studies of the structure-property relationship of these materials are in progress.

4.5.- Notes and references

[1] a) M. Yoon, K. Suh, S. Natarajan, K. Kim, *Angew. Chem. Int. Ed.*, **2013**, *52*, 2688; b) A. Morozan, F. Jaouen, *Energy Environ. Sci.*, **2012**, *5*, 9269.

[2] a) M. P. Suh, H. J. Park, T. K. Prasad, D.-W. Lim, *Chem. Rev.*, **2012**, *112*, 782; b) T. A. Makal, J.-R. Li, W. Lu, H.-C. Zhou, *Chem. Soc. Rev.*, **2012**, *41*, 7761.

[3] J. Rocha, L. D. Carlos, F. A. A. Paz, D. Ananias, *Chem. Soc. Rev.*, **2011**, *40*, 926.

[4] a) M. Yoon, R. Srirambalaji, K. Kim, *Chem. Rev.*, **2012**, *112*, 1196; b) L. Ma, W. Lin, *Top. Curr. Chem.*, **2010**, *293*, 175.

[5] a) Y. Yu, Y. Ren, W. Shen, H. Deng, Z. Gao, *TrAC, Trends Anal. Chem.*, **2013**, *50*, 33; b) J.-R. Li, J. Sculley, H.-C. Zhou, *Chem. Rev.*, **2012**, *112*, 869.

[6] a) P. Gütlich, G. Goodwin, *Top. Curr. Chem.*, **2004**, *233*; b) A. B. Gaspar, V. Ksenofontov, M. Seredyuk, P. Gütlich, *Coord. Chem. Rev.*, **2005**, *249*, 2661; c) M. C. Muñoz, J. A. Real, *Coord. Chem. Rev.*, **2011**, *255*, 2068; d) M. A. Halcrow, *John Wiley & Sons Ltd*, **2013**.

[7] P. Gütlich, H. A. Goodwin, *Top. Curr. Chem.,* **2004**, *233*, 1.

[8] V. Niel, J. M. Martínez-Agudo, M. C. Muñoz, A. B. Gaspar, J. A. Real, *Inorg. Chem.*, **2001**, *40*, 3838.

[9] a) M. Ohba, K. Yoneda, G. Agustí, M. C. Muñoz, A. B. Gaspar, J. A. Real, M. Yamasaki, H. Ando, Y. Nakao, S. Sakaki, S. Kitagawa, *Angew. Chem. Int. Ed.*, **2009**, *48*, 4767; b) P. D. Southon, L. Liu, E. A. Fellows, D. J. Price, G. J. Halder, K. W. Chapman, B. Moubaraki, K. S. Murray, J.-F. Letard, C. J. Kepert, *J. Am. Chem. Soc.*, **2009**, *130*, 10998.

[10] G. Agustí, R. Ohtani, K. Yoneda, A. B. Gaspar, M. Ohba, J. F. Sanchez-Royo, M. C. Muñoz, S. Kitagawa, J. A. Real, *Angew. Chem., Int. Ed.*, **2009**, *48,* 8944.

[11] G. Agustí, S. Cobo, A. B. Gaspar, G. Molnár, N. O. Moussa, P. A. Szilagyi, V. Palfi, C. Vieu, M. C. Muñoz, J. A. Real, A. Bousseksou, *Chem. Mater.*, **2008**, *20*, 6721.

[12] F. J. Muñoz-Lara, A. B. Gaspar, M. C. Muñoz, M. Arai, S. Kitagawa, M. Ohba, J. A. Real, *Chem.-Eur. J.*, **2012**, *18*, 8013.

[13] R. Ohtani, M. Arai, A. Hori, M. Takata, S. Kitao, M. Seto, S. Kitagawa, M. Ohba, *J. Inorg. Organomet. Polym. Mater.*, **2013**, *23*, 104.

[14] C. Bartual-Murgui, L. Salmon, A. Akou, N. A. Ortega-Villar, H. J. Shepherd, M. C. Muñoz, G. Molnár, J. A. Real, A. Bousseksou, *Chem.-Eur. J*, **2012**, *18*, 507.

[15] C. Bartual-Murgui, N. A. Ortega-Villar, H. J. Shepherd, M. C. Muñoz, L. Salmon, G. Molnár, A. Bousseksou, J. A. Real, *J. Mater. Chem.*, **2011**, *21*, 7217.

[16] N. F. Sciortino, K. R. Scherl-Gruenwald, G. Chastanet, G. J. Halder, K. W. Chapman, J.-F. Létard, C. J. Kepert, *Angew. Chem., Int. Ed.*, **2012**, *51*, 10154.

[17] F. J. Muñoz-Lara, A. B. Gaspar, M. C. Muñoz, V. Ksenofontov, J. A. Real, *Inorg. Chem.*, **2012**, *52*, 3.

[18] N. Moliner, C. Muñoz, S. Létard, X. Solans, N. Menéndez, A. Goujon, F. Varret, J. A. Real, *Inorg. Chem.*, **2000**, *39*, 5390.

[19] A. Spek, *Acta Crystallogr. Sect. D: Biol. Crystallogr.*, **2009**, *65*, 148.

4.6.- Supporting Information

4.6.1.- Synthesis.

All chemicals were purchased from commercial suppliers and used without further purification.

Synthesis of bis(4-pyridyl)butadiyne (bpb). To a solution of CuCl (130 mg, 0.96 mmol) in pyridine (2-3 mL) under oxygen atmosphere was added 4-ethynylpyridine (600 mg, 5.81 mmol) with stirring and heated at 40-45 °C for 2 h. The pyridine was removed at reduced pressure and the residual solid was washed with an aqueous solution of ammonium chloride (30 mL, 10%) and dissolved in chloroform. The organic layer was dried over $MgSO_4$, filtered and dried giving bpb as lustrous dirty plates. The compound was purified by recrystallization from hot ethyl acetate to give yellowish lustrous plates (312 mg, 53%). ^{1}H NMR (300 MHz, $CDCl_3$): δ 8.56 (4H, m, $pyH^{2,6}$), 7.64 (4H, m, $pyH^{3,5}$); ^{13}C NMR (100 MHz, $CDCl_3$): δ 148.7, 128.6, 125.1, 79.2, 76.3. Elemental analysis calcd (%) for $C_{14}H_8N_2$: C, 82.33; H, 3.95; N, 13.72; found C, 82.53, H, 4.05, N, 13.69.

Synthesis of {[Fe(bpb)Pt(CN)$_4$]·2G} [G = naphthalene (1), nitrobenzene (2)]. Single crystals of **1** and **2** were grown using a slow diffusion technique. One side of a multi-arm shaped vessel contains $(NH_4)_2Fe(SO_4)_2\cdot 6H_2O$ (20 mg, 51 mmol) dissolved in water (0.5 mL). The contiguous arm contains solid bpb (11 mg, 49 mmol) and guest (50 mg), and the third arm contains $K_2Pt(CN)_4\cdot 3H_2O$ (22 mg, 51 mmol) in water (0.5 mL). The vessel was filled with a water-methanol (1:1) solution. Square shaped yellow (**1**) and brown (**2**) crystals suitable for single crystal X-ray analysis were obtained after 6 weeks. Elemental analysis calcd (%) for **1** ($C_{38}H_{24}FeN_6Pt$): C, 55.96; H, 2.97; N, 10.30; found C, 55.59; H, 10.26; N, 3.10. EDAX calc. for **1**: Fe, 50.00; Pt, 50.00; found: Fe, 51.32; Pt, 48.68. Elemental analysis calcd (%) for **2** ($C_{30}H_{18}FeN_8O_4Pt$): C, 44.74; H, 2.25; N, 13.91; found C, 44.62; H, 1.92; N, 14.37. EDAX calc. for **2**: Fe, 50.00; Pt, 50.00; found: Fe, 48.76; Pt, 51.14.

4.6.2.- Physical characterization

4.6.2.1.- Thermogravimetric analysis

The TGA of **1** and **2** display two well defined loss of weight. The former at lower temperatures occurs in both compounds between ca. 415 K and 550 K and corresponds to the loss of two molecules of naphthalene or nitrobenzene. The second loss of weight taking place in the interval 625-840 K corresponds to the decomposition of the framework (see Figure 1 below).

Figure S1.- TGA of compounds **1** (left) and **2** (right).

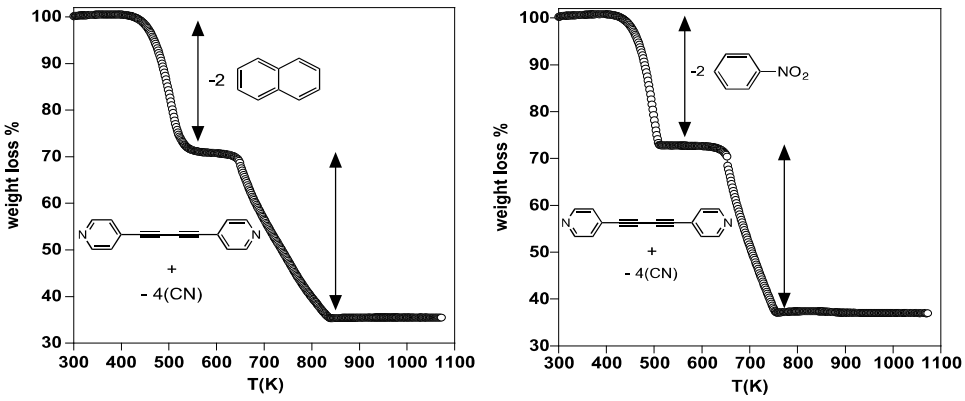

*4.6.2.2.- Infra-red spectra of **1** and **2***

The infrared spectra of **1** and **2** shown in Figures S2a and S2b, respectively clearly display the most characteristic features of both derivatives:

Compound 1: ν(CNcyanide) = 2161.2 cm^{-1} (vs); ν(C=Npyridine) = 1602.0 cm^{-1} (s); ν(pyridine ring) = 1418.7 cm^{-1} (m); ν(pyridine ring) = 819.9 cm^{-1} (s); ν(naphthalene rings) = 781.8 cm^{-1} (vs); ν(naphthalene rings) = 541.6 cm^{-1} (s); ν(Pt-CN) = 475.3 cm^{-1} (s) (Figure S1a) (vs = very strong, s = strong, m = medium, w = weak).

Compound 2: ν(CNcyanide) = 2166.8 cm^{-1} (vs); ν(C=Npyridine) = 1602.6 cm^{-1} (s); ν(pyridine ring) = 1420.4 cm^{-1} (m); $\nu_{as}(NO_2)$ = 1522.7 cm^{-1} (vs); $\nu_s(NO_2)$ = 1346.1 cm^{-1} (vs); ν(pyridine ring) = 852.8 (w), 829.3 (s), 793 (s) cm^{-1}; ν ($C_6H_5NO_2$) = 704.6 cm^{-1} (s);

ν(Pt-CN) = 466.7 cm^{-1} (m) (Figure S1b) (vs = very strong, s = strong, m = medium, w = weak).

Figure S2.- Infrared spectra of compound **1** (a).

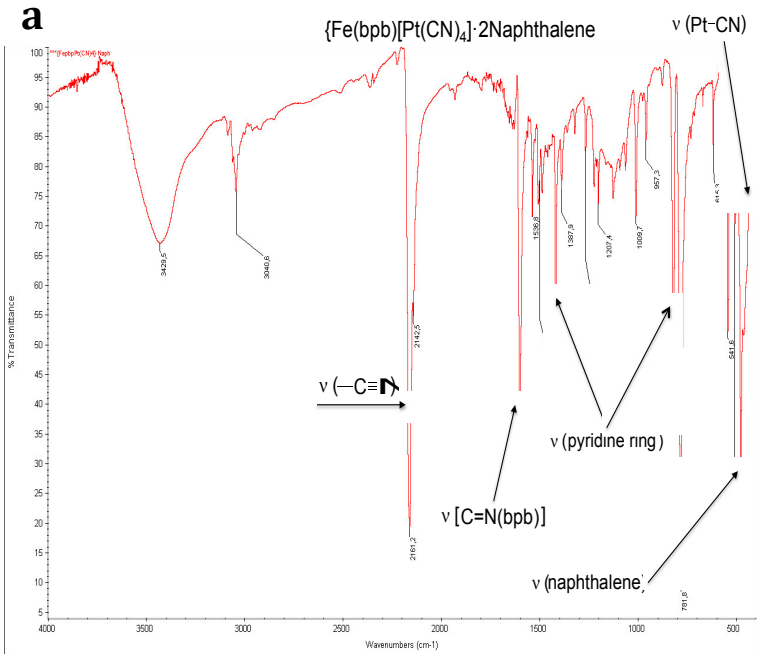

Figure S2 cont.- Infrared spectra of compound **2** (b)

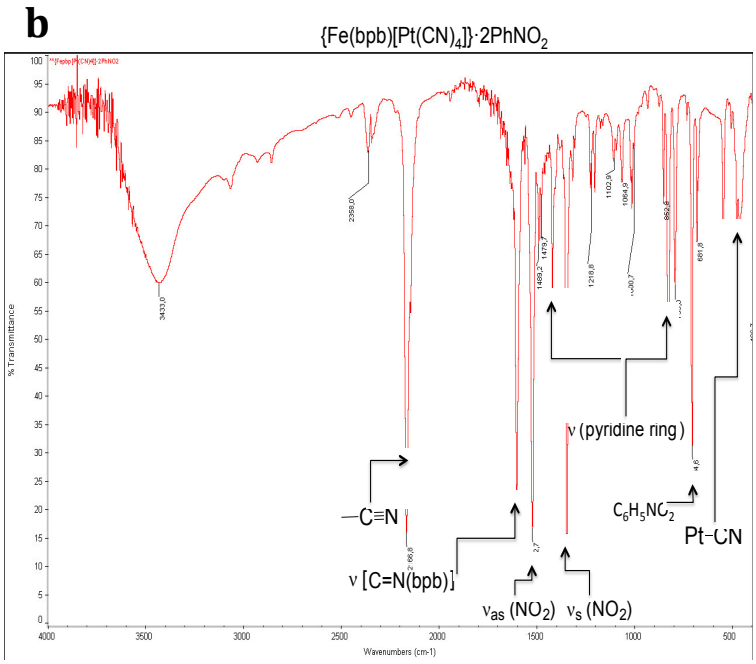

*4.6.2.3.- Variable-temperature magnetic measurements of **1** and **2***

Variable-temperature magnetic susceptibility data were recorded on samples of **1** and **2** constituted of single crystals (10-15 mg) with a Quantum Design MPMS2 SQUID susceptometer equipped with a 7 T magnet, operating at 1 T and at temperatures 10-400 K. Experimental susceptibilities were corrected for diamagnetism of the constituent atoms by the use of Pascal's constants. TGA measurements were performed on a Mettler Toledo TGA/SDTA 851e, in the 150-400 K temperature range under a nitrogen atmosphere with a rate of 10 K min^{-1}. The thermodynamic parameters were analyzed with Netzsch Proteus software (Netzsch-Geraetebau GMBH). Analysis for C, H, and N were performed after combustion at 850 °C using IR detection and gravimetry by means of a Perkin-Elmer 2400 series II device. ^{1}H and ^{13}C NMR spectroscopic measurements were done on an Advance DRX Bruker 300 MHz Spectrometer. IR spectra were recorded at 293 K by using a Nicolet 5700 FTIR spectrometer with the samples prepared as KBr discs.

*4.6.2.4.- Single crystal X-ray diffraction measurements over **1** and **2***

Single-crystal X-ray data of **1** and **2** were collected on a Nonius Kappa-CCD single crystal diffractometer using graphite mono-chromated MoKα radiation (λ = 0.71073 Å). A multi-scan absorption correction was performed. The structures were solved by direct methods using SHELXS-97 and refined by full-matrix least squares on F^2 using SHELXL-97.[1] Non-hydrogen atoms were refined anisotropically and hydrogen atoms were placed in calculated positions refined using idealized geometries (riding model) and assigned fixed isotropic displacement parameters for **1** (120-250 K) and **2** (120 K). For compound **2** at 250 K only Fe and Pt atoms could be anisotropically refined. In general the crystals deteriorate as a consequence of the phase transition associated with the spin crossover transition. This is particularly more marked for compound **2** because the quality of the single crystals was systematically low. CCDC files 971021-971025 contain the supplementary crystallographic data for **1** (120 K), **1** (195 K), **1** (250 K), **2** (120 K) and **2** (250 K), respectively. These data can be obtained free of charge from The Cambridge Crystallographic Data Centre via www.ccdc.cam.ac.uk/data_request/cif.

Table S1.- Crystal data of compounds **1** and **2**.

	1			**2**	
Temperature (K)	120(1)	195(1)	250(1)	120(1)	250(1)
Empirical formula	$C_{38}H_{24}N_6PtFe$			$C_{30}H_{18}N_8O_4PtFe$	
Mr	815.57			805.46	
Crystal system	triclinic			triclinic	
Space group	*P*-1			*P*-1	
a (Å)	7.2452(2)	7.3635(2)	7.5174(2)	7.2443(4)	7.4872(7)
b (Å)	13.9706(5)	14.1112(4)	14.3676(7)	13.8127(8)	14.3024(7)
c (Å)	16.3779(7)	16.3906(5)	16.350(2)	15.4746(9)	15.0203(15)
α (°)	73.531(3)	74.663(3)	76.831(8)	80.352(5)	86.393(6)
β (°)	83.678(3)	82.349(2)	84.282(6)	87.669(5)	84.502(8)
γ (°)	89.998(3)	89.878(2)	89.965(3)	89.842(5)	89.936(5)
V (Å^3)	1579.24(10)	1626.86(8)	1710.5(3)	1525.26(15)	1597.9(2)
Z	2			2	
D_c (mg cm^{-3})	1.715	1.665	1.584	1.754	1.674
F(000)	796			780	
μ (Mo-K$_\alpha$)(mm^{-1})	4.921	4.777	4.544	5.105	4.873
Crystal size (mm)	0.08 x 0.12 x 0.12			0.06 x 0.08 x 0.08	
No. of total reflections	10484	10926	7909	8234	8591
No. of reflections [$I>2\sigma(I)$]	9658	9980	6281	7033	6945
R_1 [$I>2\sigma(I)$]	0.0505	0.0239	0.0921	0.0511	0.0955
R_1 [all data]	0.0553	0.0289	0.1160	0.0635	0.1249
S	1.002	0.902	1.061	1.072	1.161

$R_1 = \Sigma \, ||Fo| - |Fc|| \, / \, \Sigma \, |Fo|$; $\omega R = [\, \Sigma \, [\omega(Fo^2 - Fc^2)^2] \, / \, \Sigma \, [\omega(Fo^2)^2]]^{1/2}$.
$\omega = 1/ \, [\sigma^2(Fo^2) + (m \, P)^2 + n \, P]$ where $P = (Fo^2 + 2Fc^2) \, / \, 3$;
m = 0.0656 (**1** (**120 K**)), 0.0273 (**1** (**195 K**)), 0.1516 (**1** (**250 K**)), 0.0580 (**2 (120 K)**) and 0.0621 (**2 (250 K)**);
n = 23.2445 (**1** (**120 K**)), 1.3390 (**1** (**195 K**)), 49.4900 (**1** (**250 K**)), 4.6644 (**2 (120 K)**) and 0.0000 (**2 (250 K)**).

Table S2.- Selected bond lengths [Å] and angles [°] for **1**.

120 K	**195 K**	**250 K**	
Fe(1)-N(1)	2.001(5)	2.000(2)	2.19(2)
Fe(1)-N(2)	1.934(4)	1.935(2)	2.10(2)
Fe(1)-N(6)	1.944(4)	1.938(2)	2.11(2)
Fe(2)-N(3)	1.935(4)	2.124(2)	2.13(2)
Fe(2)-N(4)	1.938(4)	2.127(2)	2.11(2)
Fe(2)-N(5)	1.996(5)	2.229(2)	2.19(2)
N(1)-Fe(1)-N(2)	88.2(2)	88.62(8)	87.8(7)
N(1)-Fe(1)-N(6)	88.2(2)	88.33(8)	87.8(6)
N(2)-Fe(1)-N(6)	90.9(2)	92.13(8)	91.4(6)
N(3)-Fe(2)-N(4)	90.5(2)	90.05(8)	91.2(6)
N(3)-Fe(2)-N(5)	90.7(2)	89.60(8)	87.7(8)
N(4)-Fe(2)-N(5)	88.8(2)	88.99(8)	86.7(8)

Table S3.- Selected bond lengths [Å] and angles [°] for **2**.

	120 K	**250 K**
Fe(1)-N(1)	2.000(5)	2.199(12)
Fe(1)-N(2)	1.933(5)	2.167(12)
Fe(1)-N(6)	1.934(5)	2.141(12)
Fe(2)-N(3)	1.934(5)	2.161(12)
Fe(2)-N(4)	1.937(5)	2.144(13)
Fe(2)-N(5)	1.997(6)	2.232(15)
N(1)-Fe(1)-N(2)	88.4(2)	89.0(4)
N(1)-Fe(1)-N(6)	88.2(2)	88.4(4)
N(2)-Fe(1)-N(6)	91.1(2)	90.7(5)
N(3)-Fe(2)-N(4)	89.7(2)	89.2(5)
N(3)-Fe(2)-N(5)	89.2(2)	89.3(5)
N(4)-Fe(2)-N(5)	89.8(2)	89.8(5)

Table S4.- Short contacts between invited molecules and bpb in **1**.

	C atoms	Distance C···C/Å		
		120 K (LS-LS)	**195 K** (LS-HS)	**250 K** (HS-HS)
bpb···naph 1 (blue)	C(19)···C(13)	-	3.624(7)	-
	C(23)···C(13)	-	-	3.656(4)
	C(24)···C(13)	3.553(10)	-	
	C(24)···C(14)	3.499(11)	-	3.667(4)
	C(25)···C(12)	3.546(11)	-	
	C(25)···C(13)	3.560(12)	-	3.697(5)
	C(25)···C(14)	3.646(13)	-	
	C(26)···C(1) (T-Shaped)	3.670(11)	-	-
	C(26)···C(14)	-	3.628(6)	-
	C(2)···C(30)	-	-	3.609(5)
bpb···naph 2 (red)	C(2)···C(31)		3.510(10)	3.545(5)
	C(1)···C(32)	-	3.620(10)	3.546(4)
	C(2)···C(32)	-	3.519(5)	3.655(6)
	C(1)···C(33)		-	3.572(4)
	C(3)···C(34)	3.589(11)	-	3.698(5)
	C(4)···C(35)	3.491(12)	-	
	C(4)···C(36)	3.482(13)	-	-

Table S5.- Short contacts between invited molecules and bpb in **2**.

	C atoms	Distance C···C/Å	
		120 K (LS)	**250 K (HS)**
bpb···phNO$_2$ 1 (blue)	C(1)···C(23)	3.657(12)	-
	C(13)···C(19)	3.646(12)	-
bpb···PhNO$_2$ 2 (red)	C(1)···C(23)	3.657(12)	-
	C(13)···C(19)	3.646(12)	-
	C(13)···C(27)	3.685(11)	-
	C(13)···C(28)	-	3.567(38)
	C(14)···C(28)	3.693(11)	-
	C(11)···C(29)	3.527(12)	3.518(38)

Table S6.- Mössbauer parameters, isomer shift (δ, relative to -iron), quadrupole splitting (ΔE_Q), half-width of the lines ($\Gamma_{1/2}$) and percentage of the multiplet populations in the HS and LS states (A) at different temperatures for **1** and **2**.

Compound	T/K	Doublet	δ/mm s^{-1}	ΔE_Q /mm s^{-1}	$\Gamma_{1/2}$/mm s^{-1}	A%
1	80	LS1	0.47(2)	0.32(1)	0.14(6)	50.0(1)
		LS2	0.49(2)	0.16(2)	0.16(7)	50.0(1)
	199	LS	0.47(1)	0.14(3)	0.13(2)	49.5(3)
		HS	1.11(2)	1.53(4)	0.16(2)	50.5(5)
	300	HS1	1.05(1)	0.51(2)	0.13(1)	45.9(3)
		HS2	1.06(1)	1.21(2)	0.15(1)	54.1(4)
2	80	LS1	0.47(1)	0.15(2)	0.12(2)	47.0(2)
		LS2	0.46(1)	0.33(3)	0.15(1)	53.0(2)
	300	HS1	1.07(1)	0.90(1)	0.14(1)	54.1(4)
		HS2	1.05(1)	0.30(1)	0.12(1)	45.9(3)

Figure S3.- Projection of the crystal structure of **2** along *a* axis. Two types of invited nitrobenzene molecules are coloured in red and blue.

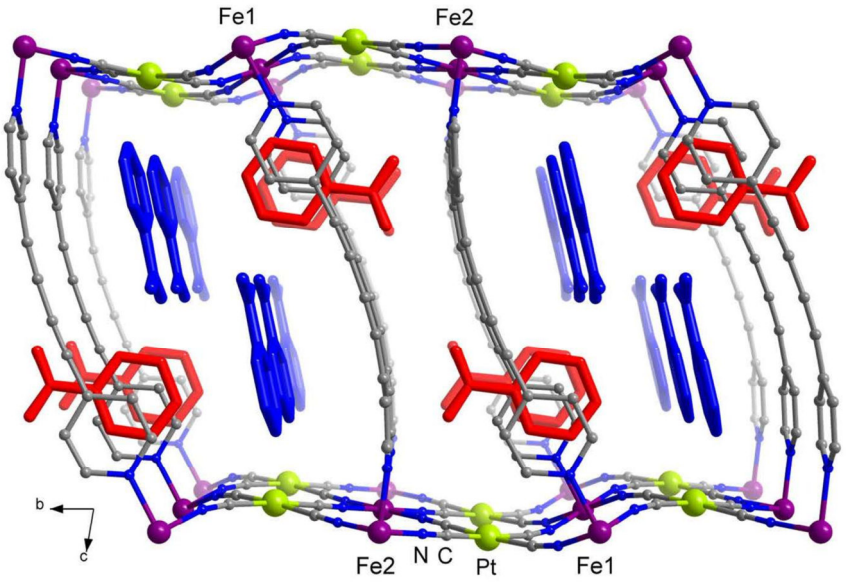

CAPÍTULO 5

Guest induced strong cooperative one and two-step spin crossover in a highly porous iron(II) Hofmann-type metal-organic framework

CAPÍTULO 5

Guest induced strong cooperative one and two-step spin crossover in a highly porous iron(II) Hofmann-type metal-organic framework

5.1.- Abstract

The synthesis, crystal structure, magnetic, calorimetric and Mössbauer studies of a series of new Hofmann-type SCO metal-organic frameworks (MOFs) is reported. The new SCO-MOFs arise from self-assembly of Fe^{II}, bis(4-pyridyl)butadiyne) (bpb) and $[Ag(CN)2]^-$ or $[M^{II}(CN)_4]^{2-}$ (M^{II} = Ni, Pd). Interpenetration of four identical 3D networks with α-Po topology are obtained for $\{Fe(bpb)[Ag^{I}(CN)_2]_2\}$ due to the length of the rod-like bismonodentate bpb and $[Ag(CN)_2]^-$ ligands. The four networks are tightly packed and organized in two subsets orthogonally interpenetrated, while the networks in each subset display parallel interpenetration. This non-porous material undergoes a very incomplete SCO, which is rationalized from its intricate structure. In contrast, the single network Hofmann-type MOFs $\{Fe(bpb)[M^{II}(CN)_4]\}\cdot nGuest$ (M^{II} = Ni, Pd) feature enhanced porosity and display complete one-step or two-step cooperative SCO behaviours when the pores are filled with 2 molecules of nitrobenzene or naphthalene that interact strongly with the pyridyl and cyano moieties of the bpb ligands via π-π stacking. The lack of these guest molecules favors stabilization of the HS state in the whole range of temperature. However, application of hydrostatic pressure induces one and two-step SCO.

5.2.- Introduction

Much interest in the area of material sciences is focused on the search for new molecular materials displaying switchable physical properties controlled by external stimuli, as they can be basic components in the design of technologically valuable molecular devices.[1] Fe^{II} complexes that exhibit SCO between the HS (S = 2) (HS) and the LS (S = 0) (LS) spin states are among the most studied families of switchable molecular materials. The HS↔LS spin state change is reversible and detectable and occurs with concomitant variation of relevant physical magnitudes including magnetic susceptibility, colour, dielectric constant and electric conductivity, controlled by the action of temperature, pressure, light and analytes.[2] The HS↔LS electronic reorganization associated with the SCO is strongly coupled with structural changes at the Fe^{II} centers,

which, in favorable conditions, are transmitted to the neighbouring Fe^{II} centers in a cooperative way.

Cooperativity may be achieved when the Fe^{II} centers are strongly coupled in the crystal, a fact that confers bistability to the physical properties, one of the most appealing features of SCO materials. The use of rigid coordination bonds as connectors between Fe^{II} SCO centers fueled the so-called polymeric approach, developed from the 1990s, and afforded an important number of 1-3D SCO coordination polymers.[3] In this context, we reported the first 3D Hofmann SCO coordination polymers, $\{Fe(pz)[M^{II}(CN)_4]\}\cdot$Guest (pz = pyrazine; M^{II} = Ni, Pd, Pt) and $\{Fe(L)_x[Ag^{I}(CN)_2]_2\}$ (L = pz (x =1), 4,4'-bipyridine (x = 2), tvp (x = 2)).[4] Then this study was extended to new $\{Fe(L)[M^{II}(CN)_4]\}\bullet$Guest clathrate systems derived from bismonodentate pyridine-like ligands (L) other than pyrazine. Interestingly, this work originated an isoreticular series of 3D SCO porous metal-organic frameworks (SCO-MOFs) (see Scheme 1) which represents an interesting example of modulation of the accessible volume in the LS state: 63.3 $Å^3$ (18.1% of the unit cell volume) for pz,[5] 270-290 $Å^3$ (40-42%) for bpe,[6] azpy,[7] and bpac,[8] 511 $Å^3$ (48.9%) for bpeben[9] and 692.9 $Å^3$ (49%) for dpsme.[10] More importantly, this series provided a very rich variety of relevant examples in which host-guest interactions influence the cooperative nature of the SCO, i.e. hysteresis width and/or critical temperatures.[11]

The $\{Fe(L)[M^{I}(CN)_2]_2\}\cdot$Guest ($M^{I}$ = Ag, Au) system has afforded a more moderate series of isoreticular SCO-MOFs (Scheme 1). Compared with the tetradentate nature of the $[M^{II}(CN)_4]^{2-}$ units, the ditopic linear $[M^{I}(CN)_2]^{-}$ bridges generate much more open structures thereby favoring interpenetration of two identical frameworks. This limits the degree of porosity, nevertheless, there is enough space between the frameworks to place guest molecules, a fact that has enabled to investigate new relevant host-guest-SCO correlations.[12]

In a recent communication we reported on the synthesis and characterization of the new SCO-MOF $\{Fe(bpb)[Pt^{II}(CN)_4]\}\cdot$2Guest where bpb is the pillar ligand bis(4-pyridyl)butadiyne) (Scheme 1).[13] This ligand provides the largest available volume, ca. 820 $Å^3$ in the LS, of the isoreticular series $\{Fe(L)[M^{II}(CN)_4]\}\cdot$Guest. Indeed, it hosts two molecules of naphthalene or nitrobenzene. Both clathrates undergo cooperative SCO with large hysteresis. The SCO takes place in two well-defined steps for the naphthalene clathrate while only one step characterizes the SCO in the nitrobenzene derivative. As a

continuation of this preliminary work, herein we report on the magnetic and calorimetric properties, Mössbauer spectra and crystal structures of {Fe(bpb)[$Ag^{I}(CN)_2]_2$} (**1Ag**), {Fe(bpb)[$M^{II}(CN)_4$]}·nGuest (**2M-Guest**; M^{II} = Ni, Pd) with n = 2 and Guest = naphthalene, nitrobenzene and the synthesis and characterization of the microcrystalline compounds {$Fe(bpb)_{1.1}[M^{II}(CN)_4]$}·$nCH_3OH$ (**2M**; M^{II} = Ni, Pd, Pt; n is in the interval 0-1).

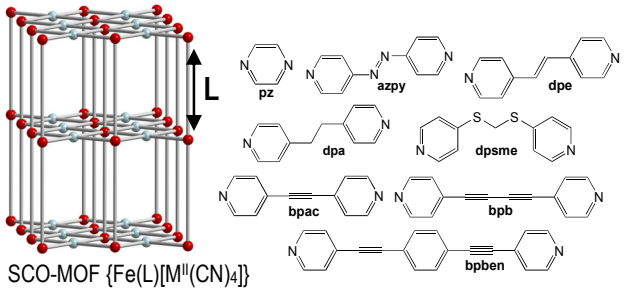

Scheme 1. Illustration of the two types of Hofmann-like SCO-MOFs and bismonodentate pillar ligands employed (M^{II} = Ni, Pd, Pt; M^{I} = Ag, Au).

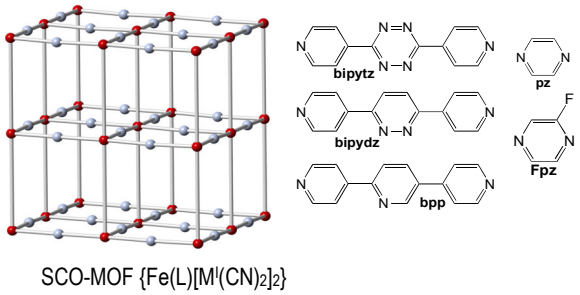

Scheme 1 cont. Illustration of the two types of Hofmann-like SCO-MOFs and bismonodentate pillar ligands employed (M^{II} = Ni, Pd, Pt; M^{I} = Ag, Au).

5.3.- Results

5.3.1.- Synthesis and stability

The title compounds have been synthesized by slow diffusion methods in methanol-water solutions. The presence of appropriate guest molecules during the diffusion enables the growth of single crystals of **2M-Guest** (M = Ni, Pd). The thermal

analysis indicates an occupation of the pores by about 2 guest molecules per unit formula in agreement with elemental and crystallographic analyses. These clathrate derivatives show relatively low thermal stability, i.e. nitrobenzene starts to desorb at ca. 346 K (Ni), 398 K (Pd) while naphthalene starts to desorb at ca. 379 K (Ni) and 400 K (Pd). The system **1Ag** was obtained independently of the presence or absence of guest molecules in the diffusion process. The thermogravimetric analysis shows the lack of guest molecules in the framework, which decomposes in one step from 500 K (Figure S1).

The lack of guest molecules other than water-methanol solvent in the diffusion medium favors precipitation of compounds **2M** (M = Ni, Pd and Pt), in these conditions only microcrystalline powders form. Their elemental analyses are consistent with the presence of an excess of bpb by 10% and the presence of 0-1 labile methanol molecules. Thermogravimetric data (Figure S2) show that **2M** decompose at ca. 520 K (Ni), 550 K (Pd) and 560 K (Pt), which are very close (ca. 600 K) to that observed for the guest-free network. The three derivatives are isostructural and display essentially the same PXRD pattern that the simulated one for the crystal structure of **2M-Guest** (*vide infra*) to which the guest molecules were artificially removed (Figure S3). Particularly significant is the 001 reflection at 2θ = 5.55° which corresponds to d = 15.836 Å, a distance that matches quite well the separation between planes that contain $\{Fe[M^{II}(CN)_4]\}_n$ layers pillared by the bpb ligand in **2M-Guest** (*vide infra*).

5.3.2.- Magnetic Properties

The thermal dependence of the $\chi_M T$ product (χ_M is the molar magnetic susceptibility and T the temperature) was measured at 1 K min^{-1} for all derivatives. Figure 1 shows $\chi_M T$ vs. T plots for **1Ag**, and "guest-free" **2Ni**, **2Pd** and **2Pt** derivatives at 1bar and at high pressure. Concerning **1Ag**, $\chi_M T$ is about 3.50 cm^3 K mol^{-1} at 300 K and remains practically constant down to 206 K. Then it drops to a value of 2.00 cm^3 K mol^{-1} at 75 K indicating that this derivative undergoes an incomplete spin conversion involving ca. 43% of the Fe^{II} atoms. The spin transition is centered at ca. 130 K. The decrease of $\chi_M T$ below 75 K corresponds to the zero-field splitting of the remaining HS (S = 2) Fe^{II} centers.

The derivatives **2Ni**, **2Pd** and **2Pt** are essentially HS. However, the onset of a SCO involving ca. 8-13% of HS-to-LS conversion and the effect of zero-field splitting of

the HS centers are observed, respectively, upon cooling below 150 and 75 K. These results stimulated the investigation of external hydrostatic pressure effects (up to ca. 8 kbar) on the variable-temperature magnetic susceptibilities of the unloaded derivatives (see Figure 1). The pressure expectedly shifts the equilibrium transition temperature upwards [i.e. $T_{1/2}$ = 208 K (**2Pd**) and 156 K (**2Pt**)] and increases completeness [67% (**2Pd**) and 58% (**2Pt**)] of the initially incipient HS↔LS transition. Particularly interesting is the appearance of gradual double step transition in **2Ni** with $(T_{1/2})_1$ = 287 K and $(T_{1/2})_2$ = 171 K and ca. 74% of completeness.

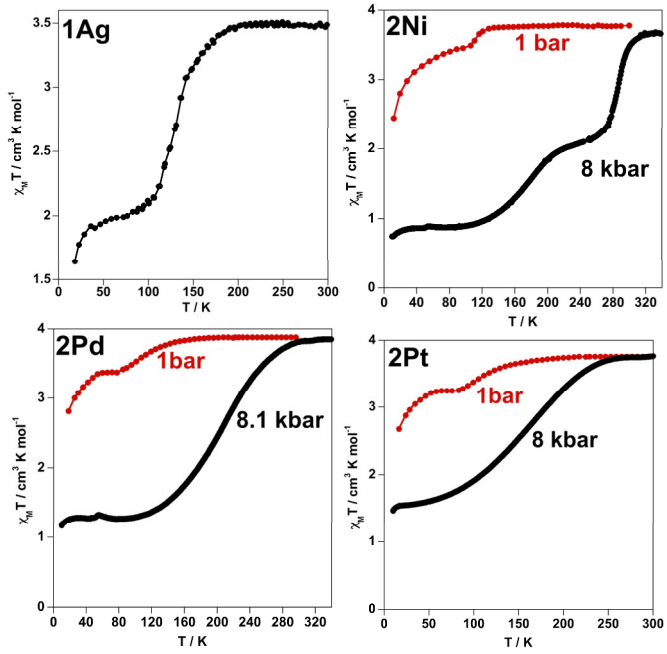

Figure 1. $\chi_M T$ vs. T plot for **1Ag** and **2Ni**, **2Pd** and **2Pt** at 1bar and ca. 8 kbar.

The magnetic properties of guest loaded derivatives **2Ni-naph, 2Ni-phNO$_2$, 2Pd-naph, 2Pd-phNO$_2$** are shown in Figure 2. The $\chi_M T$ value for **2Ni-naph** and **2Pd-naph** is about 3.83 cm^3 K mol^{-1} at 300 K and remains constant down to 179 K (Ni) and 211 K (Pd) then follows an abrupt drop of $\chi_M T$ to 2.0 cm^3 K mol^{-1}, which remains constant in the interval 172-134 K (Ni) and 209-199 K (Pd). A second drop in $\chi_M T$ occurs upon cooling at temperatures just below 134 K (Ni) and 199 K (Pd) to attain values in the range of 0.1-0.2 cm^3 K mol^{-1}. This complete and cooperative two-step spin transition behaviour is

characterized by critical temperatures $T_{c1}\downarrow$ = 175.0 K (Ni) and 211.2 K (Pd), $T_{c2}\downarrow$ = 122.5 K (Ni) and 195.6 K (Pd). In the heating mode the $\chi_M T$ vs. T curves are shifted to higher temperatures and do not match those of the cooling mode being the critical temperatures $T_{c1}\uparrow$ = 185.0 K (Ni) and 217.5 K (Pd), $T_{c2}\uparrow$ = 140.0 K (Ni) and 205.0 (Pd). The generated thermal hysteresis for each step are ΔT_{c1} = 10 K (Ni) and 6.3 K (Pd) and ΔT_{c2} = 17.6 (Ni) and 9.4 K (Pd).

The $\chi_M T$ value for **2Ni-phNO$_2$** and **2Pd-phNO$_2$** is about 3.70 cm^3 K mol^{-1} and practically constant in the interval 300-230 K. Just below 230 K in the cooling mode, the Ni derivative displays two sharp steps separated by a quite narrow plateau (ca. 2 K wide) centered at 224 K and $\chi_M T$ = 1.97 cm^3 K mol^{-1}, while only one complete step transition is observed for the Pd derivative. The critical temperatures are $T_{c1}\downarrow$ = 227.2 K (Ni), $T_{c2}\downarrow$ = 220.6 K (Ni) and $T_c\downarrow$ = 227.0 K (Pd). Similarly to the naphthalene derivatives, the heating mode defines hysteresis loops characterized by $T_{c1}\uparrow$ = 240.8 K (Ni) [ΔT_{c1} = 13.6 K], $T_{c2}\uparrow$ = 231.4 K (Ni) [ΔT_{c2} = 10.8 K] and $T_c\uparrow$ = 246.4 (Pd) [ΔT = 19.4 K]. Table S1 gathers the critical temperatures for the **2M-naph** and **2M-phNO$_2$** including the previously reported Pt systems.

Given that **2Ni-naph** exhibits the lowest transition temperature, photo-generation of the metastable HS* state at low temperature, the so called Light Induced Spin State Trapping experiment (LIESST) was carried out.[14] Photo excitation of the powdered sample at 10 K with green light during 3 h resulted in an increase of the $\chi_M T$ up to ca. 0.5 cm^3 K mol^{-1}. Upon heating at 0.3 K min^{-1} with switched off light source the susceptibility value increases up to ca. 0.62 cm^3 K mol^{-1} at 40 K. This suggests ca. 16% of the Fe^{II} ions undergoing light-induced population of the HS* state. The T_{LIESST} temperature,[15] determined as the inflection point of the curve HS*-to-LS, is 54 K.

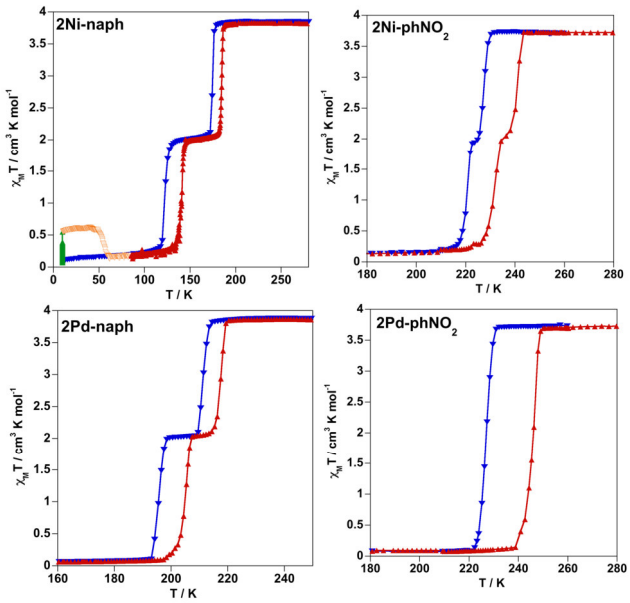

Figure 2. $\chi_M T$ vs. T plots for **2Ni-naph**, **2Ni-phNO$_2$**, **2Pd-naph** and **2Pd-phNO$_2$**.

5.3.3.- Mössbauer studies

The spin transition in **1Ag** and **2Ni-naph** was monitored by Mössbauer spectroscopy (Figure 3). For **1Ag** the spectra were collected above and below the transition temperature at 200 and 80 K, respectively (Figure 3a). At higher temperature, presence of a single doublet with isomer shift δ = 1.14(2) mm s^{-1} and quadrupole splitting ΔE_Q = 0.75(1) mm s^{-1} points out the HS state of Fe^{II} ion. Upon cooling down another doublet appears, whose parameters (ΔE_Q = 0.69(1) mm s^{-1} and δ = 0.13(2) mm s^{-1}) correspond to the LS Fe^{II} ion. The ratio between doublets area is close to 1:1, which indicates incomplete spin transition and corroborates well with the magnetic data.

The Mössbauer spectrum of **2Ni·naph** at 80 K consist of strong LS doublets with isomer shift values δ^{LS} = 0.49(2) mm s^{-1} and quadrupole splitting parameters ΔE_Q^{LS} = 0.24(1) mm s^{-1} (Figure 3b). Another minor doublet with relative area of 8.9(2)% indicates HS fraction with δ^{HS} = 1.36(1) mm s^{-1} and ΔE_Q^{HS} = 2.90(1) mm s^{-1}. Upon heating up to 150 K and according to the transition of a Fe^{II}-site to the HS state, the ratio between areas of the LS and HS doublets gets equal to 1:1 and the parameters of the doublets

slightly change (δ^{LS} = 0.47(1) mm s^{-1} and ΔE_Q^{HS} = 0.18(0) mm s^{-1}; δ^{HS} = 1.16(1) mm s^{-1} and ΔE_Q^{HS} = 1.99(0) mm s^{-1}). Upon further heating up to 200 K, the spectrum contains two overlapping equally populated HS doublets with similar isomer shift values (δ^{HS1} = 1.13(1) mm s^{-1} and δ^{HS2} = 1.12(1) mm s^{-1}) and strongly different quadrupole splitting parameters (ΔE_Q^{HS1} = 1.72(2) mm s^{-1} and ΔE_Q^{HS2} = 1.09(1) mm s^{-1}). The ΔE_Q value is a very sensitive tool to probe local geometry around Fe^{II} ions.[16] At higher temperature the values reflect different geometric distortion of the corresponding coordination polyhedra, while at lower temperature in the LS state the difference is relatively small making the two different LS Fe^{II} ions undistinguishable. The deconvolution analysis data are collected in Table 1.

Table 1. Least-squares-fitted ^{57}Fe Mössbauer spectra for **1Ag** and **2Ni-naph**.

	T/K	**Doublet**	**ΔE_Q/mm s^{-1}**	**δ/mm s^{-1}**	**Population**
1Ag	80 K	LS	0.69(1)	0.13(2)	43.7(3)
		HS	1.01(0)	1.29(2)	56.3(4)
	200 K	HS	1.14(2)	0.75(1)	100
2Ni-naph	80 K	LS	0.49(1)	0.24(1)	91.1(2)
		HS	1.36(1)	2.90(1)	8.9(2)
	150 K	LS	0.47(1)	0.18(0)	51.3(2)
		HS	1.16(1)	1.99(0)	48.7(2)
	200 K	HS1	1.13(1)	1.72(2)	46.6(3)
		HS2	1.12(1)	1.09(1)	53.4(3)

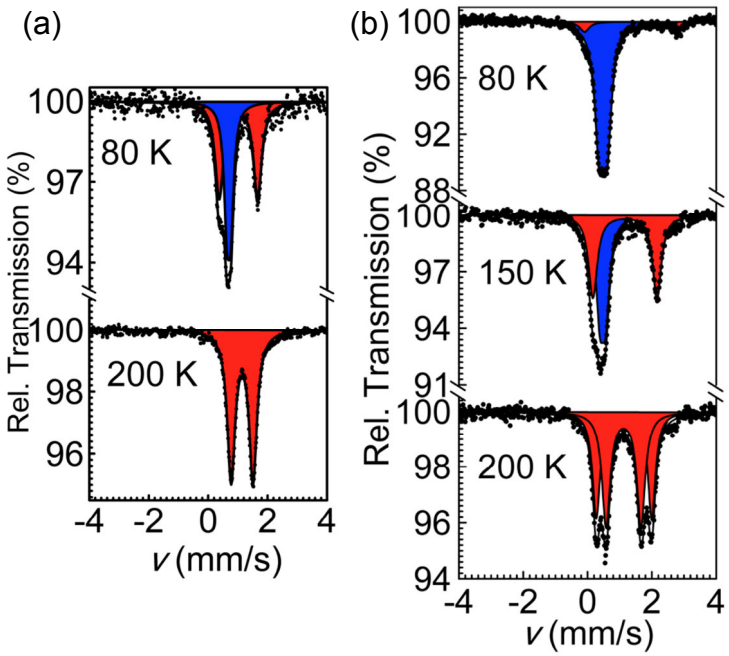

Figure 3. ^{57}Fe Mössbauer spectra for **1Ag** (a) and **2Ni-naph** (b).

5.3.4.- Calorimetric studies

DSC measurements performed on the loaded samples reveal the anomalous heat capacity ΔC_p associated with the spin transitions. For **2Ni-naph** only the high-temperature transition could be recorded due to limitation of the temperature window of the calorimeter. Figure 4 shows ΔC_p vs. T plots and Table 2 gathers relevant thermodynamic parameters extracted from them, ΔH and ΔS average variations and average critical temperatures ($T_{ci}\downarrow$ + $T_{ci}\uparrow$/2). The critical temperatures obtained from magnetic measurements agree reasonably well with those obtained from the maxima of ΔC_p vs. T plots. The overall ΔH and ΔS values are, respectively, in the range 16-22 kJ mol^{-1} and 70-109 J K^{-1} mol^{-1}, consistent with values typically observed in Hofmann-like clathrates of Fe^{II} featuring strong cooperative SCO behaviour.[11]

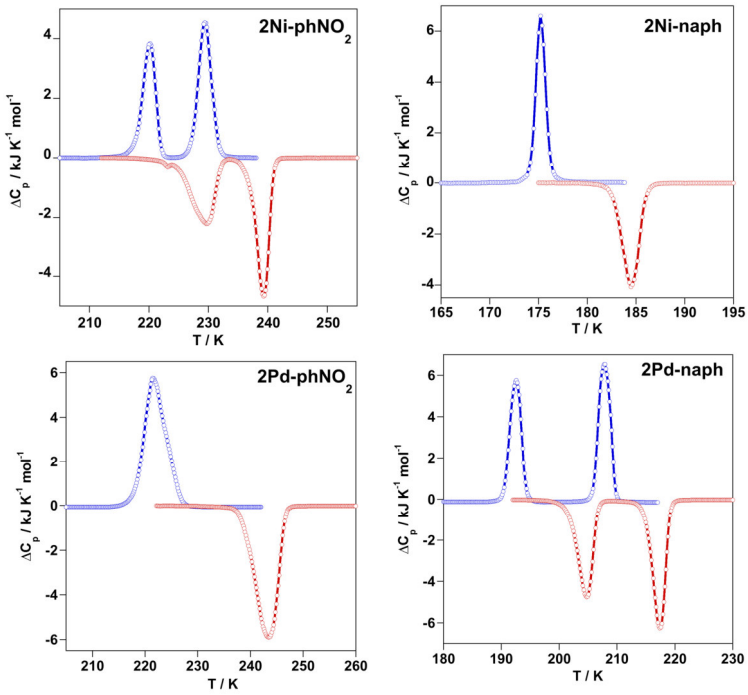

Figure 4. Anomalous heat capacity (DSC) for **2M-Guest** (M = Ni, Pd; Guest = naphthalene, nitrobenzene). Blue and red curves correspond to the cooling and heating modes, respectively.

Table 2. Thermodynamic parameters calculated from calorimetric (DSC) measurements [ΔH/ kJ mol^{-1}; ΔS/J K^{-1} mol^{-1}; T_{ci}/K; ΔT_{ci}/K].

	ΔH_1^{av}	ΔS_1^{av}	T_{c1}^{av}	ΔT_{c1}	ΔH_2^{av}	ΔS_2^{av}	T_{c2}^{av}	ΔT_{c2}	Ref.
Ni-naph	8.85	49.3	179.7	9.1	-	-	-	-	this work
Ni-phNO$_2$	8.53	36.4	234.2	9.5	7.60	32.2	225.0	10	this work
Pd-naph	12.00	56.5	212.5	9.6	10.42	52.4	198.8	11.3	this work
Pd-phNO$_2$	20.22	87.1	232.4	22.1	-	-	-	-	this work
Pt-naph	9.45	44.9	210.5	9.1	8.62	44.1	195.7	13.4	12
Pt-phNO$_2$	19.29	86.3	226.4	19.2	-	-	-	-	12

5.3.5.- Single crystal X-ray studies

Single crystals of the compounds under discussion were prepared using the slow diffusion method. The crystal structure determination was carried out at several temperatures to characterize the compounds in different spin states. Compound **1Ag**

crystallizes in the tetragonal $I4_122$ space group, **2Ni-phNO$_2$** in the monoclinic space group *P2/m*, whereas **2Ni-naph**, **2Pd-naph** and **2Pd-phNO$_2$** share the same triclinic space group *P-1*, similarly to **2Pt-naph** and **2Pt-phNO$_2$**.[13] Tables 3-5 contain the crystallographic data, selected distances and angles.

Structure of 1Ag. The crystal structure of **1Ag** was determined at 120 and 250 K. The Fe^{II} sites define slightly elongated [FeN_6] octahedrons centered at the crossing point of two perpendicular binary axes bisecting the equatorial N-Fe-N angles (Table 4). The four equatorial positions are occupied by four equivalent $[Ag(CN)_2]^-$ units while the axial positions are occupied by the pyridine groups of the bpb ligand. At 250 K, the axial and equatorial bond lengths are 2.212(5) Å and 2.189(4) Å and decrease by 0.063 and 0.061 Å, respectively, at 120 K. The Fe-N bond lengths at 250 K are consistent with the Fe^{II} in the HS state, however, the shortening of these lengths suggest a very incomplete HS-to-LS conversion at 120 K. The CN moieties of the $[Ag(CN)_2]^-$ groups are slightly tilted (10.6º) with respect to the C-Ag-C axis and do not change significantly with temperature. The Fe^{II} sites are equatorially linked by the $[Ag(CN)_2]^-$ groups thus generating slightly undulating $\{[FeAg(CN)_2]_4\}_n$ 2D grids. The windows of the $\{[FeAg(CN)_2]_4\}$ units are rhombus-like with distances between Fe^{II} ions of 10.716 (10.621) Å and angles 102.1º/77.8º (102.6º/77.4º) at 250 (120) K. The bpb ligands act as pillars connecting the Fe^{II} centers of consecutive layers generating a distorted α-Po type framework generated by tessellation of parallelepipeds $\{[FeAg(CN)_2]_8(bpb)_4\}$ (Figure 5a). The interlayer separation, measured between two Fe^{II} centers linked by bpb, is 16.681 (16.581) Å at 250 (120) K. Furthermore, three other identical frameworks are passing through the windows of the grid (Figure 5b). Consequently, the crystal structure of **1Ag** is made up of four identical 3D networks interlocked in an unusual way. There are two different pairs of interpenetrated networks represented in Figure 5b with different colours, ie. yellow and red (set 1) and green and blue (set 2). The nodes (Fe centers) of the parallelepipeds of one framework are placed on the barycenter of the parallelepipeds of the other framework belonging to the same set, in a similar way as described for other $\{Fe(L)[M^I(CN)_2]_2\}$ compounds. Within a set the $\{[FeAg(CN)_2]_8(bpb)_4\}$ units are oriented in the same direction while the units of the different sets are orthogonally oriented.

The compactly packed crystal components exhibit short-distance interatomic contacts. The pyridine rings of neighbour concatenated networks exhibit strong π-π stacking interactions with the distance of the shortest contact $C1\cdots C1^i$ being 3.244(7)

[3.304(8)] Å at 120 [250] K. The C≡N groups of neighbour networks form a C6···C6^{i} very short contact with separation distance of 3.189(8) [3.226(8)] Å at 120 [250] K (i = x, 1-y, 1-z). Finally, Ag atoms exhibit weak argentophilic interactions with an Ag···Ag distance of 3.3778(2) [3.4299(3)] Å (Figure S4). As a consequence of the chiral crystal structure, the chains of Ag atoms form helices running along [001].

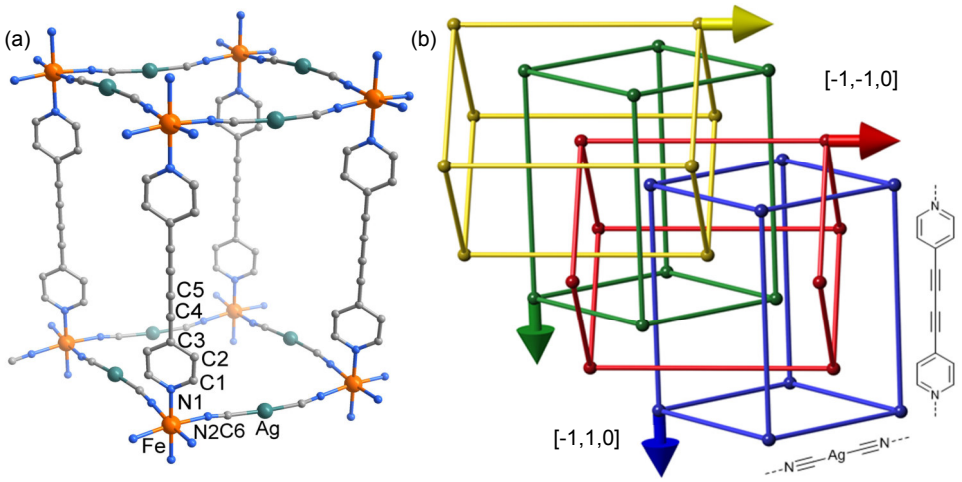

Figure 5. (a) Projection of a parallelepiped fragment of the 3D polymeric frameworks of **1Ag**; (b) Schematically shown four-fold concatenation of independent 3D polymeric networks. Arrows indicate the relative orientation of the $\{[FeAg(CN)_2]_8(bpb)_4\}$ units.

Structures of 2Ni-naph and 2Pd-naph. According to the magnetic properties the structural analysis was carried out at three relevant temperatures where the crystals are HS (250 K), HS-LS [150 K **2Ni-naph**; 204 K (**2Pd-naph**)] and LS (120 K). Both compounds are isostructural and the space group *P-1* (triclinic) remains in the interval of temperatures investigated. There are two crystallographically distinct Fe^{II} centers (Fe(1) and Fe(2)) lying on inversion centers defining elongated [FeN_6] octahedrons (Figure 6a). The equatorial positions are occupied by the CN groups of four equivalent $[M^{II}(CN)_4]^{2-}$ (M^{II} = Ni, Pd) counterions. Each $[M^{II}(CN)_4]^{2-}$ group connect four Fe^{II} centers defining slightly corrugated 2D $\{Fe[M^{II}(CN)_4]\}_n$ layers which stack along [001]. The axial positions of the Fe^{II} centers are occupied by the pyridyl groups of bpb, which pillar consecutive layers thereby generating a 3D Hofmann SCO-MOF (Figure 6b) with large channels running along [100]. As already observed for the Pt compound, the bpb ligand is strongly

bent and the pyridine moieties are almost orthogonal to each other in Ni and Pd homologues, a fact that contrasts with the Ag complex.

At 120 K, the average Fe(1,2)-N bond lengths (<Fe-N>) are in the range 1.957-1.966 Å for both derivatives. These values are consistent with the LS state according to the magnetic data. At 150 K (Ni) and 204 K (Pd) the <Fe(1)-N> remains essentially unchanged, while <Fe(2)-N> experiences an increase of 0.198 Å (Ni) and 0.203 Å (Pd), what suggests the transformation of this site to the HS state. This is consistent with the plateau observed in the magnetic data at these temperatures. In this ordered mixed state, the Fe centers in the $\{Fe[M^{II}(CN)_4]\}_n$ layers define -LS-HS-LS- chains running along [010], while along [100] the chains display homogeneous spin states -HS-HS-HS- and -LS-LS-LS (Figure S5). In addition, the bpb ligands connect consecutive layers through Fe atoms with distinct spin state (Figure S5). At 250 K, <Fe(1)-N> changes by 0.2 Å attaining both compounds the HS state. Interestingly, the N-Fe-N angles do not change significantly during the spin transition (Table 5).

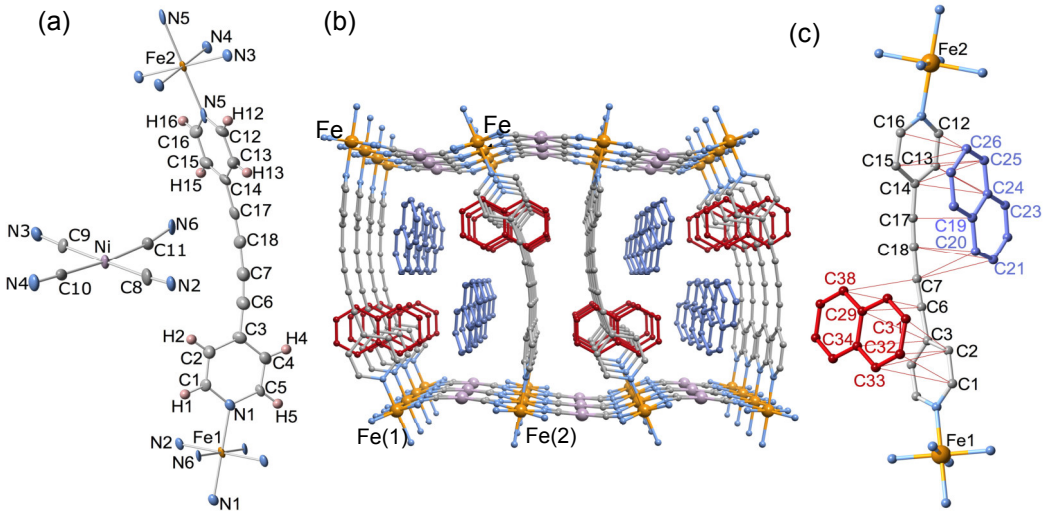

Figure 6. (a) ORTEP representation of relevant molecular fragments of **2Ni-naph** at 120 K. Atom numbering is the same for **2Pd-naph** (thermal ellipsoids are represented at 50% probability). (b) Projection of the framework down to [100]. Crystallographically distinct naphtalene guest molecules are denoted in red and lilac. (c) Short C···C contacts between naphthalene and bpb at 120 K (red lines correspond to C···C distances smaller than 3.7 Å).

The accessible guest free volume[17] of the SCO-MOF at 120 K is close to that observed for the Pt derivative, namely 809 and 846 $Å^3$ for Ni and Pd, respectively. This space is densely occupied by two crystallographically different naphthalene molecules. One, marked red in Figure 6b is located half-way between the pyridine rings of the bpb ligand, coordinated to Fe(1), while the other (lilac colour) lies closer to the pyridine ring coordinated to Fe(2). An important number of short contacts, smaller than the sum of the Van der Waals radius of C (ca. 3.7 Å) is defined between the latter guest and the pyridine coordinated to Fe(1) and Fe(2) and the cyano groups of bpb (Figure 6c). Furthermore, there is an extended network of C···C short contacts between naphthalene molecules located in the channels running along [100] (Figure S6, Tables S2-S7). The number of host-guest and guest-guest intermolecular contacts decreases significantly as temperature increases due to thermal expansion and the change of volume associated with the population of the HS state.

Structures of 2Ni-phNO$_2$ and 2Pd-phNO$_2$. The structure of the host framework of both nitrobenzene clathrates is essentially the same as described for the naphthalene derivatives. The most relevant difference was found in **2Ni-phNO$_2$** since crystallizes in the space group *P2/m* (monoclinic) instead of *P-1* (triclinic). Consequently, the sites Fe(1) and Fe(2) lie on inversion centers and on a plane of reflection which contains the pyridine group coordinated to the Fe1 and bisects the pyridine group coordinated to Fe2 (Figure 7a). Similarly to **2Pt-phNO$_2$**, **2Pd-phNO$_2$** undergoes one step SCO while **2Ni-phNO$_2$** undergoes two-step SCO behaviour with a small step, which could not be analyzed. At 120 K, <Fe-N> values for Fe(1) and Fe(2) sites, in the range 1.950-1.970 Å, are consistent with the LS state for both derivatives and increase around 0.207-0.215 Å at 260 K (**2Pd-phNO$_2$**) and 295 K (**2Ni-phNO$_2$**) as expected for a complete LS-to-HS transition (Table 5).

As in the precedent case, there are two crystallographically distinct guest molecules, which are organized in a similar way as described for the naphthalene derivatives. One $phNO_2$ show short contacts with the pyridine coordinated to Fe(2) and one cyano moiety of bpb while the other interacts with the pyridine coordinated to Fe(1) (Figure 7b,c) (see Tables S2-S7).

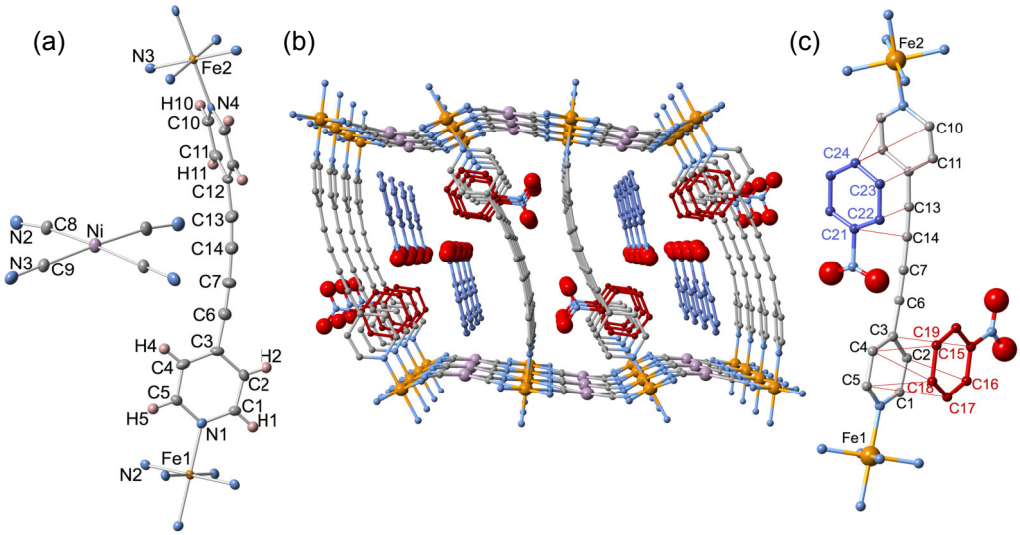

Figure 7. (a) ORTEP representation of relevant molecular fragments of **2Ni-phNO$_2$** at 120 K (thermal ellipsoids are represented at 50% probability). (b) Projection of the framework down to [100]. Crystallographically distinct nitrobenzene guest molecules are denoted in red and lilac. (c) Short C···C contacts between nitrobenzene and bpb at 120 K (red lines correspond to C···C distances smaller than 3.7 Å).

Table 3. Crystallographic parameters of indicated compounds at different temperatures.

	Ag	
Temperature (K)	120(2)	250(2)
Empirical formula	$C_{18}H_8Ag_2FeN_6$	
Mr	579.89	
Crystal system	Tetragonal	
Space group	$I4_122$	
Crystal size (mm)	0.20 × 0.17 × 0.06	
a (Å)	11.7245 (3)	1825.42 (12)
b (Å)		
c (Å)	13.2791 (5)	13.4581 (11) Å
α (°)		
β (°)		
γ (°)		
V (Å^3)	1825.42 (12)	1872.3 (2)
Z	4	4
D_c (mg cm^{-3})	2.110	2.070
F(000)	1112	1112
μ (Mo-K$_\alpha$)(mm^{-1})	2.92	2.85
No. of total reflections	4555	3505
No. of reflections [$I>2\sigma(I)$]	1397	1370
R [$I>2\sigma(I)$][a]	0.033	0.038
R [all data][a]	0.089	0.088
S	1.02	1.06

[a] $R = \Sigma \, ||F_o| - |F_c|| \, / \, \Sigma \, |F_o|$;

Table 3 cont. Crystallographic parameters of indicated compounds at different temperatures.

	Ni·naph			**Ni·phNO$_2$**	
Temperature (K)	120(1)	150(1)	250(1)	120(1)	295(1)
Empirical formula	$C_{38}H_{24}N_6NiFe$			$C_{30}H_{18}N_8O_4NiFe$	
Mr	679.19			669.08	
Crystal system	triclinic			monoclinic	
Space group	*P*-1			*P*2/m	
Crystal size (mm)	0.04 x 0.06 x 0.06			0.05 x 0.08 x 0.15	
a (Å)	7.0404(3)	7.1878(5)	7.3262(5)	13.5575(8)	14.018(5)
b (Å)	13.7679(7)	13.9259(13)	14.1439(6)	7.0586(3)	7.324(5)
c (Å)	16.4902(8)	16.469(2)	16.3846(8)	15.6600(10)	15.702(5)
α (°)	106.946(4)	74.782(8)	76.394(4)		
β (°)	96.413(4)	82.112(6)	83.496(5)	100.703(2)	98.402(5)
γ (°)	90.009(4)	89.881(6)	89.942(4)		
V (Å^3)	1518.55(13)	1574.6(2)	1639.0(2)	1472.54(14)	1594.8(13)
Z	2			2	
D_c (mg cm^{-3})	1.485	1.432	1.376	1.509	1.393
F(000)	696			680	
μ (Mo-K$_\alpha$)(mm^{-1})	1.137	1.096	1.053	1.182	1.091
No. of total reflections	7635	7073	8300	3673	3940
No. of reflections [$I>2\sigma(I)$]	4969	3788	5252	2565	3173
R [$I>2\sigma(I)$][a]	0.0670	0.0772	0.0796	0.0678	0.0524
R [all data][a]	0.1127	0.1566	0.1260	0.1073	0.0689
S	0.939	0.917	1.117	1.071	1.079

[a] $R = \Sigma \, ||F_o| - |F_c|| \, / \, \Sigma \, |F_o|$;

Table 3 cont. Crystallographic parameters of indicated compounds at different temperatures.

	Pd·naph			**Pd·phNO$_2$**	
Temperature (K)	120(1)	204(1)	250(1)	120(1)	260(1)
Empirical formula	$C_{38}H_{24}N_6PdFe$			$C_{30}H_{18}N_8O_4PdFe$	
Mr	726.88			716.77	
Crystal system	triclinic			Triclinic	
Space group	*P*-1			*P*-1	
Crystal size (mm)	0.04 x 0.08 x 0.08			0.03 x 0.05 x 0.08	
a (Å)	7.2261(5)	7.3789(4)	7.5133(7)	7.2355(4)	7.4860(2)
b (Å)	13.9453(8)	14.1403(7)	14.3298(10)	13.7948(7)	14.2688(4)
c (Å)	16.3288(11)	16.3935(10)	16.1925(15)	15.4309(10)	15.0260(6)
α (°)	106.288(5)	74.809(5)	102.716(7)	80.619(5)	86.069(3)
β (°)	96.496(5)	82.406(5)	95.108(8)	86.873(5)	84.010(3)
γ (°)	89.999(5)	89.939(5)	90.031(7)	89.870(5)	89.597(2)
V (Å^3)	1568.4(2)	1635.2(2)	1693.5(3)	1517.3(2)	1592.50(9)
Z	2			2	
D_c (mg cm^{-3})	1.539	1.476	1.425	1.569	1.495
F(000)	732			716	
μ (Mo-K$_\alpha$)(mm^{-1})	1.074	1.030	0.994	9.030	8.604
No. of total reflections	7883	8180	8535	5992	6243
No. of reflections [$I>2\sigma(I)$]	6434	6632	5904	5174	5072
R [$I>2\sigma(I)$][a]	0.1174	0.0908	0.0785	0.0554	0.0385
R [all data][a]	0.1327	0.1105	0.1157	0.0646	0.0858
S	1.010	1.016	1.020	1.031	1.116

[a] $R = \Sigma \, ||F_o| - |F_c|| \, / \, \Sigma \, |F_o|$;

Table 4. Selected bond lengths [Å] and angles [°] for **Ag**.

Temperature (K)	**120(2)**	**250(2)**
Fe-N(1)	2.149(5)	2.212(5)
Fe-N(2)	2.128(4)	2.189(4)
<Fe-N>	2.135	2.197
N(1)-Fe-N(2)	86.07(13)	85.57(11)

Table 5. Selected bond lengths [Å] and angles [°] for indicated compounds.

	Ni·naph			**Ni·phNO$_2$**	
	120(1)	**150(1)**	**250(1)**	**120(1)**	**295(1)**
Fe(1)-N(1)	2.002(4)	2.000(5)	2.205(4)	1.997(5)	2.204(5)
Fe(1)-N(2)	1.942(4)	1.941(5)	2.139(4)	1.936(4)	2.144(3)
Fe(1)-N(6)	1.946(4)	1.954(5)	2.153(4)		
<Fe(1)-N>	1.963	1.965	2.166	1.967	2.174
Fe(2)-N(3)	1.944(4)	2.139(5)	2.141(4)	1.938(4)	2.138(3)
Fe(2)-N(4)	1.952(4)	2.127(5)	2.140(4)	2.001(6)	2.219(4)
Fe(2)-N(5)	2.002(4)	2.225(5)	2.222(4)		
<Fe(2)-N>	1.966	2.164	2.168	1.970	2.179
N(1)-Fe(1)-N(2)	88.1(2)	88.5(2)	87.8(2)	87.6(2)	88.16(10)
N(1)-Fe(1)-N(6)	88.0(2)	87.9(2)	88.4(2)		
N(2)-Fe(1)-N(6)	89.3(2)	88.4(2)	89.7(2)		
N(3)-Fe(2)-N(4)	89.9(2)	89.6(2)	88.9(2)	89.2(2)	89.36(10)
N(3)-Fe(2)-N(5)	89.1(2)	89.3(2)	89.3(2)		
N(4)-Fe(2)-N(5)	89.3(2)	89.2(2)	89.0(2)		

Table 5 cont. Selected bond lengths [Å] and angles [°] for indicated compounds.

	Pd·naph			**Pd·phNO$_2$**	
	120(1)	**204(1)**	**250(1)**	**120(1)**	**260(1)**
Fe(1)-N(1)	2.003(9)	2.008(6)	2.201(5)	1.993(4)	2.192(4)
Fe(1)-N(2)	1.948(8)	1.947(6)	2.148(5)	1.933(4)	2.154(3)
Fe(1)-N(6)	1.936(8)	1.943(6)	2.144(5)	1.929(4)	2.145(3)
<Fe(1)-N>	1.962	1.966	2.164	1.952	2.164
Fe(2)-N(3)	1.937(8)	2.124(7)	2.132(5)	1.928(4)	2.140(3)
Fe(2)-N(4)	1.934(8)	2.129(6)	2.134(5)	1.933(4)	2.143(3)
Fe(2)-N(5)	1.999(9)	2.227(7)	2.224(6)	1.988(4)	2.211(4)
<Fe(2)-N>	1.957	2.160	2.163	1.950	2.165
N(1)-Fe(1)-N(2)	88.2(4)	88.4(2)	88.0(2)	88.3(2)	88.14(13)
N(1)-Fe(1)-N(6)	88.9(4)	88.9(2)	88.5(2)	88.2(2)	88.35(13)
N(2)-Fe(1)-N(6)	88.8(3)	87.5(2)	89.6(2)	88.8(2)	89.47(13)
N(3)-Fe(2)-N(4)	89.2(3)	89.7(2)	89.0(2)	89.8(2)	89.75(13)
N(3)-Fe(2)-N(5)	88.4(4)	89.0(3)	89.9(2)	89.8(2)	88.14(14)
N(4)-Fe(2)-N(5)	89.5(4)	89.6(3)	88.8(2)	88.8(2)	89.52(14)

5.4.- Concluding remarks

Self-assembly of Fe^{II}, bpb ligand and $[Ag(CN)_2]^-$ or $[M^{II}(CN)_4]^{2-}$ (M^{II} = Ni and Pd) counterions has afforded a new series of interesting examples of Hofmann-like SCO coordination polymers. Similar to other $\{Fe(L)[M^{I}(CN)_2]_2\}$ related systems where L is a bismonodentate ligand (Scheme 1), the ligand bpb acts as a pillar between consecutive $\{Fe[Ag(CN)_2]_2\}_n$ layers defining a simple 3D open network with the topology of α-Po in **1Ag**. Typically, this open network features wide windows defined by $\{FeM^{I}(CN)_2]\}_4$ rhombuses which favors the growth of two identical interlocked $\{Fe(L)[M^{I}(CN)_2]_2\}$ structures.[11] Their relative orientation can be viewed as the result of a parallel shift with respect to each other. However, this situation is much more complex in **1Ag** since there is enough space for a second subset of doubly interpenetrated networks which, in addition, is orthogonally interlocked to the first subset. This unprecedented situation is due to the increase of separation between the $\{Fe[M^{I}(CN)_2]_2\}_n$ layers, considered as the distance Fe(HS)-L-Fe(HS), which is 1.18 Å, 1.055 Å, 0.961 Å and 0.836 Å larger for bpb (16.681 Å) than for L = bipytz,[12a] bipydz,[12a] bpp[12b] and dpb,[12c] respectively. Other consequences of this singular interpenetration are the drastic decrease of accessible volume and the highly incomplete SCO behaviour exhibited by **1Ag**. Regarding the first aspect, all attempts to avoid the orthogonal interpenetration, i.e. trying to include guest molecules such as naphthalene or nitrobenzene during the diffusion process, resulted unsuccessful. Concerning the second aspect, we believe that incompleteness of the SCO in **1Ag** is a consequence of structural frustration essentially stemming from the balance of two opposite forces, contraction of the networks due to thermal induced SCO, on one hand, and strong π-π interactions between the pyridine rings present in the HS structure, which supposedly become more repulsive as temperature decreases, on the other hand (Figure S4).

The denser nature of the $\{Fe[M^{II}(CN)_4]\}_n$ grids prevents interpenetration of identical networks in the series $\{Fe(L)[M^{II}(CN)_4]\}\cdot$Guest thus affording reliable porosity, a fact which is also true for L = bpb. Indeed, the length of bpb has afforded the highest effective loading capacity so far described for the family of Hofmann-like SCO-MOFs. The structure of the six **2M-Guest** (M = Ni, Pd, Pt; Guest = naphthalene, nitrobenzene) clathrates is essentially the same. They are characterized by the presence of two crystallographically distinct Fe^{II} nodes joined through a bpb ligand, which is markedly curved. The three **2M-naph** derivatives and **2Ni-phNO$_2$** undergo cooperative two-step

SCO without change of symmetry of the crystal.[18] The former derivatives show well-defined LS-HS intermediate plateaus while the plateau is quite narrow for the latter. In contrast **2M-phNO$_2$** (M = Pd, Pt) display strong cooperative spin transition in one step. The structural differences between the two Fe^{II} sites, i.e. average <Fe-N> bond lengths, are of the order of magnitude of the standard deviations and consequently insignificant. The most remarkable differences involve their second coordination sphere where the coordinated pyridyl rings and CN groups of bpb interact via intermolecular short π-π contacts differently with the guest molecules. In the **2M-naph** series, the Fe(1) node coordinated to the pyridyl group exhibits the largest number of contacts with the naphthalene molecules (Tables S2-S7) and undergoes SCO at higher temperatures giving rise to the ordered intermediate -Fe2(HS)-Fe1(LS)-Fe2(HS)- state in the plateau. Most likely, the same happens to **2Ni-phNO$_2$**, however, the interval of temperatures in which the intermediate mixed spin state exists is very narrow. This fact together with the lack of steps in the homologous Pd and Pt derivatives points to the dramatic decrease of intermolecular host-guest and guest-guest interactions with respect to the **2M-naph** series (Tables S2-S7) as a key influence to explain the differences in SCO behaviour between the **2M-naph** and **2M-phNO$_2$** series. Similarly, the much larger intermediate plateau in **2Ni-naph** (ca. 40 K) with respect to that of **2Ni-phNO$_2$** (ca. 4 K) could reflect the same fact.

Another important conclusion arising from these results is that the presence of guest molecules is crucial for the occurrence of complete SCO in the porous frameworks under study. Despite XRPD data suggest that the crystal structure of **2M** series should not be significantly distinct to that of **2M-Guest**, the former derivatives are essentially HS at all temperatures. However, the compounds **2M** display the onset of SCO below ca. 130 K involving 8-13% of the Fe^{II} centers at ambient pressure. This observation is consistent with the presence of ca. 10% of included bpb ligand in the pores of the framework. Furthermore, **2M** undergo much more complete SCO behaviour at pressures of about 8 kbar. The lack of SCO in the **2M** series contrasts significantly with the related Hofmann SCO-MOFs {Fe(pz)[M^{II}(CN)$_4$]},[5] {Fe(azpy)[M^{II}(CN)$_4$]},[7] and {Fe(bpac)[M^{II}(CN)$_4$]}[19] which remain SCO at ambient pressure in the unloaded form. This suggests that in addition to tune the cooperativeness of the SCO (two-step, one step, hysteresis) the guests also influence on the stabilization of the LS state of the Fe^{II} nodes through host-guest π-π interactions in the present case.

5.5.- Experimental Section

5.5.1.- Physical measurements

Variable-temperature magnetic susceptibility data were recorded with a Quantum Design MPMS2 SQUID magnetometer equipped with a 7 T magnet, operating at 1 T and at temperatures 1.8-400 K. Experimental susceptibilities were corrected for diamagnetism of the constituent atoms by the use of Pascal's constants. Magnetic measurements under pressure were performed on **2M** (M = Ni, Pd, Pt) operating at 1 T in the temperature interval 1.8-300 K using a hydrostatic pressure cell made of hardened beryllium bronze with silicon oil as the pressure transmitting medium and operating over the pressure range 1 bar-10 kbar. The compounds were packed in a cylindrically shaped sample holder (1 mm in diameter and 5-7 mm in length) made up of very thing aluminum foil. The pressure was calibrated using the transition temperature of superconducting lead of high-purity 99.999%. TGA measurements were performed on a Mettler Toledo TGA/SDTA 851e, in the 150-400 K temperature range under a nitrogen atmosphere with a rate of 10 K min^{-1}. Analysis for C, H, and N were performed after combustion at 850 °C using IR detection and gravimetry by means of a Perkin-Elmer 2400 series II device. Powder X-ray measurements where performed on a PANalytical Empyrean X-ray powder diffractometer (monochromatic CuK_α radiation). All the samples were exclusively composed of single crystals prepared by using the slow liquid-liquid diffusion technique (layering) in standard test tubes. All manipulations involving solutions of Fe^{II} were performed in an argon atmosphere. Furthermore, very small quantities of ascorbic acid were added to these solutions to prevent oxidation of the Fe^{II} species.

5.5.2.- Single crystal X-ray diffraction

Single-crystal X-ray data were collected on an Oxford Diffraction Supernova diffractometer using graphite mono-chromated MoK_α radiation (λ = 0.71073 Å). A multi-scan absorption correction was performed. The structures were solved by direct methods using SHELXS-2014 and refined by full-matrix least squares on F^2 using SHELXL-2014.[20] Non-hydrogen atoms were refined anisotropically and hydrogen atoms were placed in calculated positions refined using idealized geometries (riding model) and assigned fixed isotropic displacement parameters.

5.5.3.- Synthesis

All chemicals were purchased from commercial suppliers and used without further purification. Ligand bpb was synthesized according to the procedure reported elsewhere.[21]

Synthesis of 2Ni, 2Pd, 2Pt. Microcrystalline samples were prepared in Ar atmosphere by adding dropwise water-methanolic solution of $K_2[M^{II}(CN)_4]$ (M^{II} = Ni, Pd or Pt) (0.2 mmol, 5 mL) to a methanolic solution containing $Fe(BF_4)_2 \cdot 6H_2O$ (0.4 mmol, 3 mL) and bpb (0.4 mmol) under vigorous stirring. The resulting red (**2M**) solid was stirred for 15 min, filtered, washed with water and dried in air (yield ca. 85%). EDX analysis (Energy dispersive X-ray analysis) confirmed the stoichiometry of bimetallic compounds: Fe:Ni or Fe:Pd or Fe:Pt = 1:1. Elemental analysis (%) for **2Ni** ($C_{20.14}H_{12.8}N_{6.2}OFeNi$) C, 51.17; H, 2.44; N, 18.30; found C, 51.55; H, 2.71; N, 18.27. Elemental analysis (%) for **2Pd** ($C_{20.14}H_{12.8}N_{6.2}OFePd$) C, 46.85; H, 2.47; N, 16.60; found C, 46.86; H, 2.14; N, 16.73. Elemental analysis (%) for **2Pt** ($C_{20.14}H_{12.8}N_{6.2}OFePt$) C, 40.06; H, 2.11; N, 14.20; found C, 39.97; H, 1.99; N, 14.01.

Synthesis of 2Ni-naph, 2Ni-phNO$_2$, 2Pd-naph, 2Pd-phNO$_2$ and 1Ag. Single crystals of the compounds were grown using a slow diffusion technique. A three-arm tube, containing in one arm $(NH_4)_2Fe(SO_4)_2 \cdot 6H_2O$ (20 mg, 51 mmol) dissolved in water (0.5 mL), in the second arm solid bpb (11 mg, 49 mmol) and guest (50 mg), and the third arm $K_2Ni(CN)_4 \cdot 3H_2O$ or $K_2Ni(CN)_4 \cdot H_2O$ (51 mmol) in water (0.5 mL), was carefully filled with a water-methanol (1:1) solution and sealed with parafilm. Square shaped yellow (**2Ni-naph**, **2Ni-phNO$_2$** and **2Pd-naph**) or brown (**2Pd-phNO$_2$**) crystals suitable for single crystal X-ray analysis were obtained in 6 weeks with yield ca. 20%. EDX analysis confirmed the stoichiometry of bimetallic compounds: Fe:Ni or Fe:Pd = 1:1, Fe:Ag = 1:2.

Elemental analysis (%) for **1Ag** ($C_{18}H_8Ag_2FeN_6$): calcd. C, 37.28; H, 1.39; N, 14.49; found C, 36.74; H, 1.35; N, 14.33. Elemental analysis (%) for **2Ni-naph** ($C_{38}H_{24}FeN_6Ni$): calcd. C, 67.20; H, 3.56; N, 12.37; found C, 65.75; H, 3.48; N, 12.06. Elemental analysis (%) for **2Ni-phNO$_2$** ($C_{30}H_{18}FeN_8O_4Ni$): calcd. C, 53.86; H, 2.71; N, 16.75; found C, 52.65; H, 2.64; N, 16.28. Elemental analysis (%) for **2Pd-naph** ($C_{38}H_{24}FeN_6Pd$): calcd. C, 62.79; H, 3.33; N, 11.56; found C, 61.66; H, 3.25; N, 11.33. Elemental analysis (%) for **2Pd-phNO$_2$** ($C_{30}H_{18}FeN_8O_4Pd$): calcd. C, 50.27; H, 2.53; N, 15.63; found C, 49.61; H, 2.47; N, 15.

5.6.- References

[1] O. Sato, *Nat. Chem.*, **2016**, *8*, 644.

[2] a) E. König, *Struct. Bonding (Berlin)*, **1991**, *76*, 51; b) P. Gütlich, A. Hauser, H. Spiering, *Angew. Chem., Int. Ed. Engl.*, **1994**, *33*, 2024; c) J. A. Real, A. B. Gaspar, V. Niel, M. C. Muñoz, *Coord. Chem. Rev.*, **2003**, *236*, 121; d) P. Gütlich, H. A. Goodwin, *Top. Curr. Chem.*, **2004**, Vols. *233-235*; e) J. A. Real, A. B. Gaspar, M. C. Muñoz, *Dalton Trans.*, **2005**, 2062; f) A. Bousseksou, G. Molnár, L. Salmon, W. Nicolazzi, *Chem. Soc. Rev.*, **2011**, *40*, 3313; g) M. A. Halcrow, John Wiley & Sons, **2013**.

[2] a) Y. García, V. Niel, M. C. Muñoz, J. A. Real, *Top. Curr. Chem.*, **2004**, *233*, 229; b) M. C. Muñoz, J. A. Real, John Wiley & Sons, **2013** pag. 121.

[3] a) V. Niel, J. M. Martínez-Agudo, M. C. Muñoz, A. B. Gaspar, J. A. Real, *Inorg. Chem.*, **2001**, *40*, 3838; b) V. Niel, M. C. Muñoz, A. B. Gaspar, A. Galet, G. Levchenko, J. A. Real, *Chem. Eur. J.*, **2002**, *8*, 2446.

[4] M. Ohba, K. Yoneda, G. Agustí, M. C. Muñoz, A. B. Gaspar, J. A. Real, M. Yamasaki, H. Ando, Y. Nakao, S. Sakaki, S. Kitagawa, *Angew. Chem. Int. Ed.*, **2009**, *48*, 4767.

[5] F. J. Muñoz-Lara, A. B. Gaspar, M. C. Muñoz, M. Arai, S. Kitagawa, M. Ohba, J. A. Real, *Chem. Eur. J.*, **2012**, *18*, 8013.

[6] G. Agustí, S. Cobo, A. B. Gaspar, G. Molnár, N. O. Moussa, P. Á. Szilágyi, V. Pálfi, C. Vieu, M. C. Muñoz, J. A. Real, A. Bousseksou, *Chem. Mater.*, **2008**, *20*, 6721.

[7] C. Bartual-Murgui, N. A. Ortega-Villar, H. J. Shepherd, M. C. Muñoz, L. Salmon, G. Molnár, A. Bousseksou, J. A. Real, *J. Mater. Chem.*, **2011**, *21*, 7217.

[8] F. J. Muñoz-Lara, A. B. Gaspar, M. C. Muñoz, V. Ksenofontov, J. A. Real, *Inorg. Chem.*, **2013**, *52*, 3.

[9] N. F. Sciortino, K. R. Scherl-Gruenwald, G. Chastanet, G. J. Halder, K. W. Chapman, J.-F. Létard, C. J. Kepert, *Angew. Chem. Int. Ed.*, **2012**, *51*, 10154.

[10] a) M. C. Muñoz, J. A. Real, *Coord. Chem. Rev*., **2011**, *255*, 2068; b) Z.-P. Ni, J.-L. Liu, Md. N. Hoque, W. Liu, J.-Y. Li, Y.-C. Chen, M.-L. Tong, *Coord. Chem. Rev*., **2017**, *335*, 28.

[11] a) J. E. Clements, J. R. Price, S. M. Neville, C. J. Kepert, *Angew. Chem. Int. Ed*., **2014**, *53*, 10164; b) J.-Y. Li, C.-T. He, Z.-M. Zhang, W. Liu, Z.-P. Ni, M.-L. Tong, *Chem. Eur. J*., **2015**, *21*, 1645; c) J.-Y. Li, C.-T. He, Y.-C. Chen, Z.-M. Zhang, W. Liu, Z.-P. Ni, M.-L. Tong, *J. Mater. Chem. C,* **2015**, *3*, 7830; d) I. A. Gural'skiy, B. O. Golub, S. I. Shylin, V. Ksenofontov, H. J. Shepherd, P. R. Raithby, W. Tremel, I. O. Fritsky, *Eur. J. Inorg. Chem.*, **2016**, 3191; e) F. J. Valverde-Muñoz, M. Seredyuk, M. C. Muñoz, K. Znovjyak, I. O. Fritsky, J. A. Real, *Inorg. Chem*., **2016**, *55*, 10654.

[12] L. Piñeiro-López, M. Seredyuk, M. C. Muñoz, J. A. Real, *Chem. Commun*., **2014**, *50*, 1833.

[13] A. Hauser, *Top. Curr. Chem.*, **2004**, *234*, 155.

[14] J. F. Létard, *J. Mater. Chem.,* **2006**, *16*, 2550.

[15] P. Gütlich, E. Bill, A. X. Trautwein, Springer, Heidelberg, **2010**.

[16] A. Spek, *Acta Crystallogr*. D, **2009**, *65*, 148.

[17] N. Ortega-Villar, M. C. Muñoz, J. A. Real, *Magnetochemistry*, **2016**, *2*, 16.

[18] C. Bartual-Murgui, A. Akou, H. J. Shepherd, G. Molnár, J. A. Real, L. Salmon, A. Bousseksou, *Chem. Eur. J.*, **2013**, *19*, 15036.

[19] G. M. Sheldrich, *SHELXL 2014*, University of Göttingen, Germany, **2014**.

[20] L. D. Ciana, A. J. Haim, *Heterocycl. Chem*., **1984**, *21*, 607.

5.7.- Supporting Information

Figure S1.- Thermal analysis of **1Ag** and **2M-Guest** (M = Ni, Pd; Guest = nitrobenzene and naphthalene).

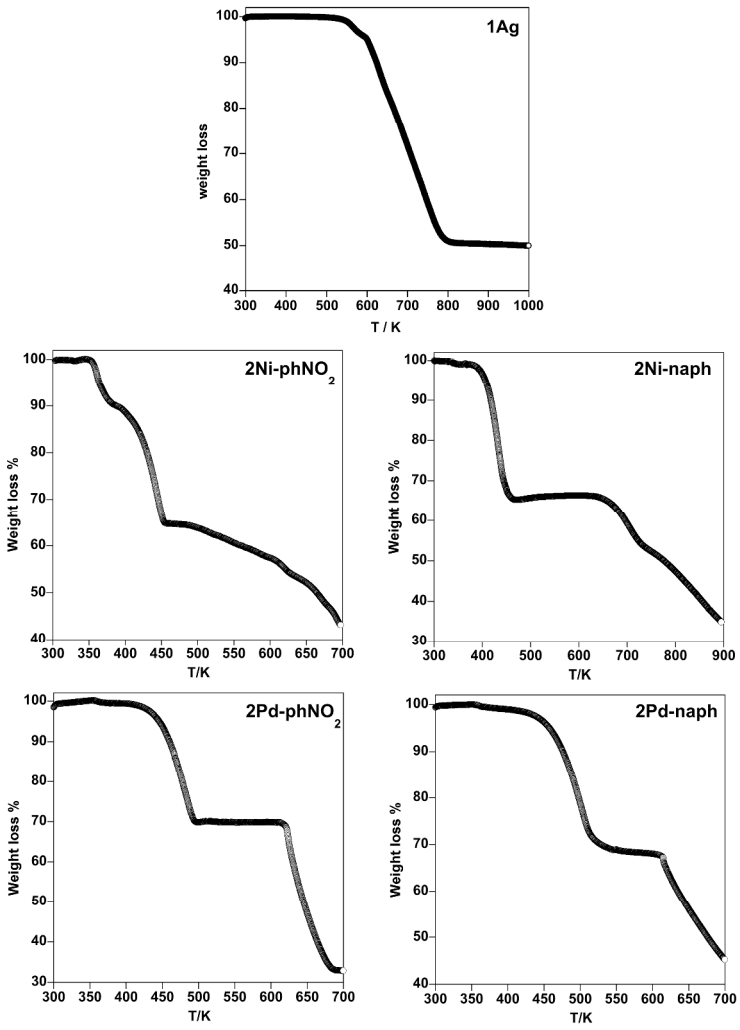

Figure S2.- TGA of **2Ni**, **2Pd** and **2Pt.**

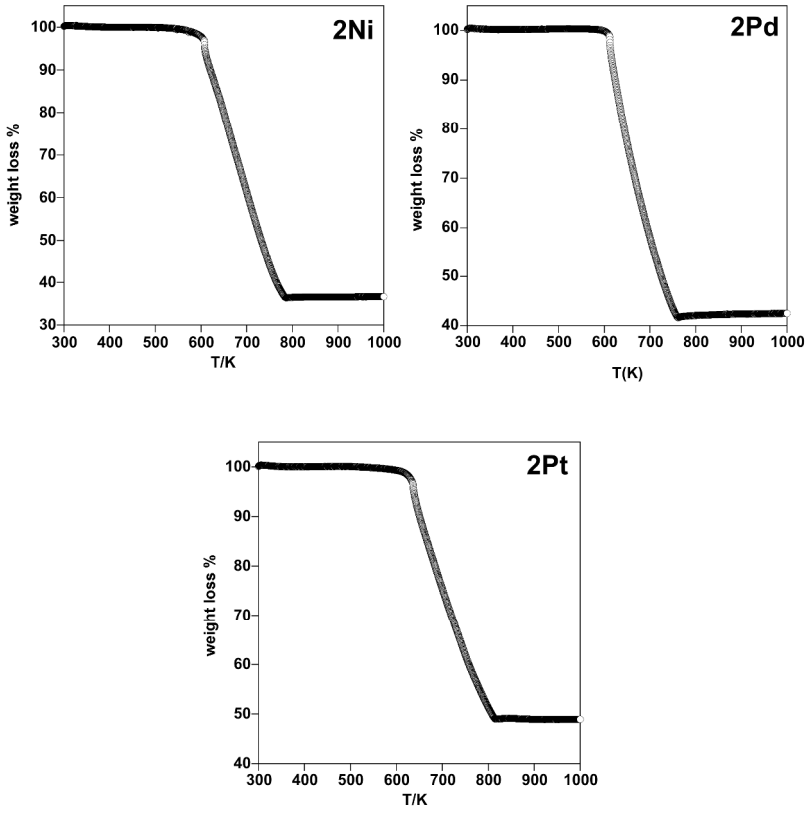

Figure S3.- (a) Experimental powder X-ray diffraction patterns for **2Ni**, **2Pd**, **2Pt** and simulated for **2Pt** from the single crystal structure of **2Pt-naph** at 250 K. (b) Fragment of the framework showing the plane 001 marked in red.

(a)

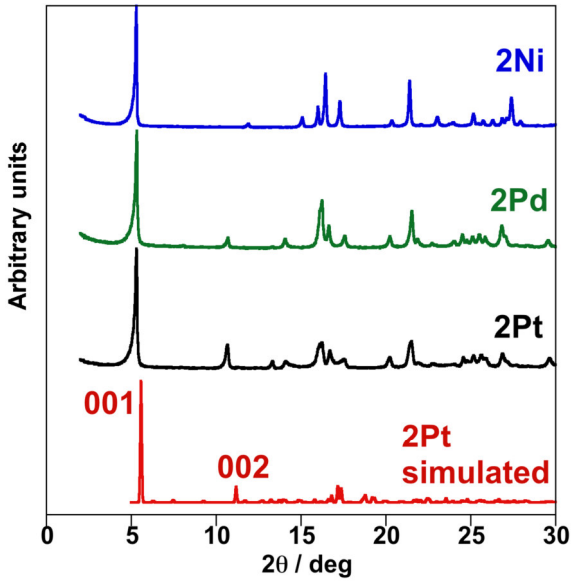

(b)

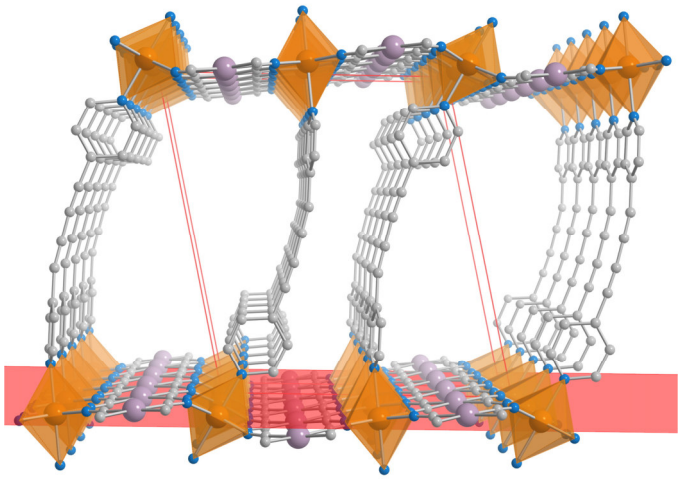

Figure S4.- (a) and (b) Projection on [001] direction of the four interpenetrated frameworks (highlighted with distinct colours) of **1Ag** showing the stacking of the pyridine moieties. (c) View of the same pyridine moieties projected approximately on [100]. (d) Three networks of **1Ag** passing through the rhombus-like window of the fourth network. Red lines correspond to short distance contacts below sum of Van der Waals radii of Ag atoms.

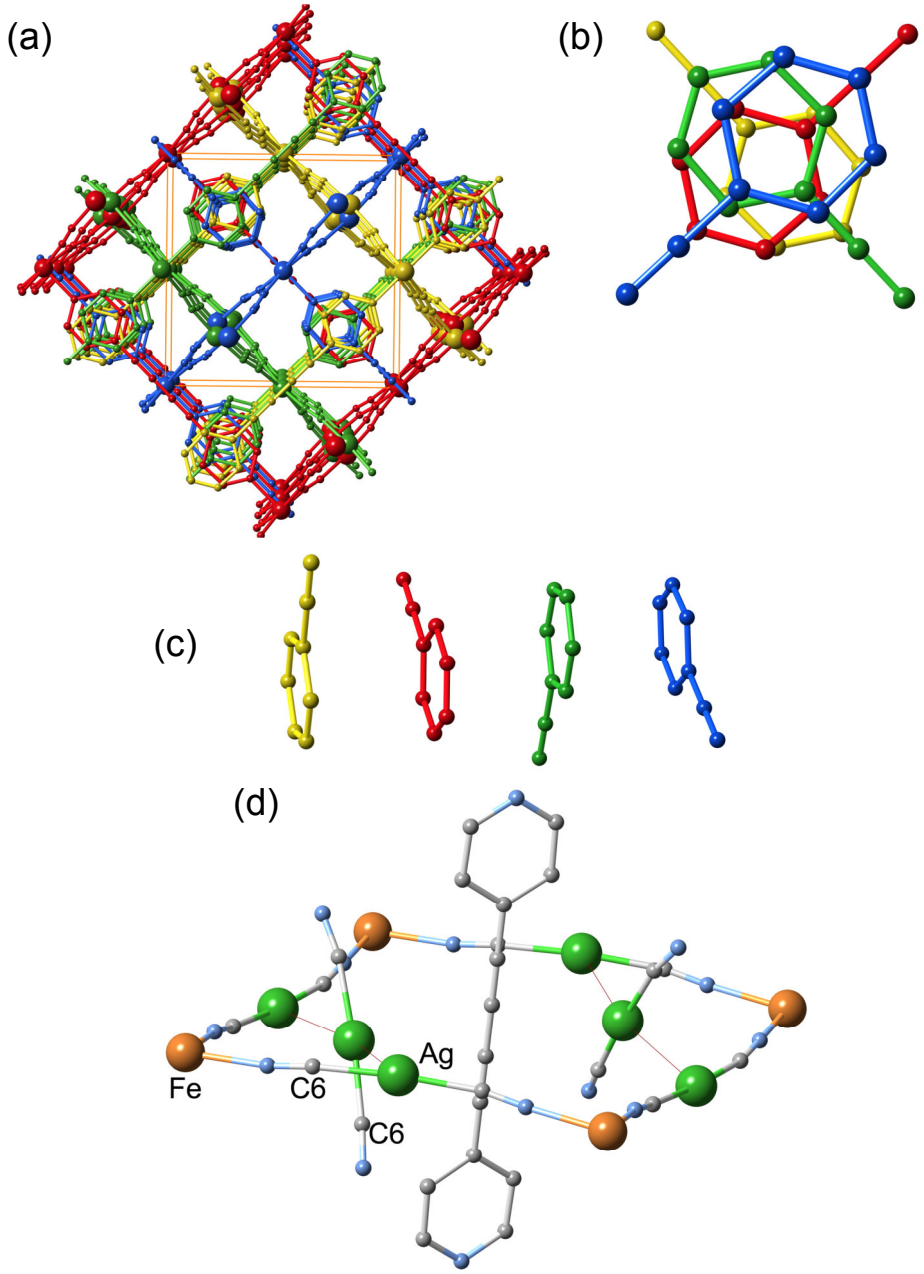

Figure S5.- 2Ni-naph and **2Pd-naph** structure in the mixed spin state. The Fe^{II} centers in the $\{Fe[M^{II}(CN)_4]\}_n$ layers define -LS-HS-LS- chains running along [010], while along [100] the chains display homogeneous spin states -HS-HS-HS- and -LS-LS-LS. Blue and orange octahedrons correspond to the LS and HS states, respectively.

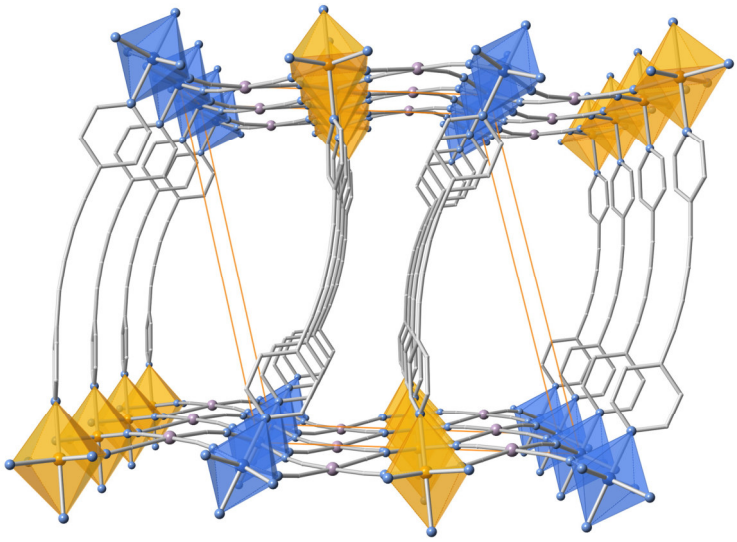

Figure S6.- Intermolecular contacts between naphthalene molecules **2Ni-naph** at 120 K.

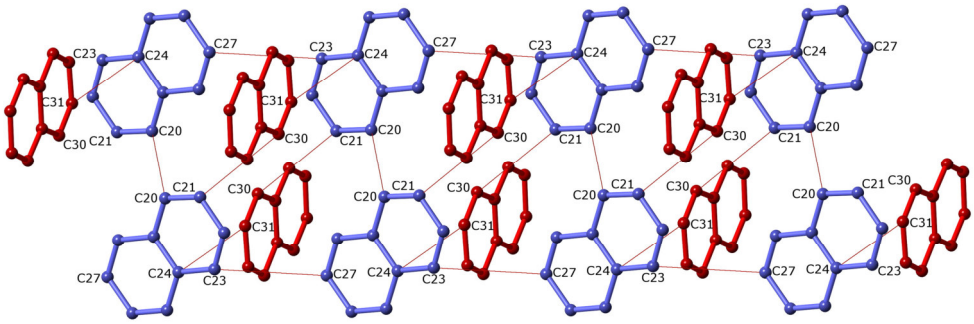

Table S1.- Critical temperatures (K) obtained from magnetic data [$\Delta T_{ci} = (T_{ci}\downarrow - T_{ci}\uparrow)$; $\Delta T_c^{av} = (T_{ci}\downarrow + T_{ci}\uparrow)/2)$].

	$T_{c1}\downarrow$	$T_{c1}\uparrow$	ΔT_{c1}	T_{c1}^{av}	$T_{c2}\downarrow$	$T_{c2}\uparrow$	ΔT_{c2}	T_{c2}^{av}		
Ni-naph	175	185	10	180	122.5	140	17.5	131.2	Two-step	this work
Pd-naph	211.2	217.5	6.3	214.5	195.6	205	9.4	200.3	Two-step	this work
Pt-naph	205.0	216.0	11.0	210.5	188.0	203	15	195.5	Two-step	Ref.12
Ni-phNO_2	227.2	240.8	13.6	234.0	220.6	231.4	10.8	226.0	Two-step	this work
Pd-phNO_2	227.0	246.4	19.4	236.7	-	-	-	-	One-step	this work
Pt-phNO_2	210.0	237	27	223.5	-	-	-	-	One-step	Ref. 12

Table S2.- Intermolecular contacts in **2Ni-naph** at different temperatures [Å].

		120 K	**150 K**	**250 K**
Intermolecular	C1···C26	3.625(8)	-	-
contacts of	C1···C27	3.580(9)	3.643(12)	3.66(2)
moieties around	C1···C32	3.502(8)	3.575(10)	3.597(13)
Fe(1)	C1···C33	3.474(7)	3.555(8)	3.598(11)
	C2···C31	3.560(8)	3.648(11)	3.67(2)
	C2···C32	3.489(8)	3.501(9)	3.600(13)
	C2···C33	3.569(7)	3.579(8)	3.687(11)
	C2···C34	3.637(8)	-	-
	C3···C29	3.502(7)	3.667(10)	3.675(11)
	C3···C34	3.523(7)	3.573(9)	3.660(10)
	C4···C34	3.651(8)	-	-
	C4···C35	3.424(8)	3.453(9)	3.561(13)
	C4···C36	3.619(8)	3.432(9)	3.506(14)
	C5···C11	3.361(6)	3.379(8)	3.508(7)
	C5···C35	3.472(7)	3.503(8)	3.594(12)
	C6···C21	3.661(9)	-	-
	C6···C29	3.392(7)	3.481(8)	3.586(11)
	C6···C30	3.604(8)	-	-
	C6···C38	3.616(8)	3.600(10)	3.692(11)
	C7···C20	3.568(9)	3.615(12)	3.645(13)
	C7···C21	3.387(9)	3.448(12)	3.52(2)
	C7···C29	3.665(7)	3.690(9)	-
	C7···C38	3.431(8)	3.476(10)	3.618(14)
	C5···C8	3.503(7)	3.547(9)	-
	C8···C25	-	-	3.69(2)
	C8···C32	3.652(7)	-	-
	C8···C33	3.673(7)	-	-
	C11···C33	3.614(6)	3.617(8)	-

Table S2 cont.- Intermolecular contacts in **2Ni-naph** at different temperatures [Å].

		120 K	**150 K**	**250 K**
Intermolecular contacts of moieties around Fe(2)	C12···C25	3.407(7)	3.574(10)	3.644(16)
	C13···C23	3.457(8)	3.606(10)	3.529(10)
	C13···C24	3.445(7)	3.621(10)	3.672(10)
	C13···C25	3.417(8)	3.595(11)	3.658(18)
	C13···C36	3.551(8)	3.606(11)	3.699(15)
	C14···C24	3.436(7)	3.480(10)	3.554(11)
	C14···C25	3.589(8)	3.633(11)	-
	C15···C25	3.683(10)	3.697(11)	-
	C15···C26	3.697(11)	3.684(11)	-
	C16···C25	-	3.670(10)	-
	C16···C26	3.541(8)	3.497(10)	3.687(15)
	C17···C19	3.637(8)	3.696(10)	-
	C17···C24	3.658(8)	-	-
	C18···C18*	-	3.699(11)	3.662(11)
	C18···C20	3.495(9)	3.539(11)	3.600(14)
	C18···C21	3.491(9)	3.519(11)	3.59(2)
	C9···C12	3.437(6)	3.693(8)	-
	C9···C16	3.609(8)	-	-
	C10···C12	3.642(8)	-	-
	C10···C25	3.491(7)	3.552(9)	3.67(2)
Intermolecular contacts between guest molecules	C20···C20*	3.553(9)	3.617(11)	-
	C21···C30	3.576(9)	3.678(12)	3.64(2)
	C23···C27	3.612(9)	3.693(11)	-
	C24···C31	3.594(8)	3.665(11)	-
	C25···C32	3.695(8)	-	-
	C27···C23	3.612(9)	-	-
	C28···C22	3.613(9)	-	3.68(2)

Table S3.- Intermolecular contacts in **2Ni-phNO$_2$** at different temperatures [Å].

		120 K	**295 K**
Intermolecular contacts of moieties around Fe(1)	C1···C8	3.365(6)	3.557(5)
	C2···C16	3.654(4)	-
	C3···C15	3.5414(11)	3.6684(7)
	C4···C18	3.688(4)	-
	C4···C19	3.700(5)	-
	C5···C17	3.557(2)	3.689(2)
	C5···C18	3.668(5)	-
	C7···C13	3.613(12)	-

Table S3 cont.- Intermolecular contacts in **2Ni-phNO$_2$** at different temperatures [Å].

		120 K	**295 K**
Intermolecular contacts of moieties around Fe(2)	C9···C10	3.532(7)	-
	C10···C24	3.677(9)	-
	C11···C23	3.537(10)	3.632(11)
	C13···C21	3.647(10)	-
	C14···C13	3.644(13)	3.633(11)
	C14···C14	3.513(12)	3.627(10)
	C14···C21	3.673(17)	-

Table S4.- Intermolecular contacts in **2Pd-naph** at different temperatures [Å].

		120 K	**204 K**	**250 K**
Intermolecular contacts of moieties around Fe(1)	C1···C26	3.64(2)	-	-
	C1···C32	3.58(2)	3.63(2)	3.65(2)
	C1···C33	3.55(2)	3.624(14)	3.68(2)
	C2···C31	3.60(2)	3.69(2)	-
	C2···C32	3.55(2)	3.56(2)	3.68(2)
	C2···C33	3.62(2)	3.640(14)	-
	C3···C29	3.59(2)	-	-
	C3···C34	3.60(2)	3.639(14)	-
	C4···C35	3.51(2)	3.52(2)	3.64(2)
	C4···C36	3.52(2)	3.49(2)	3.64(2)
	C5···C11	3.332(14)	3.539(11)	3.511(9)
	C5···C35	3.56(2)	3.612(14)	-
	C6···C29	3.46(2)	3.52(2)	3.642(14)
	C6···C30	3.69(2)	-	-
	C6···C38	3.52(2)	3.65(2)	-
	C7···C20	3.60(2)	-	-
	C7···C21	3.44(2)	-	-
	C7···C27	-	3.51(2)	-
	C7···C28	-	3.67(2)	-
	C7···C38	3.45(2)	3.55(2)	3.68(2)
	C8···C33	-	3.679(12)	-
	C11···C33	3.67(2)	-	-

Table S4 cont.- Intermolecular contacts in **2Pd-naph** at different temperatures [Å].

		120 K	**204 K**	**250 K**
Intermolecular contacts of moieties around Fe(2)	C9···C12	3.471(13)	-	-
	C9···C16	3.57(2)	-	-
	C9···C23	-	3.58(2)	-
	C10···C12	3.55(2)	3.693(10)	-
	C10···C25	3.52(2)	-	-
	C12···C25	3.52(2)	-	-
	C13···C22	-	-	3.63(2)
	C13···C23	3.50(2)	-	3.50(2)
	C13···C24	3.54(2)	-	-
	C13···C25	3.51(2)	3.62(2)	-
	C13···C36	3.69(2)	-	-
	C14···C24	3.49(2)	3.55(2)	-
	C14···C25	3.62(2)	-	-
	C16···C22	-	3.64(2)	-
	C17···C20	-	-	3.69(2)
	C17···C24	3.70(2)	-	-
	C18···C18*	-	3.69(2)	3.63(2)
	C18···C20	3.58(2)	-	3.54(2)
	C18···C21	3.56(2)	-	-
	C18···C27	-	3.58(2)	-
	C18···C28	-	3.63(2)	-
Intermolecular contacts between guest molecules of naphthalene	C20···C20*	3.60(2)	-	-
	C21···C30	3.60(2)	-	-
	C24···C31	3.62(2)	-	-
	C27···C23	3.68(2)	-	-
	C28···C22	3.70(2)	-	-

Table S5.- Intermolecular contacts in **2Pd-phNO$_2$** at different temperatures [Å].

		120 K	**260 K**
Intermolecular contacts of moieties around Fe(1)	C3···C19	3.632(8)	-
	C4···C24	3.691(8)	-
	C8···C28	-	3.579(10)
	C11···C30	-	3.661(9)
Intermolecular contacts of moieties around Fe(2)	C13···C30	-	3.662(9)
	C14···C30	-	3.644(9)
	C15···C29	-	3.614(9)
	C18···C25	3.66(2)	3.671(10)
	C18···C26	-	3.693(9)

Table S6.- Intermolecular contacts in **2Pt-naph** at different temperatures [Å].

		120 K	**150 K**	**250 K**
Intermolecular contacts of moieties around Fe(1)	C1···C26	3.670(11)	-	-
	C1···C33	3.561(9)	3.622(5)	3.67(4)
	C1···C32	3.568(12)	3.620(5)	3.69(5)
	C2···C31	3.619(12)	3.674(6)	-
	C2···C32	3.552(11)	3.541(5)	-
	C2···C33	3.644(10)	3.623(5)	-
	C3···C34	3.590(10)	3.637(4)	-
	C3···C29	3.588(10)	-	-
	C4···C35	3.490(12)	3.518(5)	3.60(4)
	C4···C36	3.481(12)	3.507(5)	3.63(5)
	C5···C35	3.573(10)	3.620(4)	-
	C6···C29	3.447(10)	3.526(5)	3.66(4)
	C6···C38	3.522(12)	3.665(5)	-
	C7···C38	3.444(12)	3.539(5)	3.61(5)
	C7···C21	3.457(14)	3.487(6)	3.58(6)
	C7···C20	3.597(14)	3.643(6)	3.67(6)

Table S6 cont.- Intermolecular contacts in **2Pt-naph** at different temperatures [Å].

		120 K	**150 K**	**250 K**
Intermolecular contacts of moieties around Fe(2)	C13···C25	3.561(12)	-	-
	C13···C24	3.553(10)	-	-
	C13···C23	3.490(11)	3.624(6)	3.63(5)
	C14···C25	3.648(12)	-	-
	C14···C24	3.501(10)	3.558(5)	3.65(4)
	C16···C26	3.670(11)	3.628(6)	-
	C16···C25	-	3.693(6)	-
	C18···C20	3.554(12)	3.607(6)	-
	C18···C21	3.545(13)	3.575(6)	-
	C20···C20*	3.644(12)	3.684(6)	-
	C27···C23	3.695(13)	-	-
Intermolecular contacts between guest molecules of naphthalene	C28···C22	3.690(12)	-	-
	C21···C30	3.597(13)	-	3.67(6)
	C24···C31	3.634(12)	-	-

Table S7.- Intermolecular contacts in **2Pt-phNO$_2$** at different temperatures [Å].

		120 K	**250 K**
Intermolecular contacts of moieties around Fe(1)	C1···C23	3.645(11)	-
	C3···C19	3.618(12)	-
	C4···C24	3.696(12)	-
	C1···C19	3.656(11)	-
	C3···C19	3.648(12)	-
Intermolecular contacts of moieties around Fe(2)	C8···C23	3.681(11)	3.59(3)
	C11···C29	3.554(12)	-

CAPÍTULO 6

Spin-crossover behaviour in a new family of porous coordination polymers formulated $\{Fe(3,8\text{-phen})_2[Au(CN)_2]_2\}\cdot G$

CAPÍTULO 6

Spin-crossover behaviour in a new family of porous coordination polymers formulated $\{Fe(3,8\text{-phen})_2[Au(CN)_2]_2\}\cdot G$

6.1.- Abstract

Self-assembly of Fe^{II}, 3,8-phenantroline (3,8-phen) and dicyanoaurate ($[Au(CN)_2]^-$) building blocks in presence of different aromatic guest molecules has afforded a new series of 3D Hofmann-like clathrate compounds formulated $\{Fe(3,8\text{-phen})[Au(CN)_2]_2\cdot G\}$ (**1**·G) where G = 2,5-dimethylthiophene, thiophene, benzonitrile, benzaldehyde, nitrobenzene, 1,3-dibromobenzene, fluorobenzene, chlorobenzene, bromobenzene. The structure of **1**·G is made up of two interpenetrated 3D networks with the topology of the archetypal α-Po structure. Each network consists of a stack of $\{Fe[Au(CN)_2]_2\}_n$ layers lying parallel to the *x*-*y* plane and pillared by 3,8-phen ligands which connect the Fe^{II} sites of consecutive layers along *z*. The networks interact each other through strong aurophilic interactions thereby generating an accessible void of 787.5 $Å^3$ (35% of the unit cell) at 120 K where the guest molecules are located. These clathrates display abrupt multi-step SCO behaviours in the temperature interval 80-280 K. The presence of the guest molecules in the pores influences markedly the nature of the SCO i.e. the number of SCO steps, its characteristic temperatures, the occurrence of hysteresis loop and its width. Magnetic, calorimetric (**1**·G), photomagnetic (**1**·$bzNO_2$, **1**·thiophene) and structural (**1**·$bzNO_2$) properties have been studied. Calorimetric, powder X-ray diffraction and thermal stability studies of **1**·G are also presented and discussed.

6.2.- Introduction

Undoubtedly, the use of Fe^{II} SCO building blocks has proved to be a suitable strategy for the construction of functional materials with switch and memory transduction properties[1] since they are capable of reversibly changing their magnetic, structural, dielectric and optical properties in response to an external stimulus such as the variation of the temperature, pressure, light irradiation or analyte.[2] In particular, Hofmann-like coordination polymers generally formulated $\{Fe(L)[M^{II}(CN)_4]\}\cdot G$ (L = pz, [3] bpe, [4] azpy, [5] bpac,[6] bpben,[7] dpsme,[8] bpb[9] M^{II}= Ni, Pd, Pt) have led to highly cooperative thermo-,

piezo-, and photo-switchable 2-3D coordination polymers. In these compounds, the host interact with the enclathrated guest molecule through intermolecular interactions, i.e. hydrogen bonds, van der Waals or π-π interactions. In turn, these noncovalent interactions greatly affect the Fe^{II} switching transitions (globally, HS↔LS, S = 2↔S = 0) in solid-state which result in guest-dependent SCO properties.[10]

The formal replacement of the $[M^{II}(CN)_4]^{2-}$ anions by $[M^{I}(CN)_2]^{-}$ groups (L = bpe, pmd, 5-Brpmd, 3CNpy, 3Xpy, M^{I} = Ag, Au) has led to 2-3D SCO polymers with interesting pressure and light induced properties coupled with cooperative spin transitions which also show different chemical properties such as crystalline-state ligand-substitution reactions[11] with remarkable structural changes or metallophilicity.[12] In the case of halogen-pyridine SCO compounds, it has been shown that the presence of guest molecules inside the framework plays an important role in the stabilization of the LS spin state favoring the occurrence of SCO phenomenon.[13] Also, it has been proved that the use of larger organic bridges such as bpe favors interpenetration of identical layers which generates voids where solvent molecules could be installed.[14] Unfortunately, the lack of rigidity of these bridging ligands usually makes the SCO poorly cooperative and incomplete.

Recently, the use of Fe^{II} and $[Au(CN)_2]^{-}$ in combination with organic ligands derived from pyridine or bis-monodentate pyridine-like linear bridging ligands (i.e. pz[15], Fpz[16], 2,5-bpp[17], bipytz[18], bipydz[19]) has afforded an exceptionally rich variety of Hofmann-type CPs with interesting structural, physical and chemical properties including abrupt and complete SCO behaviours near room temperature. In general, these compounds display a twofold-interpenetrated 3D network. In the case of pz, 2,5-bpp and bipytz derivatives, strong aurophilic interactions are observed between two perpendicular sides of the $\{Fe_4[Au(CN)_2]_4\}$ grids of two closest layers. Despite the interpenetration and due to the long length of the pillar ligands, these compounds exhibit large accessible cavities where guest molecules are located. Since these frameworks do not substantially change upon guest removal/absorption, they can serve as platforms to study the influence of guest molecules over the intrinsic SCO properties displayed by the unloaded framework. In the case of 2,5-bpp and bipytz derivatives, the interpenetrated 3D framework is further stabilized by a network of host-guest and host-host contacts, respectively. Covalent post-synthetic modification of bipytz derivative leads to bipydz derivative which also displays the aforementioned interpenetrated Hofmann-type 3D

topology. Moreover, a bipydz derivative has recently been synthetized by slow diffusion of its components in ethanol. In spite of both complexes having the same general structure, the as-synthesized phase displays an abrupt, hysteretic, four-step SCO behaviour as a consequence of host-guest and guest-guest interactions arising from ligand and solvent ordering. In contrast, the post-synthetic modificated phase, displaying neither ligand nor solvent ordering, features a gradual SCO behaviour.

Considering that the pillar ligand in SCO Hofmann-type compounds presents aromatic units, the use of aromatic molecules as guest molecules will lead to host-guest π-π interactions as the primary noncovalent intermolecular interactions within the framework. Therefore, specific SCO properties could be achieved by adjusting these π-π interactions i.e. selecting a suitable guest molecule for a particular framework. However, understanding how these interactions truly work[20] and how they consequently affect the ligand field felt by Fe^{II} centers[21] is out of reach, so far. Therefore, the synthesis and physical characterization of new guest-dependent SCO materials[22] together with theoretical studies on host-guest interactions and their influence over the spin transition[23] seem essential for the rational design of nanomaterials with enhanced, controllable and reproducible properties.

As a continuation of this research line, herein we report the synthesis and characterization of a new Hofmann-type SCO-CPs series generally formulated {Fe(3,8-phen)$[Au(CN)_2]_2$·G} (**1**·G) where G = thiophene, 2,5-dimethylthiophene, benzonitrile, benzaldehyde, nitrobenzene, fluorobenzene, chlorobenzene, bromobenzene and 1,3-dibromobenzene as guest molecules. The aromatic guests were incorporated during the formation of the framework by the one-pot synthetic approach. In general, the crystal structure of **1**·G consists of a twofold-interpenetrated 3D network where 2D $\{Fe[Au(CN)_2]_2\}_\infty$ layers are pillared by the 3,8-phen ligand in the [001] direction. Interestingly, strong Au···Au contacts that change with temperature are observed between two closest layers. Interpenetration does not preclude the formation of a 1D channel which runs along the *b* axis; hence, aromatic guest molecules are located within this cavity and interact with the pillar ligand through π-π interactions. Single crystal X-ray diffraction studies (**1**·$bzNO_2$), the magnetic data (**1**·G) and DSC measurements (**1**·G) show that these compounds undergo complete, cooperative and multi-step spin transitios in the temperature interval 80-280 K. Since **1**·G clatrathes display the same spatial distribution (location, density and orientation within the framework), as evidenced

by single-crystal and powder X-ray diffraction studies (**1**·bzNO$_2$ and **1**·G, respectively) plus TGA (**1**·G), we conclude that the different SCO behaviours displayed by the present series i.e. the number of SCO steps, their characteristic temperatures, the occurrence of hysteresis loops and their width, are due to different substituent-induced changes in the host-guest π-π stacking which, in turn, affects the ligand field felt by the Fe^{II} centers. Appealingly, **1**·thiophene and **1**·bzNO$_2$ display the well-known LIESST effect[24] with T_{LIESST} ca. 44 K. Meanwhile, the variations in the thermodynamic parameters ΔH and ΔS associated with the occurrence of SCO phenomena in the present series are within the range of values typically displayed by strong cooperative SCO Hofmann-like clathrates based on Fe^{II} centers.[10] Finally, some **1**·G clathrates (G = thiophene, bzCl, bzBr and 1,3-diBrbz) seem ideal for the development of expanded information storage devices since they display multi-step and multi-stable hysteretic SCO transitions.

6.3.- Results

6.3.1.- Synthesis

The 3,8-phen ligand was synthetized following a standard procedure which is summarized in the Supporting Information (6.8.1). The herein reported **1**·G compounds were synthesized by means of slow liquid-liquid diffusion techniques using a modified H-vessel. Yellow cube-shaped single crystals were formed with relative high yield (ca. 50%) two weeks later. The presence and quantification of the guest molecules in **1**·G (G = 2,5-dmthiophene, thiophene, bznitrile, bzaldehyde, bzNO$_2$ and 1,3-diBrbz) were confirmed by TGA. Complete structural characterization of **1**·bzNO$_2$ was achieved by means of single crystal X-ray diffraction studies whereas the XRPD patterns displayed by **1**·G show that all these clathtrates are isostructural.

6.3.2.- Magnetic properties

Plots of $\chi_M T$ vs. T, where $\chi_M T$ is the molar magnetic susceptibility and T is the temperature, are displayed in Figure 2 for **1**·G. The $\chi_M T$ values are ≈ 3.73 cm^3 K mol^{-1} at 300 K for the whole series. Upon cooling, the $\chi_M T$ value decreases to ≈ 0 cm^3 K mol^{-1} at 80 K, which implies the occurrence of a complete spin transition from the HS state to the LS state for all **1**·G clathrates. In general, **1**·G feature multi-step SCO behaviours. In the

case of **1**·2,5-dmthiophene, **1**·bzF and **1**·bznitrile, the Fe^{II} centers undergo spin transition in two equally spaced steps defining a plateau centered around 184, 250 and 255 K, respectively. In these clathrates, the heating mode shows a quite narrow hysteresis (1 K) at high temperature whereas a much wider hysteresis loop takes place at low temperature (10, 6.5 and 5.6 K wide, respectively). A particular unequally spaced two-step spin transition can be seen for **1**·bzaldehyde. Upon cooling, $\chi_M T$ decreases steeply to ≈ 1.33 cm^3 K mol^{-1} at 182 K. Afterwards, $\chi_M T$ varies less steeply until $\chi_M T$ ≈ 1.20 cm^3 K mol^{-1} at 163 K. Finally, a new inflection followed by a sharp drop leads to $\chi_M T$ ≈ 0 cm^3 K mol^{-1} at 100 K. The heating mode shows a 5 K wide hysteresis loop at low temperature.

1·$bzNO_2$ displays an unequally spaced three-step spin transition. Initially, $\chi_M T$ decreases quite steeply as the temperature is lowered. Below 236 K, $\chi_M T$ vs. T plot defines a plateau (ca. 223 K) involving ≈ 52% of Fe^{II} centers in the LS state. For temperatures below 212 K, $\chi_M T$ experiences a new drop and defines a second plateau (ca. 204 K) which involves an additional ≈ 35% of Fe^{II} centers in the LS state. A very narrow hysteresis (≤ 1 K wide) can be seen from comparison with the heating mode.

1·bzBr, **1**·bzCl and **1**·1,3-diBrbz display more abrupt and hysteretic three-step SCO behaviours than **1**·$bzNO_2$. In these clathrates, $\chi_M T$ decreases quite steeply below 248 K. Upon cooling, $\chi_M T$ vs. T curves show a plateau (ca. 197, 218 and 212 K, respectively) which involves ≈ 50% of Fe^{II} centers in the LS state. Further cooling leads to a smaller plateau (ca. 170, 194 and 185 K, respectively) involving an additional ≈ 29% of Fe^{II} centers in the LS state. After a new sharp drop on $\chi_M T$ vs. T plots, $\chi_M T$ ≈ 0 cm^3 K mol^{-1} at 139, 175 and 178 K, respectively. In all three cases, the heating mode evidences the occurrence of a narrow hysteresis at low temperatures (10, 9 and 5 K wide, respectively). Moreover, **1**·bzBr and **1**·bzCl display 7 K wide hysteresis loop at medium high temperature whereas **1**·1,3-diBrbz barely shows 1 K wide hysteresis loop in the same temperature range. Finally, only **1**·bzBr and **1**·bzCl present narrow hysteresis (4 and 3 K wide, respectively) at high temperature.

Interestingly, in **1**·thiophene the Fe^{II} centers undergo spin transition in four unequally spaced steps. $\chi_M T$ ≈ 3.62 cm^3 K mol^{-1} at 300 K remains almost constant until 184 K. Below this temperature, $\chi_M T$ decreases steeply until it describes an 11 K wide plateau (ca. 175 K) involving ≈ 32% of Fe^{II} centers in the LS state. For temperatures

below 168 K, $\chi_M T$ experiences a new sharp drop and defines a 36 K wide plateau (ca. 155 K) which involves an additional ≈ 16% of Fe^{II} centers in the LS state. Below 125 K, another sharp drop of $\chi_M T$ (≈ 1.07 cm^3 K mol^{-1} at 119 K) is consistent with an additional ≈ 23% of Fe^{II} centers in the LS state. From now on, $\chi_M T$ decreases less steeply to a value of ≈ 0 cm^3 K mol^{-1} at 86 K. The heating mode shows 25, 30, 11 and 4 K wide hysteresis loops at low, medium, medium-high and high temperatures, respectively. Further details on the critical temperatures, Tc, in both cooling and heating modes for **1**·G clathrates are given in Table 1.

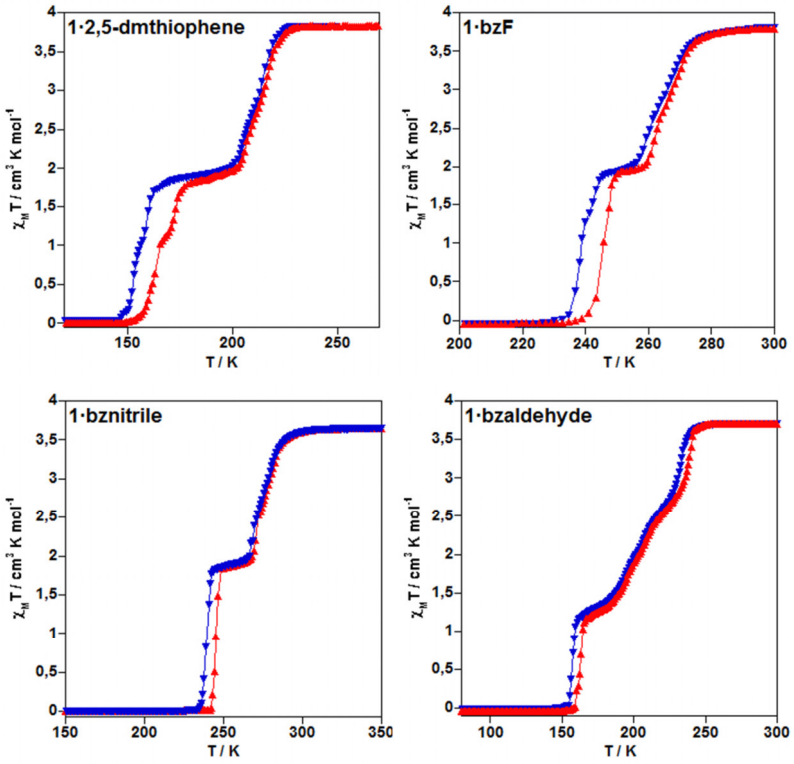

Figure 2.- Magnetic behaviours displayed by **1**·G. The cooling and heating modes are shown in blue and red colours, respectively.

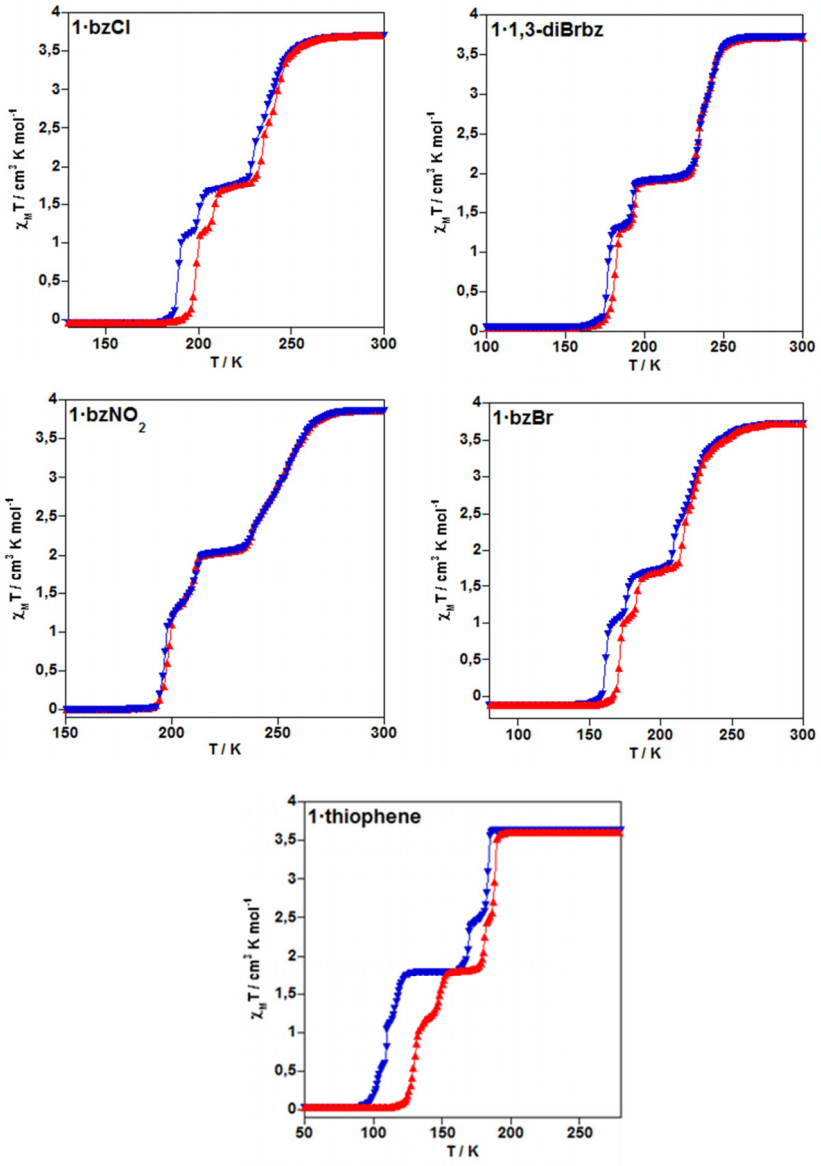

Figure 2 cont.- Magnetic behaviours displayed by **1**·G. The cooling and heating modes are shown in blue and red colours, respectively.

Table 1.- Critical temperatures (Tc) displayed by **1**·G both in the cooling and heating modes.

Compound	T_c^{down}- T_c^{up} [K]			
	1st Step	2nd Step	3rd Step	4th Step
1·2,5-dmthiophene	212-214	155-165	-	
1·bzF	264-266	239-245	-	
1·bznitrile	274-276	239-245	-	
1·bzaldehyde	208	158-163	-	
1·bzNO_2	250	211	196-197	
1·bzBr	223	176-184	161-171	
1·bzCl	236-239	200-208	189-199	
1·1,3-diBrbz	239	192-194	177-182	
1·thiophene	184-185	169-180	116-148	103-129

Table 1 cont.- Average Tc displayed by **1**·G.

Compound	Tc [K]$_{average}$			
	1st Step	2nd Step	3rd Step	4th Step
1·2,5-dmthiophene	213	160	-	
1·bzF	265	242	-	
1·bznitrile	275	242	-	
1·bzaldehyde	209	160	-	
1·bzNO_2	250	211	197	
1·bzBr	223	180	166	
1·bzCl	238	204	194	
1·1,3-diBrbz	239	193	179	
1·thiophene	185	175	132	116

Photogeneration of the metastable HS* state at low temperature, the so-called Light-Induced Spin State Trapping experiment (LIESST)[24], was carried out on a microcrystalline sample of **1**·bzNO_2 (2.214 mg) and **1**·thiophene (1.859 mg). The results are displayed in Figure 3. Firstly, their magnetic responses were measured in the cooling mode at 1 K min^{-1} rate from 300 to 10 K with an applied magnetic field of 1 T (χ_MT ≈ 0 cm^3 K mol^{-1}). After that, the samples were irradiated with green light (λ = 532 nm) for 3 h, i.e. the time required to attain saturation values of χ_MT ≈ 2.58 and 2.84 cm^3 K mol^{-1} which represents ≈ 67% and ≈ 79% of LS→HS conversion, respectively (percentages were obtained from comparison with the corresponding value of χ_MT at room temperature). The light irradiation was then switched off and the temperature increased to 300 K at 0.3 K min^{-1} rate. Consequently, χ_MT increases in the temperature region 10-15 and 10-25 K to a maximum value of ≈ 2.78 and ≈ 2.84 cm^3 K mol^{-1} at 15 and 25 K, respectively. This indicates a thermal population of the different microstates arising from zero-field splitting of the S = 2 excited state, thus, the light-induced population of the HS state is virtually complete at 15 K for **1**·bzNO_2 and at 25 K in the case of **1**·thiophene. At

temperatures greater than ≈ 23 K, $\chi_M T$ drops rapidly to ≈ 0 cm^3 K mol^{-1} at 56 K, indicating the occurrence of a complete HS→LS relaxation for both clathrates. The T_{LIESST} temperatures, determined from the maximum variation of $\chi_M T$ in the HS→LS relaxations are 44 and 43 K, respectively (Figure S2, Supporting Information). A detailed study of the relaxation kinetics is ongoing to prove the presence of intermediate phases in the photo-induced state lifetime of both clathrates.

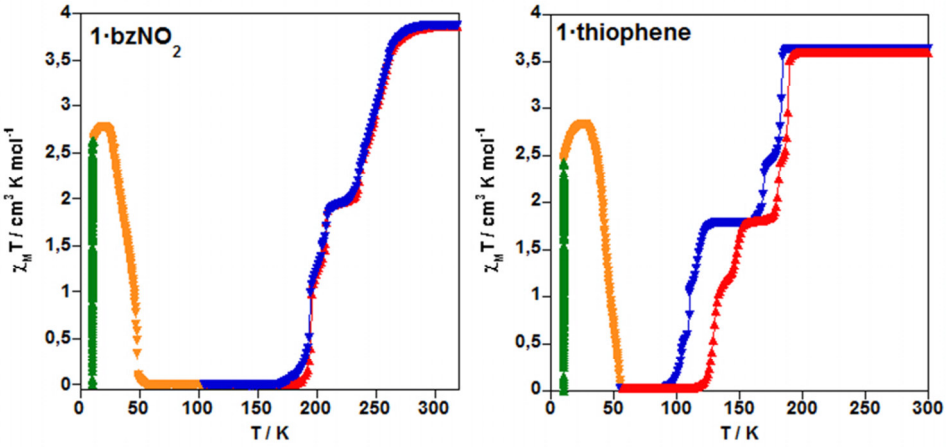

Figure 3.- LIESST experiment for **1**·$bzNO_2$ and **1**·thiophene.

6.3.4.- Calorimetric and thermogravimetric studies

DSC measurements were carried out for **1**·G clathrates. The anomalous variations of the molar specific heat, ΔCp, vs. the temperature, T, for the cooling and heating modes are displayed together with the $\chi_M T$ vs. T plots in Figure 4. The ΔCp vs. T plots show the presence of two or three sets of peaks that overlap to a greater or lesser extent and reflect the changes in the slope observed in the $\chi_M T$ vs. T curves. Moreover, each set of peaks and inner peaks are reminiscent of those detected in the $(\chi_M T)/\delta T$ vs. T plots (Figure S1, Supporting Information). The obtained Tc temperatures agree reasonably well with those deduced from the magnetic data. Furthermore, the average ΔH and ΔS variations for each step associated with the cooling and heating modes are gathered in Table 2.

For **1**·G (G = 2,5-dmthiophene, bzF, bznitrile and bzaldehyde), the ΔCp vs. T plots show two sets of peaks, each of them corresponding to one spin transition step observed in the $\chi_M T$ vs. T curves. In the case of **1**·2,5-dmthiophene and **1**·bzF, each set of peaks consist of two inner peaks. Regarding **1**·bznitrile, the low-temperature spin transition step is reflected by a set of peaks while the high-temperature spin transition step is mirrored by a sharp unique peak. In particular, **1**·bzaldehyde ΔCp vs. T plot shows two sets of peaks corresponding to an unequally spaced two-step spin transition. In contrast, the presence of three sets of peaks in **1**·$bzNO_2$, **1**·bzBr, **1**·bzCl and **1**·1,3-diBrbz ΔCp vs. T plots are in agreement with unequally spaced three-step spin transitions. Unfortunately, only two peaks reminiscent of the two high-temperature spin transition steps are visible on ΔCp vs. T plot for **1**·thiophene since the remaining low-temperature spin transition steps take place below the minimum operating temperature displayed by the used differential scanning calorimeter. The overall ΔH and ΔS values for **1**·G are in the range of 14-25 kJ mol^{-1} and 70-96 J K^{-1} mol^{-1}, respectively, consistent with values typically displayed by Hofmann-like clathrates of Fe^{II} featuring strong cooperative SCO behaviour.[10]

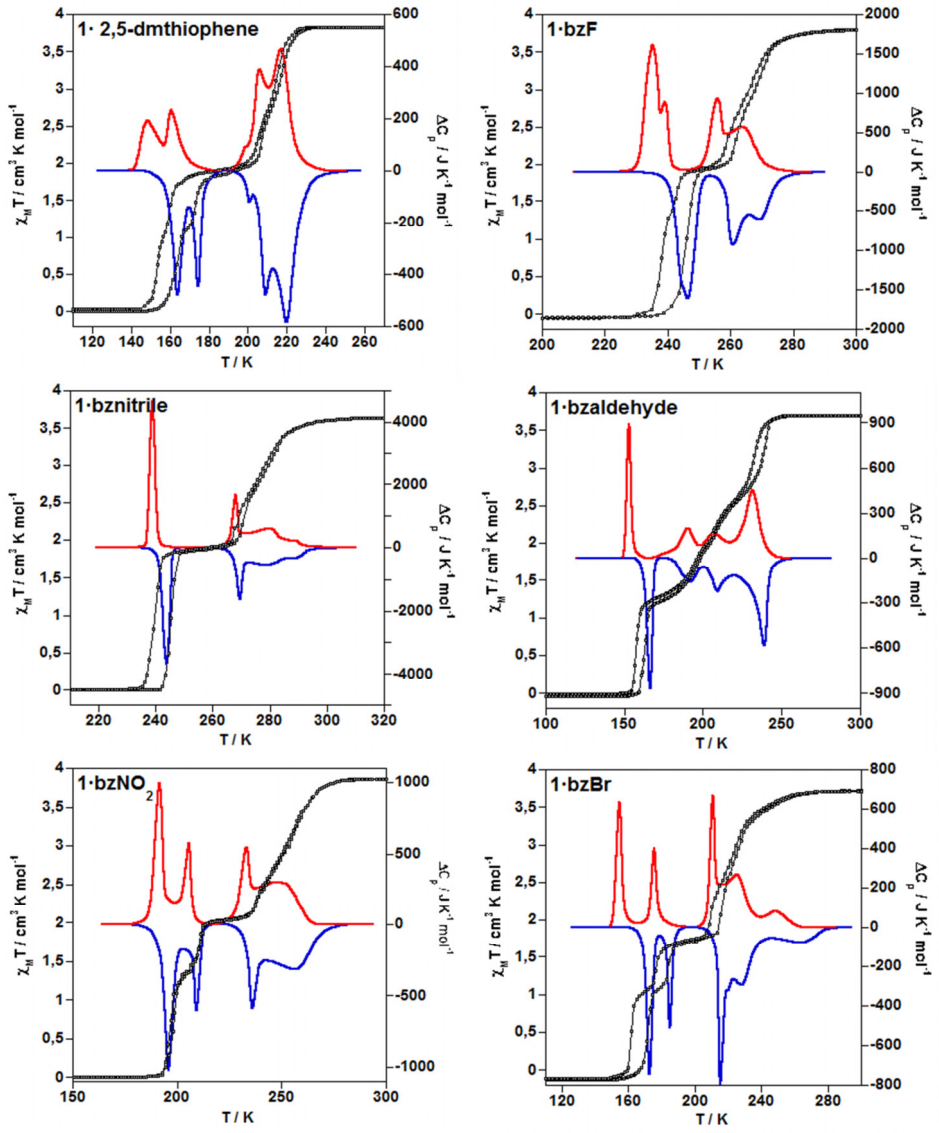

Figure 4.- Magnetic and calorimetric properties of **1**·G (the cooling and heating modes are shown in red and blue colours, respectively).

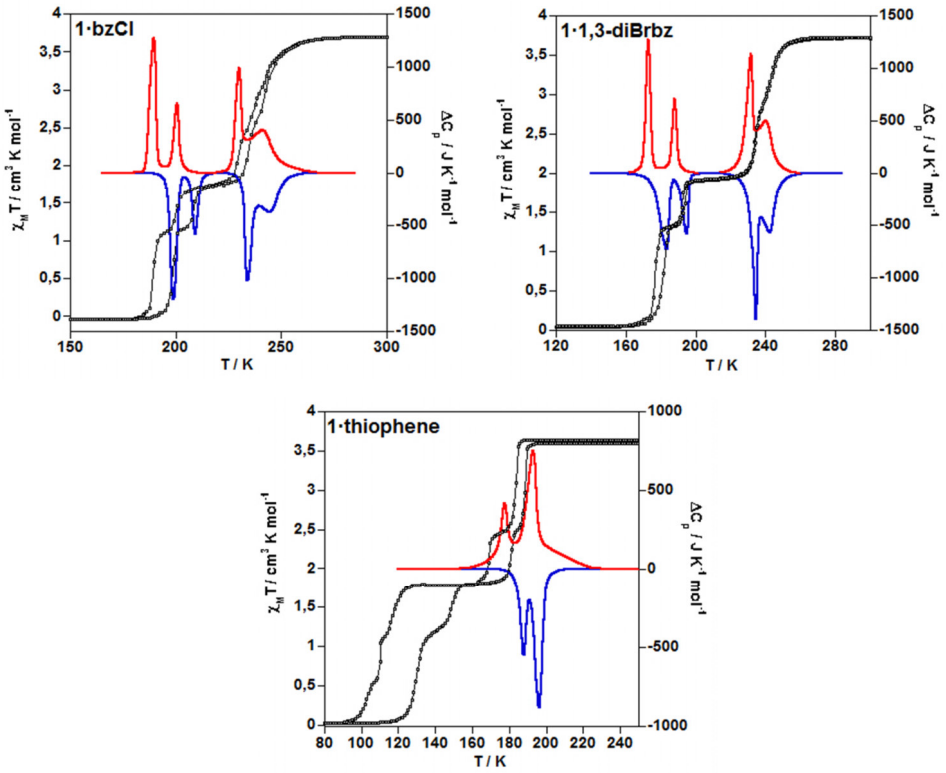

Figure 4 cont.- Magnetic and calorimetric properties of **1**·G (the cooling and heating modes are shown in red and blue colours, respectively).

Table 2.- Average ΔH and ΔS variations of the SCO for **1**·G (G = 2,5-dmthiophene, bzF, bzCl, bzBr, bznitrile, bzaldehyde, $bzNO_2$ and 1,3-diBrbz).

Compound	$\Delta H_{average}$ 1st Step [kJ mol^{-1}]	$\Delta H_{average}$ 2nd Step [kJ mol^{-1}]	$\Delta H_{average}$ 3rd Step [kJ mol^{-1}]	$\Delta H_{average}$ 4th Step [kJ mol^{-1}]	ΔH [kJ mol^{-1}]
1·2,5-dmthiophene	9.40	4.80	-	-	14.20
1·bzF	10.38	10.45	-	-	20.83
1·bznitrile	13.78	11.10	-	-	24.88
1·bzaldehyde	10.94	3.40	-	-	14.34
1·$bzNO_2$	10.08	8.89		-	18.97
1·bzBr	9.74	1.96	3.15	-	14.85
1·bzCl	9.20	2.35	4.66	-	16.21
1·1,3-diBrbz	11.24	2.75	4.92	-	18.91
1·thiophene	-	-	9.23*		9.23*

*Due to the equipment operational limitations, 1st and 2nd steps $\Delta H_{average}$ remain unknown for **1**·thiophene.

Table 2 cont.- Average ΔH and ΔS variations of the SCO for **1**·G (G = 2,5-dmthiophene, bzF, bzCl, bzBr, bznitrile, bzaldehyde, $bzNO_2$ and 1,3-diBrbz).

Compound	$\Delta S_{Average}$ 1st Step [J K^{-1} mol^{-1}]	$\Delta S_{Average}$ 2nd Step [J K^{-1} mol^{-1}]	$\Delta S_{Average}$ 3rd Step [J K^{-1} mol^{-1}]	$\Delta S_{Average}$ 4th Step [J K^{-1} mol^{-1}]	ΔS [J K^{-1} mol^{-1}]
1·2,5-dmthiophene	44.0	29.4	-	-	73.4
1·bzF	39.9	43.5	-	-	83.4
1·bznitrile	50.0	46.2	-	-	96.2
1·bzaldehyde	52.0	21.3	-	-	73.3
1·$bzNO_2$	41.5	42.9		-	84.4
1·bzBr	43.9	10.9	19.2	-	74.0
1·bzCl	39.4	11.5	24.9	-	74.9
1·1.3-diBrbz	47.8	14.4	27.6	-	89.8
1·thiophene	-	-	48.6		48.6*

*Due to the equipment operational limitations, 1st and 2nd steps $\Delta S_{average}$ remain unknown for **1**·thiophene.

The TGA on **1**·G clathrates can be divided into two categories. The first type (**1**·G, G = $bzNO_2$, 1,3-diBrbz, bznitrile and 2,5-dmthiophene) displays three well-defined weight-loss processes. In the first step, half of the total amount of guest is desorbed. Afterwards, a second step consistent with the loss of the second half guest molecule takes place leading to the unloaded framework **1**. Finally, the pyrolysis of **1** can be followed above ≈ 560 K. **1**·bzaldehyde and **1**·thiophene lose a small amount of their guest molecules before being put through the TGA and then undergo a two-step weight-loss process. During the first step, the total amount of guest is desorbed giving **1**. Finally, the second step or pyrolysis of **1** takes place (≈ 560 K). The thermal analysis of **1**·G together with calculated and experimental weight loss (%) are presented in Figure S3 and Table S1 in the Supporting Information.

6.3.4.- Structure

X-ray single crystal studies were carried out for **1**·$bzNO_2$. However, full analysis of its crystal structure was prevented due to the severe disorder found with the $bzNO_2$ guest molecule and one of the pyridyl rings of the 3,8-phen bridging ligand. The crystal structure of **1**·$bzNO_2$ was analyzed at 15 (15_dark), 120, 205, 220 and 290 K. Besides, X-ray single-crystal studies on the metastable HS state (HS*, performed at 15 K after irradiating with green light, λ ≈ 532 nm) are also herein presented. The relevant

crystallographic data and a selection of significant bond lengths [Å] and angles [º] are collected in Tables 3-5.

The structure of **1**·bzNO$_2$ found at 15 K (both in the dark and after irradiation) 120, 205 and 290 K correspond to the monoclinic *P2$_1$/n* space group whereas the one found at 220 K displays the same crystal system but a different space group (*I2/a)*. All iron atoms are crystallographically equivalent at all five temperatures. Therefore, the crystal structure at 120 K is representatively analyzed and compare with that found at 290 K in this section.

Table 3.- Crystallographic data for **1**·bzNO$_2$ at different temperatures.

T / K	**120 K**	**205 K**	**220 K**
Empirical formula	$C_{22}H_{13}FeAu_2N_7O_2$	$C_{11}H_{6.5}Fe_{0.5}AuN_{3.5}O$	$C_{38}H_{12}Fe_2Au_4N_{12}$
Mr	857.18	428.59	**1536.16**
Crystal system	monoclinic		
Space group	*P*2$_1$/*n*	*P*2$_1$/*n*	*I*2/*a*
a (Å)	10.10970(10)	10.2302(2)	14.9146(2)
b (Å)	11.12410(10)	11.2561(2)	22.6166(3)
c (Å)	10.10760(10)	10.2284(2)	14.1490(2)
β	91.8430(10)	92.671(2)	90.0020(10)
V (Å^3)	1136.13(2)	1176.54(4)	4772.71(11)
Z	2	2	4
D_c (mg cm^{-3})	2.506	1.210	2.138
F(000)	788	394	2768
μ (Mo-K$_\alpha$)(mm^{-1})	13.547	6.541	12.878
No. of total reflections [$I>2\sigma(I)$]	3908	3434	6562
R [$I>2\sigma(I)$]	0.0294	0.0724	0.0534
R [all data]	0.0407	0.1009	0.0954
S	1.051	1.100	0.952

Table 3 cont.- Crystallographic data for **1**·bzNO$_2$ at different temperatures.

T / K	**290 K**	**15 K (dark)**	**15 K (532 nm)**
Empirical formula	$C_{22}H_{13}FeAu_2N_7O_2$	$C_{22}H_{13}FeAu_2N_7O_2$	$C_{22}H_{13}FeAu_2N_7O_2$
Mr	857.18	857.18	857.18
Crystal system			
Space group	*P*2$_1$/n	*P*2$_1$/n	*P*2$_1$/n
a (Å)	10.4618(2)	10.1143(3)	10.5001(3)
b (Å)	11.5106(3)	11.1281(3)	11.4879(3)
c (Å)	10.4670(2)	10.1146(4)	10.4660(4)
β	95.605(2)	91.745(3)	93.387(3)
V (Å^3)	1254.43(5)	1137.90(6)	1260.25(7)
Z	2	2	2
D_c (mg cm^{-3})	2.269	2.502	2.259
F(000)	788	788	788
μ (Mo-K$_\alpha$)(mm^{-1})	12.269	13.525	12.212
No. of total reflections [$I>2\sigma(I)$]	3312	1748	2046
R [$I>2\sigma(I)$]	0.0377	0.0384	0.0366
R [all data]	0.0839	0.0596	0.0555
S	1.023	0.819	1.133

	120 K	205 K	220 K	290 K	15 K_dark	15* K
Fe-N1	2.022(4)	2.081(13)	2.032(9)	2.237(5)	1.942(8)	2.211(9)
Fe-N2	2.010(4)	2.087(13)	1.939(8)	2.226(5)	1.930(7)	2.193(8)
Fe-N3	1.933(6)	1.974(13)	1.932(8)	2.140(8)	2.022(10)	2.124(6)
Fe-N4	1.921(6)	2.008(12)	2.038(9)	2.122(8)	2.011(11)	2.119(6)
Au1-C9	1.976(7)	2.01(2)	1.973(10)	1.965(8)	1.974(10)	1.982(8)
Au1-C9A			1.964(10)			
Au2-C10	1.983(7)	1.96(2)	1.982(12)	2.009(9)	1.986(10)	1.984(7)
Au2-C10A			1.975(11)			
Au1-Au2	2.9945(3)	3.0207(8)	3.0349(5)	3.0733(4)	2.9944(7)	3.0626(6)

Table 4.- Selected bond lengths [Å] for **1**·bzNO_2 at different temperatures.

	120 K	205 K	220 K	290 K	15 K_dark	15* K
N1-Fe-N2	180	180	180	180	180	180
N1-Fe-N3	89.92(14)	89.6(3)	90.5(2)	89.9(2)	90.0(2)	90.3(2)
N1-Fe-N4	90.51(13)	89.7(3)	90.5(2)	90.79(13)	90.5(2)	90.5(2)
N2-Fe-N3	90.08(14)	90.4(2)	89.5(2)	90.24(13)	90.3(3)	90.4(2)
N2-Fe-N4	89.49(13)	90.3(3)	89.5(2)	89.21(13)	89.5(2)	89.6(2)
N3-Fe-N4	89.5(2)	91.0(6)	92.0(3)	89.76(13)	89.7(3)	89.7(2)
C9-Au1-C9	178.1(3)	178.7(7)	178.3(4)	177.6(3)	177.9(5)	177.6(4)
C10-Au2-C10	178.7(3)	178.4(8)	178.4(4)	178.3(3)	179.3(5)	178.9(4)

Table 5.- Selected bond angles [º] for **1**·bzNO_2 at different temperatures.

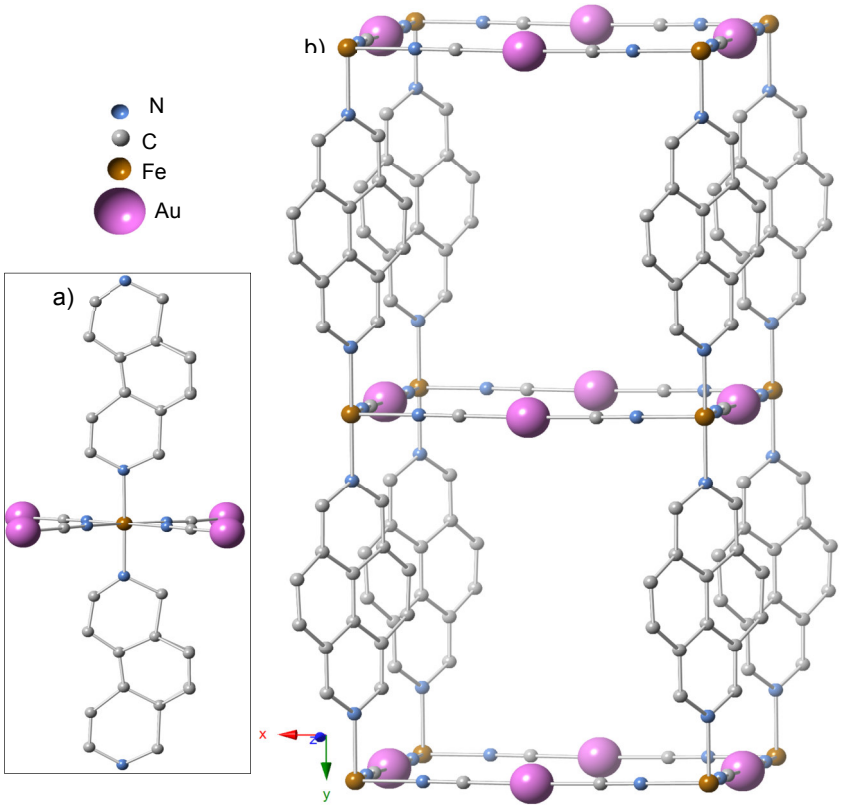

Figure 5.- a) Coordination environment of the iron atom in **1**·$bzNO_2$. b) View in the [001] direction of one 3D network of **1**·$bzNO_2$ showing 3,8-phen ligands bridging Fe^{II} centers from adjacent 2D $\{Fe[Au(CN)_2]_2\}_n$ layers. All hydrogen atoms are omitted for clarity.

As it is shown in Figure 5a, each iron atom defines a distorted elongated octahedron $[FeN_6]$ with its equatorial positions occupied by four nitrogen atoms from four separate $[Au(CN)_2]^-$ groups whereas the axial positions are occupied by two nitrogen atoms from terminal pyridyl donors of two 3,8-phen ligands. The average bond lengths <Fe-N> are 1.96 Å and 2.14 Å at 120 and 290 K, respectively, indicating the occurrence of a complete spin transition. Meanwhile, each $[Au(CN)_2]^-$ linker connects two iron atoms defining the edges of a $\{Fe_4[Au(CN)_2]_4\}_n$ rhombus. In turn, edge-shared rhombuses define a grid-layer structure with all the iron and the aurum atoms in the same coplanar sheet (*x*-*y* plane). Each 3,8-phen ligand binds two iron atoms from two adjacent 2D $\{Fe[Au(CN)_2]_2\}_\infty$ layers defining a 3D network where the Fe···Fe distances along the [001] direction are ≈ 11.124 Å and ≈ 11.511 Å at 120 and 290 K, respectively (Figure 5b). Two 3D networks A and B interpenetrate in such a way that the 2D $\{Fe[Au(CN)_2]_2\}_\infty$

layers of A alternate with those of B so the iron atoms of A are above/below but strictly at the center of the $\{Fe_4[Au(CN)_2]_4\}_n$ rhombuses defined in B (Figure S4, Supporting Information). Moreover, layers A and B are held together by strong aurophilic interactions between two perpendicular sides of their $\{Fe_4[Au(CN)_2]_4\}$ square grids (Au···Au ≈ 2.995 Å and ≈ 3.073 Å at 120 and 290 K, respectively, Figure 6). As a result, the crystal structure of **1**·bzNO_2 consists of a twofold-interpenetrated 3D framework characterized by pores of different size. Four narrow voids (35 $Å^3$ each per unit cell) are located between two closest layers of $\{Fe[Au(CN)_2]_2\}_\infty$ displaying Au···Au interactions. In addition, this pillared network presents a 1D channel along the *b* direction where disordered molecules of nitrobenzene are placed (Figure 7). After artificially removing the guest molecules, the void space is calculated as 787.5 $Å^3$ per unit cell, which corresponds to 35% of the unit-cell volume. The nitrobenzene molecules lie almost parallel between two 3,8-phen ligands, each from a different 3D networks (A or B). Although we cannot report precise values due to disorder of both the guest molecule and the pillar ligand, short C···C contacts (smaller than the sum of the van der Walls radii of ca. 3.7 Å) evidence the occurrence of host-guest π-π interactions. The thermal dependence of the unit-cell volume, V, reproduces reasonably well the $\chi_M T$ vs. T plot for **1**·bzNO_2 (Figure S5, Supporting Information). Meanwhile, powder X-ray diffraction patterns for the remaining **1**·G compounds compare well with that of **1**·bzNO_2 thus confirming that all **1**·G clathrates are isostructural (Figure 8). Considering that the crystal structure of the host is essentially the same in all **1**·G clathrates, the drastic variations in SCO properties along this series should be ascribed to the different chemical nature of the aromatic guests and the corresponding intermolecular interactions between them and the framework.

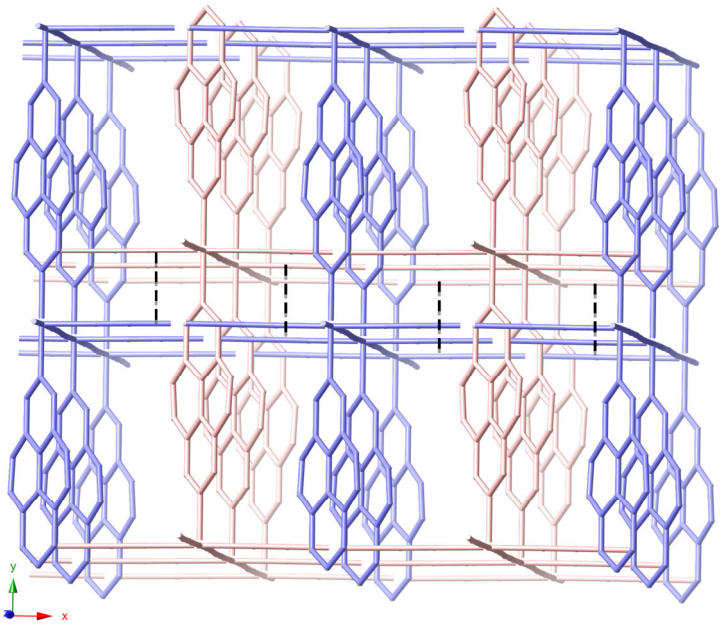

Figure 6.- View in the [001] direction of a fragment of **1**·$bzNO_2$ showing the two interpenetrated 3D networks A and B where 2D $\{Fe[Au(CN)_2]_2\}_\infty$ A and B layers are held together by strong aurophilic interactions (black dashed line).

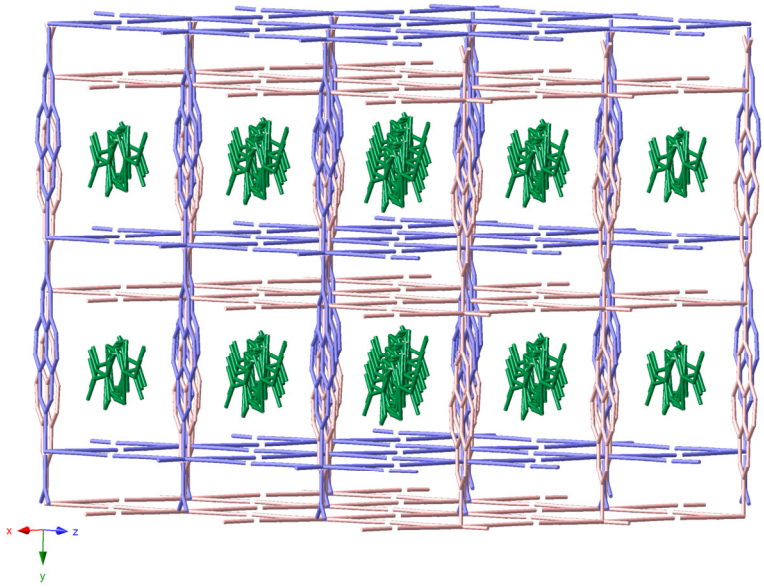

Figure 7.- Perspective view along [101] direction of a fragment of **1**·$bzNO_2$ displaying disorder $bzNO_2$ molecules as guest molecules.

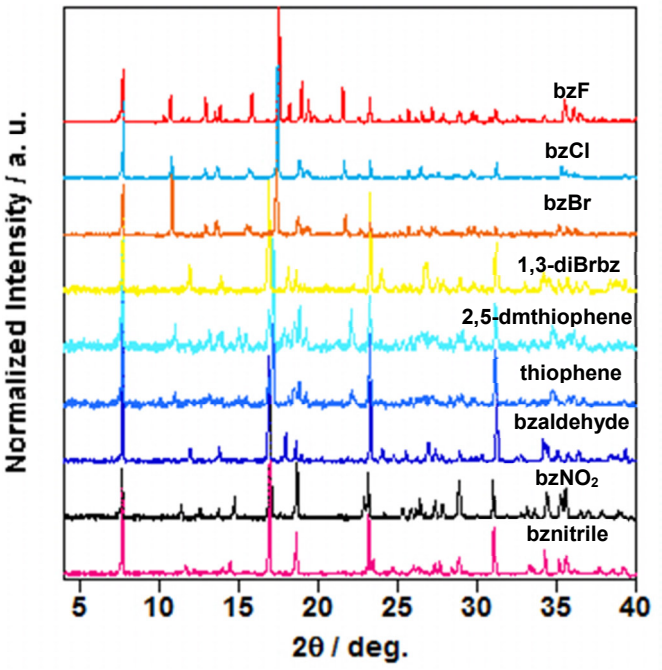

Figure 8.- Powder X-ray diffraction patterns for **1**·G at room temperature.

6.4.- Discussion

In this work we have accomplished the synthesis and physico-chemical characterization of the new Hofmann-like SCO-CPs {Fe(3,8-phen)[Au(CN)$_2$]$_2$·G}. The title series represent an outstanding example of molecular materials generally formulated [Fe(L)(M^I(CN)$_2$] (M^I = Ag, Au)[17-19] which, despite being interpenetrated, display permanent porosity and feature guest molecule-dependent SCO behaviours[10a]; thus, allowing the study of host-guest chemistry and its influence on the SCO properties.

The plots of χ_MT vs. T show the occurrence of a complete HS↔LS spin transition through a multi-step SCO pathway for all **1**·G clathrates. In particular, **1**·2,5-dmthiophene, **1**·bzF and **1**·bznitrile undergo an equally spaced two-step spin transition which defines a plateau ca. 184, 250 and 255 K, respectively, involving Fe^{II} centers in 1:1 ratio (HS:LS) states. Narrow (1 K) and wider (10, 6.5 and 5.6 K) hysteresis loops take place at high and low temperatures, respectively. In contrast, **1**·bzaldehyde displays

a singular unequally spaced two-step spin transition in the temperature interval 150-250 K together with a 5 K wide hysteresis loop at low temperature. Regarding **1**·bzNO$_2$, it features an unequally spaced three-step spin transition where χ_MT vs. T plot defines two plateaus: the first one is ca. 223 K while the second plateau takes place at 204 K. They comprise ≈ 52% and an additional ≈ 35% of Fe^{II} centers in the LS state, respectively. An almost insignificant hysteresis (≤ 1 K wide) is evidenced by the heating mode.

1·bzBr, **1**·bzCl and **1**·1,3-diBrbz undergo more abrupt and hysteretic three-step SCO behaviours than **1**·bzNO$_2$. χ_MT vs. T curves show a plateau ca. 197, 218 and 212 K, respectively, which involves ≈ 50% of Fe^{II} centers in the LS state. A smaller plateau ca. 170, 194 and 185 K, respectively, comprises an additional ≈ 29% of Fe^{II} centers in the LS state. In all three cases, the heating mode evidences the occurrence of hysteresis at low temperature (10, 9 and 5 K wide, respectively) whereas only **1**·bzBr and **1**·bzCl present narrow hysteresis (4 and 3 K wide, each) at high temperature. In addition, **1**·bzBr and **1**·bzCl display a 7 K wide hysteresis loop at medium-high temperature whereas 1 K wide hysteresis loop takes place for **1**·1,3-diBrbz in the same temperature range.

Finally, **1**·thiophene features an alluring SCO behaviour consisting of an abrupt and hysteretic four-step spin transition where χ_MT describes an 11 and 36 K wide plateaus ca. 175 and 155 K, respectively. The first one comprises ≈ 32% while the second involves ≈ 48% of Fe^{II} centers in the LS state. The heating mode shows 25, 30, 11 and 4 K wide hysteresis loops at low, medium, medium-high and high temperatures, respectively.

Similar power X-ray diffraction patterns indicate that all **1**·G clathrates display the same twofold-interpenetrated 3D network as **1**·bzNO$_2$. Therefore, their different SCO properties may arise from the different chemical nature of the enclathrated aromatic molecule and the intermolecular interactions between the guest molecule and the framework. For some SCO series, it has been experimentally[25] and theoretically[23b-23c] proved that their SCO behaviours follow a size-dependent trend, i.e. the larger the guest volume, the lower the spin transition temperature. This tendency was ascribed to an increasing internal pressure caused by large guest molecules favoring the HS over the LS state since they hinder the necessary contraction to the latter state. For the sake of

comparison, the equilibrium temperature $T_{1/2}$ (temperature at which the molar fractions $\gamma_{HS} = \gamma_{LS} = 0.5$) for the whole **1**·G series are collected in Table 6.

Table 6.- Equilibrium $T_{1/2}$ temperatures for the SCO title compounds and Hammett parameters (σ_p) for some aromatic guest molecules.

Compound	$T_{1/2}$ [K]	σ_p
1·thiophene	158	-
1·2,5-dmthiophene	186	-
1·1,3-diBrbz	195	-
1·bzaldehyde	198	0.4
1·bzBr	210	-
1·bzNO_2	213	0.7
1·bzCl	229	-
1·bznitrile	246	0.6
1·bzF	249	-

No direct correlation was found between $T_{1/2}$ and the size and/or shape of the guest molecule for the present series. In 2009, Kepert and co-workers firstly reported the influence of solvent molecules over the SCO properties of the SCO-CPs $[Fe(bpbd)_2(NCS)_2]$ characterized by large pores.[26] A new trend based on electronic considerations was proposed: the smaller the dielectric constants (ε) displayed by the solvent, the more stabilized the LS state. In particular, the SCO properties exhibited by 2,5-bppAu derivative[17], which displays the same twofold-interpenetrated 3D framework as **1**·G clathrates, were greatly affected after introducing a range of protic solvents into the 1D channel. The bulkier guests *s*-BuOH and *i*-BuOH, displaying the largest volume and lowest ε values in the studied solvents, resulted in lower Tc values showing that the steric effect played the major role. However, when the guest volume decreased, a Tc ordering consistent with Kepert's dielectric constant trend was observed: EtOH (234 K) < *n*-PrOH (242 K) < *i*-PrOH (260 K). The O-H···N(2,5-bpp) hydrogen-bonding interaction between the guest molecule and the uncoordinated pyridyl group in the framework was presumably responsible for the stabilization of the LS state and the enhancement of the cooperativity. Therefore, in the case of small guest molecules, the steric effect should be less pronounced while the electronic influences may be of greater importance. In the title **1**·G clathrates, displaying a larger void than 2,5-bppAu derivative (787.5 $Å^3$ vs. 621.4 $Å^3$ per unit cell), the electronic influence is expected to outweigh the steric effect since the guest molecules might be loosely packed in such large pores. In previous Hofmann-type SCO-MOFs, π-π interactions between the aromatic rings of the pillar ligand and the aromatic guest molecules deeply affect the Fe^{II} ligand field and; thus, the corresponding

SCO properties.[23a-b] In general, subtle changes in the π-electronic density (δ_π) of the aromatic molecules modulate the strength of the π-π interactions[27], consequently, π-stacking might be optimized when repulsive interactions between the aromatic rings are minimized. In the case of the SCO-CPs $\{Fe(bpac)[Pt(CN)_4]\}\cdot G$ (G = bzCl, bzBr and bzI) presented by Real et al. in 2013[22b], the authors suggested that the π-stacking between the bpac ligands and the aromatic guest molecules was optimized in the order bzCl > bzBr > bzI since $\delta_\pi(bzCl) < \delta_\pi(bzBr) < \delta_\pi(bzI)$. Apparently, the reinforcement of the π-π interactions might induce a redistribution of the electronic density on the π system, presumably, increasing the electron density around the pyridinic nitrogen of the bpac ligand. By following this reasoning, a further stabilization of the LS state together with higher critical temperatures in the order $T_{1/2}(bzCl) > T_{1/2}(bzBr) > T_{1/2}(bzI)$ was expected and experimentally confirmed. Consistently, the $T_{1/2}$ values for the herein presented **1**·bzF, **1**·bzCl and **1**·bzBr clathrates with $\delta_\pi(bzF) < \delta_\pi(bzCl) < \delta_\pi(bzBr)$ follow the aforementioned trend since $T_{1/2}(bzF) = 249$ K > $T_{1/2}(bzCl) = 229$ K > $T_{1/2}(bzBr) = 210$ K.

In 2015, Real et al. presented the porous SCO-MOF (Metal-organic Framework) generally formulated $\{[Fe(tvp)_2(NCS)_2]\cdot 2G\}$ (**1@2G**) where G = benzonitrile (bznitrile), benzaldehyde (bzaldehyde), nitrobenzene ($bzNO_2$).[22d] The π-π interactions between the tvp ligand and the aromatic guest molecules were thought to be responsible for the variations in the SCO properties of these clathrates. Reasonably, the authors proposed that the π-stacking enhanced the π-acceptor character of the tvp bridging ligand increasing the ligand field felt by the Fe^{II} centers which results in a further stabilization of the LS state and higher $T_{1/2}$ values. The strength of the π-stacking was rationalized in terms of the Hammet parameters (σ_p)[28]: the greater the electron-withdrawing nature of the substituent X ($\sigma_p(bzNO_2) > \sigma_p(bznitrile) > \sigma_p(bzaldehyde)$, Table 6), the stronger the π-stacking. Therefore, the more stabilized the LS state and the higher the $T_{1/2}$ ($T_{1/2}(bzNO_2) > T_{1/2}(bznitrile) > T_{1/2}(bzaldehyde)$). In contrast, the $T_{1/2}$ values displayed by the herein presented **1**·$bzNO_2$, **1**·bzaldehyde and **1**·bznitrile, follow the trend: $T_{1/2}(bznitrile) > T_{1/2}(bzNO_2) > T_{1/2}(bzaldehyde)$ which cannot be explained by Real et al. hypothesis.

For the last two decades, substituent effects in π-π interactions between two aromatic rings, Ph-X···bz (Ph-X = substituted, bz = unsubstituted aromatic rings) have been explained by the Hunter and Sanders (H-S) model[27] where substituent-induced

changes in the aryl π-system of Ph-X (X adding or withdrawing density from Ph) affects the electrostatic interaction in the Ph-X···bz system. In the early 2000s, high-accuracy gas-phase computational studies led to unexpected results from the viewpoint of the electrostatic H-S model.[29] Therefore, in 2008 Wheeler and Houk presented a second hypothesis (W-H) which suggested that the influence of the substituent on the interaction energy between both aromatic rings could be understood by considering the interaction of the local Ph-X and C-H dipoles in the nearest vertex of the second ring with π-resonance effects playing no significant role.[20a] In general, the H-S model is supported by the correlation of the substituent effect with σ_p in several experiments.[30] In contrast, in 2014, Parish and co-workers[20c] applied a developed functional-group SAPT (F-SAPT) analysis[31] which allowed them to compute the SAPT interaction energy in Ph−X···bz and in Ph−H···bz systems. The difference in interaction energies between them is the substituent effect. They also performed difference density analysis of the Ph unit and plot differences in the electrostatic potential (ESP) for substituted and unsubstituted benzene monomers. In general, F-SAPT, density analyses and ESP showed that, although both the H-S and W-H pictures contribute to the substituent effect in benzene dimers, the latter was usually the dominant contributor to the total substituent effect. Furthermore, the minor contributive H-S picture was much more complicated than the simple picture of π donation or withdrawal usually explained by σ_p. Interestingly, recent experimental studies performed by Shimizu and co-workers[32] clearly support the W-H picture.

The large variation in the $T_{1/2}$ values across the present series together with the different shape of the spin transition displayed by **1**·G clathrates (featuring chemically comparable guest molecules, loading and, presumably, spatial orientation within the pores of the framework) indicates that the π-π interactions between the different aromatic guest molecules and the pillar 3,8-phen ligand strongly affect the ligand field at the Fe^{II} centers. Therefore, understanding the effect of substituents on these noncovalent interactions is of great importance in order to obtain appealing SCO behaviours by adjusting the host-guest π-π interactions.

6.5.- Conclusion

In this work we have presented the new 3D porous Hofmann-like SCO-CPs series based on Fe^{II}, $[Au(CN)_2]^-$, 3,8-phen bridging ligand and aromatic molecules i.e. thiophene, 2,5-dimethylthiophene, benzonitrile, benzaldehyde, nitrobenzene, fluorobenzene, chlorobenzene, bromobenzene and 1,3-dibromobenzene as guest molecules. In the case of **1**·$bzNO_2$, single crystals suitable for single-crystal X-ray diffraction measurements were obtained. The crystal structure of **1**·$bzNO_2$, studied at five different temperatures, is the result of the interpenetration of two 3D frameworks (A and B) in which alternating 2D $\{Fe[Au(CN)_2]_2\}_\infty$ A and B layers are organized in pairs held by strong Au···Au contacts. X-ray diffraction studies performed at high and low temperature show that these metallophilic contacts vary in a synergetic mode with the SCO phenomena, a remarkable feature for the generation of new switchable, multiproperty materials. In addition, within this twofold-interpenetrated network, a 1D channel occupied by disordered nitrobenzene molecules runs along the *b* axis. These guest molecules interact with the 3,8-phen bridging ligand through π-π interactions. The remaining **1**·G clathrates have been characterized by powder X-ray diffraction studies whose similar diffraction patterns evidence the same general framework displayed by **1**·$bzNO_2$. The identity and number of guest molecules were established by single-crystal X-ray studies (**1**·$bzNO_2$) and TGA (**1**·G).

The SCO behaviours featured by the title series have been investigated by single-crystal X-ray diffractions studies (**1**·$bzNO_2$) and the thermal dependence of the $\chi_M T$ product (**1**·G). The magnetic data show that these compounds undergo complete and cooperative spin transitions in the temperature region of 80-280 K. Differences in general SCO features i.e. number of SCO steps, characteristic temperatures, whether the occurrence of hysteresis loops of a particular width, are ascribed to the distinct chemical nature of the guest molecule inside the pores of the framework and the corresponding π-π interactions between them and the pillar 3,8-phen ligand.[10b] Therefore, the title Hofmann-type series can be seen as a useful prototype for investigating the interplay between SCO properties and π-π host-guest interactions. Interestingly, photomagnetic studies performed over **1**·thiophene and **1**·$bzNO_2$, show that these clathrates display the well-known LIESST effect[24] with T_{LIESST} ca. 44 K. Meanwhile, the plot of the thermal dependence of ΔCp for all **1**·G clathrates leads to a

set of peaks that reflect the changes in the slope observed in the $\chi_M T$ vs. T curves. Moreover, each set of peaks are reminiscent of those detected in the $\delta(\chi_M T)/\delta T$ vs. T plots. In addition, Tc values displayed by **1**·G series and deduced from ΔCp vs. T plots are consistent with those obtained from the magnetic data. Besides, the overall ΔH and ΔS variations are within the expected range of values typically displayed by Hofmann-like clathrates of Fe^{II} centers featuring strong cooperative SCO behaviours.[10] Finally, **1**·G clathrates (G = thiophene, bzCl, bzBr and 1,3-diBrbz) displaying multi-step and multi-stable hysteretic SCO transitions, seem ideal for the development of expanded information storage devices.

6.6.- Experimental Section

6.6.1.- Materials

$K[Au(CN)_2]$, and $Fe(BF_4)_2 \cdot 7H_2O$ were purchased from commercial sources and used as received whereas the synthesis of the 3,8-phen ligand was performed as it is described in Section 6.8.1 in the Supporting Information.

6.6.2.- Crystal growth

Single crystals of **1**·G were grown by slow liquid-liquid diffusion technique using a modified H-vessel with a third tube added due to the poor solubility of the 3,8-phen ligand in methanol where the $Fe(BF_4)_2 \cdot 7H_2O$ and $K[Au(CN)_2]$ salts were dissolved. The peripheral tubes (total volume ca. 10 mL) contained $Fe(BF_4)_2 \cdot 7H_2O$ (0.056 mmol, 19 mg) and $K[Au(CN)_2]$ (0.116 mmol, 33.5 mg) salts, respectively. The central tube (total volume ca. 10 mL) contained 3,8-phen ligand (0.055 mmol, 10 mg). Each individual tube was filled with methanol and finally with a solution 1:10 of the corresponding guest molecule in methanol. Afterwards, the tubes were sealed with parafilm. Two weeks later, yellow cube-shaped single crystals were formed in the tube which originally contained $Fe(BF_4)_2 \cdot 7H_2O$ salt with relative high yield (ca. 50%). The presence and quantification of the guest molecules were confirmed by means of single-crystal X-ray diffraction in the case of **1**·$bzNO_2$ and by thermogravimetric analyses on **1**·G samples where G = $bzNO_2$, 1,3-diBrbz, bznitrile, 2,5-dmthiophene, bzaldehyde and thiophene. In the case of **1**·bzF,

1·bzCl and **1**·bzBr, the presence and quantification of the guest molecules were deduced from their magnetic data, however, TGA on these clathrates are on course.

6.6.3.- Physical characterization

-Magnetic and Photomagnetic measurements: The variable temperature magnetic susceptibility measurements were carried out by using samples (15-20 mg) consisting of single crystals of the titled compounds, using a Quantum Design MPMS2 SQUID susceptometer equipped with a 5.5 T magnet, operating at 1 T and at temperatures from 300-1.8 K. The susceptometer was calibrated with $(NH_4)_2Mn(SO_4)_2 \cdot 12H_2O$. Photomagnetic experiments were carried out using a Xe lamp with a 350-800 nm filter system coupled through an optical fiber to the sample chamber of the SQUID susceptometer. The power output was 2 mW cm^{-2}. Experimental susceptibilities were corrected for diamagnetism of the constituent atoms by the use of Pascal's constants.

-Thermogravimetric Analysis (TGA): Thermogravimetric measurements were performed on a Mettler Toledo TGA/SDTA 851e instrument in the 300-900 K temperature range in nitrogen atmosphere with a rate of 10 K min^{-1}.

-Differential Scanning Calorimetry (DSC): Calorimetric measurements were performed using a differential scanning calorimeter Mettler Toledo DSC 821e. Low temperatures were obtained with an aluminium block attached to the sample holder, refrigerated with a flow of liquid nitrogen and stabilized at a temperature of 110 K. The sample holder was kept in a dry box under a flow of dry nitrogen gas to avoid water condensation. The measurements were carried out using around 20 mg of powdered sample sealed in aluminium pans with a mechanical crimp. Temperature and heat flow calibrations were made with standard samples of indium by using its melting transition (429.6 K, 28.45 J g^{-1}). An overall accuracy of ±0.2 K in temperature and ±2% in the heat capacity is estimated. The uncertainty increases for the determination of the anomalous enthalpy and entropy due to the subtraction of an unknown baseline.

6.6.4.- X-ray diffraction

6.6.4.1.- Single-crystal X-ray diffraction

Single-crystal X-ray diffraction studies for {Fe(3,8-phen)[Au(CN)$_2$]$_2$}·bzNO$_2$ were performed at the Institut de Physique de Rennes on a four-circle Oxford Diffraction

Xcalibur 3 diffractometer (MoKα radiation). The single crystals were mounted in an Oxford Cryosystems nitrogen-flow cryostat for experiments above 78 K and in an Oxford Diffraction Helijet cryostat for measurements down to 10 K.

3.6.4.2.- Powder X-ray diffraction

Powder X-ray diffraction data were collected using a Bruker D8 at room temperature.

6.7.- References

[1] O. Sato, *Nat. Chem*., **2016**, *8*, 644.

[2] a) E. König, *Struct. Bonding (Berlin)*, **1991**, *76*, 51; b) P. Gütlich, A. Hauser, H. Spiering, *Angew. Chem., Int. Ed. Engl*., **1994**, *33*, 2024; c) J. A. Real, A. B. Gaspar, V. Niel, M. C. Muñoz, *Coord. Chem. Rev.*, **2003**, *236*, 121; d) P. Gütlich, H. A. Goodwin, *Top. Curr. Chem*., **2004**, *233*; e) J. A. Real, A. B. Gaspar; M. C. Muñoz, *Dalton Trans.*, **2005**, 2062; f) A. Bousseksou, G. Molnár, L. Salmon, W. Nicolazzi, *Chem. Soc. Rev*., **2011**, *40*, 3313; g) M. A. Halcrow, John Wiley & Sons, **2013**.

[3] M. Ohba, K. Yoneda, G. Agustí, M. C. Muñoz, A. B. Gaspar, J. A. Real, M. Yamasaki, H. Ando, Y. Nakao, S. Sakaki, S. Kitagawa, *Angew. Chem. Int. Ed*., **2009**, *48*, 4767.

[4] F. J. Muñoz-Lara, A. B. Gaspar, M. C. Muñoz, M. Arai, S. Kitagawa, M. Ohba, J. A. Real, *Chem. Eur. J*., **2012**, *18*, 8013.

[5] G. Agustí, S. Cobo, A. B. Gaspar, G. Molnár, N. O. Moussa, P. Á. Szilágyi, V. Pálfi, C. Vieu, M. C. Muñoz, J. A. Real, A. Bousseksou, *Chem. Mater*., **2008**, *20*, 6721.

[6] C. Bartual-Murgui, N. A. Ortega-Villar, H. J. Shepherd, M. C. Muñoz, L. Salmon, G. Molnár, A. Bousseksou, J. A. Real, *J. Mater. Chem.*, **2011**, *21*, 7217.

[7] F. J. Muñoz-Lara, A. B. Gaspar, M. C. Muñoz, V. Ksenofontov, J. A. Real, *Inorg. Chem.*, **2013**, *52*, 3.

[8] N. F. Sciortino, K. R. Scherl-Gruenwald, G. Chastanet, G. J. Halder, K. W. Chapman, J.-F. Létard, C. J. Kepert, *Angew. Chem. Int. Ed.*, **2012**, *51*, 10154.

[9] L. Piñeiro-López, M. Seredyuk, M. C. Muñoz, J. A. Real, *Chem. Commun*., **2014**, *50*, 1833.

[10] a) M. C. Muñoz, J. A. Real, *Coord. Chem. Rev*., **2011**, *255*, 2068; b) Z.-P. Ni, J.-L. Liu, Md. N. Hoque, W. Liu, J.-Y. Li, Y.-C. Chen, M.-L. Tong, *Coord. Chem. Rev*., **2017**, *335*, 28.

[11] V. Niel, A. L. Thompson, M. C. Muñoz, A. Galet, A. E. Goeta, J. A. Real, *Angew. Chem. Int. Ed.*, **2003**, *42*, 3760.

[12] a) A. Galet, V. Niel, M. C. Muñoz, J. A. Real, *J. Am. Chem. Soc.*, **2003**, *125*, 14224; b) A. Galet, M. C. Muñoz, V. Martinez, J. A. Real, *Chem. Commun.*, **2004**, 2268; c) V. Niel, A. L. Thompson, A. E. Goeta, C. Enachescu, A. Hauser, A. Galet, M. C. Muñoz, J. A. Real, *Chem. Eur. J.*, **2005**, *11*, 2047.

[13] a) M. C. Muñoz, A. B. Gaspar, A. Galet, J. A. Real, *Inorg. Chem.*, **2007**, *46*, 8182; (b) G. Agustí, M. C. Muñoz, A. B. Gaspar, J. A. Real, *Inorg. Chem.*, **2008**, *47*, 2552.

[14] V. Niel, M. C. Muñoz, A. B. Gaspar, A. Galet, G. Levchenko, J. A. Real, *Chem. Eur. J.*, **2002**, *8*, 2446.

[15] A. Il'ya, O. G. Bohdan, G. Sergii, I. Shylin, V. Ksenofontov, H. J. Shepherd, P. R. Raithby, W. Tremel, I. O. Fritsky, *Eur. J. Inorg. Chem.*, **2016**, 3191.

[16] F. J. Valverde-Muñoz, M. Seredyuk, M. C. Muñoz, K. Znovjyak, I. O. Fritsky, J. A. Real, *Inorg. Chem.*, **2016**, *55*, 10654.

[17] J.-Y. Li, Y.-C. Chen, Z.-M. Zhang, W. Liu, Z.-P. Ni, M.-L. Tong, *Chem. Eur. J.*, **2015**, *21*, 1645.

[18] J. E. Clements, J. R. Price, S. M. Neville, C. J. Kepert, *Angew. Chem. Int. Ed.*, **2014**, 53, 10164.

[19] J. E. Clements, J. R. Price, S. M. Nevill, C. J. Kepert, *Angew. Chem. Int. Ed.,* **2016**, 55, 1.

[20] a) S. E. Wheeler, K. N. Houk, *J. Am. Chem. Soc.,* **2008**, *130*, 10854; b) S. E. Wheeler, *Acc. Chem. Res.*, **2013**, *46*, 1029; b) S. E. Wheeler, J. W. G. Bloom, *J. Phys. Chem. A*, **2014**, *118*, 6133; c) R. M. Parrish, C. D. Sherrill, *J. Am. Chem. Soc.*, **2014**, *136*, 17386.

[21] a) J. E. Clements, J. R. Price, S. M. Neville, C. J. Kepert, *Angew. Chem. Int. Ed*., **2014**, *53*, 10164; b) J.-Y. Li, C.-T. He, Z.-M. Zhang, W. Liu, Z.-P. Ni, M.-L. Tong, *Chem. Eur. J*., **2015**, *21*, 1645; c) J.-Y. Li, C.-T. He, Y.-C. Chen, Z.-M. Zhang, W. Liu, Z.-P. Ni, M.-L Tong, *Mater. Chem. C*, **2015**, *3*, 7830; d) I. A. Gural'skiy, B. O. Golub, S. I. Shylin, V. Ksenofontov, H. J. Shepherd, P. R. Raithby, W. Tremel, I. O. Fritsky, *Eur. J. Inorg. Chem.*, **2016**, 3191; e) F. J. Valverde-Muñoz, M. Seredyuk, M. C. Muñoz, K. Znovjyak, I. O. Fritsky, J. A. Real, *Inorg. Chem*., **2016**, *55*, 10654.

[22] a) F. J. Muñoz-Lara, A. B. Gaspar, M. C. Muñoz, M. Arai, S. Kitagawa, M. Ohba, J. A. Real, *Chem. Eur. J.*, **2012**, *18*, 8013; b) C. Bartual-Murgui, A. Akou, H. J. Shepherd, G. Molnár, J. A. Real, L. Salmon, A. Bousseksou, *Chem. Eur. J.*, **2013**, *19*, 15036; c) R. Ohtani, M. Arai, A. Hori, M. Takata, S. Kitao, M. Seto, S. Kitagawa, M. Ohba, *J. Inorg. Organomet. Polym.*, **2013**, *23*, 104; d) T. Romero-Morcillo, N. De la Pinta, L. M. Callejo, L. Piñeiro-López, M. C. Muñoz, G. Madariaga, S. Ferrer, T. Breczewski, R. Cortés, J. A. Real, *Chem. Eur. J.*, **2015**, *21*, 12112.

[23] a) J.-Y. Li, C.-T. He, Y.-C. Chen, Z.-M. Zhang, W. Liu, Z.-P. Ni, M.-L. Tong, *J. Mater. Chem. C*, **2015**, *3*, 7830; b) M. Ohba, K. Yoneda, G. Agustí, M. C. Muñoz, A. B. Gaspar, J. A. Real, M. Yamasaki, H. Ando, Y. Nakao, S. Sakaki, S. Kitagawa, *Angew. Chem. Int. Ed.*, **2009**, *48*, 4767; c) D. Aravena, Z. Arcís Castillo, M. C. Muñoz, A. B. Gaspar, K. Yoneda, R. Ohtani, A. Mishima, S. Kitagawa, M. Ohba, J. A. Real, E. Ruiz, *Chem. Eur. J.*, **2014**, *20*, 12864.

[24] S. Bonhommeau, G. Molnár, A. Galet, A. Zwick, J. A. Real, J. J. McGarvey, A. Bousseksou, *Angew. Chem. Int. Ed.,* **2005**, *44*, 4069.

[25] G. Molnár, S. Cobo, J. A. Real, F. Carcenac, E. Daran, C. Vieu, A. Bousseksou, *Adv. Mater.*, **2007**, *19*, 2163.

[26] S. M. Neville, G. J. Halder, K. W. Chapman, M. B. Duriska, B. Moubaraki, K. S. Murray, C. J. Kepert, *J. Am. Chem. Soc.*, **2009**, *131,* 12106.

[27] a) C. A. Hunter, J. K. M. Sanders, *J. Am. Chem. Soc.*, **1990**, *112*, 5525; b) C. A. Hunter, *Angew. Chem.,* **1993**, *105*, 1653, *Angew. Chem. Int. Ed. Engl.*, **1993**, *32*, 1584.

[28] C. Hansch, A. Leo, R. W. Taft, *Chem. Rev.*, **1991**, *97,* 165.

[29] a) C. D. Sherrill, K. B. Lipkowitz, T. R. Cundari, *Wiley-VCH: New York*, **2009**, *26*, 1; b) E. G. Hohenstein, J. Duan, C. D. Sherrill, *J. Am. Chem. Soc.*, **2011**, *133*, 13244; c) S. E. Wheeler, *J. Am. Chem. Soc.*, **2011**, 133, 10262; d) M. Watt, L. K. E. Hardebeck, C. C. Kirkpatrick, M. Lewis, *J. Am. Chem. Soc.*, **2011**, 133, 3854; e) R. K. Raju, J. W. G. Bloom, Y. An, S. E. Wheeler, *Chem. Phys.*, *Chem.*, **2011**, *21*, 3116.

[30] a) F. Cozzi, M. Cinquini, R. Annunziata, T. Dwyer, J. S. Siegel, *J. Am. Chem. Soc.*, **1992**, *114*, 5729; b) S. L. Cockroft, C. A. Hunter, K. R. Lawson, J. Perkins, C. J. Urch, *J. Am. Chem. Soc.*, **2005**, *127*, 8594; c) S. L. Cockroft, J. Perkins, C. Zonta, H. Adams, S. E. Spey, C. M. R. Low, J. G. Vinter, K. R. Lawson, C. J. Urch, C. A. Hunter, *Org. Biomol. Chem.*, **2007**, *5*, 1062.

[31] R. M. Parrish, T. M. Parker, C. D. Sherrill, *J. Chem. Theory Comput.*, **2014**, *10*, 4417.

[32] J. Hwang, P. Li, W. R. Carroll, M. D. Smith, P. J. Pellechia, K. D. Shimizu, *J. Am. Chem. Soc.*, **2014**, *136*, 14060.

6.8.- Supporting Information

6.8.1.- Synthesis of 3,8-phenantroline ligand

The synthesis of 3,8-phen ligand[1] was carried out in two main steps briefly summarized as follows.

*-Synthesis of 1,4-benzene-bis-N-(2,2-dimethoxyethylidene)methanamine precursor (**p**).* p-xylylenediamine (73.4 mmol, 10.0 g), 2,2-dimethoxyacetaldehyde (154 mmol, 34 mL) and 250 mL of absolute EtOH were placed in a 250 mL round-bottom flask and stirred overnight. After that, the solvent was removed at reduced pressure and a yellow oil was obtained. The oil was dissolved in toluene and the mixture was heated to boil. A Dean-Stark was used to remove the water formed as a by-product during the synthesis of ***p***. After that, the toluene surplus was removed at reduced pressure and the remained oil ***p*** was placed in the fridge. ***p*** was obtained in 98% yield.

-Synthesis of 3,8-phen ligand. Oleum (20% SO_3, 21 mL) was placed in a 100 mL round-bottom flask previously submerged in a cooling bath. ***p*** (16.2 mmol, 5 g) was added drop by drop to the cold oleum while stirring. The mixture was stirred overnight at room temperature. After that, it was carefully poured into ice (400 g), neutralized with Na_2CO_3 and further basified with NaOH. Then, the mixture was filtered to remove the excess base. The solution was extracted with diethyl ether several times; the organic phases were collected and dried over magnesium sulphate, filtered and the solvent removed at reduced pressure. The remained yellow solid was recrystallized in hot toluene. The 3,8-phen ligand was obtained in 46% yield, thus an overall 21% yield was achieved.

Figure S1.- Overlay of the $\chi_M T$ and $\delta(\chi_M T)/\delta T$ vs. T for **1**·G. The cooling and heating modes are shown in blue and red colours, respectively.

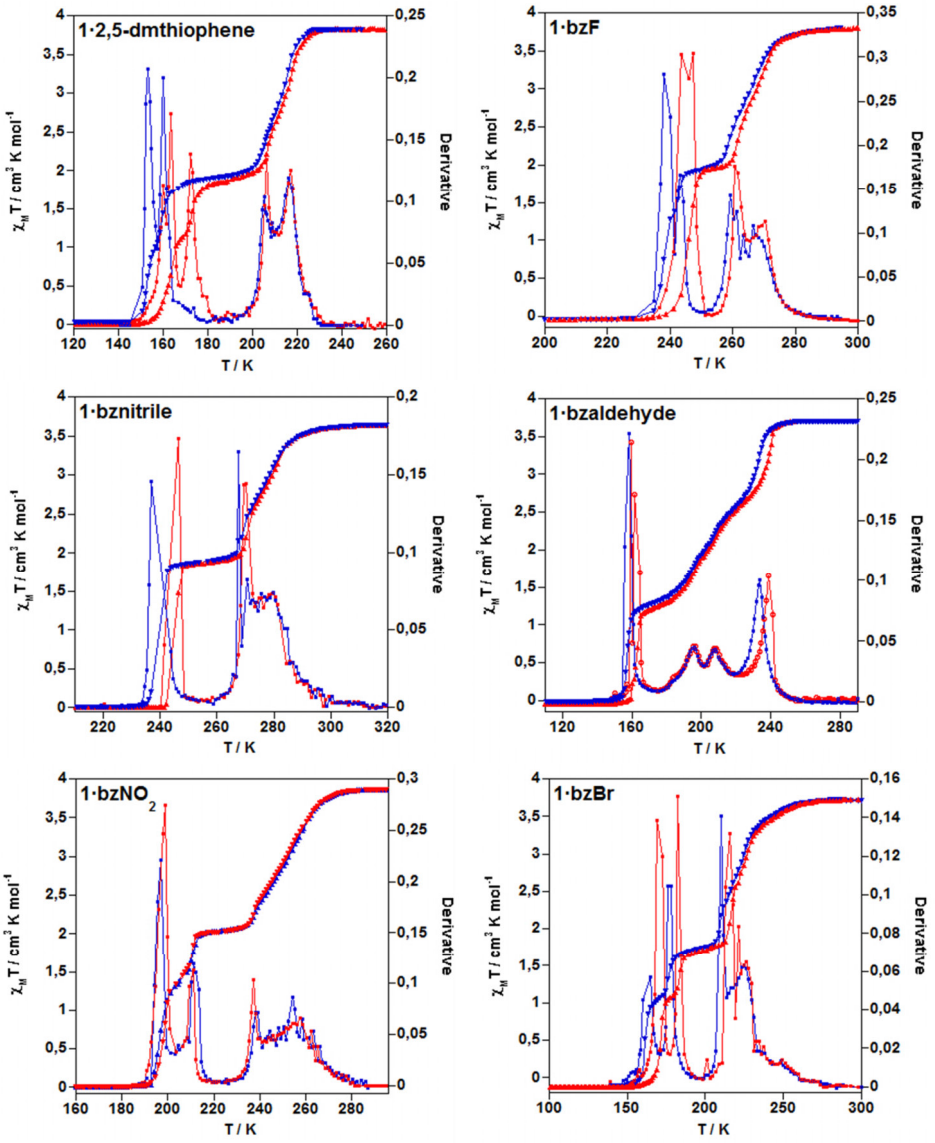

Figure S1 cont.- Overlay of the $\chi_M T$ and $\delta(\chi_M T)/\delta T$ vs. T for **1**·G. The cooling and heating modes are shown in blue and red colours, respectively.

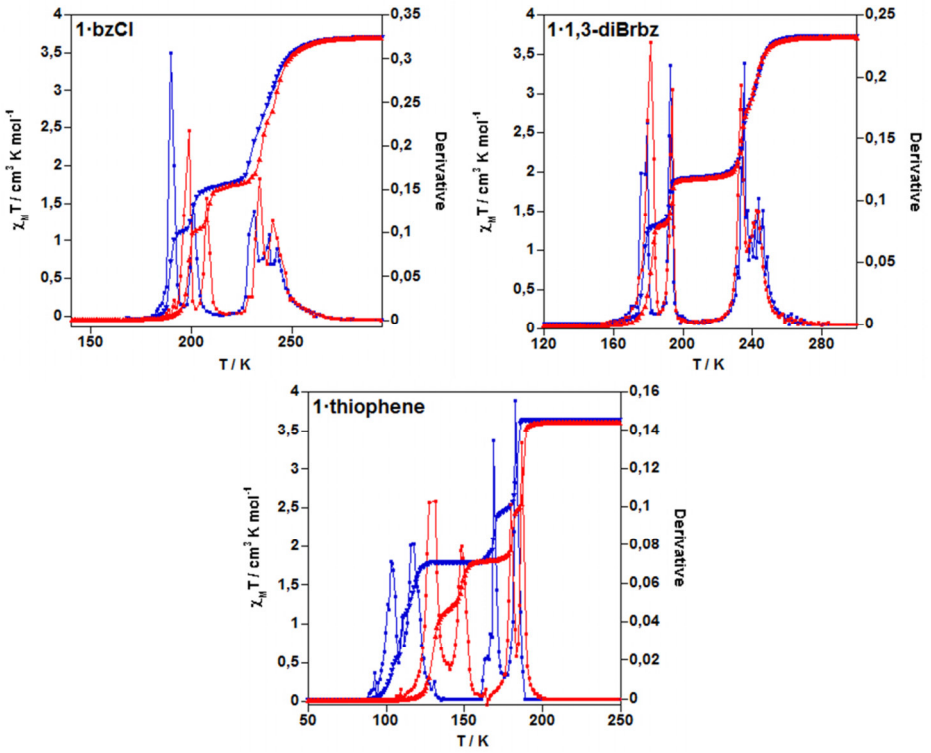

Figure S2.- LIESST temperatures (T_{LIESST}), determined from the maximum variation of $\chi_M T$ in the HS→LS relaxations for **1**·bzNO$_2$ and **1**·thiophene.

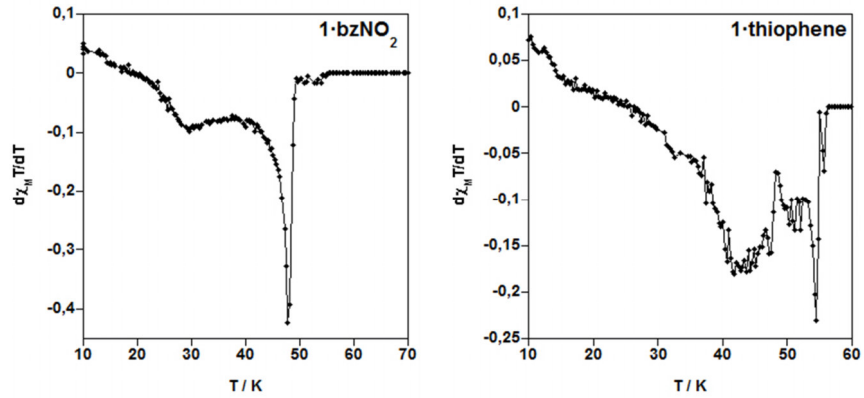

Table S1.- TGA of some **1**·G clathrates (G = 2,5-dmthiophene, thiophene, bznitrile, bzaldehyde, $bzNO_2$ and 1,3-diBrbz): temperature range [K], calculated and experimental weight loss [%].

Compound %calcd, (%exptl)	Step 1	Step 2	Step 3 (Pyrolysis)
1·$bzNO_2$	298-460 K 7.68 (-0.5 $bzNO_2$), (7.18)	460-560 K 7.52 (-0.5 $bzNO_2$), (7.18)	560 - K
1·1,3-diBrbz	298-526 K 11.56 (-0.5 1,3-diBrbz), (11.27)	526-602 K 11.2 (-0.5 1,3-diBrbz) (11.27)	602 - K
1·Bznitrile	298-461 K 5.86 (-0.5 bznitrile), (6.15)	461-561 K 6.03 (-0.5 bznitrile), (6.15)	601 - K
1·2,5-dmthiophene	298-450 K 6.13 (-0.5 2,5-dmthiophene)	450-568 K 5.65 (-0.5 2,5-dmthiophene)	568 - K
1·bzaldehyde	298-560 K 10.46 (-1 bzaldehyde)	-	560 - K
1·thiophene	298-540 K 7.16 (-1 thiophene)	-	540 - K

Figure S3.- TGA of some **1**·G clathrates (G = 2,5-dmthiophene, thiophene, bznitrile, bzaldehyde, $bzNO_2$ and 1,3-diBrbz).

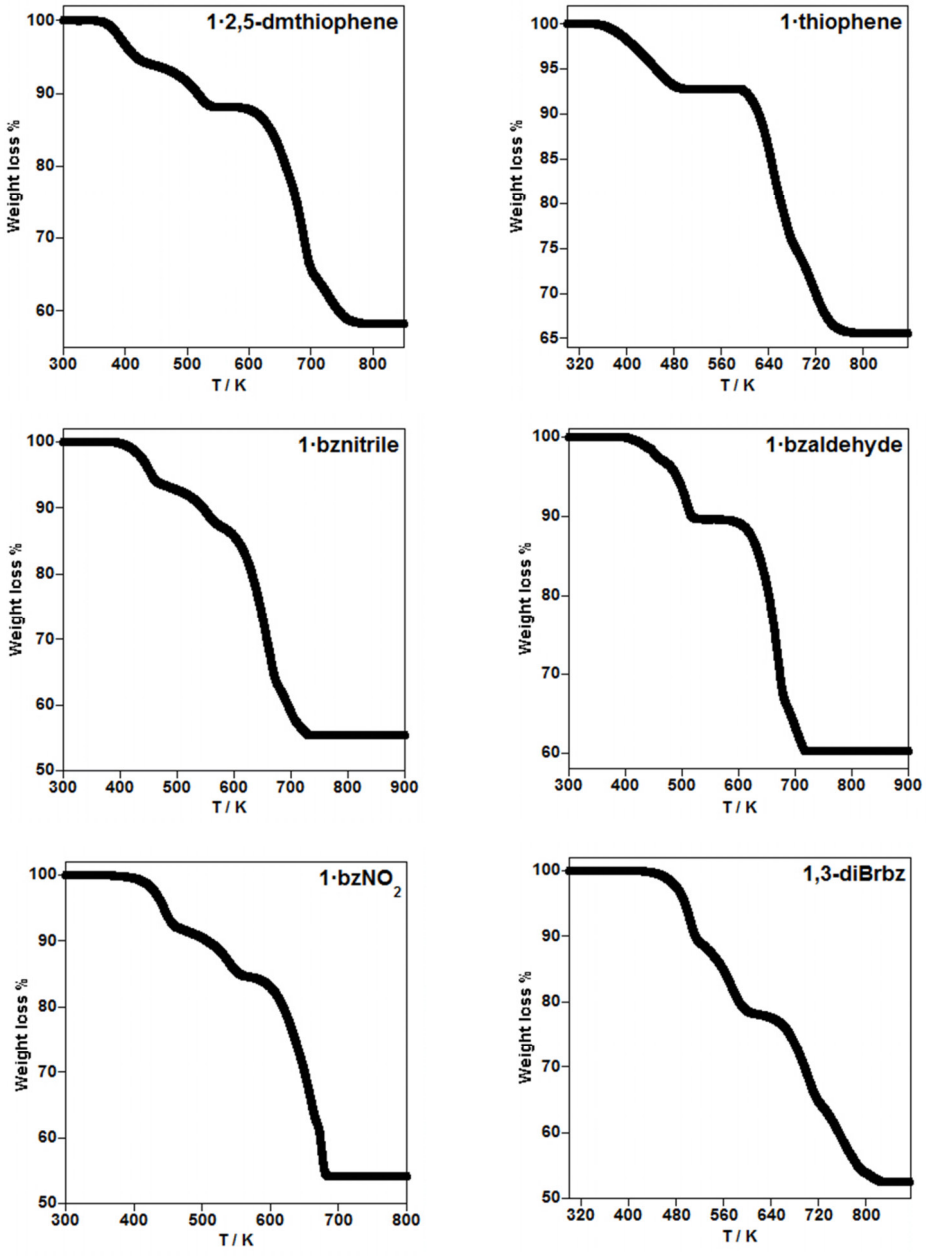

Figure S4.- View in the [010] direction of two interpenetrated 3D networks A and B. The iron atoms of one $\{Fe[Au(CN)_2]_2\}_\infty$ 2D layer are situated below/above but strictly at the center of the $\{Fe_4[Au(CN)_2]_4\}$ square grids belonging to the other layer.

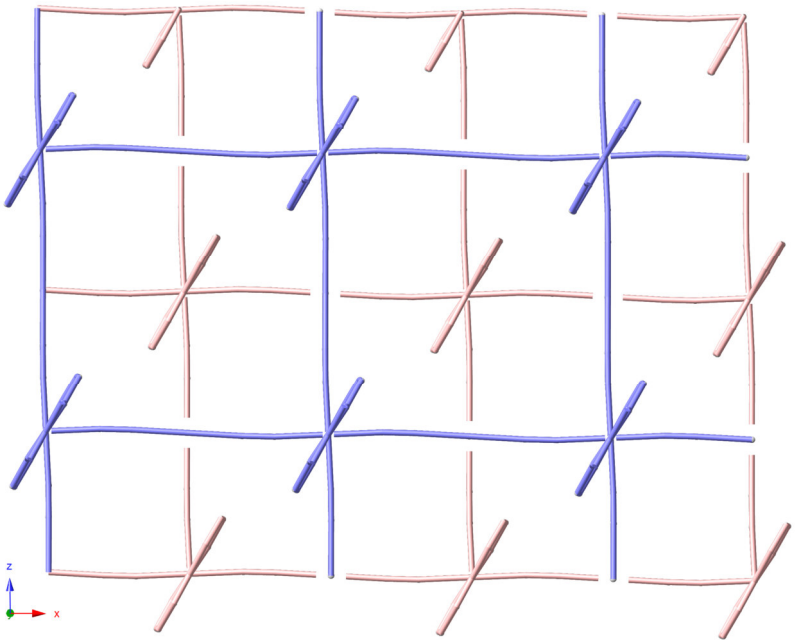

Figure S5.- Thermal dependence of the unit-cell volume of **1**·bzNO_2. The cooling and heating modes are displayed in blue and red colours, respectively.

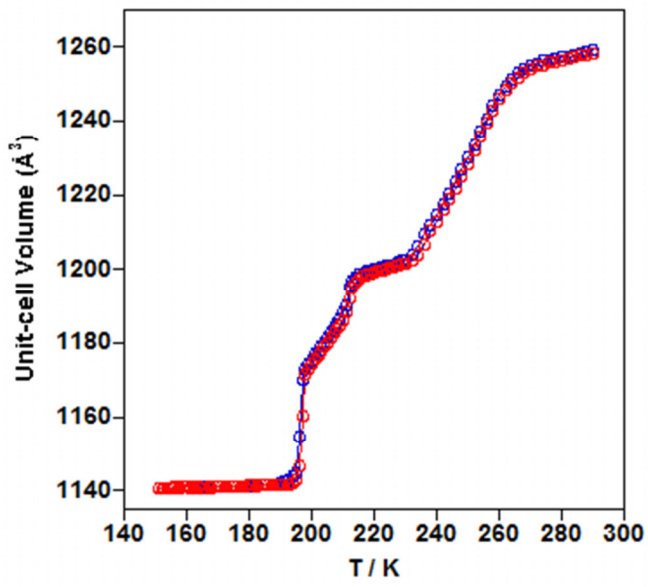

S5.- References

[1] E. Botana; E. Da Silva; J. Benet-Buchholz; P. Ballester; J. de Mendoza, *Angew. Chem. Int. Ed.*, **2007**, *46*, 198.

CAPÍTULO 7

CONCLUSIONES FINALES

CAPÍTULO 7

CONCLUSIONES FINALES

Electronic structure modulation in an exceptionally stable non-heme nitrosyl iron(II) spin-crossover complex

- Se ha sintetizado y caracterizado un complejo nitrosilo de Fe^{II} singular formulado $[Fe(bztpen)(NO)](PF_6)]$ (**1**) que presenta un equilibrio de espín S = 1/2↔S = 3/2 en el intervalo de temperatura 100-400 K, fruto del acoplamiento antiferromagnético entre el radical NO (S_{NO} = 1/2) y los estados de espín S_{Fe} = 2↔S_{Fe} = 0. Este acoplamiento es tan elevado (J > -$\left|2000\right|$ cm^{-1}) que a medida que se puebla el estado S_{Fe} = 2, el estado resultante $S_{Fe\text{-}NO}$ = 3/2 se convierte en el estado fundamental de **1**, incluso a temperaturas superiores a 500 K. Estas conclusiones resultan del análisis exhaustivo de las propiedades magnéticas, la estructura molecular, espectroscopias EPR, Mössbauer, visible, IR y Raman en función de la temperatura apoyados por cálculos DFT.

- En particular, la variación térmica experimental del producto $\chi_M T$ de **1** ha sido ajustada por mínimos cuadrados al modelo de disoluciones regulares de Slichter-Drickmer en el intervalo de temperatura 2-400 K. En dicho ajuste se ha considerado el equilibrio $S_{Fe\text{-}NO}$ = 1/2↔$S_{Fe\text{-}NO}$ = 3/2. Los resultados calculados están en un alto grado de acuerdo con los resultados experimentales [$R_{min} = 7\cdot10^{-5}$] y conducen a los parámetros de ajuste: i) $g_{3/2}$ = 2.15, ii) ΔH = 12.48 kJ mol^{-1} y iii) $T_{1/2}$ = 377.7 K. De estos datos se deduce ΔS = 33 J K^{-1} mol^{-1}. Estos valores son consistentes con lo esperado para una transición de espín $S_{Fe\text{-}NO}$ = 1/2↔$S_{Fe\text{-}NO}$ = 3/2.

- La espectroscopia EPR a temperatura baja presenta una única señal muy estrecha, centrada a $g_{1/2}$ = 2.02, característica de una especie radical que en este caso se atribuye al NO. A 300 K esta señal se ensancha (posiblemente debido a la presencia de centros de Fe^{II} en el estado S = 2) sin cambiar de posición. En principio, debería aparecer una señal a $g_{3/2} \approx 4$ característica del estado S = 3/2 pero, al igual que en el complejo TS [Fe(salen)(NO)], entre otros, ésta no se aprecia. La espectroscopia Mössbauer se caracteriza por una rápida interconversión de los estados $S_{Fe\text{-}NO}$ =

1/2↔$S_{Fe\text{-}NO}$ = 3/2 que impide distinguirlos. Esta circunstancia se ha observado en los complejos TS relacionados tales como [Fe(tmc)(NO)$(BF_4)_2$], [FeL^1(NO)] y [FeL^{1a}(NO)].

- El espectro electrónico en la región visible medido a 293 K presenta una banda de absorción centrada a λ = 555 nm cuya intensidad disminuye conforme aumenta la temperatura en el intervalo 175-425 K. Simultáneamente, los cristales cambian su color granate a un tono más amarillo. Estos cambios y su correlación con las propiedades magnéticas de **1** sugieren que una componente esencial de dicha absorción se debe a la transición $^1A\rightarrow{}^1T_1$ propia de centros de Fe^{II} en el estado LS (S = 0), la cual cambia de intensidad durante la transición de espín.

- Las medidas de espectroscopia Raman e IR realizadas sobre monocristales de **1** a diferentes temperaturas demuestran que el modo de extensión de NO, ν_{NO}, experimenta un marcado desplazamiento desde ν_{NO} = 1789 cm^{-1} a ν_{NO} = 1684 cm^{-1} conforme disminuye la temperatura de 400 a 100 K. La evolución de estos modos vibracionales característicos con la temperatura puede asociarse al predominio de especies $\{FeNO\}^7$ en los estados S = 3/2 y S = 1/2, respectivamente, ya que coexisten (en diferentes proporciones) en el intervalo de temperatura en el cual tiene lugar la conversión de espín S = 3/2↔S = 1/2. La evolución de las intensidades relativas de estos modos vibracionales reproducen razonablemente los cambios magnéticos registrados. Asimismo, la intensidad de la banda centrada a ν = 503 cm^{-1} a temperatura alta disminuye a expensas de un nuevo pico centrado a ν = 603 cm^{-1} a temperatura baja. Trabajos publicados con anterioridad a nuestros resultados permiten asignar estas señales a los modos de extensión y flexión Fe-NO acoplados de los estados S = 1/2 y S = 3/2, respectivamente. Por otro lado, las medidas de absorción IR realizadas sobre monocristales de **1** dan lugar a un espectro caracterizado por una banda de absorción ancha y su sobretono (ν = 1780 cm^{-1}, 3543 cm^{-1}) que corresponden al modo vibracional ν_{NO} en el estado S = 3/2 mientras que a 123 K se aprecian un hombro y su sobretono (ν = 1670 cm^{-1}, 3337 cm^{-1}) que pueden atribuirse al modo de vibración ν_{NO} en el estado S = 1/2. Ambas técnicas sugieren que **1** experimenta una TS completa a temperatura baja ya que no se aprecian bandas de absorción atribuibles al modo característico ν_{NO} en el estado S = 3/2 por debajo de 200 K. Asimismo, en el espectro de absorción IR realizado a 473 K no se aprecian bandas de absorción características del estado S = 1/2 lo cual indica una TS casi completa a temperatura alta.

- La elevada estabilidad de los cristales de **1** ha permitido el estudio estructural más completo publicado hasta la actualidad para un complejo nitrosilo de Fe^{II} que además presenta propiedades de transición de espín. A su vez, la conversión de espín ha permitido modular térmicamente la estructura electrónica y molecular del centro $\{FeNO\}^7$ revelando su naturaleza fuertemente covalente la cual se infiere de los espectros Raman e IR. Consistentemente con las observaciones realizadas en estos espectros, las variaciones estructurales observadas tales como el aumento de las distancias de enlace promedio <Fe-N>, el aumento del ángulo Fe-N-O desde 144º (120 K) hasta 157.9º (420 K) y la disminución de las distancias de enlace N-O desde 1.170 Å (120 K) hasta 1.099 (420 K), se han podido correlacionar con la población térmica del estado S = 3/2.

- Los cálculos DFT realizados para los estados S = 1/2 y S = 3/2 esencialmente corroboran los resultados estructurales observados. En particular, la naturaleza de campo medio-fuerte del ligando bztpen estabiliza el estado de oxidación del Fe^{II} y del NO en $\{FeNO\}^7$ en contraposición con lo inferido para otros sistemas $\{FeNO\}^7$ en los que el equilibrio $S_{Fe\text{-}NO}$ = 1/2↔$S_{Fe\text{-}NO}$ = 3/2 podría deberse a una tautomería de valencia entre Fe^{II} y el NO para dar Fe^{III} (S = 5/2)-NO^- (S = 1) acoplado antiferromagnéticamente.

Clathration of five-membered aromatic rings in the bimetallic spin-crossover metal-organic framework $[Fe(TPT)_{2/3}\{M^I(CN)_2\}_2]\cdot G$ (M^I = Ag, Au)

- Se han sintetizado y caracterizado seis clatratos tipo Hofmann de la red metal-orgánica 3D $[Fe(TPT)_{2/3}\{M^I(CN)_2\}_2]\cdot nG$ (M^I = Ag (**1**·nG), Au (**2**·nG), G = moléculas huésped aromáticas furano, pirrol y tiofeno).

- Las medidas de difracción de rayos X sobre monocristal de los compuestos **1**·nG y **2**·nG a 120 y 300 K ponen de manifiesto que las entidades $\{Fe[M^I(CN)_2]_2\}_n$, fruto de la coordinación de los grupos $[M^I(CN)_2]^-$ en las posiciones ecuatoriales de los centros de Fe^{II}, definen una red tipo NbO. Por su lado, los ligandos TPT coordinados axialmente a los centros Fe^{II} forman capas hexagonales $[Fe(TPT)_{2/3}]_\infty$ que se apilan en la dirección [010]. Dos de estas capas (A y B) se superponen de manera que los grupos triazina de la capa A ocupan los centros de las ventanas hexagonales de la capa B. A su vez, los grupos $[M^I(CN)_2]^-$ conectan capas de un mismo tipo (A o B) originando dos redes

independientes interpenetradas. Las moléculas huésped se localizan en los poros comprendidos entre capas A-A y B-B consecutivas. Para ambas series (**1**·nG y **2**·nG) y a las dos temperaturas (120 y 300 K) las dimensiones de los poros de la red aumentan al incrementarse el tamaño de la molécula huésped. Este hecho ilustra una marcada flexibilidad en las redes $[Fe(TPT)_{2/3}\{M^{I}(CN)_2\}_2]$, en especial para M^{I} = Ag.

- **1**·nG experimentan una variación promedio de la longitud de enlace <Fe-N> consistente con una TS completa en el intervalo de temperatura 120-300 K. El fenómeno TS implica cambios en los ángulos en los octaedros $[FeN_6]$. En la serie **2**·nG, únicamente **2**·1furano experimenta una TS completa mientras que **2**·2pirrol y **2**·0.5tiofeno muestran 35-40% de centros Fe^{II} en estado HS a 120 K. La variación de los ángulos en las unidades $[FeN_6]$ concuerda con los cambios apreciados **1**·nG.

- En ambas series y a temperatura baja se aprecian interacciones intermoleculares a) entre las moléculas huésped y los grupos piridina de los ligandos TPT y b) entre las moléculas huésped y los grupos $[M^{I}(CN)_2]^{-}$. Únicamente se aprecian interacciones intermoleculares huésped···huésped en **1**·0.5furano y **2**·1furano a temperatura baja. Los contactos intermoleculares, independientemente de su naturaleza, cambian como consecuencia del cambio de estado de espín.

- Los clatratos **1**·nG presentan TS térmicamente inducidas y una cooperatividad relativamente baja. En concreto, **1**·0.5furano experimenta una TS prácticamente completa en dos etapas. La primera etapa (Tc ≈ 233 K) implica la conversión de espín de 2/3 de los centros Fe^{II} mientras que los centros restantes transitan a Tc ≈ 173 K. **1**·1.5pirrol y **1**·1tiofeno muestran una TS en tres etapas. Cada etapa involucra la conversión de 1/3 de los centros Fe^{II} presentes en la red con Tc_1 = 211.5 K y 193.5 K, Tc_2 = 167.3 K y 148.3 K y Tc_3 = 103.2 y 82 K para **1**·1.5pirrol y **1**·1tiofeno, respectivamente. Los estudios cristalográficos muestran un único centro Fe^{II} en los estados HS (300 K) y LS (120 K). A pesar de ello, la TS por etapas puede atribuirse a la aparición de diferentes centros Fe^{II} durante la transformación HS↔LS. **1**·nG y **2**·nG presentan TS incompletas como consecuencia del bloqueo térmico que suele producirse por debajo de 100 K.

- **2**·nG muestran TS de menor cooperatividad. En consistencia con el análisis cristalográfico, **2**·1furano experimenta una TS prácticamente completa mientras que

2·2pirrol y **2**·0.5tiofeno presentan 30-45% de centros Fe^{II} en estado HS a temperatura baja.

- Las propiedades magnéticas de **1**·nG y **2**·nG muestran una estabilización gradual del estado HS conforme aumenta el tamaño de la molécula huésped, consistente con estudios previos en los que se ha comprobado que las redes en estado HS estabilizan especialmente moléculas huésped voluminosas.

- Las temperaturas características de la serie **2**·nG son inferiores a las temperaturas correspondientes a la serie **1**·nG. Esta tendencia se debe a la mayor electronegatividad de Au respecto de Ag lo cual se explica mediante efectos relativistas de los que participan átomos pesado tales como Au. La mayor electronegatividad de Au reduce la capacidad dadora de los átomos de nitrógeno en los aniones $[Au(CN)_2]^-$, ello implica un menor campo de ligandos sobre Fe^{II} y la correspondiente estabilización del estado HS frente al estado LS. En consecuencia, la serie **2**·nG presenta temperaturas críticas inferiores a sus homólogos **1**·nG.

Two- and one-step cooperative spin transitions in Hofmann-like clathrates with enhanced loading capacity

Guest induced strong cooperative one and two-step spin crossover in a highly porous iron(II) Hofmann-type metal-organic framework

- Se han sintetizado los compuestos $\{Fe(bpb)[Ag^I(CN)_2]_2\}$ (**1Ag**), $\{Fe(bpb)[M^{II}(CN)_4]\}\cdot 2Guest$ (**2M-Guest** (M^{II} = Ni, Pd y Pt; Guest = naftaleno (**naph**), nitrobenceno (**phNO$_2$**)) cuya caracterización incluye los estudios de sus propiedades magnéticas y calorimétricas, espectros Mössbauer y la determinación de su estructura cristalina. Además, se sintetizaron y caracterizaron los compuestos microcristalinos formulados $\{Fe(bpb)_{1.1}[M^{II}(CN)_4]\}\cdot nCH_3OH$ (**2M**; M^{II} = Ni, Pd y Pt; n: 0-1).

- **2M-Guest** (M = Ni, Pd y Pt) se obtuvieron mediante técnicas de difusión lenta en disoluciones de agua-metanol en presencia de moléculas huésped. Las TGA indican la presencia de dos moléculas huésped por centro de Fe^{II} en consistencia con los análisis elementales y los estudios cristalográficos. **1Ag** se obtuvo por difusión lenta, independientemente de la presencia/ausencia de moléculas huésped en el medio. Sin

embargo, los compuestos microcristalinos **2M** (M = Ni, Pd y Pt) se sintetizaron por difusión lenta en ausencia de moléculas huésped. Los análisis elementales de **2M** sugieren un exceso de bpb del 10% y 0-1 moléculas lábiles de metanol.

- Los estudios cristalográficos realizados sobre cristales de **1Ag** y **2M-Guest** indican que estos compuestos presentan una red 3D tipo α-Po distorsionada. En **1Ag**, dos capas $\{[FeAg^{I}(CN)_2]_4\}_n$ onduladas se unen mediante ligandos bpb y generan una red 3D, la cual es atravesada por otras tres redes idénticas. Estas redes equivalentes se organizan en dos pares que se disponen ortogonales entre sí. Los átomos de Fe de los paralepípedos de una red se encuentran en el baricentro de los paralepípedos de la otra red perteneciente al mismo par. A 250 K, las distancias promedio de enlace <Fe-N> ecuatoriales y axiales son 2.212(5) Å y 2.189(4) Å, consistentes con centros de Fe^{II} en el estado HS. Estas distancias de enlace promedio decrecen ≈ 0.063 y ≈ 0.061 Å, respectivamente, a 120 K lo cual indica la ocurrencia de una TS incompleta para **1Ag**. Además, se aprecian importantes contactos C···C entre los anillos de piridina de los ligandos bpb, contactos C···C entre los grupos C≡N de redes vecinas e interacciones argentofílicas débiles.

- **2M-Guest** son isoestructurales y consisten en capas $\{Fe[M^{II}(CN)_4]\}_\infty$ unidas mediante ligandos bpb que se coordinan a las posiciones axiales de los centros de Fe^{II}. El ligando bpb se presenta curvado en forma de plátano con sus anillos de piridina perpendiculares entre sí dando lugar a octaedros $[FeN_6]$ axialmente elongados e inclinados que confieren un aspecto ondulado a las capas $\{Fe[M^{II}(CN)_4]\}_\infty$. **2Ni-phNO$_2$** cristaliza en el sistema monoclínico *P2/m* mientras que los restantes **2M-Guest** cristalizan en el sistema triclínico *P*-1. Estos clatratos presentan dos tipos de cavidades: los poros más anchos se extienden a lo largo del eje *a* y los más estrechos se ubican sobre el eje *b*. La presente red metal-orgánica registra la mayor porosidad efectiva dentro de la serie tipo Hofmann generalmente formuladas $\{FeL[M^{II}(CN)_4]\}$ que exhiben el fenómeno TS. El volumen accesible en la red $\{Fe(bpb)[Pt(CN)_4]\}$ a 120 K equivale aproximadamente al 54% y 53% de la celda unidad de **2Pt-Naph** y **2Pt-phNO$_2$**, respectivamente. De igual manera, **2M-Guest** (M = Ni, Pd) exhiben volúmenes accesibles en la red análogos a **2Pt·Guest**.

- **2M-Guest** presentan dos centros de Fe^{II} (Fe(1) y Fe(2)) y dos moléculas huésped cristalográficamente independientes por celda unidad. Una de las moléculas se

encuentra próxima a los anillos de piridina del ligando bpb coordinado a Fe(1) mientras que la segunda se encuentra en torno al anillo de piridina coordinado a Fe(2). En estos clatratos existen numerosas interacciones anfitrión-huésped que cambian con la temperatura de acuerdo con la expansión/contracción de la red debido al cambio del estado de espín de los centros de Fe^{II}. **2M-Naph** se caracteriza por un mayor número de contactos C···C anfitrión-huésped en comparación con **2M-phNO$_2$** por lo que la presencia de un determinado huésped afecta a las esferas de coordinación de los centros Fe(1) y Fe(2) de diferente manera.

- En **2Pt-Naph** la distancia de enlace promedio <Fe(1)-N> decrece ≈ 0.2 Å conforme desciende la temperatura de 250 a 195 K. Por su lado, la longitud de enlace promedio <Fe(2)-N> se mantiene prácticamente constante en el mismo intervalo de temperatura. No obstante, decrece ≈ 0.2 Å al disminuir la temperatura de 195 a 120 K. En consecuencia, **2Pt-Naph** presenta una transición de espín en dos etapas. De forma similar, **2Ni-naph** y **2Pd-naph** muestran TS en dos etapas. En ambos casos, la longitud de enlace promedio <Fe(1,2)-N> es consistente con centros Fe(1) y Fe(2) en el estado LS a 120 K mientras que a 150 K (Ni) y 204 K (Pd), Fe(2) y Fe(1) se encuentran en los estado de espín HS y LS, respectivamente. Finalmente, ambos compuestos presentan centros Fe(1) en el estado HS a 250 K.

- **2Pt-phNO$_2$** experimenta una TS en una única etapa ya que la distancia de enlace promedio <Fe(1)-N> y <Fe(2)-N> disminuye ≈ 0.2 Å conforme desciende la temperatura de 250 a 120 K. De igual manera, **2Pd-phNO$_2$** presenta una TS en una sola etapa. Curiosamente, **2Ni-phNO$_2$** se caracteriza por una TS en dos etapas separadas por una pequeña meseta que no pudo analizarse. En **2M-phNO$_2$**, las distancias de enlace promedio <Fe(1,2)-N> se encuentran en el intervalo 1.950-1.970 Å a 120 K, consistentes con centros de Fe^{II} en el estado LS. A 250 K (**2Pt-phNO$_2$**), 260 K (**2Pd-phNO$_2$**) y 295 K (**2Ni-phNO$_2$**), <Fe(1,2)-N> aumentan 0.207-0.215 Å lo cual evidencia la ocurrencia de una TS completa en los tres derivados. Por su lado, **2M** son isostructurales y presentan el mismo patrón de difracción de rayos X en polvo que el simulado para **2M-Guest** en ausencia de huésped.

- Las medidas magnéticas evidencian que la TS de **1Ag** tiene lugar en el intervalo de temperatura 100-150 K en el que solo un 50% de los centros Fe^{II} cambian de estado de espín. Este carácter incompleto de la TS puede deberse a una frustración estructural

derivada de dos efectos presumiblemente contrapuestos: i) la contracción estructural debida a la TS y ii) las fuertes interacciones intermoleculares entre los anillos de piridina pertenecientes a diferentes redes.

- Las curvas $\chi_M T$ vs. T para **2M-naph** muestran TS completas en dos etapas ($T_{c1}\downarrow$ = 175.0 K (Ni), 211.2 K (Pd) y 205 K (Pt), $T_{c2}\downarrow$ = 122.5 K (Ni), 195.6 K (Pd) y 188 K (Pt)). El modo de calentamiento evidencia la existencia de bucles de histéresis en cada etapa (ΔT_{c1} = 10 K (Ni), 6.3 K (Pd) y 11 K (Pt) y ΔT_{c2} = 17.6 (Ni), 9.4 K (Pd) y 15 K (Pt)). Además, **2Ni-naph** presenta el efecto LIESST (T_{LIESST} = 54 K). La representación de $\chi_M T$ vs. T para **2Ni-phNO$_2$** muestra dos etapas separadas por una pequeña meseta centrada a 224 K mientras que **2Pd-phNO$_2$ y 2Pt-phNO$_2$** se caracterizan por una TS en una única etapa ($T_{c1}\downarrow$ = 227.2 K (Ni), $T_{c2}\downarrow$ = 220.6 K (Ni) y $T_c\downarrow$ = 227.0 K (Pd) y $T_c\downarrow$ = 210 K (Pt)). El modo de calentamiento indica la presencia de bucles de histéresis para los derivados **2M-phNO$_2$** (Ni) [ΔT_{c1} = 13.6 K, ΔT_{c2} = 10.8 K], (Pd) [ΔT = 19.4 K] y (Pt) [ΔT = 27 K]. El hecho de que la TS de **2Ni-phNO$_2$** presente una meseta muy pequeña en conjunto con la inexistencia de TS por etapas en **2M-phNO$_2$** (M = Pd, Pt) puede deberse al menor número de interacciones anfitrión-huésped en estos clatratos respecto de **2M-naph**. Por el contrario, $\chi_M T$ vs. T para **2M** muestra una TS muy incompleta por debajo de 150 K que se tornan más completas y tienen lugar a temperaturas más altas tras la aplicación de una presión hidrostática de 8 kbar. El caso más notable corresponde a **2Ni** (74% de los centros de Fe^{II} transitan de forma gradual y en dos etapas). Los compuestos tipo Hofmann con TS análogos a la presente serie, $\{Fe(L)[M^{II}(CN)_4]\}$ (L = pz, azpy, bpac) presentan TS a presión ambiente incluso en ausencia de moléculas huésped en la red. Sin embargo, **2M**, isostructurales a **2M-Guest**, permanecen en el estado HS independientemente de la temperatura. En consecuencia, las moléculas invitadas en la presente red son responsables de la existencia de TS completas. Además, el número e intensidad de las interacciones intermoleculares anfitrión-huésped determinan la naturaleza cooperativa de la TS (anchura de la histéresis y/o temperaturas críticas).

- La representación de ΔC_p vs. T para **2M-Guest** dio lugar a valores promedio de ΔH y ΔS consistentes con los valores típicamente asociados a compuestos de tipo Hofmann basados en Fe^{II} que exhiben TS fuertemente cooperativas.

- Los compuestos **1Ag**, **2Ni-naph**, **2Pt-naph** y **2Pt-phNO$_2$** fueron estudiados mediante espectroscopia Mössbauer. En todos los casos, los resultados obtenidos concuerdan con las medidas magnéticas y los estudios cristalográficos realizados. El espectro Mössbauer de **1Ag** recogido a 200 K presenta un único doblete con desplazamiento isomérico δ = 1.14(2) mm s^{-1} y desdoblamiento cuadrupolar ΔE_Q = 0.75(1) mm s^{-1}, característico de centros de Fe^{II} en el estado HS. Este doblete es sustituido por un nuevo doblete con δ = 0.13(2) mm s^{-1} y ΔE_Q = 0.69(1) mm s^{-1}, propio de centros de Fe^{II} en el estado LS. En consistencia con las medidas magnéticas y los estudios cristalográficos, la relación 1:1 entre las áreas de ambos dobletes indica una transición de espín incompleta.

- El espectro Mössbauer de **2Ni-naph** y **2Pt-naph** a 80 K consiste en dos centros de Fe^{II} en el estado LS en relación 1:1, caracterizados por dobletes de desplazamiento isomérico (Ni) [δ^{LS} = 0.49(2) mm s^{-1}] y (Pt) [δ^{LS} = 0.47(2), 0.49(2) mm s^{-1}] con desdoblamientos cuadrupolares (Ni) [ΔE_Q^{LS} = 0.24(1) mm s^{-1}] y (Pt) [ΔE_Q^{LS} = 0.47(2), 0.49(2) mm s^{-1}, ΔE_Q^{LS} = 0.32(1)]. A 150 K (Ni) y 199 K (Pt), uno de los dobletes LS desaparece dando lugar a un doblete HS (Ni) [δ^{HS} = 1.16(1) mm s^{-1}, ΔE_Q^{HS} = 1.99(0) mm s^{-1}] y (Pt) [δ^{HS} = 1.11(2) mm s^{-1}, ΔE_Q^{HS} = 1.53(4) mm s^{-1}] mientras que el segundo doblete LS presenta prácticamente los mismos parámetros Mössbauer. A 220 K (Ni) y 300 K (Pt), los espectro Mössbauer de **2Ni-naph** y **2Pt-naph** muestran dos dobletes HS igualmente poblados caracterizados por desplazamientos isoméricos (Ni) [δ^{HS1} = 1.13(1) mm s^{-1}, δ^{HS2} = 1.12(1) mm s^{-1}) y (Pt) (δ^{HS2} = 1.05(1) mm s^{-1}, δ^{HS2} = 1.06(1) mm s^{-1}] con desdoblamientos cuadrupolares (Ni) [ΔE_Q^{HS1} = 1.72(2) mm s^{-1}, ΔE_Q^{HS2} = 1.09(1) mm s^{-1}] y (Pt) [ΔE_Q^{HS1} = 0.51(2) mm s^{-1}, ΔE_Q^{HS2} = 1.21(2)] lo cual refleja la distinta distorsión geométrica de los poliedros de coordinación [Fe(1)N$_6$] y [Fe(2)N$_6$]. Por su lado los espectros Mössbauer de **2Pt-phNO$_2$** medidos a 80 y 300 K en los estados LS y HS, respectivamente, son similares a los espectros Mössbauer de **2Pt-naph** recogidos a la misma temperatura.

Spin-crossover behaviour in a new family of porous coordination polymers formulated {Fe(3,8-phen)$_2$[Au(CN)$_2$]$_2$}·G

- Se han sintetizado y caracterizado nueve clatratos tipo Hofmann basados en una nueva red metal-orgánica 3D formulados {Fe(3,8-phen)[Au(CN)$_2$]$_2$}·G (**1**·G), donde G representa a las moléculas huésped tiofeno, 2,5-dimetiltiofeno, benzonitrilo, benzaldehído, nitrobenceno, fluorobenceno, clorobenceno, bromobenceno y 1,3-dibromobenceno.

- Los estudios cristalográfico realizados sobre **1**·bzNO$_2$ muestran octaedros [FeN$_6$] axialmente elongados en los que cuatro grupos [Au(CN)$_2$]$^-$ y dos grupos 3,8-phen se coordinan a las posiciones ecuatoriales y axiales de los centros de Fe^{II}, respectivamente. La evolución de la variación promedio de la longitud de enlace <Fe-N> en el intervalo de temperaturas 290-120 K es consistente con una TS completa. Los grupos [Au(CN)$_2$]$^-$ conectan átomos de Fe definiendo capas {Fe[Au(CN)$_2$]$_2$}$_\infty$ que se extienden paralelas al plano *x-y*. Los ligandos 3,8-phen conectan átomos de hierro pertenecientes a capas adyacentes dando lugar a una red 3D. La estructura cristalina de **1**·bzNO$_2$ resulta de la interpenetración de dos redes 3D (A y B) dando lugar a una estructura cristalina con topología tipo α-Po en la cual capas {Fe[Au(CN)$_2$]$_2$}$_\infty$ de A y B se alternan estableciendo fuertes interacciones aurofílicas entre sí (Au···Au ≈ 2.995 Å y ≈ 3.073 Å a 120 y 290 K, respectivamente). Las moléculas de nitrobenceno ocupan el canal 1D que se extiende sobre el eje *b* (el volumen accesible corresponde a 787.5 Å^3 ≡ 35% del volumen total de la celda unidad). Las moléculas huésped establecen interacciones π-π con los ligandos 3,8-phen. Por su lado, la dependencia térmica del volumen de la celda unidad reproduce la curva χ_MT vs. T. Además, los difractogramas en polvo de **1**·G prueban que estos clatratos son isoestructurales.

- La serie **1**·G presenta TS completas y abruptas que tienen lugar en varias etapas. **1**·2,5-dmthiophene, **1**·bzF y **1**·bznitrile, experimentan TS en dos etapas separadas por una meseta (centrada a 184, 250 y 255 K, respectivamente) en la que coexisten ambos estado de espín. Estos clatratos presentan bucles de histéresis de un 1 K y de ≈ 8 K a temperatura baja y alta, respectivamente. **1**·bzaldehyde muestra una TS gradual en dos etapas en el intervalo de temperatura 250-145 K, con un bucle de histéresis de 5 K a temperatura baja. Por su lado, **1**·bzNO$_2$ experimenta una TS en tres etapas. La primera y segunda meseta, centradas a 223 K y 204 K, comprenden el ≈ 52% y el ≈ 87% de los

centros de Fe^{II} en el estado LS cada una. **1**·bzBr, **1**·bzCl y **1**·1,3-diBrbz presentan TS fuertemente cooperativas en tres etapas. La primera meseta (centrada a 197, 218 y 212 K, respectivamente) y la segunda (centrada a 170, 194 y 185 K, en cada caso) representan el ≈ 50% y el ≈ 79% de los centros de Fe^{II} en el estado LS, respectivamente. Estos clatratos muestran bucles de histéresis a temperatura baja (≈ 8 K), a temperatura intermedia (≈ 7 K, **1**·bzBr y **1**·bzCl) y a temperatura alta (≈ 4 K, **1**·bzBr y **1**·bzCl) Finalmente, **1**·thiophene experimenta una TS en cuatro etapas donde notables mesetas de 11 y 36 K se hayan centradas a 175 y 155 K, respectivamente. La primera comprende el ≈ 32% y la segunda el ≈ 48% de los centros de Fe^{II} en el estado LS. **1**·thiophene registra bucles de histéresis a temperatura baja (25 K), media-baja (30 K), intermedia (11 K) y alta (4 K). **1**·$bzNO_2$ y **1**·thiophene presentan el fenómeno LIESST con T_{LIESST} ≈ 44 K.

- Las representaciones ΔCp vs. T y $\delta(\chi_M T)/\delta T$ vs. T de **1**·G coinciden. De igual manera, los valores Tc que derivan de las medidas calorimétricas y magnéticas son consistentes entre sí. Además, los valores promedio ΔH y ΔS concuerdan con ΔH y ΔS característicos de los compuestos tipo Hofmann basados en Fe^{II} con TS fuertemente cooperativas. TGA realizadas sobre **1**·G prueban la presencia de una molécula de huésped por átomo de Fe, en congruencia con los estudios cristalográficos de **1**·$bzNO_2$.

- **1**·G (isoestructurales, con mismo número, tipo de molécula huésped y orientación espacial relativa dentro de los poros de la red) presentan comportamientos TS diferentes, fruto de la distinta naturaleza de las interacciones intermoleculares π-π entre el huésped y los ligandos 3,8-phen que, a su vez, afectan al campo de ligandos percibido por los centros de Fe^{II} y a la cooperatividad de la TS. En la familia de clatratos con TS formulados {Fe(bpac)[$Pt(CN)_4$]}·G (G = bzCl, bzBr y bzI) y {[$Fe(tvp)_2(NCS)_2$]·2G} (G = benzonitrilo, benzaldehído y nitrobenceno), publicados por Real y colaboradores, la evolución de $T_{1/2}$ se relaciona con la influencia del sustituyente sobre las interacciones π-π que se establecen entre la molécula huésped aromática y el anillo aromático del ligando orgánico (bpac o tvp) según el modelo electroestático H-S. La evolución de $T_{1/2}$ en **1**·bzF, **1**·bzCl y **1**·bzBr concuerda con la variación apreciada en la serie {Fe(bpac)[$Pt(CN)_4$]}·G. Sin embargo, la progresión de $T_{1/2}$ en **1**·$bzNO_2$, **1**·bzaldehyde y **1**·bznitrile no coincide con la tendencia descrita para la familia {[$Fe(tvp)_2(NCS)_2$]·2G}. Recientemente, estudios teóricos presentados por Parish y colaboradores demuestran que, en contraposición al modelo H-S, el sustituyente de un anillo aromático influye

directamente sobre el segundo anillo aromático y que los efectos del sustituyente sobre la nube π de su anillo aromático juegan un papel menor en la naturaleza de las interacciones π-π que tienen lugar entre dos anillos aromáticos. Dado que el papel de los sustituyentes en estas interacciones no covalentes aún no se ha esclarecido, tampoco podemos generalizar su impacto sobre los centros de Fe^{II} en los sistemas TS. De esta manera, **1**·G representa un modelo útil para el estudio del fenómeno TS en relación con las interacciones intermoleculares π-π, lo cual, en compañía de cálculos teóricos, resultará de gran utilidad en el diseño racional de materiales TS.

CAPÍTULO 7

CONCLUSIONS

Electronic structure modulation in an exceptionally stable non-heme nitrosyl iron(II) spin-crossover complex

- We have synthetized and characterized a singular nitrosyl Fe^{II} complex formulated [Fe(bztpen)(NO)](PF_6)] (**1**). It displays an S = 1/2↔S = 3/2 SCO behaviour in the temperature interval 100-400 K steming from a strong antiferromagnetic coupling (J > -|2000| cm^{-1}) between the NO radical (S = 1/2) and thermally interconverted (S = 0↔S = 2) ferrous spin states. This has been proved by magnetic and structural studies together with EPR, Mössbauer, visible, IR and Raman spectroscopies. Furthermore, DFT calculations reproduce reasonably well the structure of compound **1** in the LS and HS states supporting the idea that the strong ligand field bztpen ligand stabilizes the Fe^{II} and the NO.

- The thermodynamic parameters associated with the spin-transition were estimated by fitting the magnetic curve of **1** using the Slichter-Drickamer model in the temperature interval 2-400 K. For this purpose, the spin state equilibrium $S_{Fe\text{-}NO}$ = 1/2↔$S_{Fe\text{-}NO}$ = 3/2 was considered. A least-squares fit procedure which minimizes the function $R_{min} = \sum(x_M T^{obs} - x_M T^{calcd})^2 / \sum(x_M T^{obs})^2$ led to $g_{3/2}$ = 2.15, R_{min} = $7 \cdot 10^{-5}$, ΔH = 12.48 kJ mol^{-1}, $T_{1/2}$ = 377.6 K and ΔS = $\Delta H/T_{1/2}$ = 33 J K^{-1} mol^{-1}. These values are in agreement with experimental data and are consistent with an S = 1/2↔S = 3/2 transformation.

- The X-band EPR solid-state spectrum of compound **1** collected at low temperature is characterized by a sharp signal centered at g = 2.02. This signal becomes wider without moving significantly at 300 K, probably due to the presence of Fe^{II} centers in the S = 2 spin state. This EPR spectrum is reminiscent of that reported for the classical SCO nitrosyl compound [Fe(salen)(NO)] for which no signal at g ≈ 4 characteristic of the S = 3/2 state, was observed at high temperature.

- Similar to the related SCO complexes [Fe(tmc)(NO)(BF_4)$_2$], [FeL^1(NO)] and [FeL^{1a}(NO)], the Mössbauer spectrum of **1** collected at 293 K displays only one doublet

(δ = 0.295(4) mm s^{-1} and ΔE_Q = 0.590(8) mm s^{-1}) suggesting a fast $S_{Fe\text{-}NO}$ = 1/2↔$S_{Fe\text{-}NO}$ = 3/2 interconversion which leads to an averaged spectrum.

- The electronic spectrum collected at 293 K (LS:HS, 73:23) is characterized by three absorption bands. The thermal variation of the λ = 555 nm absorption band, the thermochromism displayed by **1** in the temperature interval 175-425 K and its magnetic properties suggest that this band might be due to $^1A \rightarrow {}^1T_1$ transitions in Fe^{II} centers in the LS state (S = 0). This has been noticed before in many Fe^{II} complexes exhibiting an S = 0↔S = 2 spin-state change.

- Variable-temperature, single-crystal Raman spectra of **1** shows that the NO stretching mode ν_{NO} undergoes a remarkable downshift from ν = 1789 to 1684 cm^{-1} when going from 400 to 100 K. These characteristic vibrational modes can be associated with the S = 3/2 and S = 1/2 states, respectively, since they co-exist in the temperature interval where the conversion between these two magnetic states takes place. Their relative intensities reproduce reasonably well the magnetic changes. The intensity of a medium band (ν = 503 cm^{-1}) recorded at high temperature, decreases upon cooling at expense of a new peak (ν = 603 cm^{-1}). According to previous works, these peaks are feasibly assignable to coupled Fe-NO stretching and bending modes in the S = 1/2 and S = 3/2 states, respectively. The temperature-dependent, single-crystal IR absorption spectra confirm well the Raman data. At 473 K, the IR absorption spectra of **1** shows a broad absorption band and its overtone (ν = 1780 cm^{-1}, 3543 cm^{-1}) attributable to the ν_{NO} mode in the S = 3/2 state whereas at 123 K, an ill-resolved shoulder and its overtone (ν = 1670 cm^{-1}, 3337 cm^{-1}) can be assigned to the ν_{NO} mode in the S = 1/2 state. Both techniques evidences a complete spin conversion at low temperature (no characteristic ν_{NO} absorption bands of S = 3/2 state can be seen below 200 K). Furthermore, there is no residual S = 1/2 state fraction in the IR spectra at 473 K which indicates a complete SCO at high temperatures.

- The robustness of the single crystals of **1** has allowed the most complete single-crystal analysis of Fe^{II} nitrosyl complexes reported so far. Performed in the temperature range 120-420 K, this structural analysis shows the adaptability of the NO molecule to the change of spin states in the Fe^{II} center. Upon heating from 120 to 420 K, the N-O bond length gradually decreases from 1.170(4) to 1.099(10) Å while the Fe-N-O bond angle increases from 144.0(3)° to 157.9(10)°, both changes arise from the gradual population

of the S = 3/2 state. This evidences the strong covalence of the Fe-NO bond involved in the {FeNO} unit.

- The DFT calculations correlate well with the LS and HS observed crystal structures and show that the strong ligand field bztpen ligand stabilizes the Fe^{II} and the NO radical. Therefore, the occurence of an S = 2↔S = 0 spin equilibrium in the Fe^{II} center antiferromagnetically coupled with the NO radical result in the observed S = 3/2↔S = 1/2 spin equilibrium.

Clathration of five-membered aromatic rings in the bimetallic spin-crossover metal-organic framework $[Fe(TPT)_{2/3}\{M^{I}(CN)_2\}_2]\cdot G$ (M^{I} = Ag, Au)

- We have synthesized and characterized six clathrate compounds of the 3D SCO metal-organic framework formulated $[Fe(TPT)_{2/3}\{M^{I}(CN)_2\}_2]\cdot nG$, where M^{I} = Ag (**1**·nG), Au (**2**·nG) and G represents the aromatic molecules furan, pyrrole and thiophene.

- Single crystals of **1**·nG and **2**·nG were measured at 120 and 300 K. Each Fe^{II} center defines an axial elongated $[FeN_6]$ octahedron with its equatorial positions occupied by four $[M^{I}(CN)_2]^{-}$ anions whereas the axial positions are occupied by two TPT ligands. Each TPT ligand links three Fe^{II} sites, thus, the Fe^{II}-TPT assembly defines infinite hexagonal $[Fe(TPT)_{2/3}]_\infty$ layers that stack in [010] direction. Two layers (A and B) superpose in such a way that the triazine groups of one layer lies on the centre of the hexagonal windows of the other layer. The $[M^{I}(CN)_2]^{-}$ anions connect layers of the same type (A or B) generating two interlocked 3D frameworks with the NbO topology. In addition, two consecutive A-A and B-B layers define large pores where the guest molecules are located. **1**·nG and **2**·nG display a good correlation between the size of the guest molecule and the increase of the pore dimension at 120 and 300 K which reflects a certain degree of flexibility of the 3D networks.

- The **1**·nG are characterized by an average bond length <Fe-N> change within the range of values consistent with the occurrence of a complete SCO in the temperature interval 120-300 K. The SCO is also accompanied by changes in the bond angles in the coordination core $[FeN_6]$. Regarding **2**·nG, only **2**·1furan shows practically complete SCO whereas **2**·2pyrrole and **2**·0.5thiophene present 35-40% of Fe^{II} centers in the HS state at 120 K. The angular parameters of the coordination centers (Fe and Au) are

comparable to those of **1**·nG.

- Intermolecular interactions occur between the guest molecules and both, the pyridine group of the TPT ligand and the $[M^{I}(CN)_2]^-$ groups at low temperature whereas short guest···guest contacts are only observed for **1**·0.5furan and **2**·1furan in the LS state. These contacts change with temperature due to the occurrence of SCO.

- **1**·nG present relatively poor cooperative thermal induced SCO. **1**·0.5furan displays an almost complete two-step SCO. The first step (Tc ≈ 233 K) involves 2/3 of the SCO whereas the remaining HS↔LS transformation occurs at ≈ 173 K. In contrast, **1**·1.5pyrrole and **1**·1thiophene undergo an equal spaced three-step SCO with Tc_1 = 211.5 K and 193.5 K, Tc_2 = 167.3 K and 148.3 K, Tc_3 = 103.2 and 82 K for **1**·1.5pyrrole and **1**·1thiophene, respectively. Multi-step SCO behaviours probably arise from the generation of different Fe^{II} sites during the HS↔LS transformation since only one Fe^{II} was observed in the LS and HS structures. Due to thermal quenching, the SCO is incomplete for both derivatives. **2**·nG display even less cooperative one-step SCO at lower temperature than **1**·nG. **2**·1furan displays a rather complete SCO whereas **2**·2pyrrole and **2**·0.5thiophene present 30-45% of Fe^{II} HS centers at low temperatures in agreement with the crystallographic analysis. The magnetic properties of **1**·nG and **2**·nG suggest a gradual stabilization of the HS state as the molecular volume of the guest increases, consistent with previous studies on the relative higher stability of bulky guest molecules compare to small guest molecules in the same framework.

- Tc of **2**·nG are lower than the corresponding Tc displayed by **1**·nG. This tendency has been ascribed to the much higher electronegativity of Au with respect to Ag due to relativistic effects in the former. A poorer donor capacity of the nitrogen atoms in the $[Au(CN)_2]^-$ anions implies a further stabilized HS state in **2**·nG compare to **1**·nG. Therefore, lower Tc are expected for **2**·nG.

Two- and one-step cooperative spin transitions in Hofmann-like clathrates with enhanced loading capacity

Guest induced strong cooperative one and two-step spin crossover in a highly porous iron(II) Hofmann-type metal-organic framework

- We have synthesized seven new compounds formulated $Fe(bpb)[Ag^{I}(CN)_2]_2\}$ (**1Ag**), $\{Fe(bpb)[M^{II}(CN)_4]\}\cdot 2Guest$ (**2M-Guest** (M^{II} = Ni, Pd and Pt; Guest = naphthalene (**naph**), nitrobenzene (**phNO$_2$**)). Their magnetic and calorimetric properties, Mössbauer spectra and crystal structures have been studied. Furthermore, the synthesis and characterization of the microcrystalline compounds $\{Fe(bpb)_{1.1}[M^{II}(CN)_4]\}\cdot nCH_3OH$ (**2M**; M^{II} = Ni, Pd and Pt; n: 0-1) have been also accomplished.

- Slow diffusion methods in methanol, water and the appropriate guest solutions afforded **2M-Guest** (M = Ni, Pd and Pt). The thermal analysis on **2M-Guest** indicates the presence of 2 guest molecules per unit formula consistent with elemental and crystallographic analyses. **1Ag** was obtained independently of the presence or absence of guest molecules in the diffusion process. In the absence of guest molecules, the **2M** (M = Ni, Pd and Pt) were obtained as microcrystalline powders. Their elemental analyses suggest an excess of bpb by 10% and 0-1 labile methanol molecules.

- Single-crystal X-ray diffraction studies show that **1Ag** and **2M-Guest** display distorted α-Po frameworks. In **1Ag**, undulating $\{[FeAg(CN)_2]_4\}_n$ 2D grids are pillared by bpb ligands generating a 3D framework. Three other identical frameworks pass through the windows of the previous grid. Indeed, **1Ag** is made up of two different pairs of interpenetrated networks orthogonally oriented where the Fe^{II} centers of the parallelepipeds of one framework are placed on the barycenter of the parallelepipeds of the other framework in the same set. The shortening of the average bond lengths <Fe-N> from 250 K to 120 K is consistent with a very incomplete HS-to-LS conversion. There are short C···C contacts between pyridine rings of neighbour concatenated networks and between the C≡N groups of neighbour networks. **1Ag** also displays weak argentophilic interactions.

- **2M-Guest** are isostructural and consist of $\{Fe[M^{II}(CN)_4]\}_n$ layers pillared by bpb ligands giving rise to 3D frameworks. In contrast with **1Ag**, in **2M-Guest** (M = Ni, Pd and Pt) the bpb ligands are strongly bent with their pyridine moieties almost perpendicular to each

other which result in tilted axially elongated [FeN_6] octahedrons and corrugated {$Fe[M^{II}(CN)_4]$}$_\infty$ layers. **2Ni-phNO$_2$** features the *P2/m* (monoclinic) space group whereas the remaining **2M-Guest** display the *P-1* (triclinic) space group. **2M-Guest** exhibit two types of cavities: the wider pores run along the *a* axis whereas the narrower ones are located on the *b* axis. The **2M-Guest** clathrates display the largest effective porosity among Hofmann-like {$FeL[M^{II}(CN)_4]$} SCO-PMOF reported up to now (accessible free-guest volumes equal to ≈ 54% (**naph**) and ≈ 53% (**phNO$_2$**) of their unit cell at 120 K).

- **2M-Guest** series present two crystallographically distinct Fe^{II} centers (Fe(1) and Fe(2)) and two crystallograpically distinct guest molecules per unit cell. One guest molecule is located half-way between the pyridine ring of the bpb ligand coordinated to Fe(1) while the second lies closer to the pyridine ring coordinated to Fe(2). There are numerous host-guests contacts that change with temperature according to the expansion/contraction of the lattice due to the SCO of Fe^{II} centers. Depending on the guest molecule (**naph** or **phNO$_2$**), the coordination spheres of the Fe(1) and Fe(2) centers are influenced by these C···C contacts in a particular way.

- In **2Pt-Naph**, the average bond length <Fe(1)-N> value decreases ≈ 0,2 Å when cooling from 250 K down to 195 K and remains constant upon further cooling. <Fe(2)-N> value does not vary much when cooling from 250 K down to 195 K, but decreases ≈ 0,2 Å upon cooling to 120 K. Therefore, **2Pt-Naph** undergoes SCO in two steps. Similarly, **2Ni-naph** and **2Pd-naph** experiment two-step spin transitions. For both compounds, <Fe(1,2)-N> are consistent with Fe(1) and Fe(2) in the LS state at 120 K. However, at 150 K (Ni) and 204 K (Pd), Fe(2) and Fe(1) are in the HS and LS states, respectively. Finally, both clathrates display Fe(1) centers in the HS state at 250 K.

- **2Pt-phNO$_2$** <Fe(1)-N> and <Fe(2)-N> values decrease ≈ 0,2 Å upon cooling from 250 K down to 120 K, thus, a simultaneous spin change of both Fe(1) and Fe(2) takes place. Similarly, **2Pd-phNO$_2$** undergoes a one step SCO behaviour. In contrast, **2Ni-phNO$_2$** undergoes a two-step spin transition with a small step which could not be analyzed. At 120 K, <Fe-N> values for Fe(1) and Fe(2) centers are in the range of 1.950-1.970 Å, consistent with Fe^{II} centers in the LS state and increase around 0.207-0.215 Å at 260 K (**2Pd-phNO$_2$**) and 295 K (**2Ni-phNO$_2$**) as expected for a complete SCO. **2M** are isostructural and display the same PXRD pattern that the simulated one for **2M-Guest** where the guest molecules were artificially removed.

- $\chi_M T$ vs. T plot shows that **1Ag** undergoes half spin transition centered at 130 K. The contraction of the networks due to thermal induced SCO and repulsive π-π interactions between the pyridine rings in the LS state could cause the structural frustration responsible for the incompleteness of the SCO in **1Ag**. $\chi_M T$ vs. T plots show that **2M-naph** undergo complete SCO in two equal steps ($T_{c1}\downarrow$ = 175.0 K (Ni), 211.2 K (Pd) and 205 K (Pt), $T_{c2}\downarrow$ = 122.5 K (Ni), 195.6 K (Pd) and 188 K (Pt)). The heating mode evidences the occurrence of thermal hysteresis for each step (ΔT_{c1} = 10 K (Ni), 6.3 K (Pd) and 11 K (Pt)) and (ΔT_{c2} = 17.6 (Ni), 9.4 K (Pd) and 15 K (Pt)). In addition, **2Ni-naph** exhibits the well-known LIESST effect (T_{LIESST} = 54 K). $\chi_M T$ vs. T plot for **2Ni-phNO$_2$** displays two steps separated by a 2 K wide plateau ca. 224 K while complete one-step transitions are observed for **2Pd-phNO$_2$** and **2Pt-phNO$_2$** ($T_{c1}\downarrow$ = 227.2 K (Ni), $T_{c2}\downarrow$ = 220.6 K (Ni), $T_c\downarrow$ = 227.0 K (Pd) and 203 K (Pt)). The heating mode defines hysteresis loops (Ni) [ΔT_{c1} = 13.6 K], (Ni) [ΔT_{c2} = 10.8 K], (Pd) [ΔT = 19.4 K] and (Pt) [ΔT = 27 K]. The fact that **2Ni-phNO$_2$** SCO exhibits a narrower plateau than **2Ni-naph** together with the lack of steps in **2Pd-phNO$_2$** and **2Pt-phNO$_2$** SCO may be related to the lesser number of host-guest interactions in **2M-phNO$_2$** in comparison with **2M-naph**. **2M** display very incomplete HS-to-LS conversions (8-13%) below 150 K that a hydrostatic pressure of 8 kbar shifts to higher temperatures enhancing the completeness of these preliminary incipient SCO. Interestingly, **2Ni** features a gradual, two-step and 74% complete HS↔LS spin transition. The related Hofmann SCO-MOFs {Fe(L)[$M^{II}(CN)_4$]} (L = pz, azpy, bpac) display SCO at ambient pressure despite being unloaded while **2M**, isostructural to **2M-Guest,** are almost HS in the same experimental conditions. This suggests that the presence of guest molecules within the pores of the present framework is responsible for the occurrence of complete SCO in the corresponding **2M-Guest** clathrates. Moreover, the number and strength of π-π intermolecular interactions between the host and the guest molecules determines the cooperative nature of the SCO i.e. hysteresis width and/or Tc.

- DSC data expressed as ΔC_p vs. T plots for **2M-Guest** led to ΔH and ΔS average variations consistent with those typically displayed by Hofmann-type SCO-CPs based on Fe^{II} centers featuring cooperative SCO behaviours. In addition, the Tc obtained from the maxima of ΔCp vs. T plots for **2M-Guest** are in agreement with the magnetic data.

- **1Ag**, **2Ni-naph**, **2Pt-naph** and **2Pt-phNO$_2$** were also monitored by Mössbauer

spectroscopy. In all cases, the obtained data are in agreement with crystallographic and magnetic results**.** The Mössbauer spectrum of **1Ag** collected at 200 K shows the presence of a HS doublet with isomer shift δ = 1.14(2) mm s^{-1} and quadrupole splitting ΔE_Q = 0.75(1) mm s^{-1}. At 80 K, another doublet, consistent with Fe^{II} centers in the LS state (ΔE_Q = 0.69(1) mm s^{-1} and δ = 0.13(2) mm s^{-1}), appears. The ratio between doublets area is 1:1, which indicates an incomplete spin transition. The Mössbauer spectrum of **2Ni·naph** collected at 80 K shows two LS doublets (δ^{LS} = 0.49(2) mm s^{-1} and quadrupole splitting parameters ΔE_Q^{LS} = 0.24(1) mm s^{-1}). Another minor HS doublet (δ^{HS} = 1.36(1) mm s^{-1} and ΔE_Q^{HS} = 2.90(1) mm $s^{-}1$) can be seen. Upon heating up to 150 K, the ratio between areas of the LS and HS doublets is equal to 1:1. At 200 K, the spectrum contains two overlapping equally populated HS doublets with similar isomer shift values (δ^{HS1} = 1.13(1) mm s^{-1} and δ^{HS2} = 1.12(1) mm s^{-1}) and strongly different quadrupole splitting parameters (ΔE_Q^{HS1} = 1.72(2) mm s^{-1} and ΔE_Q^{HS2} = 1.09(1) mm s^{-1}). The Mössbauer spectrum of **2Pt-naph** collected at 80 K is consistent with two different Fe^{II} centers in the LS state in 1:1 ratio (δ = 0.47(2), 0.49(2) mm s^{-1} and ΔE_Q^{LS} = 0.32(1), 0.16(2) mm s^{-1}). Upon increasing the temperature to 199 K, an HS doublet (δ^{HS} = 1.11(2) mm s^{-1} and ΔE_Q^{HS} = 1.53(4) mm s^{-1}) is detected instead of one LS doublet whereas the parameters of the other LS doublet remain almost unchanged. At 300 K, the Mössbauer spectrum of **2Pt-naph** shows two overlapping equally populated HS doublets with similar isomer shift values (δ^{HS} = 1.05(1) mm s^{-1}, 1.06(1) mm s^{-1}) but strongly different quadrupole splitting parameters (ΔE_Q^{HS} = 0.51(2), 1.21(2) mm s^{-1}) that reflect the different geometric distortion displayed by [Fe(1)N_6] and [Fe(2)N_6] coordination polyhedrons. The Mössbauer spectra of **2Pt-phNO$_2$**, recorded at 80 and 300 K in the LS and HS states, respectively, are similar to those of **2Pt-naph** at the same temperatures. Therefore, Mössbauer spectroscopy evidences the occurrence of two-step spin transitions for **2Ni-naph** and **2Pt-naph** whereas a one-step spin transition can be seen in **2Pt-phNO$_2$** Mössbauer spectra.

Spin crossover behaviour in a new family of porous coordination polymers formulated {Fe(3,8-phen)$_2$[Au(CN)$_2$]$_2$}·G

- We have synthesized and characterized nine Fe^{II} Hofmann-like 3D clathrates

formulated {Fe(3,8-phen)[Au(CN)$_2$]$_2$}·G (**1**·G) where G = thiophene, 2,5-dimethylthiophene, benzonitrile, benzaldehyde, nitrobenzene, fluorobenzene, chlorobenzene, bromobenzene and 1,3-dibromobenzene as guest molecules.

- Single-crystal X-ray diffraction studies on **1**·bzNO$_2$ show that the Fe atom defines a distorted elongated [FeN$_6$] octahedron where four [Au(CN)$_2$]$^-$ groups and two 3,8-phen organic ligands coordinate to Fe^{II} equatorial and axial positions, respectively. Average <Fe-N> bond lengths changes in the temperature interval 290-120 K are consistent with the occurrence of a complete SCO. [Au(CN)$_2$]$^-$ linkers connect Fe atoms defining 2D {Fe[Au(CN)$_2$]$_2$}$_\infty$ layers lying parallel to the *x*-*y* plane. Meanwhile, 3,8-phen ligands bind Fe atoms from adjacent layers defining a 3D network. Two 3D networks A and B interpenetrate with the topology of the archetypal α-Po structure hence, 2D {Fe[Au(CN)$_2$]$_2$}$_\infty$ layers of A alternate with those of B and are held together by strong aurophilic interactions (Au···Au ≈ 2.995 Å and ≈ 3.073 Å at 120 and 290 K, respectively). Disordered nitrobenzene molecules are located within a 1D channel that runs along the *b* axis (the void space is calculated as 787.5 Å^3 ≡ 35% of the unit cell volume). Short C···C contacts between nitrobenzene molecules and 3,8-phen ligand evidence the occurrence of host-guest π-π interactions. The thermal dependence of the unit-cell volume reproduces the magnetic data. Meanwhile, powder X-ray diffraction patterns for **1**·G compounds prove that all **1**·G clathrates are isostructural.

- **1**·G clathrates show complete, abrupt and multi-step SCO behaviours. **1**·2,5-dmthiophene, **1**·bzF and **1**·bznitrile, undergo two-step spin transitions with plateaus centered around 184, 250 and 255 K, respectively. These clathrates display 1 K wide hysteresis loops at low temperature while wide hysteresis loops take place at high temperature (10, 6.5 and 5.6 K, respectively). **1**·bzaldehyde features unequally spaced two-step spin transition in the temperature interval 250-145 K with a 5 K wide hysteresis loop at low temperature. An unequally spaced three-step spin transition characterizes **1**·bzNO$_2$. The first and second plateau (ca. 223 and 204 K each) comprises ≈ 52% and ≈ 87% of Fe^{II} centers in the LS state, respectively. **1**·bzBr, **1**·bzCl and **1**·1,3-diBrbz display more abrupt and hysteretic three-step SCO behaviours than **1**·bzNO$_2$. Their first plateau (ca. 197, 218 and 212 K, respectively) and second plateau (ca. 170, 194 and 185 K, respectively) involve ≈ 50% and ≈ 79% of Fe^{II} centers in the LS state, each. These clathrates features hysteresis loops at low temperatures (10, 9 and 5 K wide, respectively). **1**·bzBr and **1**·bzCl present a 7 K wide hysteresis loop at medium high

temperature. However, only **1**·bzBr and **1**·bzCl show narrow hysteresis at high temperature (4 and 3 K wide, each). Finally, **1**·thiophene, undergoing a four unequally spaced step spin transition, shows notable 11 K wide plateau (ca. 175 K) and 36 K wide plateau (ca. 155 K) involving ≈ 32% and ≈ 48% Fe^{II} centers in the LS state, each. Wide hysteresis loops of 25, 30, 11 and 4 K take place at low, medium, medium-high and high temperatures, respectively. **1**·$bzNO_2$ and **1**·thiophene exhibit the LIESST effect with T_{LIESST} ≈ 43 K each.

- **1**·G ΔCp vs. T plots are reminiscent of $\delta(\chi_M T)/\delta T$ vs. T plots and the obtained Tc temperatures agree with those deduced from the magnetic data. In addition, the overall ΔH and ΔS values are consistent with values typically displayed by Hofmann-like clathrates of Fe^{II} featuring strong cooperative SCO behaviour. TGA on **1**·G clathrates show the presence of one aromatic guest molecule per Fe^{II} center, consistent with crystallographic studies (**1**·$bzNO_2$).

- Since all **1**·G clathrates are isostructural (featuring comparable aromatic guest molecules, loading and relative spatial orientation within the pores of the framework) its different SCO properties may be due to distinct π-π host-guest intermolecular interactions which affect the ligand field felt by the Fe^{II} centers and the SCO cooperativity in a particular manner. Generally, substituent effects in π-π interactions between aromatic rings are explained by the H-S electrostatic model as in the SCO-CPs {Fe(bpac)[$Pt(CN)_4$]}·G (G = bzCl, bzBr and bzI), the SCO-MOFs generally formulated {[$Fe(tvp)_2(NCS)_2$]·2G} (G = benzonitrile, benzaldehyde, nitrobenzene) both presented by Real et al. in 2013 and 2015, respectively, and the herein reported **1**·bzF, **1**·bzCl and **1**·bzBr. However, the $T_{1/2}$-trend exhibitted by **1**·$bzNO_2$, **1**·bzaldehyde and **1**·bznitrile cannot be explained by analogous reasoning. Recently, Parish et. al. theoretical studies have proved that, in contrast to the H-S model, the substituent effects in π-π interactions involving aromatic rings can be mainly explained in terms of direct, through-space interactions of the substituents over the unsubstituted aromatic ring, with π-resonance effects playing a minor role. Therefore, as substituents effects on π-π interactions remain unclear, so does their impact on the Fe^{II} SCO centers. Therefore, **1**·G represent a useful model where to study the nature of the spin transition in relation to the host-guest π-π interactions which, together with the corresponding theoretical studies, might be extremely helpful in the rational design of SCO materials with tailored properties.

APÉNDICE

ChemPubSoc Europe

DOI: 10.1002/chem.201601172

CHEMISTRY A European Journal Full Paper

Iron(II) Complexes

Electronic Structure Modulation in an Exceptionally Stable Non-Heme Nitrosyl Iron(II) Spin-Crossover Complex

Lucía Piñeiro-López,[a] Norma Ortega-Villar,[b] M. Carmen Muñoz,[c] Gábor Molnár,[d] Jordi Cirera,[e] Rafael Moreno-Esparza,[b] Víctor M. Ugalde-Saldívar,[b] Azzedine Bousseksou,[d] Eliseo Ruiz,[e] and José A. Real*[a]

Abstract: The highly stable nitrosyl iron(II) mononuclear complex $[Fe(bztpen)(NO)](PF_6)_2$ (bztpen = N-benzyl-*N*,*N*′,*N*′-tris(2-pyridylmethyl)ethylenediamine) displays an $S = 1/2 \leftrightarrow S = 3/2$ spin crossover (SCO) behavior ($T_{1/2} = 370$ K, $\Delta H = 12.48\ kJ\,mol^{-1}$, $\Delta S = 33\ J\,K^{-1}\,mol^{-1}$) stemming from strong magnetic coupling between the NO radical ($S = 1/2$) and thermally interconverted ($S = 0 \leftrightarrow S = 2$) ferrous spin states. The crystal structure of this robust complex has been investigated in the temperature range 120–420 K affording a detailed picture of how the electronic distribution of the t_{2g}–e_g orbitals modulates the structure of the {FeNO}^{7} bond, providing valuable magneto–structural and spectroscopic correlations and DFT analysis.

Introduction

Heme and non-heme iron-nitrosyl complexes have been intensively investigated during the last three decades as chemical models of active Fe–NO biologically relevant sites.[1] Ferrous heme-nitrosyl complexes are Fe^{II} $S = 0$ low-spin (LS) species with a doublet ground spin state ($S = 1/2$) formally originated from the NO ligand.[2] Ferric heme-nitrosyl complexes derive from the LS state of Fe^{III} ($S = 1/2$) and afford singlet ground spin state ($S = 0$) species.[2] In contrast, non-heme iron-nitrosyl complexes can exist either in the $S = 3/2$ or the $S = 1/2$ spin states depending on the ancillary ligands.[3] Interestingly, a small number of non-heme iron-nitrosyl complexes show $S = 3/2 \leftrightarrow S = 1/2$ spin-crossover (SCO) behavior. Six of them are pentacoordinate complexes formulated [FeL(NO)] (with L = salen,[4] salphen,[5] (L^1),[6] (L^{1a}),[6] (L^2)[7]), and $[Fe(TMC)(NO)](BF_4)_2$ (TMC = 1,4,8,11-tetramethyl-1,4,8,11-tetraazacyclotetradecane),[8] whereas the remaining are the hexacoordinate complexes $[FeL^3(NO)(CH_3OH)]$,[7] $[FeL^4(NO)(CH_3OH)]$,[7] and $[FeL^{pr}(NO)]$[9] (see Scheme 1).

In the Enemark and Feltham systematization of the M–NO bonding, non-heme iron-nitrosyl complexes are considered {FeNO}^{7} species, where seven is the total number of electrons in the Fe d and NO π* orbitals.[10] The radical character of the non-innocent NO ligand and the close energetic proximity to the Fe d orbitals determine the essence of the bonding in the {FeNO}^{7} moiety. Depending on the d–π* energy difference, different electronic structures have been envisaged. However, the substantial degree of covalence involved in the {FeNO} unit makes an unambiguous assignation of specific oxidation and ground spin states difficult.[11] For example, from an analysis of

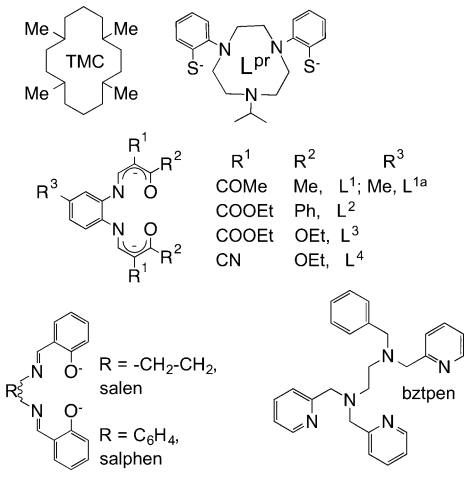

Scheme 1. Ligands concerned with the synthesis of iron-nitrosyl complexes exhibiting SCO properties.

[a] *L. Piñeiro-López, Prof. Dr. J. A. Real*
Instituto de Ciencia Molecular (ICMol), Universidad de Valencia
46980 Paterna, Valencia (Spain)
E-mail: jose.a.real@uv.es

[b] *Dr. N. Ortega-Villar, Prof. Dr. R. Moreno-Esparza, Prof. Dr. V. M. Ugalde-Saldívar*
Facultad de Química (UNAM), Edificio B., Av. Universidad 3000, Coyoacán, México D.F. 04510 (México)

[c] *Prof. Dr. M. C. Muñoz*
Departamento de Física Aplicada, Universitat Politècnica de València
46022, Valencia (Spain)

[d] *Dr. G. Molnár, Dr. A. Bousseksou*
LCC, CNRS & Université de Toulouse (UPS, INP)
205 route de Narbonne, 31077 Toulouse, (France)

[e] *Dr. J. Cirera, Prof. Dr. E. Ruiz*
Departament de Química Inorgànica i Orgànica, Secció de Química Inorgànica, Institut de Recerca de Química Teòrica i Computacional, Universitat de Barcelona, Diagonal 645, Barcelona, 08028 (Spain)

Supporting information for this article is available on the WWW under http://dx.doi.org/10.1002/chem.201601172.

the Fe K-edge X-ray absorption spectra of a series of $S=3/2$ non-heme iron-nitrosyl complexes, which included [Fe(salen)(NO)], Solomon et al. concluded that the $S=3/2$ $\{FeNO\}^7$ species are more precisely specified as a high-spin (HS) ($S=5/2$) ferric center antiferromagnetically coupled with the NO^- ($S=1$) ion.[12] The same conclusion was achieved by Lehnert et al. from vibrational correlations along with DFT calculations for the complexes [Fe(bmpa-Pr)(NO)(X)] (BMPA-Pr = *N*-propanoate-*N*,*N*-bis(2-pyridylmethyl)amine; $X=Cl^-$, ClO_4^-, I^-, or $CF_3SO_3^-$) and $[Fe(tpa)(NO)(CH_3CN)](ClO_4)_2$ (TPA = tris(2-pyridylmethyl)-amine).[13] This study also indicates that the NO^- ion acts mostly as a π-donor ligand in these complexes. Based on a combination of electron spin resonance and Mössbauer spectroscopy and DFT methods, Wieghardt et al. reached the same conclusion for the SCO complex $[FeL^{pr}(NO)]$ in the $S=3/2$ state.[9] Furthermore, these authors proposed for the $S=1/2$ spin state a LS ($S=0$) ferrous center coupled with $NO^\bullet$ ($S=1/2$). The latter conclusion has recently been supported by Salomon et al. from sulfur-K-edge X-ray absorption spectroscopy and DFT studies on two model complexes that contain sulfur ligands.[14] In this respect, non-heme $\{FeNO\}^7$ complexes with $S=1/2$ ground states have very similar electronic structures as the corresponding heme complexes.[2,15] Thus, for $\{FeNO\}^7$ SCO species the observed $S=3/2 \leftrightarrow S=1/2$ equilibrium could be more precisely described as a valence tautomerism process.[9] In contrast, based on DFT calculations of the Mössbauer parameters of the [Fe(salen)(NO)] SCO complex and other studies on the isopenicillin N synthase, Oldfield et al. have concluded that the investigated $S=3/2$ $\{FeNO\}^7$ species can be described as a HS ($S=2$) ferrous Fe^{II} antiferromagnetically coupled with NO ($S={}^1/_2$).[16] The same conclusion was drawn from a recent spectroscopic and computational study of a non-heme iron-nitrosyl center in a biosynthetic model of nitric oxide reductase.[17]

In previous studies, we investigated the suitability of the pentadentate *N*-benzyl-*N*,*N*′,*N*″-tris(2-pyridylmethyl)ethylenediamine (bztpen) ligand in the synthesis of new $\{[Fe^{II,III}(bztpen)]_xL\}(PF_6)_y$ SCO complexes with the sixth coordination site occupied by suitable ancillary monodentate L^- ligands such as dicyanamide (Fe^{II}, $x=2$, $y=3$)[18] or alkoxydes (Fe^{III}, $x=1$, $y=2$).[19] In addition, Schindler et al. have compared the stability of the $[Fe(bztpen)(NO)]^{2+}$ ion in solution with respect to that of the homologous Fe^{III} peroxo and hydroperoxo complexes, and the crystal structure of the triflate derivative $[Fe(bztpen)(NO)](CF_3SO_3)_2$ was succinctly described in this study.[20]

Following our research line and in principle motivated by the study of the interplay between the SCO phenomenon and strong magnetic coupling, here we report the synthesis and characterization of the complex $[Fe(bztpen)(NO)](PF_6)_2$ (**1**) in the solid state. Complex **1** is a new non-heme $\{FeNO\}^7$ species displaying a SCO equilibrium that extends beyond 400 K. Facilitated by the extraordinary robustness of the single crystals, a detailed single-crystal analysis carried out in the temperature range 120–420 K shows the adaptability of the NO molecule to the change of spin states in the Fe center. Furthermore, multi-temperature EPR, Mössbauer, IR, Raman, and UV-Vis spectroscopy as well as theoretical calculations have been carried out to clarify the nature of the observed $S=3/2 \leftrightarrow S=1/2$ equilibrium.

Results and Discussion

Synthesis

When NO(g) is bubbled under anaerobic conditions into a saturated pale yellow methanolic solution of $[Fe^{II}(bztpen)(MeOH)]^{2+}$ ($\approx 3\times10^{-3}$ M) a deep purple solution is instantaneously formed followed by rapid and quantitative precipitation of the microcrystalline brown–purple solid **1**. Starting from diluted solutions ($\geq 9\times10^{-4}$ M) of $[Fe^{II}(bztpen)(MeOH)]^{2+}$ and following the same procedure single crystals of compound **1** were obtained in a few days.

Magnetic properties

The thermal dependence of the product $\chi_M T$ in the temperature interval 2–400 K for compound **1** is shown in Figure 1 (χ_M is the magnetic susceptibility and T is the temperature). At 400 K the product $\chi_M T$ is 1.35 $cm^3 K mol^{-1}$ and continuously decreases with cooling until 0.38 $cm^3 K mol^{-1}$ at approximately 150 K. Below this temperature the value of $\chi_M T$ remains practically constant down to 15 K. In the temperature range 15–2 K a quite small decrease denotes the onset of very weak intermolecular antiferromagnetic interactions. The value $\chi_M T=$ 0.38 $cm^3 K mol^{-1}$ is consistent with an $S=1/2$ ground state with $g=2.01$. The increase of the product $\chi_M T$ above 150 K is consistent with a gradual SCO. Assuming that the SCO takes place between the LS ($S=0$) and HS ($S=2$) states of a Fe^{II} strongly antiferromagnetically coupled to the $S=1/2$ state of NO, the SCO can be considered to occur in an effective way between the resulting $S=1/2$ and 3/2 states. In this framework approximately 54.3% of the molecules are in the $S=3/2$ state at 400 K. According to previous work,[9,14] an equivalent scenario could involve the occurrence of valence tautomerism in the

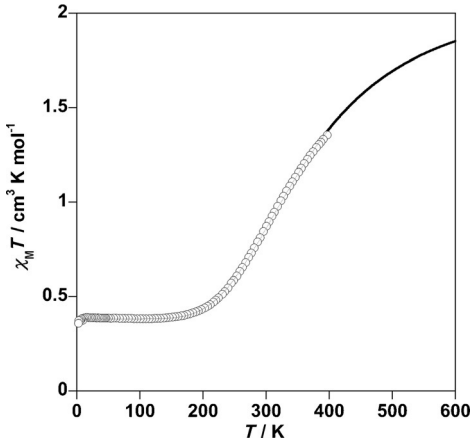

Figure 1. Magnetic behavior of complex **1** in the temperature range 2–400 K. The black line corresponds to the best fit of the experimental data (see text).

Fe–NO moiety. This would afford the strong antiferromagnetically coupled $S=5/2$ (Fe^{III}) and $S=1$ (NO^-) spin states and the uncoupled $S=0$ (Fe^{II}) and $S=1/2$ (NO) spin states.

In order to evaluate the thermodynamic parameters associated with the spin change we have considered that the term $\chi_M T$ can be expressed as given in Equation (1):

$$\chi_M T^{obs} = (\chi_M T)_{NO}(1-f)+(\chi_M T)_{Fe-NO} f \quad (1)$$

and

$$f = \frac{1}{\left\{1+\exp\left[\left(\frac{\Delta H}{R}\right)\left(\frac{1}{T}-\frac{1}{T_{1/2}}\right)\right]\right\}} \quad (2)$$

where $(\chi_M T)_{NO}$ is the $\chi_M T$ value at low temperatures due to the presence of the radical $NO^{\bullet}$ ($S=1/2$) and Fe^{II} ($S=0$), $(\chi_M T)_{Fe-NO}$ is the expression of a dinuclear species derived from the Hamiltonian $\mathbf{H}=-JS_aS_b$ with $S_a=1/2$ or 1 and $S_b=2$ or 5/2 species, respectively,[21a] f is the molar fraction of the HS species expressed by the theory of regular solutions in the form given by Slichter and Drickamer.[21b] In Equation (2), ΔH is the enthalpy variation, R is the universal constant of gases, and $T_{1/2}$ is the temperature at which HS and LS species are present at 50% ($\Delta G=0$). Given the expected large magnitude of the antiferromagnetic coupling constant (J), it is safe to consider that only the $S=3/2$ state plays an effective role in $(\chi_M T)_{Fe-NO}$. A least-squares fit procedure, which minimizes the function $R_{min}=\Sigma(\chi_M T^{obs}-\chi_M T^{calcd})^2/\Sigma(\chi_M T^{obs})^2$, leads as adjustable parameters $g_{3/2}=2.15$, $\Delta H=12.48\ kJ\,mol^{-1}$, $T_{1/2}=377.6$ K, and $R_{min}=7\cdot10^{-5}$. The total entropy variation is given by $\Delta S=\Delta H/T_{1/2}=33\ J\,K^{-1}\,mol^{-1}$.

The excellent agreement between the calculated and experimental data supports the assumption of synchronous reversible spin-state conversion and strong antiferromagnetic coupling between Fe^{II} and $NO^{\bullet}$. This strong antiferromagnetic coupling is in line with the magnitude of the J parameter estimated from our DFT calculations for complex **1** (see below) and those reported by Wieghardt and co-workers for the complex [Tp*Co(NO)] (Tp* = hydro-tris(3,5-Me_2-pyrazolyl)borate).[22] The ΔS value is found clearly smaller than typically observed for Fe^{II} SCO complexes[23] and in the lower limit observed for Fe^{III} SCO complexes[24] but consistent with a $S=1/2 \leftrightarrow S=3/2$ transformation.[25]

It is worth mentioning the similarities between the magnetic behavior of complex **1** and that reported by Krügger and co-workers for [Fe(L-N_4Me_2)(bian$^-$)](ClO_4), where L-N_4Me_2 and bian$^-$ are *N*,*N*′-dimethyl-2,11-diaza[3.3]-(2,6)pyridinophane and the radical anion of *N*,*N*′-diphenylacenaphtene-1,2-diimine, respectively.[26] In the temperature interval 22–240 K, this compound displays a $\chi_M T$ value of 0.37 $cm^3\,K\,mol^{-1}$, which is consistent with an $S=1/2$ ground state. Then upon heating the value of $\chi_M T$ smoothly increases reaching a value of 0.75 $cm^3\,K\,mol^{-1}$ at 380 K indicating partial population of the $S=3/2$ state. Based on the magnetic properties as well as EPR and Mössbauer spectra Krügger et al. concluded that the observed behavior corresponds to a combined effect of strong antiferromagnetic coupling between the radical ligand bian$^-$ and the Fe^{II} ion switching between the $S=0$ and $S=2$ states. Much weaker magnetic coupling was reported for a series of five-coordinate halido and pseudohalido-bis(*o*-iminobenzosemiquinonato)iron(III) complexes that undergo SCO between the effective spin states $S=3/2$ and $S=1/2$.[27]

Spectroscopic characterization of compound 1

EPR spectra

The X-band EPR solid-state spectra of compound **1** collected at 4 and 300 K are shown in Figure 2a. At 4 K the spectrum is characterized by a sharp signal centered at $g=2.02$, which

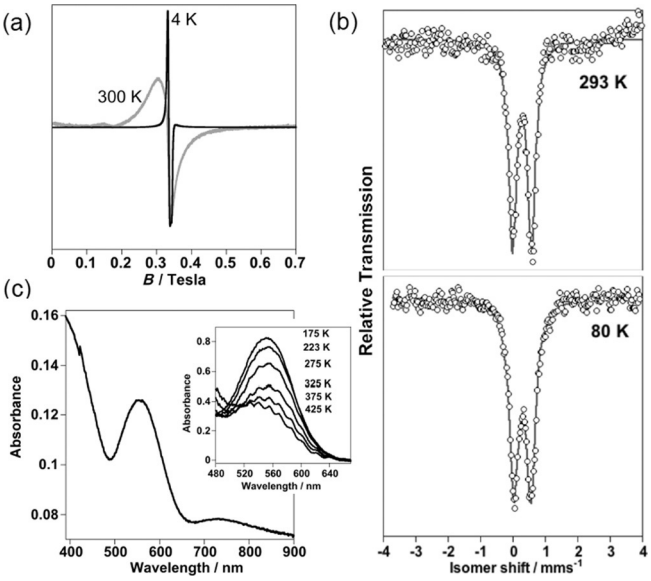

Figure 2. Spectroscopic measurements for compound **1**. a) EPR spectra at 4 (black line) and 300 K (gray line). b) Mössbauer spectra at 293 and 80 K (lines are fitted spectra). c) Diffuse reflectance spectrum at 300 K (the inset shows the thermal variation of the $\lambda=555$ nm peak in the temperature interval 175–425 K).

becomes wider without moving significantly ($g=2.05$) at 300 K where, according to the magnetic properties, approximately 30% of the molecules are in the $S=3/2$ state. This EPR spectrum is reminiscent of that reported for the classical SCO nitrosyl compound [Fe(salen)(NO)], for which no signal at $g\approx4$, which is characteristic of the $S=3/2$ state, is observed, which was considered consistent with an electron essentially residing in the NO molecule.[28] Similarly, no observation of the $S=3/2$ signal was reported for the SCO complex [FeL^{Pr}(NO)].[9] In contrast the EPR spectrum of the non-heme HS iron(II)-nitrosyl model complex [Fe(bmpa-Pr)(NO)(Cl)][13] is characterized by a dominant signal at $g\approx4$ attributable to the $S=3/2$ state.

Mössbauer spectra

Zero-field ^{57}Fe Mössbauer spectra at 80 and 293 K for compound **1** are shown in Figure 2b. The poor signal-to-noise ratio of the 293 K spectrum discouraged us from recording Mössbauer spectra at higher temperatures. The fitted spectral pa-

rameters (assuming Lorenzian line shapes) are given in Table S1 in the Supporting Information. The 80 K spectrum can be assigned to a low-spin ferrous or ferric species (not distinguishable by Mössbauer spectroscopy) with an isomer shift $\delta = 0.306(5)\ mm\,s^{-1}$ and a quadrupole splitting $\Delta E_Q = 0.523(9)\ mm\,s^{-1}$. Detection of only one doublet at 293 K, $\delta = 0.295(4)\ mm\,s^{-1}$ and $\Delta E_Q = 0.590(8)\ mm\,s^{-1}$, is consistent with a fast spin-state interconversion rate compared to the timescale of Mössbauer spectroscopy leading to an averaged spectrum. This is also supported by the unusual and almost insignificant thermal variation of the spectrum parameters ΔE_Q and δ. A similar situation was reported for the nitrosyl SCO complexes $[Fe(tmc)NO](BF_4)_2$,[8] $[FeL^1(NO)]$,[29] and $[FeL^{1a}(NO)]$[29] (see Scheme 1) and for the aforementioned SCO complex $[Fe(L\text{-}N_4Me_2)(bian^-)](ClO_4)$.[26] In contrast, the characteristic signals of both spin states were observed for [Fe(salen)(NO)],[28] [Fe(salphen)(NO)],[5] and $[Fe(L^{pr})(NO)]$.[9] All these Fe^{II} SCO nitrosyl complexes, including complex **1**, display δ values of the same order of magnitude, found in the interval 0.3–0.5 $mm\,s^{-1}$.

Electronic spectra

Figure 2c displays the diffuse reflectance spectrum of compound **1** at 293 K, where the relative population of the $S = 1/2$ and $S = 3/2$ states is estimated to be LS/HS ≈ 73:27. This spectrum is characterized by three absorption bands centered at approximately $\lambda = 400$, 555, and 730 nm. The two first maxima are reminiscent of Fe^{II} complexes in the LS state and could be tentatively ascribed to the $^1A \rightarrow {}^1T_2$ and $^1A \rightarrow {}^1T_1$ transitions, respectively.[30] However, a number of metal–ligand (pyridine and NO) charge-transfer (CT) bands may occur in the same energy window making difficult a precise identification of the d–d bands. In this respect, a similar spectrum has been reported for the $S = 1/2$ $\{FeNO\}^7$ complex *trans*-$[(cyclam)Fe^{II}(NO)Cl](ClO_4)$ in acetonitrile with bands at $\lambda = 398$ ($\varepsilon = 300$) and 560 nm ($\varepsilon = 145\ M^{-1}\,cm^{-1}$). These bands were reasonably ascribed to the Fe^{II} in the LS state, because they disappear after one-electron oxidation suggesting a metal-centered process.[31] Interestingly, compound **1** displays thermochromism in the temperature interval 175–425 K. Upon heating, the brown-violet color of the crystal becomes pale (see Figure S1 in the Supporting Information). This color change is primarily related to the bleaching of the $\lambda = 555$ nm absorption, which starts above approximately 200 K to be completed to around 80% at 425 K (see the inset of Figure 2c). The remarkably good correlation between the temperature dependence of its intensity and the magnetic behavior of complex **1**, which is shown in Figure 3, supports the idea that the $^1A \rightarrow {}^1T_1$ transition is a relevant component of the $\lambda = 555$ nm absorption band. In this respect, it is worth mentioning that this thermochromism is reminiscent of the thermochromism associated with the LS↔HS state change in Fe^{II} SCO complexes observed in the $\lambda = 500$–600 nm window in solution and the solid state.

A number of relevant studies, by Brunold et al.[32] and Solomon and co-workers,[12,33] which combine UV/Vis absorption spectroscopy, magnetic circular dichroism measurements, and DFT studies have been devoted to analyze the electronic spectra of $\{FeNO\}^7$ species in the $S = 3/2$ state. They display characteristic broad CT bands centered at approximately $\lambda = 660$ and 430 nm. These bands have been formally attributed to $NO^- \rightarrow Fe^{3+}$ CT processes, in complexes with much weaker ligand-field donor groups than complex **1**. Then, the $\lambda = 730$ nm maximum in compound **1** should be tentatively assigned to such CT transitions because, at 293 K the LS state co-exists with 27% of the Fe centers in the HS state.

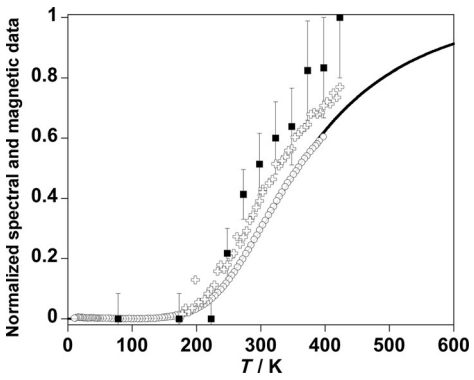

Figure 3. Correlation of the magnetic (experimental = open circles and calculated = lines) and spectroscopic (UV/VIS and Raman) data. Full squares indicate the Raman peak intensity ratio $I_{1789}/(I_{1789}+I_{1684})$ of the ν_{NO} stretching mode. Open crosses show the (normalized and inversed) absorbance variation at $\lambda = 555$ nm.

Vibrational spectra

Variable-temperature, single-crystal Raman spectra were acquired by using both $\lambda = 532$ and 633 nm laser excitations. Representative spectra are shown in Figure 4a. The NO stretching mode ν_{NO} undergoes a remarkable shift from $\tilde{\nu} = 1789$ to 1684 cm^{-1} (for both excitation wavelengths) when going from 400 to 100 K. These characteristic vibrational modes can be clearly associated with the $S = 3/2$ and $S = 1/2$ states, respectively, because they co-exist (in different proportions) in the temperature interval where the conversion between these two magnetic states takes place. Indeed, as shown in Figure 3, the relative intensity of these modes follows reasonably well the magnetic changes (a better correlation would be rather fortui-

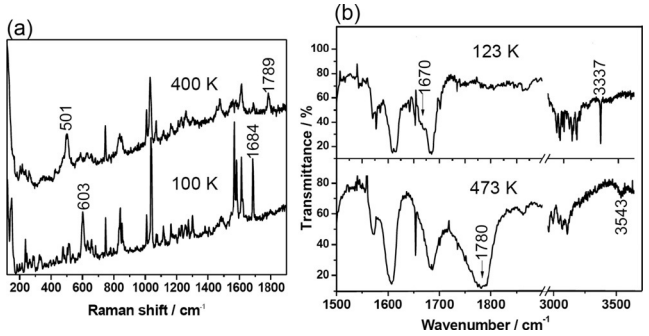

Figure 4. Representative variable-temperature a) Raman scattering ($\lambda = 532$ nm excitation, $-z(yy)z$ configuration) and b) non-polarized infrared absorption spectra of a single crystal of compound **1**.

tous as the intensity of the Raman modes is not directly proportional to the population of the two electronic states).

The temperature-dependent, single-crystal IR absorption spectra (Figure 4b) confirm well the Raman data. At 473 K, a broad absorption band is observed at around $\tilde{\nu}=1780\ cm^{-1}$ as well as its overtone around $\tilde{\nu}=3543\ cm^{-1}$, which can be attributed to the ν_{NO} mode of the complex in the $S=3/2$ state. At 123 K, these bands disappear and an ill-resolved shoulder, assigned to the ν_{NO} mode in the $S=1/2$ state, appears at around $\tilde{\nu}=1670\ cm^{-1}$. This assignment is further substantiated by the observation of the overtone of this mode at $\tilde{\nu}=3337\ cm^{-1}$. Similar to the Raman spectra, the NO stretching peaks (fundamental as well as overtone) associated with the $S=3/2$ state are much broader than their $S=1/2$ state counterparts, which may indicate a disorder in the former. These results agree reasonably well with the corresponding ν_{NO} IR modes reported for [Fe(salen)(NO)], that is, $\tilde{\nu}=1712$ ($S=3/2$) and $1630\ cm^{-1}$ ($S=1/2$).[4] Nevertheless, the shift of the ν_{NO} mode is approximately 20% larger for complex **1** most likely reflecting the distinct chemical nature of the ligands salen and bztpen and the coordination number of both complexes.[2,13]

In the case of the IR absorption spectra, the temperature dependence of the peak intensities is considerably altered by heating due to the IR probe beam. For this reason, the quantitative correlation of IR absorbance changes with the magnetic data was not possible. It is important to note, however, that the spin conversion at low temperatures is fully complete because the characteristic ν_{NO} IR absorption bands (and also Raman peaks) of the high-temperature form disappear completely below approximately 200 K. Due to the weak spectral intensities above 400 K, it is more difficult to conclude about the completeness of the transition at high temperatures, but we can note that no residual fraction is observed in the IR spectra at 473 K, indicating a nearly complete transition (Figure 4b).

Besides the ν_{NO} stretching mode, several other spectral changes are observed in the Raman spectra. At high temperature, where the $S=3/2$ state is significantly populated, a medium band dominates over $\tilde{\nu}=503\ cm^{-1}$ the Raman spectrum of compound **1**. Interestingly, the intensity of this peak decreases upon cooling down to 100 K at expense of a new peak centered at $\tilde{\nu}=603\ cm^{-1}$. According to the important previous work, which include ^{15}NO isotope labeling, it is reasonable to tentatively assign the $\tilde{\nu}=603$ and $501\ cm^{-1}$ frequencies to coupled Fe–NO stretching and Fe–NO bending modes (see below) in the $S=1/2$ and $S=3/2$ states, respectively.[3,34–37]

Structure of compound 1

The crystal structure of the title compound was investigated at 120, 200, 250, 275, 300, 340, 380, 400, and 420 K on the same single crystal. The crystal belongs to the orthorhombic *Pbca* space group in the temperature range investigated. Selected crystallographic data are gathered in Table 1. The molecular structure is displayed in Figure 5 (left) together with the atom-numbering scheme and representative bond lengths and angles are collected in Table 2. The iron atom is in a distorted octahedral [FeN_6] environment defined by five nitrogen atoms belonging to the pentadentate bztpen ligand and the nitrogen atom of the nitroxyl group. Two PF_6^- ions balance the charge of the $[Fe(bztpen)(NO)]^{2+}$ ion. The bztpen ligand coordinates the Fe, defining a distorted square pyramid, in which the N2 atom lies on the axial apex. The opposite apex is occupied by the N6 atom of the NO molecule. The N atom is in the center of a tripod whose arms are defined by two picolylamine-type moieties [N2-C7-C8-N3 and N2-C6-C5-N1] and an ethylenediamine-type moiety [N2-C13-C14-N4]. These arms are anchored to the Fe through the atoms N3, N1, and N4, respectively. An additional picolylamine-type arm, [N4-C15-C16-N5], originates

Table 1. Crystal data of compound **1**.[a]

empirical formula	$C_{27}H_{29}N_6OP_2F_{12}Fe$								
M_r [g mol^{-1}]	799.35								
crystal system	orthorhombic								
space group	*Pbca*								
Z	8								
crystal size [mm]	0.06×0.10×0.10								
F(000)	3240								
T [K]	120	200	250	275	300	340	380	400	420
a [Å]	17.1485(3)	17.2552(2)	17.3540(5)	17.3638(2)	17.4065(4)	17.4527(2)	17.4819(5)	17.5159(3)	17.5396(4)
b [Å]	18.8049(4)	18.8664(2)	18.9388(5)	18.9585(2)	18.9710(5)	19.0622(3)	19.1080(4)	19.1566(4)	19.2019(5)
c [Å]	19.2745(4)	19.3440(2)	19.4544(5)	19.4477(2)	19.5023(5)	19.5749(2)	19.6398(5)	19.6896(3)	19.7292(4)
V [Å^3]	6215.6(2)	6297.31(12)	6393.9(3)	6402.05(12)	6440.0(3)	6512.33(14)	6560.6(3)	6606.8(2)	6644.7(3)
D_{calcd} [g cm^{-3}]	1.708	1.686	1.661	1.659	1.649	1.631	1.619	1.607	1.598
$\mu(Mo_{K\alpha})$ [mm^{-1}]	0.696	0.687	0.676	0.676	0.672	0.664	0.659	0.655	0.651
number of total reflns	8462	8475	9262	9293	8579	8941	8940	9057	9017
number of reflns [$I>2\sigma(I)$]	4874	6568	6468	6309	5865	5669	5424	4881	4276
R_1 [$I>2\sigma(I)$]	0.0584	0.0453	0.0606	0.0651	0.0677	0.0740	0.0749	0.0930	0.1031
R_1 [all data]	0.1255	0.0638	0.0902	0.0968	0.0983	0.1140	0.1182	0.1495	0.1363
S	0.862	0.812	0.904	0.831	0.860	1.036	1.028	1.133	1.223

[a] $R_1=\Sigma||F_o|-|F_c||/\Sigma|F_o|$; $wR=[\Sigma[w(F_o^2-F_c^2)^2]/\Sigma[w(F_o^2)^2]]^{1/2}$; $w=1/[\sigma^2(F_o^2)+(mP)^2+nP]$ where $P=(F_o^2+2F_c^2)/3$; $m=0.1058$ (120 K), 0.1088 (200 K), 0.1355 (250 K), 0.1635 (275 K), 0.1809 (300 K), 0.1282 (340 K), 0.1316 (380 K), 0.2000 (400 K), 0.2000 (420 K); $n=16.5463$ (120 K), 12.8834 (200 K), 9.4233 (250 K), 13.1359 (275 K), 11.1178 (300 K), 7.2081 (340 K), 4.877 (380 K), 0.0000 (400 K), 0.0000 (420 K).

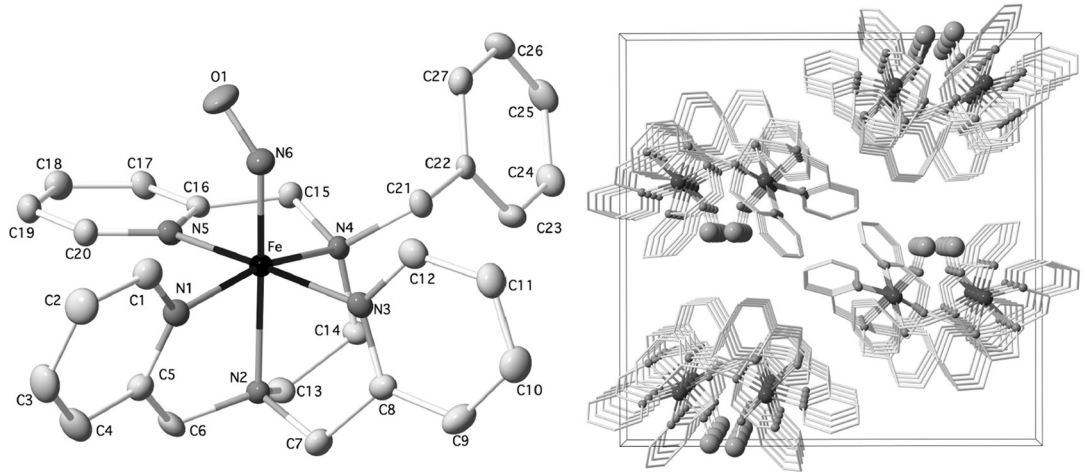

Figure 5. Molecular structure (left) and perspective view of the crystal packing in the [100] direction (PF_6^- ions are not shown) (right) of compound **1**.

Table 2. Selected experimental and computed bond lengths and angles for compound **1**.

	Experimental										Computed	
	120 K $S=1/2$	200 K	250 K	275 K	300 K	340 K	380 K	400 K	420 K	extrapolate $S=3/2$*	{FeNO}^{7} ($S=1/2$)	{FeNO}^{7} ($S=3/2$)
Fe–N1	1.994(3)	1.999(2)	2.012(3)	2.023(3)	2.034(3)	2.056(3)	2.072(3)	2.085(4)	2.098(7)	2.085	2.004	2.175
Fe–N2	2.100(3)	2.105(2)	2.115(2)	2.123(2)	2.138(3)	2.154(3)	2.166(3)	2.171(4)	2.190(5)	2.231	2.082	2.255
Fe–N3	1.987(3)	1.999(2)	2.014(3)	2.025(3)	2.033(3)	2.063(3)	2.078(3)	2.080(4)	2.085(7)	2.158	2.005	2.161
Fe–N4	2.084(3)	2.084(2)	2.102(2)	2.113(2)	2.128(3)	2.163(3)	2.179(3)	2.193(3)	2.203(5)	2.285	2.071	2.260
Fe–N5	1.992(3)	1.992(2)	2.007(2)	2.021(3)	2.032(3)	2.065(3)	2.087(3)	2.094(4)	2.099(6)	2.180	2.006	2.193
Fe–N6	1.733(3)	1.738(2)	1.745(3)	1.740(3)	1.745(3)	1.751(4)	1.753(3)	1.745(5)	1.751(7)	1.755	1.759	1.782
N6-O	1.170(4)	1.157(3)	1.143(4)	1.133(4)	1.126(5)	1.111(5)	1.102(5)	1.106(7)	1.099(10)	1.052	1.170	1.156
Fe–N_{bztpen}	2.031	2.036	2.050	2.061	2.073	2.100	2.116	2.125	2.135	2.204	2.034	2.209
Fe–N^{av}	1.982	1.986	1.999	2.008	2.018	2.042	2.056	2.061	2.071	2.127	1.988	2.138
Fe-N-O	144.0(3)	144.5(2)	145.8(3)	147.4(3)	148.8(4)	151.0(4)	154.7(9)	156.5(6)	157.9(10)	167	143.4	165.6
Σ	60.88	60.87	62.20	65.16	67.34	71.31	74.55	77.24	76.80	90.95	59.23	92.48
Φ	4.4	4.4	4.4	4.6	4.8	5.1	5.3	5.5	5.5	6.42	3.63	5.60

at the N(4) atom and coordinates the remaining equatorial position of the Fe center through the N5 atom.

The average Fe–N bond length of the Fe–bztpen moiety, $<Fe–N_{bztpen}>N_{av}$, gradually increases with increasing temperature from 2.031 Å (120 K) until 2.135 Å (420 K) involving a total variation of practically 0.1 Å. Consistently, the sum of deviations from the ideal octahedron of the twelve "*cis*" N-Fe-N angles ($\Sigma=\sum_{i=1}^{12}|\theta_i-90|$) shows that the coordination center is strongly distorted at 120 K with $\Sigma=60.9^\circ$ and this distortion increases as the temperature increases until reaching a value of 76.8° at 420 K. In contrast, the trigonal distortion parameter, defined as $\Phi=\sum_{i=1}^{24}(|\phi_i-60|)/24$ (there are twenty-four Φ_i angles generated by superposition of four pairs of opposite triangular faces of an octahedron; $\Phi_i=60^\circ$ for a regular octahedron), is small at 120 K ($\Phi=4.4^\circ$) and increases up to 5.5° at 420 K. The Fe–NO bond length (Fe–N6) displays a very small increase from 1.733(3) to 1.751(7) Å making slightly less pronounced the overall change of the average [FeN_6] bond length, $\Delta R(<Fe–N6>)=0.089$ Å (Table 2). The thermal dependence of $<Fe–N6>$ shows an excellent correlation with the thermal dependence of the product $\chi_M T$ (Figure 6a). As mentioned above approximately 54.4% of the cations populate the $S=3/2$ state at 400 K. Extrapolation of this population to 100% gives a total variation $\Delta R(Fe–N_{av})\approx0.145$ Å, which is about 27% shorter than usually observed for an Fe^{II} center undergoing complete SCO behavior (0.2 Å). In part, this is mitigated by the small variation observed for the Fe–N6O bond length, which contrasts with the approximate 100 cm^{-1} shift of the $\nu_{Fe–NO}$ mode upon spin-state change. A fact that suggests a complete change in the Fe–NO bonding between the $S=1/2$ and $S=3/2$ spin states.

The strong covalence of the Fe–NO bond is reflected specially on the thermal dependence of the N6–O bond length and the Fe-N-O tilt angle (Table 2). Upon heating from 120 to 420 K, the N–O bond length gradually decreases from 1.170(4) to 1.099(10) Å. This latter value is slightly shorter than usually observed for non-heme $S=3/2$ {FeNO}^{7} species (≈1.114 Å). Short values of the N–O bond length have been observed associated with the occurrence of reversible thermally driven rotational disorder and phase transition in the [Co(tetraphenylporphinato)(NO)] complex.[38] However, we have not detected this type of disorder in the title compound. The significant decrease of 0.071 Å, resulting from the gradual population of

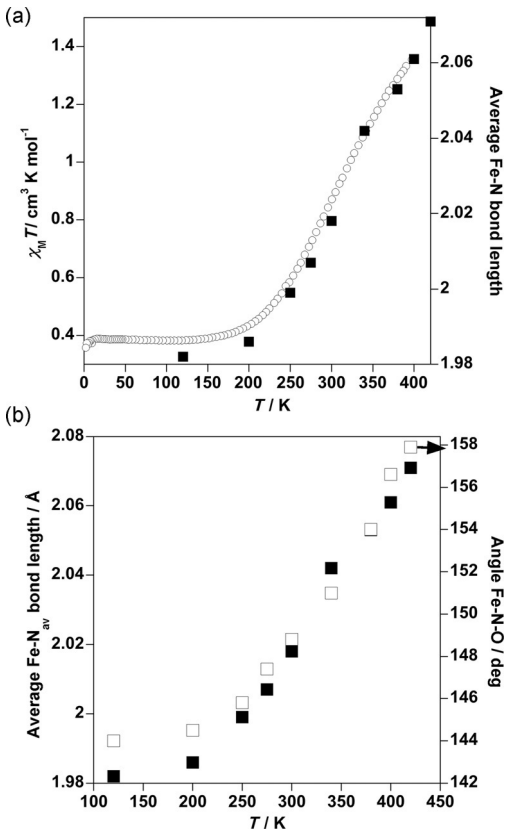

Figure 6. Magneto–structural correlation. a) Thermal variation of the product $\chi_M T$ (open circles) and the average Fe–N bond length (full squares). b) Thermal variation of the average Fe–N bond length (full squares) and the Fe–NO bond angle (white squares).

the $S=3/2$ state, can be rationalized from the molecular orbital (MO) diagrams calculated for both spin states (see below). In the $S=1/2$ state, the small Fe-N-O bond angle favors significant contribution of the nitrosyl N atom thus imparting an antibonding character to the five occupied MOs, namely, three α orbitals (i.e., d_{xz}, d_{yz}, and π(NO)) and two β orbitals (i.e., d_{xz}, d_{yz}). In contrast, in the $S=3/2$ state, only two occupied β-MO with nitrosyl contribution have N–O antibonding character (i.e., d_{xz} and π(NO)).

The Fe-N-O1 angle increases from 144.0(3) to 157.9(10)° when moving from 120 to 420 K. This thermal dependence clearly follows the thermal dependence of the Fe–N^{av} bond length and the product $\chi_M T$ (Figure 6b). Hence, the Fe-N-O1 angle also changes with the population of the $S=3/2$ and $S=1/2$ molecular states, each one characterized by a different Fe-N-O bond angle. Extrapolation of this variation to 100% of the $S=3/2$ state population predicts an increase of the Fe-N-O angle up to 167°. Interestingly, this extrapolated angle is similar to that found by Speelman and Lehnert for the pentacoordinate $S=3/2$ complex [Fe(tmg$_3$tren)(NO)](OTf)$_2$ (TMG$_3$tren = 1,1,1-tris{2-[*N*2-(1,1,3,3-tetramethylguanidinio)]ethyl}amine).[39]

The only known crystal structure of a {FeNO}^{7} SCO system in the pure $S=1/2$ and $S=3/2$ states were reported for [Fe(salen)(NO)].[40] For this compound, the average Fe-N-O angle changes from 127° in the $S=1/2$ state to 147° in the $S=3/2$ state. Although the magnitude of these angles is markedly smaller than the one found for compound **1**, the change of 20° is very close to the 23° variation estimated upon complete SCO in complex **1**. Furthermore, the average variation of the bond lengths in the FeN_2O_2 core, that is, 0.040 Å, is approximately 50% smaller than observed for compound **1** at 420 K or about 73% smaller than expected for a complete conversion in compound **1**. As mentioned above, this large difference could be accounted for the distinct chemical nature of the ligands and coordination number and geometry of both complexes.

A perspective of the crystal packing in the [100] direction is displayed in Figure 5 (right). This perspective shows an apparent organization of the cationic species by pairs that indeed correspond to the two first members of infinite supramolecular zigzag "chains" running along the [100] direction with shortest Fe···Fe distances ranging in the interval 9.4237(8)–9.5697(10) Å in the temperature range 120-400 K. There are C···C intermolecular contacts between in the infinite supramolecular chains, namely C23···C11 = 3.652(6), C26···C2 = 3.600(6), C24···C10 = 3.645(6), C25···C1 = 3.641(6), and C24···C11 = 3.588(6) Å at 120 K (see Figure S2 in the Supporting Information). Furthermore, in the low-temperature (LT) crystal packing the cationic molecules interact directly with each other through weak C···C intermolecular contacts defining a three-dimensional network. Most of these contacts are in the interval 3.6–3.7 Å. These interactions are reinforced by a number of C···F cation–anion contacts. Table S2 in the Supporting Information gathers the intermolecular distances smaller than the sum of the van der Waals radii C···C and C···F.

Electronic structure modeling

The [Fe(bztpen)(NO)]$^{2+}$ molecule has been fully optimized (see the section Computational Details) in the different possible spin topologies, this is, Fe^{II}–NO$^{\bullet}$ and Fe^{III}–NO^{-} in both ferromagnetic and antiferromagnetic schemes between the paramagnetic centers, and also allowing the iron centers to be in the HS or LS state. A complete list of atomic Cartesian coordinates for the optimized structures, as well as its energies can be found in Table S3 in the Supporting Information. When optimizing the systems in the Fe^{III}–NO^{-} motif, an electron transfer from the NO^{-} ligand to the Fe^{III} center is always observed, thus, reducing the metal to Fe^{II} and generating an NO radical. This is in line with the conclusion raised by Solomon and coworkers[14] and Lehnert et al.,[2] which states that six coordinate strong ligand field {FeNO}^{7} complexes and especially those with a strong axial donor atom in *trans* position to the NO molecule, as is the case of compound **1**, destabilizes the Fe^{III}–NO^{-} configuration in favor of the Fe^{II}–NO$^{\bullet}$ configuration. The optimized bond lengths and angles for the [Fe(bztpen)(NO)]$^{2+}$ molecule in the $S=1/2$ and $S=3/2$ states are, in general, in good agreement with the corresponding experimental data at 120 K (LS state) and extrapolated to 100% populated $S=3/2$ state (see Table 2). The most relevant discrepancy corresponds to the extrapolated N6–O bond length, that is, 1.053 Å, whereas the calculated one is 1.156 Å. This latter value is even

larger than the one obtained experimentally at 420 K, that is, 1.099(10) Å, where approximately 60% of the HS state are populated. Despite discrepancies in the magnitude of the variation of this bond length, its tendency to shorten with the increase of the population of the HS state is clearly reproduced.

The corresponding vibrational analysis was also done to ensure the minimum nature of the optimized structures. It is worth mentioning at this point that the calculated $\tilde{\nu}_{NO}(S=1/2)=1774.2\ cm^{-1}$ and $\tilde{\nu}_{NO}(S=3/2)=1837.4\ cm^{-1}$ frequencies are respectively approximately 100 and 56 cm^{-1} larger than the corresponding experimental values but are within the normal limits found for DFT calculations (about 5%). In contrast, the calculated $\tilde{\nu}_{Fe-NO}(S=3/2)=501\ cm^{-1}$ frequency is about 5% smaller than the experimental one. The most important difference corresponds to the calculated $\tilde{\nu}_{Fe-NO}(S=1/2)=494.2\ cm^{-1}$, which is approximately 18% smaller than the experimental value. This finding suggests again that the experimentally observed mode has probably an important δ_{Fe-NO} character.

A theoretical modeling of the spin-crossover curve and the transition temperature based on the thermochemical contributions has been performed, which is in fair agreement with the experimental data (see the Supporting Information).

Significant differences in the Fe–NO bonding interactions can be observed as a function of the metal spin-state when analyzing the electronic structure of the molecule in terms of the relevant molecular orbitals. In the LS state ($S=1/2$), the α and β double-occupied orbitals include the Fe–NO bonding d_{xz} and d_{yz} pair of orbitals strongly mixed with the π(NO) orbitals, and the non-bonding d_{xy} orbital. The main contributions to the antibonding SOMO comes from a mixture of the d_{xz} and d_{z^2} metal orbitals (with larger d_{z^2} participation) and one π(NO) orbital. The $d_{x^2-y^2}$ and d_{z^2} orbitals (both α and β) are strongly antibonding with the pentadentate ligand and the NO group, but remain unoccupied. Thus, despite the non-innocent nature of the ligand, the electronic structure in that spin state can be represented as a LS ($S=0$) Fe^{II} state coordinated to an NO radical. With the transition to the HS state ($S=3/2$), the α-$d_{x^2-y^2}$ and d_{z^2} metal-centered orbitals remain strongly antibonding, but are now single-occupied. Simultaneously, the Fe–NO bonding interactions are strongly reduced, and the α-occupied orbitals with important d_{xz} and d_{yz} contributions turn into formally non-bonding orbitals with the NO ligand. This situation leads to an enlargement of the Fe–NO bond length upon spin crossover of around 0.02 Å. The two β-SOMOs can now be described as a large mixture between the d_{xz} and d_{yz} orbitals with the two π(NO)-centered orbitals (Figure 7). In this case, the non-innocent behavior of the NO ligand makes a single assignment of the electronic structure difficult. These two orbitals contain around 40% contribution from the metal and 60% contribution from the NO ligand. Thus, we can distinguish between two limit situations: whether the two β-SOMOs are ascribed to the metal [$Fe^{I}(S=3/2)$–$NO^{+}(S=0)$] or to the NO ligand [$Fe^{III}(S=5/2)$–$NO^{-}(S=1)$]. Taking into account the mentioned orbital percentage, and considering the presence of two equivalent β-SOMOs, the β occupation of the metal is slightly smaller than one. Hence, we can describe the electronic structure as an intermediate situation between [$Fe^{II}(S=0)$-$NO(S=1/2)$] and [$Fe^{III}(S=5/2)$–$NO^{-}(S=1)$]. A similar proposal was done by McQuilken et al. for a non-heme Fe–NO complex.[41]

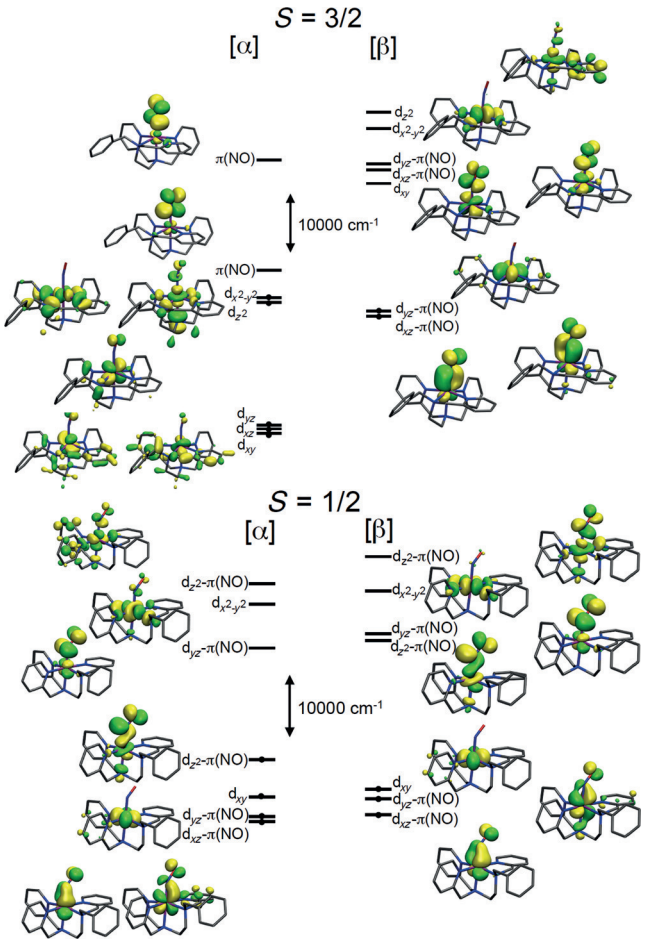

Figure 7. MO diagrams of complex **1** in the low-spin ($S=1/2$) (bottom) and high-spin ($S=3/2$) states.

The electronic structures for each spin state correspond with a low-spin Fe^{II} (d^6, $S=0$) and a high-spin Fe^{II} (d^6, $S=2$) antiferromagnetically coupled with an NO radical ($S=1/2$), thus leading to the observed spin states, that is, $S=1/2$ and $S=3/2$, respectively. The corresponding plot of the spin density shows (see Figure 8) that, indeed, for the $S=1/2$ spin state the elec-

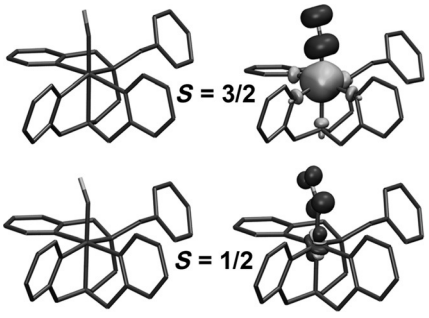

Figure 8. Optimized structures (left) and spin density (right) isocontours (0.02 e $Å^{-3}$) for the $[Fe(bztpen)(NO)]^{2+}$ molecule in the $S=3/2$ (top) and $S=1/2$ (bottom) states.

tron is mainly located on the NO ligand. In the metal, there is a blue region due to delocalization of the spin density of the radical in the orbital oriented towards the NO group whereas the red region corresponds to some spin polarization mechanism in the orbitals without overlap with the NO orbitals bearing the unpaired electron. The $S=3/2$ spin state has spin density in both, the metal center and the NO ligand with opposite signs and the N atoms of the bztpen ligand have the same sign as the metal due to the large spin delocalization (strong mixing of the orbitals with unpaired electrons of the iron center). To calculate the magnetic exchange constant, the high-spin Fe^{II} (d^6, $S=2$) ferromagnetically coupled to the NO radical ($S=1/2$) solution was also calculated. This system has a total spin state of $S=5/2$, and by using the expression in Equation (3) together with the electronic energy of the $S=3/2$ spin state, a value of $J_{calcd}=-2843\ cm^{-1}$ is obtained, which is in the right range and comparable with the calculated value for the complex [Tp*Co(NO)].[22]

Conclusion

Nitrosyl iron complexes exhibiting spin-crossover properties are scarce $\{FeNO\}^7$ species that in virtue of strong magnetic coupling invariably display $S=3/2\leftrightarrow S=1/2$ spin-state conversion. The large thermal stability of compound **1** has allowed, for the first time, to describe in a precise way how the changes in the electronic distribution of the t_{2g}–e_g orbitals due to SCO modulates the structure of the $\{FeNO\}^7$ species providing valuable magneto–structural and spectroscopic correlations.

The magnetic properties of compound **1** show the occurrence of a very gradual SCO, which extends far beyond 400 K where the population of the HS species is estimated to be 54.4%. The narrow EPR signal at $g\approx 2$ suggests that the unpaired electron essentially resides in the π^* orbitals of the NO ligand in the $S=1/2$ state. This signal widens at room temperature but remains approximately at the same g value. No feature at $g\approx 4$ associated with the $S=3/2$ state is observed despite it is approximately 30% populated at 300 K. The Mössbauer spectra of compound **1** at 80 and 293 K is consistent with the occurrence of fast spin-state interconversion rate with a nearly temperature-independent isomer shift parameter in the temperature interval 80–293 K, a fact that strongly limits the characterization of the electronic structure of the $\{FeNO\}^7$ moiety from this technique. The room temperature visible absorption spectrum of compound **1** is consistent with the presence of bands characteristic of the Fe^{II} ions in the LS state. Furthermore, the thermal variation of the $\lambda=555$ nm band tentatively attributed to the $^1A_1\rightarrow{}^1T_1$ absorption and the concomitant change of color of the complex are reminiscent of Fe^{II} complexes, which exhibit a $S=0\leftrightarrow S=2$ spin-state change. The thermal dependence of the Raman and IR spectra have enabled to characterize the ν_{NO} and ν_{Fe-NO} stretching modes in the $S=3/2$ and $S=1/2$ states. All these changes in magnetism, electronic, and vibrational spectra correlate well with the structural changes observed in the coordination $[FeN_6]$ core of compound **1**, namely, average Fe–N bonds and angles including the tilt Fe-N-O angle and the N–O bond length. Furthermore, the DFT calculations reproduce reasonably well the structure of compound **1** in the LS and HS states and support the idea that the pentadentate strong ligand field ligand bztpen stabilizes the Fe^{II} and the $NO^{\bullet}$. Consequently, the $S=3/2\leftrightarrow S=1/2$ spin equilibrium accommodates well with the concurrence of an $S=2\leftrightarrow S=0$ spin equilibrium in the Fe^{II} and strong magnetic coupling with the radical NO.

Experimental Section

General: Variable-temperature magnetic susceptibility data were recorded for single crystals and microcrystalline samples of compounds **1** and **2** at a scanning rate of $1\ K\,min^{-1}$ with a Quantum Design MPMS2 SQUID susceptometer equipped with a 7 T magnet, operating at 1 T and at temperatures between 2–400 K. Experimental susceptibilities were corrected from diamagnetism of the constituent atoms by the use of Pascal's constants. UV/Vis diffuse reflectance spectra of the microcrystalline powder of compound **1** were acquired at room temperature in the spectral range of $\lambda=$ 328–1000 nm by using a Lambda35 spectrophotometer (Perkin–Elmer) equipped with an integrating sphere. Variable-temperature absorbance data were obtained in the range $\lambda=480$–680 nm on a flat single crystal of approximately 90 μm thickness in the transmission mode by using an Olympus BX51 microscope, which was fiber-coupled to a CCD spectrometer (BWTek). Temperature-dependent, polarized Raman spectra of oriented single crystals were recorded between $\tilde{\nu}=100$–$2000\ cm^{-1}$ by using a LabramHR (Horiba) Raman microspectrometer (resolution $\approx 3\ cm^{-1}$) by using $\lambda=633$ and 532 nm laser excitations. Laser light was focused on the sample and the scattered light was collected by using the same × 50 objective (0.5 numerical aperture). Laser-induced heating effects were carefully checked by monitoring at room temperature the intensity ratio of the ν(NO) modes as a function of the laser intensity and found practically negligible below approximately 0.1 mW, which was then used in the experiments. The polarization behavior of the scattered photons versus the polarization state of the incident laser and the crystal orientation was also studied. As expected, the ν(NO) modes are strongly polarized and the highest intensity spectra were obtained in the configuration $-z(yy)z$ (Porto's notation). Non-polarized infrared absorption spectra as a function of the temperature were collected between $\tilde{\nu}=600$–$4000\ cm^{-1}$ in the transmission mode on a flat single crystal of approximately 30 μm thickness by using a Spectrum Frontier FTIR instrument (Perkin–Elmer) coupled to a Spotlight-400 microscope. To acquire variable-temperature vibrational and electronic spectra the same liquid nitrogen microscopy cryostage (THMS-600, Linkam Scientific) was used with either glass or CdSe windows. ^{57}Fe Mössbauer spectra were recorded by using a conventional constant-acceleration-type spectrometer equipped with a 50 mCi ^{57}Co source and a flow-type, liquid-nitrogen cryostat. Spectra of the powder samples were recorded at 80 and 293 K. Least-squares fittings of the Mössbauer spectra have been carried out with the assumption of Lorentzian line shapes by using the Recoil software package. Isomer shift values were given relative to metallic iron at room temperature. Elemental analysis (C, H, N) was performed by the Centro de Microanálisis Elemental de la Universidad Complutense de Madrid (Spain) by using a LECO CHNS-932 analyzer.

Variable-temperature EPR spectra were recorded on microcrystalline samples by using a Bruker ELEXYS E580 spectrometer equipped with Bruker standard resonators for the X and Q bands. Data were collected in the 20–9980.0 G field range at 4 K (frequency = 9.472 GHz, power = 0.0063 mW, power attenuation = 45.0 dB,

modulation frequency = 100.00 kHz, modulation amplitude = 1.000 G, gain = 60 dB) and at 300 K (frequency = 9.472 GHz, power = 62.84 mW, power attenuation = 5.0 dB, modulation frequency = 100.00 kHz, modulation amplitude = 1.000 G, gain = 60 dB).

Single-crystal X-ray measurements: Single-crystal X-ray data of compound **1** were collected on an Oxford Diffraction Supernova single-crystal diffractometer by using $Mo_{K\alpha}$ radiation (λ = 0.71073 Å). Data scaling and empirical absorption correction were performed. The structures were solved by direct methods by using SHELXS-97 and refined by full-matrix least squares on F^2 by using SHELXL-97.[42] Non-hydrogen atoms were refined anisotropically. Hydrogen atoms were geometrically placed (riding model) and assigned fixed isotropic displacement parameters. CCDC 1440671 (**1**, 120 K), 1440672 (**1**, 200 K), 1440673 (**1**, 250 K), 1440674 (**1**, 275 K), 1440675 (**1**, 300 K), 1440676 (**1**, 340 K), 1440677 (**1**, 380 K), 1440678 (**1**, 400 K), and 1440679 (**1**, 420 K) contain the supplementary crystallographic data for this paper. These data can be obtained free of charge from The Cambridge Crystallographic Data Centre via www.ccdc.cam.ac.uk/data_request/cif.

Materials

*Synthesis of compound **1***: Samples of compound **1** essentially constituted of single crystals were obtained in a very good yield (≈90%) by bubbling nitric oxide for 10 min through diluted solutions of $[Fe(bztpen)CH_3CN](PF_6)_2$[43] (≈30 mg 0.037 mmol in 40 mL of MeOH). The final violet solution was kept under argon in repose and closed for three days to lead the precipitation of single crystals of appropriate size for single-crystal X-ray diffraction The crystals melt with decomposition at approximately 480 K. Elemental analysis calcd (%) for $C_{27}H_{29}F_{12}FeN_6OP_2$: C 40.57, H 3.66, N 10.51; found: C 39.81, H 3.73, N 10.39.

Computational Details

All density functional theory calculations were carried out by using the Gaussian 09[44] electronic structure package with a tight convergence criterion (10^{-8} a.u. in the energy) for the density matrix elements, by using the hybrid-meta GGA functional TPSSh.[45,46] This functional has been previously used with success in the modeling of accurate thermochemical quantities for several mononuclear and dinuclear Fe^{II} spin-crossover systems.[47–50] The fully optimized contracted triple-ζ all-electron Gaussian basis set with polarization functions developed by Ahlrichs and co-workers was employed for all the elements in the molecule.[51] The different spin topologies were modeled by using the fragments option, which allows the definition of specific charges and electronic structures for the metal and for the different ligands. To calculate the exchange interaction,[52,53] a phenomenological Heisenberg–Dirac–van Vleck Hamiltonian (HDVV) was used, excluding the terms relating to magnetic anisotropy, to describe the exchange coupling [Eq. (3)]:

$$\hat{H} = -J_{ab}\hat{S}_a\hat{S}_b \qquad (3)$$

where $\hat{S}_a$ and $\hat{S}_b$ are the spin operators of the different paramagnetic centers. The J_{ab} parameter is the pairwise coupling constant between the paramagnetic centers of the molecule.

Acknowledgements

The research reported here was supported by the Spanish Ministerio de Economía y Competitividad (MINECO) and FEDER funds (CTQ2013-46275-P, CTQ2015-64579-C3-1-P, and Unidad de Excelencia María de Maeztu MDM-2015-0538) and the Generalitat Valenciana (PROMETEO/2012/049). L.P.L. thanks the Generalitat Valenciana and the Universidad de Valencia for a predoctoral fellowship. J.C. and E.R. thank the Generalitat de Catalunya for a Beatriu de Pinòs grant and an ICREA Academia award, respectively.

Keywords: antiferromagnetic coupling · iron · molecular structures · nitrosyl complexes · spin crossover

[1] a) J. C. Toledo, Jr., O. Augusto, *Chem. Res. Toxicol.* **2012**, *25*, 975–989; b) F. Roncaroli, M. Videla, L. D. Slep, J. A. Olabe, *Coord. Chem. Rev.* **2007**, *251*, 1903–1930; c) J. A. McCleverty, *Chem. Rev.* **2004**, *104*, 403–418.
[2] N. Lehnert, W. R. Scheidt, M. W. Wolf, *Struct. Bonding (Berlin)* **2013**, *154*, 155–224.
[3] T. C. Berto, A. L. Speelman, S. Zheng, N. Lehnert, *Coord. Chem. Rev.* **2013**, *257*, 244–259.
[4] A. Earnshaw, E. A. King, L. F. Larkworthy, *J. Chem. Soc. A* **1969**, 2459–2463.
[5] B. W. Fitzsimmons, L. F. Larkworthy, K. A. Rogers, *Inorg. Chim. Acta* **1980**, *44*, L53–L54.
[6] Y. Numata, K. Kubokura, Y. Nonaka, H. Okawa, S. Kida, *Inorg. Chim. Acta* **1980**, *43*, 193–197.
[7] B. Weber, H. Görls, M. Rudolph, E. G. Jäger, *Inorg. Chim. Acta* **2002**, *337*, 247–265.
[8] K. D. Hodges, R. G. Wollmann, S. L. Kessel, D. N. Hendrickson, D. G. Van Derveer, E. K. Barefield, *J. Am. Chem. Soc.* **1979**, *101*, 906–917.
[9] M. Li, D. Bonnet, E. Bill, F. Neese, T. Weyhermüller, N. Blum, D. Sellmann, K. Wieghardt, *Inorg. Chem.* **2002**, *41*, 3444–3456.
[10] J. H. Enemark, R. D. Feltham, *Coord. Chem. Rev.* **1974**, *13*, 339–406.
[11] D. M. P. Mingos, *Struct. Bonding (Berlin)* **2014**, *153*, 1–44.
[12] C. A. Brown, M. A. Pavlosky, T. E. Westre, Y. Zhang, B. Hedman, K. O. Hodgson, E. I. Solomon, *J. Am. Chem. Soc.* **1995**, *117*, 715–732.
[13] T. C. Berto, M. B. Hoffman, Y. Murata, K. B. Landenberger, E. E. Alp, J. Zhao, N. Lehnert, *J. Am. Chem. Soc.* **2011**, *133*, 16714–16717.
[14] N. Sun, L. V. Liu, A. Dey, G. Villar-Acevedo, J. A. Kovacs, M. Y. Darensbourg, K. O. Hodgson, B. Hedman, E. I. Solomon, *Inorg. Chem.* **2011**, *50*, 427–436.
[15] L. E. Goodrich, F. Paulat, V. K. K. Praneeth, N. Lehnert, *Inorg. Chem.* **2010**, *49*, 6293–6316.
[16] a) Y. Zhang, E. Oldfield, *J. Phys. Chem. A* **2003**, *107*, 4141–4150; b) Y. Zhang, E. Oldfield, *J. Am. Chem. Soc.* **2004**, *126*, 9494–9495.
[17] S. Chakraborty, J. Reed, M. Ross, M. J. Nilges, I. D. Petrik, S. Ghosh, S. Hammes-Schiffer, J. T. Sage, Y. Zhang, C. E. Schulz, Y. Lu, *Angew. Chem. Int. Ed.* **2014**, *53*, 2417–2421; *Angew. Chem.* **2014**, *126*, 2449–2453.
[18] N. Ortega-Villar, A. L. Thompson, M. C. Muñoz, V. M. Ugalde-Saldívar, A. E. Goeta, R. Moreno-Esparza, J. A. Real, *Chem. Eur. J.* **2005**, *11*, 5721–5734.
[19] N. Ortega-Villar, A. Y. Guerrero-Estrada, L. Piñeiro-López, M. C. Muñoz, M. Flores-Álamo, R. Moreno-Esparza, J. A. Real, V. M. Ugalde-Saldívar, *Inorg. Chem.* **2015**, *54*, 3413–3421.
[20] T. Nebe, A. Beitat, C. Würtele, C. Dücker-Benfer, R. van Eldik, C. J. McKenzie, S. Schindler, *Dalton Trans.* **2010**, *39*, 7768–7773.
[21] a) O. Kahn, *Molecular Magnetism*, VCH, Weinheim, **1993**; b) C. P. Slichter, H. G. Drickamer, *J. Chem. Phys.* **1972**, *56*, 2142–2161.
[22] N. C. Tomson, M. R. Crimmin, T. Petrenko, L. E. Rosebrugh, S. Sproules, W. C. Boyd, R. G. Bergman, S. DeBeer, F. D. Toste, K. Wieghardt, *J. Am. Chem. Soc.* **2011**, *133*, 18785–18801.
[23] M. Sorai, *Top. Curr. Chem.* **2004**, *235*, 153–170.
[24] P. J. van Koningsbruggen, Y. Maeda, H. Oshio, *Top. Curr. Chem.* **2004**, *233*, 259–324.
[25] H. A. Goodwin, *Top. Curr. Chem.* **2004**, *234*, 23–47.
[26] M. Schmitz, M. Seibel, H. Kelm, S. Demeshko, F. Meyer, H. J. Krüger, *Angew. Chem. Int. Ed.* **2014**, *53*, 1–6; *Angew. Chem.* **2014**, *126*, 1–1.
[27] H. Chun, E. Bill, T. Weyhermüller, K. Wieghardt, *Inorg. Chem.* **2003**, *42*, 5612–5620.

[28] F. V. Wells, S. W. McCann, H. H. Wickman, S. L. Kessel, D. N. Hendrickson, R. D. Feltham, *Inorg. Chem.* **1982**, *21*, 2306 – 2311.
[29] E. König, J. G. Ritter, J. Dengler, L. F. Larkworthy, *Inorg. Chem.* **1992**, *31*, 1196 – 1202.
[30] A. Hauser, *J. Chem. Phys.* **1991**, *94*, 2741 – 2748.
[31] C. Hauser, T. Glaser, E. Bill, T. Weyhermüller, K. Wieghardt, *J. Am. Chem. Soc.* **2000**, *122*, 4352 – 4365.
[32] T. A. Jackson, E. Yikilmaz, A. F. Miller, T. C. Brunold, *J. Am. Chem. Soc.* **2003**, *125*, 8348 – 8363.
[33] A. R. Diebold, C. D. Brown-Marshall, M. L. Neidig, J. M. Brownlee, G. R. Moran, E. I. Solomon, *J. Am. Chem. Soc.* **2011**, *133*, 18148 – 18160.
[34] V. K. K. Praneeth, F. Paulat, T. C. Berto, S. D. George, C. Näther, C. D. Sulok, N. Lehnert, *J. Am. Chem. Soc.* **2008**, *130*, 15288 – 15303.
[35] J. A. Olabe, *Dalton Trans.* **2008**, 3633 – 3648.
[36] D. P. Linder, K. R. Rodgers, J. Banister, G. R. A. Wyllie, M. K. Ellison, W. R. Scheidt, *J. Am. Chem. Soc.* **2004**, *126*, 14136 – 14148.
[37] P. Gans, A. Sabatini, L. Sacconi, *Inorg. Chem.* **1966**, *5*, 1877 – 1881.
[38] L. M. Grande, B. C. Noll, A. G. Oliver, W. R. Scheidt, *J. Am. Chem. Soc.* **2009**, *131*, 2131 – 2140.
[39] A. L. Speelman, N. Lehnert, *Angew. Chem. Int. Ed.* **2013**, *52*, 12283 – 12287; *Angew. Chem.* **2013**, *125*, 12509 – 12513.
[40] K. J. Haller, P. L. Johnson, R. D. Feltham, J. H. Enemark, J. R. Ferraro, L. J. Basile, *Inorg. Chim. Acta* **1979**, *33*, 119 – 130.
[41] A. C. McQuilken, Y. Ha, K. D. Sutherlin, M. A. Siegler, K. O. Hodgson, B. Hedman, E. I. Solomon, G. N. L. Jameson, D. P. Goldberg, *J. Am. Chem. Soc.* **2013**, *135*, 14024 – 14027.
[42] G. M. Sheldrick, *Acta Crystallogr. Sect. A* **2008**, *64*, 112 – 121.
[43] N. Ortega-Villar, V. M. Ugalde-Saldívar, M. C. Muñoz, L. A. Ortiz-Frade, J. G. Alvarado-Rodríguez, J. A. Real, R. Moreno-Esparza, *Inorg. Chem.* **2007**, *46*, 7285 – 7293.
[44] Gaussian 09, Revision D.01, M. J. Frisch, G. W. Trucks, H. B. Schlegel, G. E. Scuseria, M. A. Robb, J. R. Cheeseman, G. Scalmani, V. Barone, B. Mennucci, G. A. Petersson, H. Nakatsuji, M. Caricato, X. Li, H. P. Hratchian, A. F. Izmaylov, J. Bloino, G. Zheng, J. L. Sonnenberg, M. Hada, M. Ehara, K. Toyota, R. Fukuda, J. Hasegawa, M. Ishida, T. Nakajima, Y. Honda, O. Kitao, H. Nakai, T. Vreven, J. A. Montgomery Jr., J. E. Peralta, F. Ogliaro, M. J. Bearpark, J. Heyd, E. N. Brothers, K. N. Kudin, V. N. Staroverov, R. Kobayashi, J. Normand, K. Raghavachari, A. P. Rendell, J. C. Burant, S. S. Iyengar, J. Tomasi, M. Cossi, N. Rega, N. J. Millam, M. Klene, J. E. Knox, J. B. Cross, V. Bakken, C. Adamo, J. Jaramillo, R. Gomperts, R. E. Stratmann, O. Yazyev, A. J. Austin, R. Cammi, C. Pomelli, J. W. Ochterski, R. L. Martin, K. Morokuma, V. G. Zakrzewski, G. A. Voth, P. Salvador, J. J. Dannenberg, S. Dapprich, A. D. Daniels, Ö. Farkas, J. B. Foresman, J. V. Ortiz, J. Cioslowski and D. J. Fox, Wallingford, CT, USA **2009**.
[45] V. N. Staroverov, G. E. Scuseria, J. M. Tao, J. P. Perdew, *J. Chem. Phys.* **2003**, *119*, 12129 – 12137.
[46] J. M. Tao, J. P. Perdew, V. N. Staroverov, G. E. Scuseria, *Phys. Rev. Lett.* **2003**, *91*, 146401 1 – 4.
[47] J. Cirera, F. Paesani, *Inorg. Chem.* **2012**, *51*, 8194 – 8201.
[48] K. P. Jensen, J. Cirera, *J. Phys. Chem. A* **2009**, *113*, 10033 – 10039.
[49] J. Cirera, E. Ruiz, *J. Mater. Chem. C* **2015**, *3*, 7954 – 7961.
[50] E. Ruiz, *Phys. Chem. Chem. Phys* **2014**, *16*, 14 – 22.
[51] A. Schäfer, C. Huber, R. Ahlrichs, *J. Chem. Phys.* **1994**, *100*, 5829 – 5835.
[52] E. Ruiz, P. Alemany, S. Alvarez, J. Cano, *J. Am. Chem. Soc.* **1997**, *119*, 1297 – 1303.
[53] E. Ruiz, J. Cano, S. Alvarez, P. Alemany, *J. Comput. Chem.* **1999**, *20*, 1391 – 1400.

Received: March 11, 2016
Published online on July 15, 2016

CRYSTAL GROWTH & DESIGN

Article

pubs.acs.org/crystal

Clathration of Five-Membered Aromatic Rings in the Bimetallic Spin Crossover Metal−Organic Framework $[Fe(TPT)_{2/3}\{M^{I}(CN)_2\}_2]\cdot G$ (M^{I} = Ag, Au)

Lucía Piñeiro-López,[†] Zulema Arcís-Castillo,[†] M. Carmen Muñoz,[‡] and José A. Real*[,†]

[†]Institut de Ciencia Molecular (ICMol), Universitat de València, 46980 Paterna, València, Spain

[‡]Departament de Física Aplicada, Universitat Politècnica de València, E-46022, València, Spain

Supporting Information

ABSTRACT: Six clathrate compounds of the three-dimensional spin crossover metal−organic framework formulated $[Fe(TPT)_{2/3}\{M^{I}(CN)_2\}_2]\cdot nG$, where TPT is 2,4,6-tris(4-pyridyl)-1,3,5-triazine, M^{I} = Ag or Au and G represent the guest molecules furan, pyrrole and thiophene, were synthesized using slow diffusion techniques. The clathrate compounds were characterized by single-crystal X-ray diffraction at 120 and 300 K, thermogravimetric analysis and thermal dependence of the magnetic susceptibility. All compounds crystallize in the $R\bar{3}m$ trigonal space group. The Fe^{II} defines a unique $[FeN_6]$ crystallographic site with the equatorial positions occupied by four dicyanometallate ligands while the axial positions are occupied by the TPT ligands. Each TPT ligand links three Fe^{II} sites, while the dicyanometallate ligands bridge two Fe^{II} sites thereby generating two interlocked three-dimensional frameworks with the NbO topology. The choice of the TPT ligand favors the generation of pores where the guest molecules are located. The thermal dependence of the magnetic susceptibility of samples constituted of single crystals was investigated for the six compounds to assess the influence of the guest molecules on the spin crossover behavior. In general, the magnetic properties of the six clathrates suggest a gradual stabilization of the high-spin state as the molecular volume of the guest increases.

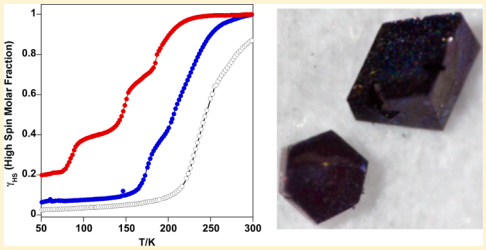

INTRODUCTION

Spin crossover (SCO) in first-row transition metal complexes with electronic configurations $3d^4$-$3d^7$ afford one of the most spectacular examples of molecule-based switchable materials. They can switch in a controllable, detectable and reversible manner between the high-spin (HS) state and the low-spin (LS) state by means of external stimuli (usually temperature, pressure and light). This change of electronic spin state, strongly coupled with a structural reorganization, occurs with concomitant changes in magnetic, dielectric and optical properties of the material. The structural reorganization, taking place primarily in the metal coordination sites (M−L bond distances and angles), are transmitted cooperatively in the solid by means of elastic interactions. In favorable conditions this cooperativity manifest hysteretic behavior and produces bistability in the physical properties, a necessary condition to deliver advanced materials with sensory and memory functions.[1−18]

By far, six-coordinate Fe^{II} SCO complexes ($3d^6$) have been the most investigated.[9,18] They switch between the paramagnetic HS state ($t_{2g}^4e_g^2$) and the diamagnetic LS state ($t_{2g}^6e_g^0$). The search for cooperativity in Fe^{II} SCO complexes led to the development of the so-called polymeric approach.[19,20] It was believed that partial or total replacement of intermolecular contacts (typically hydrogen bonds and/or $\pi-\pi$ interactions) between discrete SCO molecules by more reliable coordination bonds (provided by rigid bridging ligands) could enhance the transmission of elastic interactions between active SCO centers and hence the cooperative nature of the SCO event. This strategy has stimulated the synthesis of a considerable number of one- (1D), two- (2D), and three-dimensional (3D) SCO coordination polymers (SCO−CPs) also known as metal−organic frameworks (SCO-MOFs). Some of them are relevant examples of multifunctional molecular materials since they combine SCO and porosity functions. In particular the complex $[Fe(tvp)_2(NCS)_2]\cdot MeOH$ (tvp = *trans*-1,2-bis(4-pyridyl)ethylene), made up of orthogonal interpenetration of identical $[Fe(tvp)_2(NCS)_2]_n$ layers, represents the first porous SCO−CP.[21] Nevertheless, direct correlation between the spin state of the Fe^{II} ion and host−guest interactions in the pores was evidenced for the first time for the related complex $[Fe(azpy)_2(NCS)_2]\cdot Guest$ (azpy = 4,4′-azopyridine).[22] Another important class of metal−organic frameworks combining SCO and porosity functions are the so-called Hofmann-type clathrates formulated $\{Fe(L)[M^{II}(CN)_4]\}\cdot Guest$, where L is a pyridine-like rod-shaped bridging ligand and M^{II} = Ni, Pd, Pt. In this framework an infinite stack of 2D $\{Fe[M^{II}(CN)_4]\}_n$ layers are pillared by the organic ligand L thereby defining a 3D framework with well-defined channels. These SCO−CPs are able to express physi-

Received: July 15, 2014
Revised: October 10, 2014
Published: October 23, 2014

   dx.doi.org/10.1021/cg5010616 | *Cryst. Growth Des.* 2014, 14, 6311−6319

Table 1. Crystal Data for 1·nGuest

	1·0.5furan		1·1.5pyrrole		1·1thiophene	
	120 K	300 K	120 K	300 K	120 K	300 K
empirical formula	$C_{18}H_{10}N_8O_{0.5}Ag_2Fe$		$C_{22}H_{15.5}N_{9.5}Ag_2Fe$		$C_{20}H_{12}N_8SAg_2Fe$	
M_r	617.93		684.53		668.03	
crystal system	trigonal		trigonal		trigonal	
space group	$R\bar{3}m$		$R\bar{3}m$		$R\bar{3}m$	
a (Å)	26.2174(12)	26.8761(8)	26.2525(9)	26.8913(12)	26.2003(8)	26.8824(10)
c (Å)	9.5734(5)	10.0456(4)	9.6515(4)	10.0069(7)	9.8014(3)	10.2072(5)
V (Å^3)	5698.7(5)	6284.1(4)	5760.6(3)	6266.9(6)	5826.8(3)	6388.1(5)
Z	9		9		9	
D_c (mg cm^{-3})	1.621	1.470	1.776	1.632	1.713	1.563
$F(000)$	2682	2682	3006	3006	2916	2916
μ (Mo–K$_\alpha$) (mm^{-1})	2.116	1.919	2.103	1.933	2.153	1.963
crystal size (mm)	0.08 × 0.15 × 0.15		0.08 × 0.10 × 0.10		0.08 × 0.08 × 0.10	
no. of total reflections	2273	2085	2309	2101	1837	2138
no. of reflections $[I > 2\sigma(I)]$	1840	1501	2029	1414	1448	1443
R_1 $[I > 2\sigma(I)]^a$	0.0600	0.0560	0.0475	0.0654	0.0813	0.0785
wR $[I > 2\sigma(I)]^a$	0.1713	0.1655	0.1357	0.2118	0.2283	0.2108
S	1.081	1.011	1.087	1.096	1.040	1.154

$^aR_1 = \Sigma \|F_o| - |F_c\|/\Sigma|F_o|$; $wR = [\Sigma[w(F_o^2 - F_c^2)^2]/\Sigma[w(F_o^2)^2]]^{1/2}$. $w = 1/[s^2(F_o^2) + (mP)^2 + nP]$ where $P = (F_o^2 + 2F_c^2)/3$; $m = 0.1148$ (**1** (120 K)), 0.1214 (**1** (300 K)) 0.0702 (**2** (120 K)), 0.1265 (**2** (300 K)), 0.1574 (**3** (120 K)) and 0.1678 (**3** (300 K)); $n = 56.2195$ (**1** (120 K)), 10.5162 (**1** (300 K)) 66.7343 (**2** (120 K)), 25.3970 (**2** (300 K)), 107.5530 (**3** (120 K)), and 18.9693 (**3** (300 K).

and chemi-sorptive host–guest interactions in terms of changes in the spin state of the Fe(II) ion.[23−32]

The use of dicyanometallate complexes $[M^I(CN)_2]^-$ (M^I = Cu, Ag, Au) as building blocks in combination with ligands, typically derived from pyridine- or bis-monodentate pyridine-like linear bridging ligands, has afforded a rich variety of one- two- and three-dimensional SCO–CPs without permanent porosity.[23] Aiming at exploring the possibility of obtaining dicyanometallate based porous SCO–CPs, we decided to employ pyridine-type bridging ligands with denticity higher than two. Thus, we recently reported the synthesis, crystal structures, magnetic, Mössbauer and calorimetric studies of a new series of SCO–CPs formulated $\{Fe(TPT)_{2/3}[M^I(CN)_2]_2\}\cdot$nSolv [$M^I$ = Ag (**1·nSolv**), Au (**2·nSolv**)], where TPT is 2,4,6,-tris(4-pyridyl)-1,3,5-triazine, a tritopic C_3 symmetric pyridine-type bridging ligand, and Solv are the solvent molecules CH_2Cl_2 or CH_3OH.[33]

As a new step in this research, here we describe the synthesis, crystal structures and magnetic properties of a new series of furan, pyrrole and thiophene clathrates of $[Fe(TPT)_{2/3}\{M^I(CN)_2\}_2]\cdot G$ [M^I = Ag (**1·nG**), Au (**2·nG**)].

EXPERIMENTAL SECTION

Materials. TPT, $K[Ag(CN)_2]$, $K[Au(CN)_2]$, and $Fe(BF_4)_2\cdot 7H_2O$ were purchased from commercial sources and used as received.

Crystal growth. As previously described for the parent compounds **1·nSolv** and **2·nSolv**,[33] single crystals of **1·nG** and **2·nG** were grown by slow liquid–liquid diffusion technique using a modified H-vessel with a third tube added. This peculiar conformation was dictated by the poor solubility of the ligand TPT in common hydroxylic solvents (ethanol, methanol, etc.) where the $Fe(BF_4)_2\cdot 7H_2O$ and $K[M(CN)_2]$ salts are usually dissolved. The peripheral tubes (total volume ca. 10 mL) contained methanolic solutions of $Fe(BF_4)_2\cdot 7H_2O$ (0.08 mmol, 27 mg, 0.5 mL) and $K[M(CN)_2]$ (0.16 mmol, 32 mg [M = Ag]/46 mg [M = Au], 0.5 mL) salts, respectively. The central tube (total volume ca. 10 mL) contained a dichloromethane solution of TPT (0.053 mmol, 16 mg, 0.5 mL) mixed with an excess of the guest molecule (furan, pyrrole or thiophene). Each individual tube was filled with the corresponding solvents while the top was filled with methanol and sealed with rubber stoppers. Dark violet (**1·nG**) or red (**2·nG**) prims suitable for single crystal X-ray analysis were formed in the central tube after 1 week with relative high yield (ca. 50%). The presence and quantification of the guest molecules were confirmed by means of single crystal X-ray diffraction, thermogravimetric and elemental analyses of samples constituted exclusively of single crystals. EDX microanalysis was used to confirm the Fe/Ag and Fe/Au stoichiometric relation 1:2. The content of furan was exclusively inferred from thermogravimetric analysis due to the lability of this molecule in the pores. Anal. Calcd for $C_{16}H_8N_8FeAg_2$ (**1**): C 32.91, H 1.38, N 19.19. Found: C 33.36, H 1.30, N 18.83. Anal. Calcd for $C_{16}H_8N_8FeAu_2$ (**2**): C 25.22, H 1.06, N 14.70. Found: C 25.55, H 1.09, N 14.05. Anal. Calcd for $C_{22}H_{15.5}N_{9.5}FeAg_2$ (**1**·1.5pyrrole): C, 38.60; H, 2.28; N, 19.44. Found: C, 37.85; H, 2.32; N, 18.79. Calcd for $C_{20}H_{12}N_8SFeAg_2$ (**1**·1thiophene): C, 35.96; H, 1.81; N, 16.77. Found: C, 35.44; H, 1.87; N, 16.38. Calcd for $C_{24}H_{18}N_{10}FeAu_2$ (**2**·2pyrrole): C, 32.16; H, 2.02; N, 15.63. Found: C, 31.73; H, 1.99; N, 15.39. Calcd for $C_{18}H_{10}N_8S_{0.5}FeAu_2$ (**2**·0.5thiophene): C, 26.89; H, 1.25; N, 13.93. Found: C, 26.51; H, 1.23; N, 13.72.

Physical Characterization. Variable-temperature magnetic susceptibility measurements of samples (15–20 mg) were recorded at the rate of 2 K/min with a Quantum Design MPMS2 SQUID susceptometer equipped with a 5.5 T magnet, operating at 1 T and at temperatures from 1.8–400 K. Experimental susceptibilities were corrected for diamagnetism of the constituent atoms by the use of Pascal's constants. Thermogravimetry (TG) measurements were performed on a Mettler Toledo TGA/SDTA 851e instrument in the 300–700 K temperature range in nitrogen atmosphere with a rate of 10 K/min. Microanalysis was done by using a PV 9760 EDX system, in conjunction with a PHILIPS XL 30 ESEM scanning electron microscope.

Single Crystal X-ray Diffraction. For each compound, single-crystal X-ray data were collected successively at 120 K and at 300 K on a Nonius Kappa-CCD single crystal diffractometer using graphite monochromated MoKα radiation (λ = 0.71073 Å). A multiscan absorption correction was performed. The structures were solved by direct methods using SHELXS-97 and refined by full-matrix least-squares on F^2 using SHELXL-97.[34] Non-hydrogen atoms were refined anisotropically and hydrogen atoms were placed in calculated positions refined using idealized geometries (riding model) and assigned fixed isotropic displacement parameters. The check-CIFs of the pyrrole and

dx.doi.org/10.1021/cg5010616 | Cryst. Growth Des. 2014, 14, 6311–6319

Table 2. Crystal Data for 2·*n*Guest

	2·1furan		2·2pyrrole		2·0.5thiophene	
	120 K	300 K	120 K	300 K	120 K	300 K
empirical formula	$C_{20}H_{12}N_8OAu_2Fe$		$C_{24}H_{18}N_{10}Au_2Fe$		$C_{18}H_{10}N_8S_{0.5}Au_2Fe$	
M_r	830.16		896.27		804.15	
crystal system	trigonal		trigonal		trigonal	
space group	$R\bar{3}m$		$R\bar{3}m$		$R\bar{3}m$	
a (Å)	26.1934(10)	26.852(2)	26.4590(10)	26.9010(14)	26.4013(9)	26.8078(12)
c (Å)	9.3978(8)	9.6735(13)	9.5783(5)	9.7742(8)	9.6662(7)	9.9406(6)
V (Å^3)	5583.9(6)	6040.4(11)	5807.2(4)	6125.6(7)	5834.9(5)	6186.8(5)
Z	9		9		9	
D_c (mg cm^{-3})	2.222	2.054	2.307	2.187	2.060	1.943
F(000)	3420	3420	3744	3744	3294	3294
μ (Mo–K$_\alpha$) (mm^{-1})	12.397	11.460	11.929	11.309	11.896	11.220
crystal size (mm)	0.06 × 0.10 × 0.10		0.05 × 0.10 × 0.10		0.05 × 0.06 × 0.10	
no. of total reflections	2250	1997	2269	2027	2364	1923
no. of reflections [$I > 2\sigma(I)$]	1905	1067	1823	1575	1425	1245
R_1 [$I > 2\sigma(I)$][a]	0.0455	0.0926	0.0518	0.0405	0.0864	0.0705
wR [$I > 2\sigma(I)$][a]	0.1289	0.2004	0.1195	0.1067	0.2089	0.1850
S	1.005	1.049	1.062	0.968	1.028	1.097

[a] $R_1 = \Sigma||F_o| - |F_c||/\Sigma|F_o|$; $wR = [\Sigma[w(F_o^2 - F_c^2)^2]/\Sigma[w(F_o^2)^2]]^{1/2}$. $w = 1/[s^2(F_o^2) + (mP)^2 + nP]$ where $P = (F_o^2 + 2F_c^2)/3$; $m = 0.0824$ (**1** (120 K)), 0.1510 (**1** (300 K)) 0.0461 (**2** (120 K)), 0.0641 (**2** (300 K)), 0.0970 (**3** (120 K)) and 0.0921 (**3** (300 K)); $n = 149.9454$ (**1** (120 K)), 90.3794 (**1** (300 K)) 190.5547 (**2** (120 K)), 71.2422 (**2** (300 K)), 411.9829 (**3** (120 K)), and 157.4274 (**3** (300 K)).

Table 3. Selected Bond Lengths [Å] and Angles [°] for 1·nGuest and [2·nGuest]

	furan		pyrrole		thiophene	
	120 K	300 K	120 K	300 K	120 K	300 K
Fe–N(1)	1.993(5)	2.208(5)	1.998(4)	2.202(6)	1.986(8)	2.207(7)
	[1.987(8)]	[2.20(2)]	[2.071(9)]	[2.197(7)]	[2.04(2)]	[2.17(2)]
Fe–N(2)	1.950(4)	2.154(4)	1.947(3)	2.149(5)	1.962(6)	2.159(6)
	[1.950(6)]	[2.14(2)]	[2.033(7)]	[2.163(5)]	[2.049(14)]	[2.180(11)]
<Fe–N>[a]	1.964(5)	2.172(5)	1.964(4)	2.167(6)	1.970(8)	2.175(7)
	[1.962(8)]	[2.160(2)]	[2.046(9)]	[2.174(7)]	[2.045(19)]	[2.177(15)]
Δ[<Fe–N>][b]	0.208 [0.198]		0.203 [0.128]		0.205 [0.132]	
N(1)–Fe–N(2)	90.0(2)	89.69(14)	89.57(12)	89.3(2)	89.7(2)	89.3(2)]
	[89.2(3)]	[89.7(6)]	[89.8(3)]	[89.6(2)]	[89.9(5)]	[89.1(4)]
Fe–N(2)–C(5)	171.9(4)	169.7(5)	172.2(3)	167.8(6)	173.1(6)	170.8(7)]
	[169.9(7)]	[164.9(18)]	[167.4(6)]	[164.2(6)]	[169.4(15)]	[165.9(14)]
Σ[c]	8.4 [14.4]	17.3 [16.4]	15.2 [12.8]	20.5 [16.4]	13.6 [9.6]	25.2 [16.0]
Φ[d]	0.82 [0.77]	1.44 [1.37]	1.13 [1.08]	1.45 [1.22]	1.09 [0.87]	1.87 [0.93]
M^I–C(5)	2.063(5)	2.052(5)	2.064(4)	2.047(6)	2.068(7)	2.051(7)
	[1.992(7)]	[1.965(18)]	[1.990(8)]	[1.979(6)]	[1.990(10)]	[2.001(12)]
C(5)–M^I–C(5)	165.6(3)	167.6(3)	167.1(2)	168.3(4)	166.6(4)	166.9(5)
	[169.7(4)]	[171.5(12)]	[172.1(9)]	[172.0(4)]	[172.1(9)]	[173.4(9)]
M^I···M^I[e]	3.5466(3)^{i}	3.7252(4)^{ii}	3.6218(3)^{iii}	3.7234(6)^{ii}	3.6541(6)^{ii}	3.7760(6)^{i}
	[3.6104(4)^{iv}]	[3.7169(9)^{ii}]	[3.6890(4)^{v}]	[3.7519(4)^{ii}]	[3.7291(5)^{iv}]	[3.8355(5)^{iv}]

[a] <Fe–N> average Fe–N bond length. [b] △[<Fe–N>] difference between average bond lengths of the 300 and 120 K structures. [c] $\Sigma = \sum_{i=1}^{12}(/\theta_i - 90)$ represents the sum of the deviation from 90° of the 12 angles defined by the bonds of the pseudoctahedral [FeN6] core; [d] $\Phi = \sum_{i=1}^{24}(/\phi_i - 60/)/24$ is the angle of trigonal distortion. [e] i = $x - y + 1, -y + 2, -z + 1$; ii = $x - y, -y, -z + 1$; iii = $x - y, -y, -z + 2$; iv = $x - y + 1/3, -y + 2/3, -z - 1/3$; v = $y, x, -z + 2$.

thiophene derivatives detect a void of about 2% of the total volume of the unit cell situated between the triazine rings of two consecutive TPT ligand belonging to equivalent A-A or B–B layers (see below). Despite the presence of the mentioned voids no residual electronic density was found neither at 300 nor 120 K.

RESULTS

Synthesis. Self-assembly of the constituent building blocks (Fe^{II}, $[M^I(CN)_2]^-$ and TPT) in the presence of the guest molecules (G = furan, pyrrole, or thiophene) in CH_2Cl_2/CH_3OH solutions was unsuccessful due to the high insolubility and hence rapid precipitation of **1·nSolv** and **2·nSolv** (Solv = CH_2Cl_2 or CH_3OH). Furthermore, we did not find evidence of sorption after soaking the empty host SCO–CPs **1** and **2** with the guest molecules for 2 weeks. Slow diffusion (see Experimental Section) produced the best conditions for self-assembling and clathration of the selected guest molecules in the open frameworks **1** and **2**. Combination of single crystal diffraction studies (vide infra) together with thermogravimetric (Figure S1, Supporting Information) and elemental analyses

dx.doi.org/10.1021/cg5010616 | Cryst. Growth Des. 2014, 14, 6311–6319

have showed the presence of the targeted guest molecules without noticeable amounts of the solvents CH_2Cl_2 or CH_3OH. In principle, these solvents must compete with the five-membered rings for the voids in which both could coexist. However, the presence of solvent-accessible void and hence partial occupation of the void by the guest molecules in some of the structures here described (vide infra), is consistent with the fact that these solvent molecules are loosely attached to the frameworks **1** and **2** giving immediately the unsolvated species when the solid is not impregnated with the mother liquor at room temperature.[33]

Structure. Single crystals of **1·nG** and **2·nG** were picked out from the mother liquor, soaked in Paratone oil and mounted on a goniometer at 120 K. Then, they were measured successively at 120 K and at 300 K. At both temperatures the crystal parameters correspond to the trigonal $R\bar{3}m$ space group. These data are shown in Tables 1 and 2 together with other relevant crystallographic parameters for **1·nG** and **2·nG**, respectively. A selection of significant bond distances and angles is gathered in Table 3. The crystal structures are similar to those of the parent compounds, **1·nSolv** and **2·nSolv** (Solv = CH_2Cl_2, MeOH), previously reported.[33] The TPT molecule acts as a tritopic ligand associated with a trigonal axis perpendicular to the plane containing the TPT molecule and passing through the center of the triazine ring. The TPT ligand coordinates three crystallographically equivalent Fe^{II} ions. The pyridine moieties occupy the axial positions of the Fe^{II} sites while the equatorial positions are occupied by the cyanide groups of four crystallographically identical $[M^I(CN)_2]^-$ anions, thereby defining an axially elongated $[FeN_6]$ octahedron with the Fe^{II} ions lying in an inversion center (Figure 1). The average <Fe−N> bond length is in the range 1.960(5)−1.970(8) Å at 120 K and increases until 2.164−2.175 Å at 300 K, for the Ag derivatives. These values are characteristic for the Fe^{II} ion in the LS and HS spin state, respectively. The difference between the average bond lengths associated with the HS and LS spin states, Δ[<Fe−N>], found in the range 0.203−0.208 Å is consistent with the occurrence of a complete SCO in the three silver clathrates. The spin state change is also accompanied by changes of the bond angles of the coordination core $[FeN_6]$ (see Table 3). For example, the sum of the deviations from the ideal octahedron of the 12 cis N−Fe−N angles ($\sum_{i=1}^{12}|\theta_i - 90|$) falls in the range 8−15° in the LS state and increases until 17−25° in the HS state. The average value of the trigonal distortion parameter, $\Phi = \sum_{i=1}^{24}(|\phi_i - 60|)/24$, has been estimated to be in the interval 0.82−1.13° and 1.44−1.87° for the LS and HS states, respectively (ϕ_i represents each of the six angles defined by the superposition of two opposed triangles angles, being 60° for a regular octahedron). The Fe-cyanide linkage [Fe−N(2)−C(5)] is not linear being about 170° in the LS state. This linearity even decreases by 2−5° when the compounds change to the HS state. Similarly, the $[Ag(CN)_2]^-$ anion departs ca. 13° from linearity in the LS state and increases by 2°, 1.2° and 0.3° in the HS state for **1**·0.5furan, **1**·1.5pyrrole and **1**·1thiophene, respectively. Concomitantly with this change of angle the Ag−C(5) bond length decrease by 0.01 Å when moving from the LS state to the HS state (Table 3).

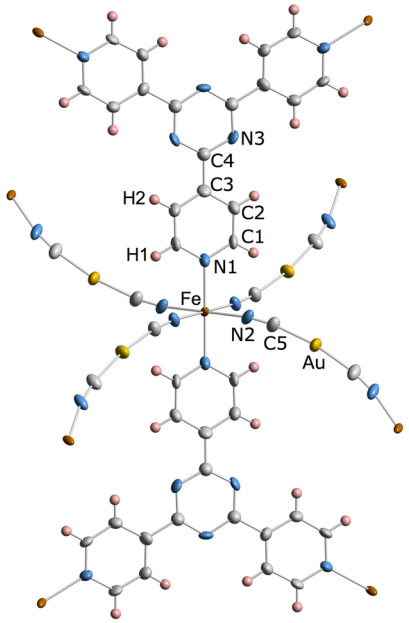

Figure 1. ORTEP representation of a significant fragment of the compound $[Fe(TPT)_{2/3}\{Au(CN)_2\}_2]\cdot 2$pyrrole (**2**·2pyrrole) at 120 K displaying the atom numbering of the asymmetric unit. Same atom numbering is applied to all silver and gold clathrates **1·nG** and **2·nG**. Thermal ellipsoids are shown at 50% probability.

Concerning the Au derivatives, only the furan clathrate shows practically complete SCO with Δ[<Fe−N >] = 0.198 Å. The Δ[<Fe−N>] value for pyrrole and thiophene derivatives (about 0.13 Å) suggests that, considering Δ[<Fe−N>] = 0.20 Å for a complete SCO, a fraction of about 35% of Fe^{II} centers remain in the HS state at 120 K. The angular parameters of the coordination centers (Fe, and Au) are comparable to those of the Ag derivatives (see Table 3). However, it is not possible to establish a similar trend for the Au−C(5) bond lengths because of the incomplete SCO and larger standard deviations.

The Fe^{II}-TPT assembly defines infinite hexagonal layers (Figure 2a). A view of two consecutive layers (hereafter named A and B) projected in *c*-direction shows that they stack in such a way that the triazine groups of one layer superpose alternately either the center of the hexagonal windows or the triazine group of the other layer (Figure 2b). The $[M^I(CN)_2]^-$ anions connect layers of the same type (A or B) generating two identical, independent and mutually interpenetrated coordination frameworks (Figure 2c,d) with the topology of the NbO (Figure S2, Supporting Information). The shortest distance between two consecutive A-B layers, d, is determined by the characteristic $\pi-\pi$ interaction observed between the triazine groups of the TPT ligands. A large volume available for clathration is formed between two consecutive A-A and B−B layers defined by the TPT ligands located over the centers of the hexagonal windows and separated by a distance hereafter called D (Table 4, Figure 3, and Figure S3, Supporting Information). For both series of clathrates there is, in general, a reasonably good correlation between the size of the guest molecule and the increase of D at both 120 and 300 K. Furthermore, the D and d values experience an increase of about 4% and 3%, respectively, when moving from the LS state to the HS state for the Ag derivatives and **2**·1furan. For **2**·2pyrrole and **2**·0.5thiophene, these variations are limited by the completeness of the SCO (vide infra).

The structural modifications associated with the SCO phenomenon are also accompanied by changes in host−guest and guest−guest intermolecular interactions. Tables 5 and 6 show a selection of relevant C···C and C···Ag or C···Au contacts. The most important interactions occur for the LS state between the guest molecules and both, the pyridine group

dx.doi.org/10.1021/cg5010616 | *Cryst. Growth Des.* 2014, 14, 6311−6319

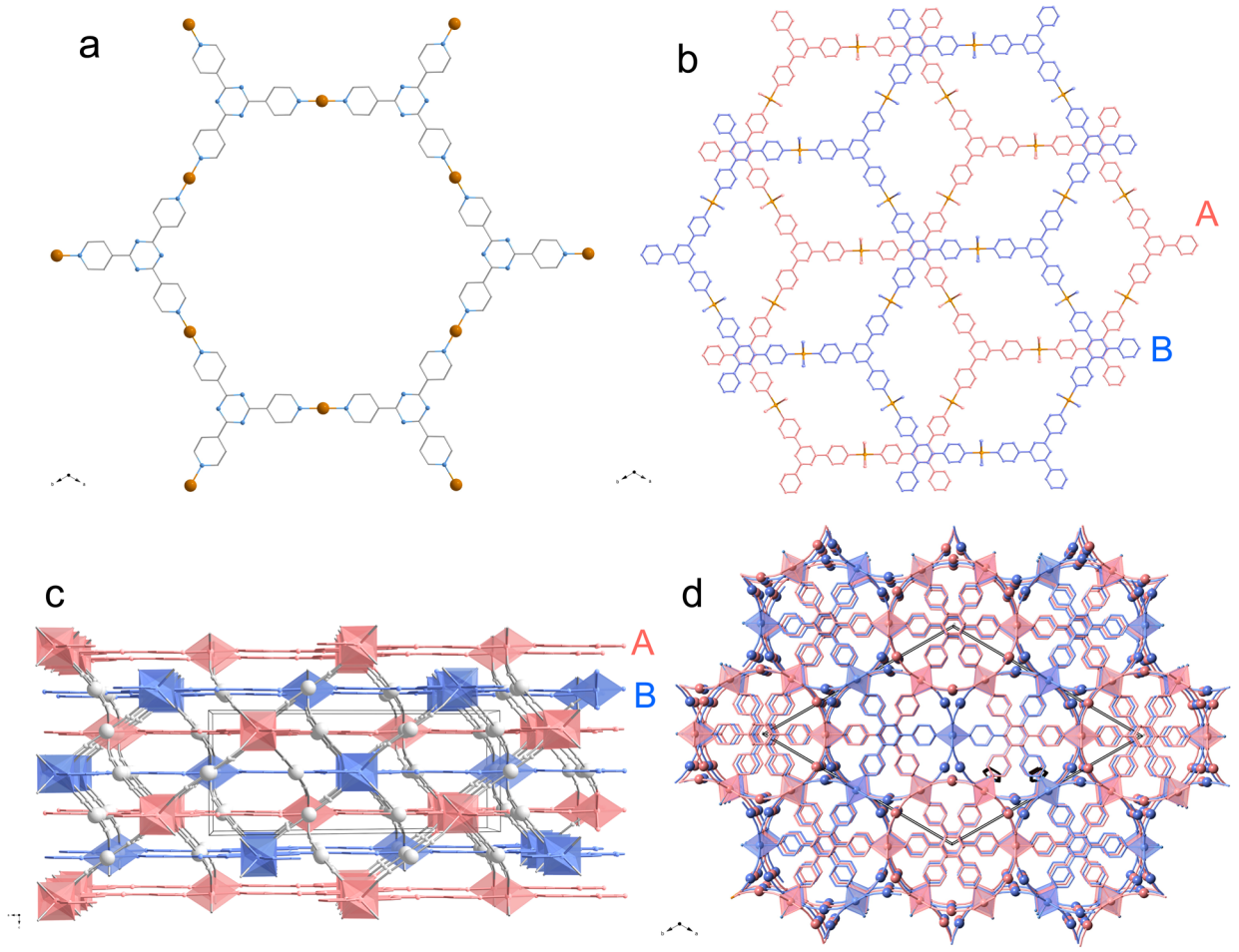

Figure 2. (a) Hexagonal motive defined by a $[Fe(TPT)]_6$ unit; (b) projection of two consecutive A and B hexagonal layers along the [001] direction; (c) view along the [010] direction of the stacking of a series of layers (blue and red colors represent the two independent interpenetrated networks); (d) Projection along the [001] direction displaying the hexagonal motives defined by interpenetration of two identical framework with NbO topology.

Table 4. Average Distances D_{av} and d_{av} (Å) between Hexagonal Fe-TPT Layers

	D		*d*	
	120 K	300 K	120 K	300 K
1·0.5furan	6.396	6.773	3.179	3.274
1·1.5pyrrole	6.452	6.715	3.201	3.293
1·1thiophene	6.636	6.942	3.167	3.266
2·1furan	6.262	6.382	3.136	3.294
2·2pyrrol	6.405	6.535	3.174	3.240
2·0.5thiophene	6.538	6.734	3.129	3.209

of the TPT ligand and the $[M^I(CN)_2]^-$ groups (Figure 3). Short guest···guest contacts (Tables 5 and 6) are only observed for the furan derivative in both series (we consider relevant contacts those smaller than the sum of the van der Waals radii, ie. smaller than 3.70 Å for C···C). There also short $M^I \cdots M^I$ contacts between the two interpenetrated networks. These contacts related by a helical axis running along the *c*-direction define characteristic pseudotrigonal motives when the structure is projected on the *a*−*b* plane (see Figure 2d). Two consecutive pseudotrigonal motives display opposite chirality. Although these contacts clearly change with the spin state of the Fe^{II}, no relevant intermetallic interactions are observed in these series.

All the changes associated with the SCO can be expressed in terms of the unit cell volume variation per Fe^{II} atom: ΔV_{HL} = 65.04, 56.29, and 62.37 Å^3 for **1**·0.5furane, **1**·1.5pyrrole, and **1**·1thiophene and ΔV_{HL} = 50.72, 54.43, and 60.15 Å^3 for **2**·1furan, **2**·2pyrrole, and **2**·0.5thiophene (the two latter volumes have been extrapolated to 100% of SCO conversion), respectively.

Spin Crossover Properties. The thermal dependence of the $\chi_M T$ product, where χ_M is the molar magnetic susceptibility and *T* is temperature, was measured in the temperature region 4−300 K for **1**·**nG** and **2**·**nG** series. In order to minimize any loss of guest molecules, the magnetic properties of samples constituted exclusively of single crystals soaked in the corresponding guest were measured in sealed tubes. This was particularly important for the furan and thiophene derivatives since their boiling points are relatively low (304.4 and 357 K, respectively). The corresponding $\chi_M T$ versus *T* curves are shown in Figure 4. Table 7 summarizes the extrema values of $\chi_M T$ versus *T* curves obtained from the low- $[(\chi_M T)_{LT}, T = 50$ K] and high-temperature limits $[(\chi_M T)_{HT}, T = 300$ K] together with the characteristic temperature $T_{1/2}$ at which the HS and LS molar fractions are equal to 0.5, where the free Gibbs energy is equal to zero for the whole series.

The clathrates **1**·**nG** display relatively poor cooperative thermal induced SCO without hysteretic behavior. For **1**·

dx.doi.org/10.1021/cg5010616 | *Cryst. Growth Des.* 2014, 14, 6311−6319

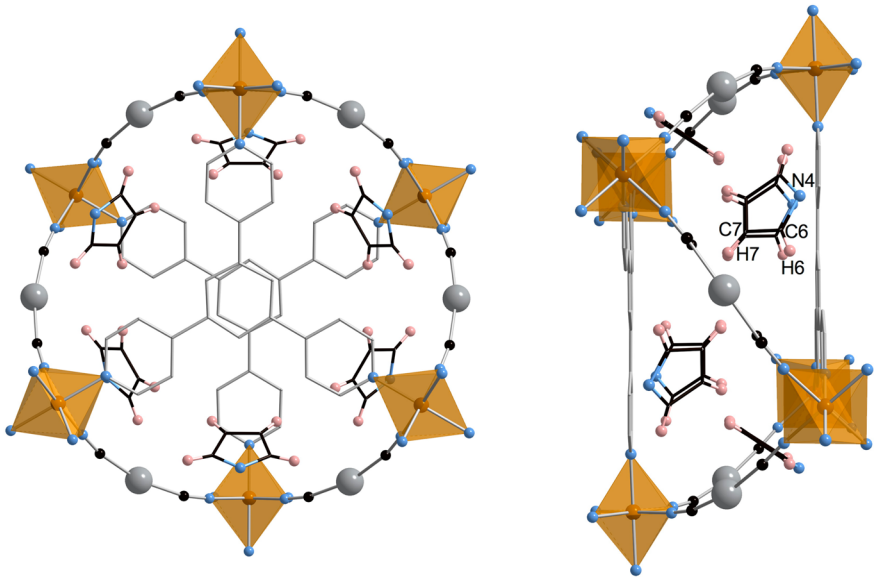

Figure 3. Views in [001] (left) and [100] (right) directions of the same fragment of **1**·1.5pyrrole at 120 K showing the pyrrole guest together with the atom numbering.

Table 5. Intermolecular Contacts between the Guest Molecule and Different Fragments of 1·nGuest[a]

compound	**1**·0.5furan		**1**·1.5pyrrol		**1**·1thiophene	
Guest···Host	120 K	300 K	120 K	300 K	120 K	300 K
			Guest···Pyridine			
C(6)···C(1)	3.60(2)^{i}	3.74(3)^{iii}	3.723(11)^{vii}	3.83(2)^{x}	3.573(11)^{xiii}	3.707(13)^{xiv}
C(6)···C(2)	3.37(2)^{i}	3.54(3)^{iv}	3.514(11)^{vii}	3.65(2)^{x}	3.487(11)^{xiii}	3.620(13)^{xiv}
C(7)···C(2)	3.67(4)^{i}	3.94(3)^{iv}	3.761(12)^{vii}	3.83(2)^{x}	3.81(3)^{xiii}	3.99(2)^{xiv}
			Guest···Cyanide			
C(6)···C(5)	3.60(3)^{ii}	3.89(2)^{v}	3.718(10)^{viii}	3.91(2)^{iv}	3.531(14)^{ii}	3.68(2)^{xv}
C(7)···C(5)	3.62(5)^{ii}		3.530(10)^{viii}	3.75(2)^{iv}	3.49(4)^{ii}	3.63(3)^{xv}
			Guest···Ag			
C(6)···Ag	3.49(2)	3.65(3)	3.562(10)^{viii}	3.74(2)^{xi}	3.23(12)^{ii}	3.70(2)^{xv}
C(7)···Ag			3.799(10)^{viii}	3.94(2)^{xi}	3.71(4)^{ii}	3.85(3)^{xv}
			Guest···Guest			
C(7)···C(7)^{i}	3.49(5)^{ii}	4.10(4)^{vi}	4.15(2)^{ix}	4.38(3)^{xii}	4.14(3)^{ii}	4.11(2)^{vi}

[a] i = $-x+1, -y+2, -z+2$; ii = $-x+2/3, -x+y+1/3, -z+4/3$; iii = $-x, +y+4/3, -x+2/3, z+2/3$; iv = $-y+2/3, x-y-2/3, z-2/3$; v = $x-y, -y, -z+1$; vi = $-x+4/3, -x+y+2/3, -z+2/3$; vii = $-y+2/3, x-y-2/3, z+1/3$; viii = $x-y, -y, -z+2$; ix = $y+2/3, x-2/3, -z+7/3$; $x = x, x-y-1, z$; xi = $-x+1, -x+y, -z$; xii = $x-y-1/3, -y-2/3, -z-2/3$; xiii = $-x+2/3, -x+y+1/3, -z+1/3$; xiv = $x+1/3, x-y+2/3, z-1/3$; xv = $-x+1, -y+1, -z+1$.

0.5furan the SCO is rather complete and characterized by two steps. One step centered at ca. 233 K involves 2/3 of the total spin state conversion, whereas the remaining HS ↔ LS conversion takes place at ca. 173 K. In contrast, **1**·1.5pyrrole and **1**·1thiophene undergo three-step SCO with characteristic temperatures 211.5 K, 167.3 K, and ≈103.2 and 193.5 K, 148.3 K, and ≈82 K, respectively. Each step involves approximately the same degree of HS ↔ LS conversion. However, due to the low temperatures involved in the low-temperature transition, the SCO is clearly incomplete for both derivatives. This thermal quenching is common below 100 K since the rate of the HS ↔ LS transformation becomes so small that no thermodynamic equilibrium can be achieved and consequently a fraction the Fe^{II} ions remain blocked in the HS state.[35]

The **2**·**nG** clathrates display even less cooperative one-step SCO with characteristic temperatures smaller than those of the silver homologous (Table 7). The conversion is essentially complete for **2**·1furan, however, 30−45% of Fe^{II} centers remain HS at low temperatures for **2**·2pyrrole and **2**·0.5thiophene in agreement with the crystallographic analysis of the three derivatives.

■ DISCUSSION

This work was undertaken to investigate clathration capabilities of the open metal−organic frameworks **1** and **2**. We also were interested in how selected five-membered aromatic guest molecules influence the SCO properties of the parent CPs **1**·**nSolv** and **2**·**nSolv** previously investigated in our group. Concerning the first point, the title compounds represent the first examples made by design involving clathration of aromatic molecules in a SCO−CP of the type $\{Fe(L)[M^{I}(CN)_2]_2\}$. In this family of compounds, L is usually a monodentate or bis-monodentate pyridine-type ligand, and $[M^{I}(CN)_2]^-$ are long building blocks that facilitate generation of open frameworks with marked tendency to fill void spaces through inter-penetration of identical networks. This is the reason why most

dx.doi.org/10.1021/cg5010616 | Cryst. Growth Des. 2014, 14, 6311−6319

Table 6. Intermolecular Contacts between the Guest Molecule and Different Fragments of 2·nGuest[a]

compound	2·1furan		2·2pyrrol		2·0.5thiophene	
Guest···Host	120 K	300 K	120 K	300 K	120 K	300 K
			Guest···Pyridine			
C(6)···C(1)	3.58(3)^{i}	3.80(8)^{v}	3.73(2)	3.7480(2)	3.60(4)^{x}	3.73(9)
C(6)···C(2)	3.29(3)^{i}	3.62(9)^{v}	3.563(14)	3.5597(2)	3.48(4)^{x}	3.55(8)
C(7)···C(2)	3.68(4)^{i}	3.55(9)^{v}	3.71(2)	3.7897(2)	3.59(8)^{x}	3.90(6)
C(7)···C(1)	3.68(3)^{ii}	3.84(8)^{vi}				
			Guest···Cyanide			
C(6)···C(5)	3.63(2)^{iii}	3.49(6)^{vii}	3.65(2)^{vii}	3.7960(2)^{ix}	3.53(3)	3.69(10)^{xi}
C(7)···C(5)	3.53(3)^{iii}	3.88(6)^{vii}	3.55(2)^{vii}	3.6656(2)^{ix}	3.64(5)	3.63(8)^{xi}
			Guest···Ag			
C(6)···Au	3.52(2)^{iii}	3.47(5)^{vii}	3.51(2)^{vii}	3.6367(4)^{ix}	3.25(3)	3.48(12)^{xi}
C(7)···Au	3.77(2)^{iii}	4.02(4)^{vii}	3.75(2)^{vii}	3.8696(5)^{ix}	3.75(4)	3.80(9)^{xi}
			Guest···Guest			
C(7)···C(7)^{i}	3.43(5)^{iv}	3.47(12)^{iv}	4.19(2)^{viii}	4.1244(2)^{ix}	4.21(10)^{iv}	3.79(9)^{ix}

[a] i = $x - y + 1/3, -y + 2/3, -z + 2/3$; ii = $-y + 2/3, x - y + 1/3, z - 2/3$; iii = $y, -x + y, -z$; iv = $y, x, -z$; v = $x - 1/3, y + 1/3, z + 1/3$; vi = $y + 1/3, x - 1/3, -z - 1/3$; vii = $-x + y + 2/3; y + 1/3, z - 2/3$; viii = $x - y + 2/3, -y + 4/3, -z + 1/3$; ix = $-x + 4/3, -x + y + 2/3, z + 2/3$; $x = -y + 1/3, -x + 2/3, z + 2/3$; xi = $x - 1/3, x - y - 2/3, z - 2/3$.

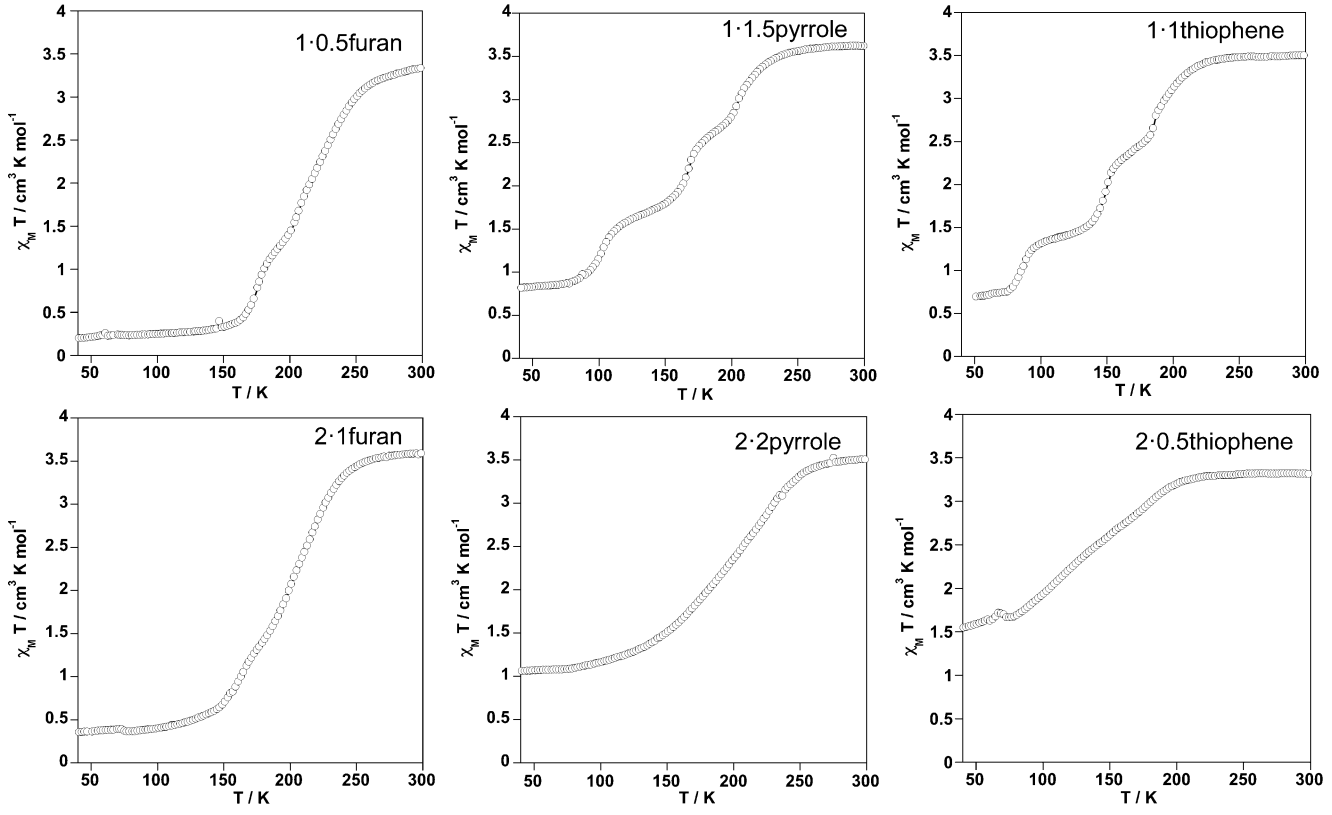

Figure 4. Magnetic behavior of **1·nG** and **2·nG**.

investigated SCO−CP of the type $\{Fe(L)_x[M^I(CN)_2]_2\}$ show poor clathration capacity. For example, when L is 4,4′-bipyridine (4,4′-bipy) or *trans*-1,2-bis(4-pyridyl)ethylene (tvp) the resulting $\{Fe(L)_2[M^I(CN)_2]_2\}$ SCO−CPs display double interpenetrated 3D frameworks with no space even for solvent molecules.[36] Similarly, the 3D SCO−CPs $\{Fe(3\text{-cyanopyridine})_2[M^I(CN)_2]_2\}\cdot 2/3H_2O$[37,38] and $\{Fe(pyrimidine)(H_2O)[M^I(CN)_2]_2\}\cdot H_2O$[39] consist of triple interpenetration of identical open frameworks with the topology of NbO and $CdSO_4$, respectively. Both series of compounds retain one loosely attached molecule of water in the small available space. Accidental clathration of aromatic ligands has been observed in the 2D layered SCO−CPs $\{Fe(3\text{-Xpy})_2[Ag(CN)_2][Ag(3\text{-Xpy})(CN)_2]\}\cdot 3\text{-Xpy}$ (3-Xpy = 3-Xpyridine and X = Br, I)[40] and $\{Fe(3\text{-Ipy})_2[Au(CN)_2]_2\}\cdot 1/2(3\text{-Ipy})$[41] when a large excess of 3-Xpy is present during the formation of the crystals.

It deserves to be noted that the systems $\{Fe(3\text{-cyanopyridine})_2[M^I(CN)_2]_2\}$ (M^I = Ag, Au)[36] and **1·nG** and **2·nG** display the same NbO topology. The organic ligand occupies the axial positions of the Fe^{II} sites in both examples. However, the tritopic C_3 nature of the TPT ligand determines the generation of robust hexagonal 2D $[Fe(TPT)_{2/3}]_\infty$ layers, thereby determining the orientation of the $[FeN_6]$ coordination

dx.doi.org/10.1021/cg5010616 | *Cryst. Growth Des.* 2014, 14, 6311−6319

Table 7. Significant Extreme Values of $\chi_M T$ Evaluated for the Low (LT) and High (HT) Temperature Limits of the $\chi_M T$ versus T Plots and $T_{1/2}$ (See Text)

	$(\chi_M T)_{LT}$	$(\chi_M T)_{HT}$	$T_{1/2}$[a]
1·0.5furan	0.21	3.33	208.9
1·1.5pyrrole	0.83	3.62	167.3
1·1thiophene	0.69	3.50	152.0
2·1furan	0.36	3.59	198.9
2·2pyrrole	1.07	3.51	197.1
2·0.5thiophene	1.58	3.32	136.6
1·2CH_2Cl_2	0.51	3.77	244.4[b]
2·2CH_2Cl_2	0.30	3.17	222.4[b]

[a] $T_{1/2}$ values have been estimated from the temperature value at which the experimental $\chi_M T$ value is equal to $\{[(\chi_M T)_{max} - (\chi_M T)_{min}]/2 + (\chi_M T)_{min}\}$. [b] Ref 6.

octahedrons and hence the geometry of the Fe−NC−M−CN−Fe linkages. Thus, these linkages strongly deviate from linearity; indeed the average angle defined by the three metallic atoms is about 153°. The lack of such structural constraints in the {Fe(3-cyanopyridine)$_2$[M^I(CN)$_2$]$_2$} system, due to the monodentate nature of the 3-cyanopyridine, apparently confers more orientational freedom to the [FeN_6] sites during the formation of the framework, and consequently the average Fe−NC−M−CN−Fe angle is 19° larger (see Figure S4, Supporting Information). This makes the NbO framework more open, thus allowing triple interpenetration of identical frameworks.

Although double interpenetration takes place in **1**·**nG** and **2**·**nG**, the C_3 symmetry of the TPT ligand generates large voids defined by the relative disposition of the hexagonal [Fe-TPT]$_n$ layers (see Figure 2b). Indeed, 50% of the TPT ligands are involved in the formation of strong $\pi-\pi$ interactions determining a perfect offset disposition between consecutive A−B−A−B layers. The remaining 50% TPT ligands define the walls of the voids formed by alternate A−A or B−B layers. Despite different guest occupation, the size of the pores expressed in terms of the distance D between A−A or B−B layers (Table 4) increases as the volume of the guest molecule increases [furan, 77.9 Å^3; pyrrole, 80.8 Å^3; thiophene, 86.5 Å^3]. This fact denotes a certain degree of flexibility of the 3D networks, which is more prominent for **1**·**nG**. This flexibility is also reflected in the change of the linkage angles Fe−N−C and C−M−C upon SCO. Interestingly, the characteristic temperature $T_{1/2}$, and hence the stabilization of the LS species, decreases as the size of the guest molecule increases. A similar trend has recently been observed for the 3D porous SCO−CP {Fe(pyrazine)[$Pt(CN)_4$]}·G with average $T_{1/2}$ = 201, 167, and 114 K for G = furan, pyrrole, and thiophene, respectively. In this case, it was inferred from the calculated host−guest energies that bulky guest molecules are stabilized by the bigger HS host framework, while small guest molecules present similar interaction energies for both spin states of the framework.[42] Hence, $T_{1/2}$ values are expected to decrease as the size of the guest increases. This correlation is in general observed for the title compounds.

1·1thiophene displays, in a first cycle, a three-step SCO with average $T_{1/2}$ = 149 K, which is smaller than that shown by the stable three-step SCO shown by **1**·1.5pyrrole, $T_{1/2}$ = 167.2 K. However, after a second cooling−heating cycle the SCO of **1**·1thiophene becomes two-step with average $T_{1/2}$ = 194.7 K. Modification of the intermolecular host−guest interactions and/or subtle changes in the more flexible host network **1** could be the cause of the observed high-temperature shift of $T_{1/2}$.

1·1.5pyrrole and **1**·1thiophene display three-step SCO behavior. Three-step transitions are rare events in SCO phenomena. A first example was reported for {Fe(3-cyanopyridine)$_2$[Au(CN)$_2$]$_2$}·2/3H_2O.[37,38,43] In this compound, only one-third of the Fe^{II} ions undergo LS ↔ HS, while the other two-thirds remain HS at all temperatures at ambient pressure (10^5 Pa). However, in the interval of pressures 0.24−0.30 GPa, it shows a two-step thermal induced spin transition, but interestingly, at 0.47 GPa undergoes an almost complete three-step thermal induced spin transition.[43] A three-step SCO behavior at 10^5 Pa has been reported for the 2D SCO−CP {Fe(4-methylpyridine)$_2$[Au(CN)$_2$]$_2$}.[44] More recently, an ambient pressure structural, magnetic, and photomagnetic study of the three-step SCO 3D-Hofmann-like MOF {Fe(dpsme)[$Pt(CN)_4$]}·2/3dpsme·xEtOH·$y$$H_2O$ (dpsme = 4,4′-di(pyridylthio)methane) has demonstrated the occurrence of different long-range orderings of the LS and HS sites with subtle structural modulation yielding inequivalent Fe^{II} sites in the four corresponding plateaus.[45] Similarly, only one Fe^{II} site was observed for the LS and HS structures of **1**·1.5pyrrole and **1**·1thiophene; however, development of elastic constrains during the HS ↔ LS transformation and hence generation of different Fe^{II} sites seem to be the most reasonable explanation for the occurrence of three steps.

Comparison of $T_{1/2}$ values of both **1**·**nG** silver and **2**·**nG** series evidence a general down-shift tendency when moving from silver to gold. This tendency has been previously noted for the two different series of isostructural compounds {Fe(3-cyanopyridine)$_2$[M^I(CN)$_2$]$_2$}·2/3H_2O[37,38] and {Fe(pyrimidine)(H_2O)[M^I(CN)$_2$]$_2$}·H_2O[39] where a decrease of the average critical temperature by ca. 52 and 62 K was observed, respectively. This effect can be understood in terms of the well-known relativistic effects observed for heavy atoms, which explain the much higher electron affinity of gold with respect to silver.[46] In this respect, stronger electron withdrawing (polarizing) effect over the CN groups of the [M(CN)$_2$]$^-$ anions, and hence a poorer donor capacity of the nitrogen atoms for the gold derivative should be expected. This should be reflected on the occurrence of shorter Au−C and longer CN−Fe bonds with respect to the Ag counterpart. In fact, this was the case for the pyrimidine and 3-cyanopyridine derivatives mentioned above. However, in the present case, like for the previously investigated compounds {Fe(3-Xpyridine)$_2$-[M(CN)$_2$]$_2$} (X = F, Cl; M = Ag, Au),[40,41] this tendency has been only clearly observed for Au−C bonds, which are shorter than the corresponding Ag−C bonds (Table 3).

CONCLUSION

Here we have demonstrated for the first time that the tridimensional spin crossover porous coordination polymers formulated [Fe(TPT)$_{2/3}${M^I(CN)$_2$}$_2$] (M^I = Ag, Au) are able to form clathrate compounds with five-membered cyclic aromatic molecules such as furan, pyrrole, and thiophene. The presence of these guest molecules in the pores does not influence the cooperative nature of the SCO, but modifies its characteristic temperature, $T_{1/2}$. The general trend is a larger stabilization of the high-spin state as the molecular volume of the guest increases. Interestingly, **1**·1.5pyrrole and **1**·1thiophene derivatives display three-step SCO behavior. Similar two-step transition occurs for **1**·0.5furan and **2**·1furan. In contrast,

dx.doi.org/10.1021/cg5010616 | Cryst. Growth Des. 2014, 14, 6311−6319

the remaining gold derivatives undergo incomplete SCO behaviors.

■ ASSOCIATED CONTENT

Supporting Information

Thermogravimetric analyses (Figure S1), representation of the NbO structure defined by the Fe^{II}-$[M^{I}(CN)_2]^-$ moieties (120 K) (Figure S2), perspective views of the pores for **1**·0.5furan (120 K), and (b) **1**·1thiophene (120 K) (Figure S3), comparative views of the hexagonal motives of **1**(**2**)·**nG** and $\{Fe(3\text{-cyanopyridine})_2[M^{I}(CN)_2]_2\}$, and CIF files. This material is available free of charge via the Internet at http://pubs.acs.org.

■ AUTHOR INFORMATION

Corresponding Author

*E-mail: jose.a.real@uv.es.

Notes

The authors declare no competing financial interest.

■ ACKNOWLEDGMENTS

The research reported here was supported by the Spanish Ministerio de Economía y Competitividad (MINECO) and FEDER funds (CTQ2013-46275-P) and Generalitat Valenciana (PROMETEO/2012/049). Z.A.C. thanks the Spanish M.E.C.D. for a predoctoral FPU fellowship. L.P.L. thanks the Generalitat Valenciana for a predoctoral fellowship in the frame of the project PROMETEO/2012/049.

■ REFERENCES

(1) Goodwin, H. A. *Coord. Chem. Rev.* **1976**, *18*, 293−325.
(2) Gütlich, P. *Struct. Bonding (Berlin)* **1981**, *44*, 83−195.
(3) König, E.; Ritter, G.; Kulshreshtha, S. K. *Chem. Rev.* **1985**, *85*, 219−234.
(4) Hauser, A. *Comments Inorg. Chem.* **1995**, *17*, 17−40.
(5) König, E. *Struct. Bonding (Berlin)* **1991**, *76*, 51−152.
(6) Gütlich, P.; Hauser, A.; Spiering, H. *Angew. Chem., Int. Ed.* **1994**, *33*, 2024−2054.
(7) Sato, O. *Acc. Chem. Res.* **2003**, *36*, 692−700.
(8) Real, J. A.; Gaspar, A. B.; Niel, V.; Muñoz, M. C. *Coord. Chem. Rev.* **2003**, *236*, 121−141.
(9) Gütlich, P.; Goodwin, H. A., Eds. *Top. Curr. Chem.* **2004**, Vols. *233*−*235*.
(10) Real, J. A.; Gaspar, A. B.; Muñoz, M. C. *Dalton Trans.* **2005**, 2062−2079.
(11) Halcrow, M. A. *Polyhedron* **2007**, *26*, 3523−3576.
(12) Nihei, M.; Shiga, T.; Maeda, Y.; Oshio, H. *Coord. Chem. Rev.* **2007**, *251*, 2606−2621.
(13) Gamez, P.; Sánchez-Costa, J.; Quesada, M.; Aromí, G. *Dalton Trans.* **2009**, 7845−7853.
(14) Halcrow, M. A. *Coord. Chem. Rev.* **2009**, *253*, 2493−2514.
(15) Salitros, I.; Madhu, N. T.; Boca, R.; Pavlik, J.; Ruben, M. *Monatsh. Chem.* **2009**, *140*, 65−733.
(16) Olguin, J.; Brooker, S. *Coord. Chem. Rev.* **2011**, *255*, 203−240.
(17) Bousseksou, A.; Molnár, G.; Salmon, L.; Nicolazzi, W. *Chem. Soc. Rev.* **2011**, *40*, 3313−3335.
(18) *Spin-Crossover Materials - Properties and Applications*; Halcrow, M. A., Ed.; John Wiley & Sons: Chichester, 2013.
(19) Kahn, O.; Kröber, J.; Jay, C. *Adv. Mater.* **1992**, *4*, 718−728.
(20) Kahn, O.; Jay, C. *Science* **1998**, *279*, 44−48.
(21) Real, J. A.; Andrés, E.; Muñoz, M. C.; Julve, M.; Granier, T.; Bousseksou, A.; Varret, F. *Science* **1995**, *268*, 265−267.
(22) Halder, G. J.; Kepert, C. J.; Moubaraki, B.; Murray, K. S.; Cashion, J. D. *Science* **2002**, *298*, 1762−1765.
(23) Muñoz, M. C.; Real, J. A. *Coord. Chem. Rev.* **2011**, *255*, 2068−2093.
(24) Ohba, M.; Yoneda, K.; Agustí, G.; Muñoz, M. C.; Gaspar, A. B.; Real, J. A.; Yamasaki, M.; Ando, H.; Nakao, Y.; Sakaki, S.; Kitagawa, S. *Angew. Chem., Int. Ed.* **2009**, *48*, 4767−4771.
(25) Agustí, G.; Ohtani, R.; Yoneda, K.; Gaspar, A. B.; Ohba, M.; Sánchez-Royo, J. F.; Muñoz, M. C.; Kitagawa, S.; Real, J. A. *Angew. Chem., Int. Ed.* **2009**, *48*, 8944−8947.
(26) Southon, P. D.; Liu, L.; Fellows, E. A.; Price, D. J.; Halder, G. J.; Chapman, K. W.; Moubaraki, B.; Murray, K. S.; Létard, J. F.; Kepert, C. J. *J. Am. Chem. Soc.* **2009**, *131*, 10998−11009.
(27) Ohtani, R.; Yoneda, K.; Furukawa, S.; Horike, N.; Kitagawa, S.; Gaspar, A. B.; Muñoz, M. C.; Real, J. A.; Ohba, M. *J. Am. Chem. Soc.* **2011**, *133*, 8600−8605.
(28) Rodríguez-Velamazán, J. A.; González, M. A.; Real, J. A.; Castro, M.; Muñoz, M. C.; Gaspar, A. B.; Ohtani, R.; Ohba, M.; Yoneda, K.; Hijikata, Y.; Yanai, N.; Mizuno, M.; Ando, H.; Kitagawa, S. *J. Am. Chem. Soc.* **2012**, *134*, 5083−5089.
(29) Sciortino, N. F.; Scherl-Gruenwald, K. R.; Chastanet, G.; Halder, G. J.; Chapman, K. W.; Létard, J.-F.; Kepert, C. J. *Angew. Chem., Int. Ed.* **2012**, *51*, 10154−10158.
(30) Muñoz-Lara, F. J.; Gaspar, A. B.; Aravena, D.; Ruiz, E.; Muñoz, M. C.; Ohba, M.; Ohtani, R.; Kitagawa, S.; Real, J. A. *Chem. Commun.* **2012**, *48*, 4686−4688.
(31) Arcís-Castillo, Z.; Muñoz-Lara, F. J.; Muñoz, M. C.; Aravena, D.; Gaspar, A. B.; Sánchez-Royo, J. F.; Ruiz, E.; Ohba, M.; Matsuda, R.; Kitagawa, S.; Real, J. A. *Inorg. Chem.* **2013**, *52*, 12777−12783.
(32) Piñeiro-López, L.; Seredyuk, M.; Muñoz, M. C.; Real, J. A. *Chem. Commun.* **2014**, *50*, 1833−1835.
(33) Arcís-Castillo, Z.; Muñoz, M. C.; Molnár, G.; Bousseksou, A.; Real, J. A. *Chem.—Eur. J.* **2013**, *19*, 6851−6861.
(34) Sheldrick, G. M. *Acta Crystallogr. A* **2008**, *64*, 112−122.
(35) Hauser, A. *Comments Inorg. Chem.* **1995**, *17*, 17−40.
(36) Niel, V.; Muñoz, M. C.; Gaspar, A. B.; Galet, A.; Levchenko, G.; Real, J. A. *Chem.—Eur. J.* **2002**, *8*, 2446−2453.
(37) Galet, A.; Niel, V.; Muñoz, M. C.; Real, J. A. *J. Am. Chem. Soc.* **2003**, *125*, 14224−14225.
(38) Galet, A.; Muñoz, M. C.; Martínez, V.; Real, J. A. *Chem. Commun.* **2004**, 2268−2269.
(39) Niel, V.; Thompson, A. L.; Muñoz, M. C.; Galet, A.; Goeta, A. E.; Real, J. A. *Angew. Chem., Int. Ed.* **2003**, *42*, 3760−3763.
(40) Muñoz, M. C.; Gaspar, A. B.; Galet, A.; Real, J. A. *Inorg. Chem.* **2007**, *46*, 8182−8192.
(41) Agustí, G.; Muñoz, M. C.; Gaspar, A. B.; Real, J. A. *Inorg. Chem.* **2008**, *47*, 2552−2561.
(42) Aravena, D.; Arcís-Castillo, Z.; Muñoz, M. C.; Gaspar, A. B.; Yoneda, K.; Ohtani, R.; Mishima, A.; Kitagawa, S.; Ohba, M.; Real, J. A.; Ruiz, E. *Chem.—Eur. J.* **2014**, *20*, 12864−12873.
(43) Galet, A.; Gaspar, A. B.; Agustí, G.; Muñoz, M. C.; Real, J. A. *Chem. Phys. Lett.* **2007**, *434*, 68−72.
(44) Kosone, T.; Tomori, I.; Kanadani, C.; Saito, T.; Mochida, T.; Kitazawa, T. *Dalton Trans.* **2010**, *39*, 1719−1721.
(45) Sciortino, N. F.; Scherl-Gruenwald, K. R.; Chastanet, G.; Halder, G. J.; Chapman, K. W.; Létard, J. F.; Kepert, C. J. *Angew. Chem., Int. Ed.* **2012**, *51*, 10154−10158.
(46) Jansen, M. *Angew. Chem., Int. Ed. Engl.* **1987**, *26*, 1098.

ChemComm

COMMUNICATION

View Article Online
View Journal | View Issue

Cite this: *Chem. Commun.*, 2014, **50**, 1833

Received 11th November 2013,
Accepted 13th December 2013

DOI: 10.1039/c3cc48595a

www.rsc.org/chemcomm

Two- and one-step cooperative spin transitions in Hofmann-like clathrates with enhanced loading capacity†

Lucía Piñeiro-López,[a] Maksym Seredyuk,‡[a] M. Carmen Muñoz[b] and José A. Real*[a]

Structural, magnetic, calorimetric and Mössbauer studies of the cooperative spin crossover naphthalene and nitrobenzene clathrates of the novel Fe^{II} Hofmann-like porous metal–organic framework {Fe(bpb)[Pt(CN)$_4$]}·2Guest are described (bpb = bis(4-pyridyl)butadiyne).

Porous three-dimensional (3D) metal–organic frameworks (PMOFs) exhibit useful physical properties such as electrical and hydrogen conductivity,[1] storage,[2] luminescence,[3] catalysis[4] and separation.[5] PMOFs provide synthetic accessibility, chemical robustness and easy modification to meet particular practical demands. Furthermore, they can offer tunable physical properties if prepared from bistable building blocks. Indeed, in the case of PMOFs based on 3d^6 Fe^{II} ions, the spin crossover (SCO) phenomenon can be observed with reversible switch between the diamagnetic low-spin (LS, S = 0) and the paramagnetic high-spin (HS, S = 2) states involving magnetic, optical, and structural changes in response to the change of temperature, pressure, or light irradiation.[6] It is well known that SCO characteristics (critical temperature, abruptness, completeness) are related to the chemical nature of the ligands coordinated to the Fe^{II} ion, however, they are also greatly influenced by crystal packing effects, particularly, exerted by non-coordinated inclusions (anions, solvents and guest molecules).[7] Particularly, the sensitivity of SCO in Fe^{II} PMOFs toward the guest molecules confers sensory function to the materials and makes them attractive from the viewpoint of the possible practical application as sensors.

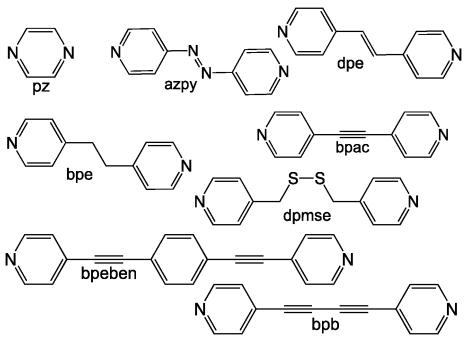

Scheme 1 Pillar ligands for {Fe(L)[M^{II}(CN)$_4$]}·G Hofmann-like PMOFs.

Cyanide-bridged Fe^{II}–M^{II} (M = Ni, Pd, Pt) bimetallic 3D networks, also known as Hofmann-like PMOFs, represent an example of materials with exceptionally abrupt hysteretic SCO and capability to sense guest molecules. Generically formulated {Fe(L)[M^{II}(CN)$_4$]}·G have been reported for L = pz,[8–10] azpy,[11] dpe,[12] bpe,[13] bpac,[14,15] dpmse[16] or bpeben[17] (Scheme 1). These SCO–PMOFs possess both accessible voids responsible for the uptake of guest molecules by the framework and coordinatively unsaturated M^{II} centres that enable oxidative addition of halogens.[10] Further development of SCO–PMOFs is guided toward increasing the pore size and pore functionality. Here we report the synthesis and characterization of two Fe^{II} Hofmann-like 3D clathrates of the unprecedented SCO–PMOF {Fe(bpb)[Pt(CN)$_4$]}·2G [G is naphthalene (**1**) or nitrobenzene (**2**)] based on the elongated ditopic ligand bis(4-pyridyl)butadiyne (bpb, Scheme 1). These clathrates exhibit cooperative SCO and, to the best of our knowledge, this new MOF system shows the highest load capacity reported up to now.

Both clathrates were synthesised by slow diffusion in multiarm-shaped vessels (see synthesis and Fig. S1 and S2 in the ESI†). They are isostructural and adopt the general topology of 3D {FeL[M(CN)$_4$]} PMOFs consisting of infinite two-dimensional {Fe[Pt(CN)$_4$]}$_\infty$ layers bridged by pillaring ligands through axially coordinated Fe^{II} ions (Fig. 1). However, in contrast to the rest of the members of the {FeL[M(CN)$_4$]} series, **1** and **2** crystallize in the triclinic $P\bar{1}$ space group.

[a] *Institut de Ciència Molecular (ICMol), Departament de Química Inorgànica, Universitat de València, C/Catedrático José Beltrán Martínez, 2, 46980 Paterna, Valencia, Spain. E-mail: jose.a.real@uv.es*

[b] *Departament de Física Aplicada, Universitat Politècnica de València, Camino de Vera s/n, 46022, Valencia, Spain*

† Electronic supplementary information (ESI) available: Experimental procedures, thermogravimetric analyses (Fig. S1), infrared spectra (Fig. S2), crystallographic data (Tables S1–S5), Mössbauer data (Table S6) and projection of structure **2** along *a* (Fig. S3). CCDC 971021–971025. For ESI and crystallographic data in CIF or other electronic format see DOI: 10.1039/c3cc48595a

‡ Permanent address: Taras Shevchenko National University, Department of Physical Chemistry, Volodymyrska Str. 64, Kyiv 01601, Ukraine.

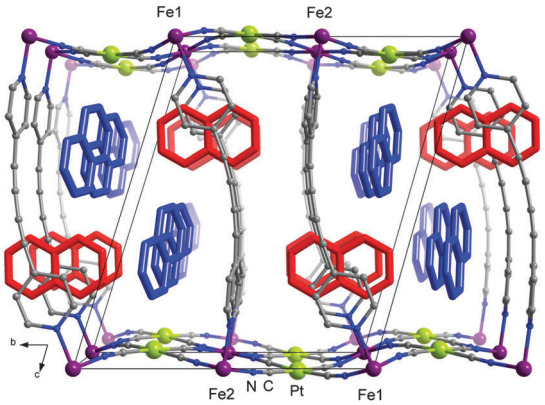

Fig. 1 Projection of the structure of **1** along *a*. Two types of guest naphthalene molecules are coloured in red and blue.

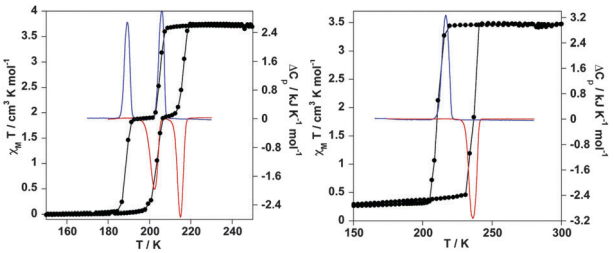

Fig. 2 Magnetic (filled circles) and calorimetric (blue and red lines refer to cooling and heating modes, respectively) measurements for **1** (left) and **2** (right).

The crystallographic parameters for both compounds are collected in Table S1 (ESI†), and selected angles and distances in Tables S2 and S3 (ESI†). The ligand bpb adopts a markedly bent conformation in contrast to other unsaturated bridging ligands mentioned above and, additionally, the pyridine moieties locate practically perpendicular to each other. Similar geometries were observed in the triply interlocked catenane SCO $[Fe(bpb)_2(NCS)_2]\cdot 1/2MeOH$ complex.[18] Due to the curvature shown by the bpb ligand, the axially elongated FeN_6 octahedrons are alternatively tilted, within the *bc* plane, in opposite directions, thereby conferring to the $\{Fe[Pt(CN)_4]\}_\infty$ layers a corrugated geometry.

Two guest molecules per unit cell are found in **1** and **2**. One is located half-way between the pyridine rings of the bpb ligand, which coordinate to Fe(1), while the second lies closer to the pyridine ring coordinated to Fe(2) (see Fig. 1 and Fig. S3, ESI†). There are numerous C···C contacts between the guest molecules and the pyridine rings changing with temperature according to expansion/contraction of the lattice due to the SCO of the Fe^{II} ions (Table S4, ESI†). These contacts influence the coordination spheres of the two Fe^{II} ions in a different way. Indeed, the averaged bond length ⟨Fe–N⟩ (*vide infra*) is slightly different for Fe(1) and Fe(2). In the case of **1**, ⟨Fe(1)–N⟩ changes from 2.13(2) Å at 250 K to 1.957(2) Å at 195 K and further remains constant upon cooling to 120 K (1.959(5) Å) where the complete transition to the LS state takes place. At 250 K, the value for ⟨Fe(2)–N⟩ is 2.14(2) Å and does not vary much upon cooling to 195 K (2.160(2) Å), but decreases to 1.966(5) Å at 120 K. Evidently, Fe(1) undergoes transition above 195 K, while Fe(2) undergoes transition below this temperature. In the case of **2**, ⟨Fe(1)–N⟩ changes from 2.175(12) Å at 250 K to 1.955(5) Å at 120 K and ⟨Fe(2)–N⟩ from 2.175(11) Å at 250 K to 1.956(5) Å at 120 K. The transition of both Fe^{II} ions takes place simultaneously.

There are two different types of pores running, respectively, along *a* and *b* axes hosting the guest molecules. The pores running along *a* are much wider than those running along *b* due to the bent shape of bpb. The cross-section of the expanded pores, defined by Fe···Fe distances through the bent ligand bpb and the corrugated $[Pt(CN)_4]^{2-}$ anions, shows *ca.* 15.87(1) Å × 6.98(1) Å at 120 K. The accessible volume[19] of the frameworks **1** (**2**) (without considering guest molecules) is 849.6 (801.8) $Å^3$ and corresponds to 53.8% (52.6%) of the unit cell volume at 120 K (1579.2 $Å^3$ (**1**) and 1523.3 $Å^3$ (**2**)). The porosity of the frameworks in **1** and **2** is larger in comparison with that found for SCO clathrates $\{FeL[Pt(CN)_4]\}$, which is 22% for pz, *ca.* 40% for azpy,[11] dpe[12] and bpac[15] and 48% for bpeben.[17]

Fig. 2 displays the magnetic and calorimetric properties of **1** and **2**. At 300 K, the $\chi_M T$ product (χ_M is the molar magnetic susceptibility and T is the temperature) is *ca.* 3.5–3.6 $cm^3\ K\ mol^{-1}$ and remains constant until approaching the SCO transition. In the case of **1**, the Fe^{II} ions undergo spin transition in two equal steps. The critical temperatures are $T_{c1}^{\downarrow}$ = 205 K and $T_{c2}^{\downarrow}$ = 188 K in the cooling mode. In the heating mode the steps appear at higher temperatures, $T_{c2}^{\uparrow}$ = 203 K and $T_{c1}^{\uparrow}$ = 216 K, thereby defining two hysteresis loops 11 K (ΔT_{c1}) and 15 K (ΔT_{c2}) wide. In **2**, the transition takes place in one step at $T_c^{\downarrow}$ = 210 K and $T_c^{\uparrow}$ = 237 K with the hysteresis loop at 27 K. In the low temperature region the $\chi_M T$ values are near to zero.

The calorimetric measurements performed on samples of **1** and **2** and the anomalous heat capacity ΔC_p *vs.* T are shown in Fig. 2. The enthalpy (ΔH) and entropy (ΔS) average variations associated with the spin transitions are: ΔH = 9.45 kJ mol^{-1} and ΔS = 44.9 J K^{-1} mol^{-1} for the high temperature hysteresis loop and ΔH = 8.62 kJ mol^{-1} and ΔS = 44.1 J K^{-1} mol^{-1} for the low temperature hysteresis loop of **1**; ΔH = 19.29 kJ mol^{-1} and ΔS = 86.3 J K^{-1} mol^{-1} for **2**. These values are typical for cooperative SCO in Hofmann-like clathrates of Fe^{II}.[6c]

The Mössbauer spectrum of **1** at 80 K consists of two LS doublets with almost identical isomer shift values (δ^{LS1} = 0.47(2) mm s^{-1} and δ^{LS2} = 0.49(2) mm s^{-1}) and different quadrupole splitting parameters (ΔE_Q^{LS1} = 0.32(1) mm s^{-1} and ΔE_Q^{LS2} = 0.16(2) mm s^{-1}) (Fig. 3, left). The relative areas A of the two doublets have a ratio close to 1 : 1. Evidently, the doublets correspond to two different Fe^{II} sites observed in the crystal lattice of the compound. Upon increasing the temperature to 199 K and according to the transition of one of the Fe^{II}-sites to the HS state, the spectrum shows disappearance of a LS doublet and instead a HS doublet is detected (δ^{HS} = 1.11(2) mm s^{-1} and ΔE_Q^{HS} = 1.53(4) mm s^{-1}). The parameters of the second LS doublet remain almost unchanged at this temperature (δ^{LS} = 0.47(1) mm s^{-1} and ΔE_Q^{LS} = 0.14(3) mm s^{-1}). Upon heating to 300 K, the spectrum of **1** shows two overlapping equally populated HS doublets with similar isomer shift values (δ^{LS1} = 1.05(1) mm s^{-1} and δ^{HS2} = 1.06(1) mm s^{-1}) and strongly different quadrupole splitting parameters (ΔE_Q^{HS1} = 0.51(2) mm s^{-1} and

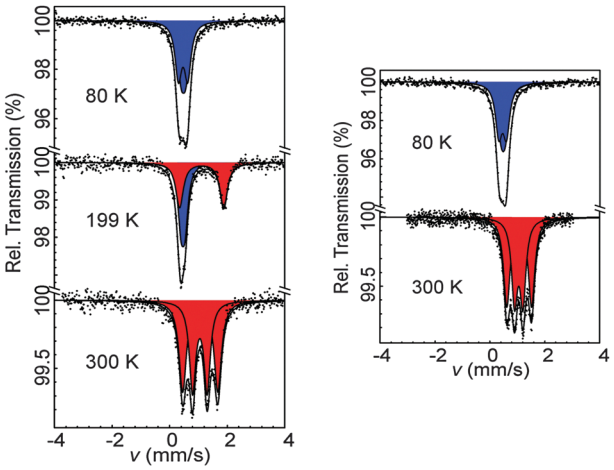

Fig. 3 Mössbauer spectra of **1** (left) and **2** (right). Red and blue colours represent the HS and LS components of the spectra.

ΔE_Q^{HS2} = 1.21(2) mm s^{-1}). The ΔE_Q values reflect different geometric distortion of the corresponding coordination polyhedrons. The spectra of **2** recorded at 80 and 300 K in the LS and HS states, respectively, are very similar to those of **1** at the same temperatures (Fig. 3, right; Table S6, ESI†).

In conclusion we have reported the synthesis, structure, spectroscopic, magnetic and calorimetric characterization of a new type of Hofmann-like SCO–MOFs exhibiting large thermal hysteresis and the largest effective porosity among Hofmann-like SCO–PMOF reported up to now. The host framework {Fe(bpb)[$Pt(CN)_4$]} displays distinct magnetic behaviour depending on the nature of the guest molecule enclathrated in the pores (naphthalene or nitrobenzene), a fact which in principle confers to the host system a sensory function. Extended studies of the structure–property relationship of these materials are in progress.

The Spanish MINECO, FEDER (CTQ2010-18414) and the GV (PROMETEO/2012/049) are acknowledged for funding. MS thanks the EU for a Marie Curie fellowship (IIF-253254). LPL thanks the GV for a pre-doctoral fellowship. We acknowledge Prof. P. Gütlich and Dr V. Ksenofontov from the University of Mainz (Germany) for providing access to Mössbauer spectrometers.

Notes and references

1 (*a*) M. Yoon, K. Suh, S. Natarajan and K. Kim, *Angew. Chem., Int. Ed.*, 2013, **52**, 2688–2700; (*b*) A. Morozan and F. Jaouen, *Energy Environ. Sci.*, 2012, **5**, 9269–9290.
2 (*a*) M. P. Suh, H. J. Park, T. K. Prasad and D.-W. Lim, *Chem. Rev.*, 2012, **112**, 782–835; (*b*) T. A. Makal, J.-R. Li, W. Lu and H.-C. Zhou, *Chem. Soc. Rev.*, 2012, **41**, 7761.
3 J. Rocha, L. D. Carlos, F. A. A. Paz and D. Ananias, *Chem. Soc. Rev.*, 2011, **40**, 926.
4 (*a*) M. Yoon, R. Srirambalaji and K. Kim, *Chem. Rev.*, 2012, **112**, 1196–1231; (*b*) L. Ma and W. Lin, *Top. Curr. Chem.*, 2010, **293**, 175–205.
5 (*a*) Y. Yu, Y. Ren, W. Shen, H. Deng and Z. Gao, *TrAC, Trends Anal. Chem.*, 2013, **50**, 33–41; (*b*) J.-R. Li, J. Sculley and H.-C. Zhou, *Chem. Rev.*, 2012, **112**, 869–932.
6 (*a*) ed. P. Gütlich and G. Goodwin, *Top. Curr. Chem.*, 2004, vol. 233–235; (*b*) A. B. Gaspar, V. Ksenofontov, M. Seredyuk and P. Gütlich, *Coord. Chem. Rev.*, 2005, **249**, 2661–2676; (*c*) M. C. Muñoz and J. A. Real, *Coord. Chem. Rev.*, 2011, **255**, 2068–2093; (*d*) *Spin-Crossover Materials: Properties and applications*, ed. M. A. Halcrow, John Wiley & Sons Ltd, 2013.
7 P. Gütlich and H. A. Goodwin, *Top. Curr. Chem.*, 2004, **233**, 1–47.
8 V. Niel, J. M. Martinez-Agudo, M. C. Muñoz, A. B. Gaspar and J. A. Real, *Inorg. Chem.*, 2001, **40**, 3838–3839.
9 (*a*) M. Ohba, K. Yoneda, G. Agusí, M. C. Munoz, A. B. Gaspar, J. A. Real, M. Yamasaki, H. Ando, Y. Nakao, S. Sakaki and S. Kitagawa, *Angew. Chem., Int. Ed.*, 2009, **48**, 4767–4771; (*b*) P. D. Southon, L. Liu, E. A. Fellows, D. J. Price, G. J. Halder, K. W. Chapman, B. Moubaraki, K. S. Murray, J.-F. Letard and C. J. Kepert, *J. Am. Chem. Soc.*, 2009, **130**, 10998–11009.
10 G. Agusti, R. Ohtani, K. Yoneda, A. B. Gaspar, M. Ohba, J. F. Sanchez-Royo, M. C. Munoz, S. Kitagawa and J. A. Real, *Angew. Chem., Int. Ed.*, 2009, **48**, 8944–8947.
11 G. Agustí, S. Cobo, A. B. Gaspar, G. Molnar, N. O. Moussa, P. A. Szilagyi, V. Palfi, C. Vieu, M. C. Muñoz, J. A. Real and A. Bousseksou, *Chem. Mater.*, 2008, **20**, 6721–6732.
12 F. J. Muñoz-Lara, A. B. Gaspar, M. C. Muñoz, M. Arai, S. Kitagawa, M. Ohba and J. A. Real, *Chem.–Eur. J.*, 2012, **18**, 8013–8018.
13 R. Ohtani, M. Arai, A. Hori, M. Takata, S. Kitao, M. Seto, S. Kitagawa and M. Ohba, *J. Inorg. Organomet. Polym. Mater.*, 2013, **23**, 104–110.
14 C. Bartual-Murgui, L. Salmon, A. Akou, N. A. Ortega-Villar, H. J. Shepherd, M. C. Muñoz, G. Molnár, J. A. Real and A. Bousseksou, *Chem.–Eur. J*, 2012, **18**, 507–516.
15 C. Bartual-Murgui, N. A. Ortega-Villar, H. J. Shepherd, M. C. Muñoz, L. Salmon, G. Molnár, A. Bousseksou and J. A. Real, *J. Mater. Chem.*, 2011, **21**, 7217.
16 N. F. Sciortino, K. R. Scherl-Gruenwald, G. Chastanet, G. J. Halder, K. W. Chapman, J.-F. Létard and C. J. Kepert, *Angew. Chem., Int. Ed.*, 2012, **51**, 10154–10158.
17 F. J. Muñoz-Lara, A. B. Gaspar, M. C. Muñoz, V. Ksenofontov and J. A. Real, *Inorg. Chem.*, 2012, **52**, 3–5.
18 N. Moliner, C. Muñoz, S. Létard, X. Solans, N. Menéndez, A. Goujon, F. Varret and J. A. Real, *Inorg. Chem.*, 2000, **39**, 5390–5393.
19 A. Spek, *Acta Crystallogr., Sect. D: Biol. Crystallogr.*, 2009, **65**, 148–155.